Università
degli Studi
di Ferrara

DOCTORAL COURSE IN PHYSICS

CYCLE XXXIV

COORDINATOR Prof. Eleonora Luppi

Testing three-body forces in light nuclei:
Lifetime measurements in ^{20}O in the femtosecond range

Scientific/Disciplinary Sector (SDS) FIS/04

Candidate

Dr. Zanon Irene

Supervisors

Prof. Bettoni Diego

Dr. Goasduff Alain

Dr. Clément Emmanuel

Years 2018/2021

Introduction

There are more things in heaven and earth, Horatio,

than are dreamt of in your philosophy.

W. Shakespeare

Exotic light nuclei have been attracting a lot of attention in the study of nuclear interaction and the oxygen isotopic chain, being known from the proton to the neutron drip line, constitutes a perfect playground. The neutron drip line, in particular, presents an anomalous pattern with respect to the neighbouring isotopic chains, that can be explained only when taking into consideration the contribution of three-body forces. From standard shell model calculations using two-body forces, the ^{28}O is expected to be the last bound isotope, while experimentally the ^{24}O has been proven to be the heaviest bound oxygen isotope. The dripline is correctly reproduced if three-body forces are included in the calculations. However, due to experimental difficulties in populating neutron-rich exotic nuclei, spectroscopic information is still scarce but essential to build a solid theoretical model. In fact, spectroscopic quantities, such as excitation energy, branching ratios or lifetime of the states, can help quantify the contribution of three-body forces in the oxygen chain.

The ^{20}O nucleus was chosen as a study case. The 2^+_2 and 3^+_1 states of this nucleus are dominated by a mixed $(d_{5/2})^3(s_{1/2})^1$ neutron configuration. It has been observed that the $d_{5/2}$, $s_{1/2}$ and $d_{3/2}$ orbitals are sensitive to the three-body forces. Therefore, information on the electromagnetic properties of the 2^+_2 and 3^+_1 states is fundamental to better understand the influence of the three-body forces in light nuclei.

An experiment aimed at measuring the lifetimes of 2^+_2 and 3^+_1 states of ^{20}O was performed at the GANIL laboratory in February 2020. The nucleus of interest was populated using a one-neutron transfer reaction from a ^{19}O radioactive ion beam provided by the SPIRAL1 complex and impinging on a 0.3 mg/cm^2 thick CD_2 target. The lifetimes of the 2^+_2 and 3^+_1 states were measured using the Doppler Shift Attenuation method, suited for lifetimes in the range of tens to hundreds of femtoseconds.

The study of three-body forces has been extended to ^{16}C. The nucleus was populated in a direct reaction from radioactive beam in an experiment performed at the Argonne National Laboratories (Illinois, U.S.A) in July 2021. A third experiment, aimed at studying ^{24}Ne with

analogous techniques has been proposed at GANIL. These experiments, by populating the nuclei of interest in a one-neutron transfer reaction, guarantee the control on the population of the states and allow for precise lifetime measurements.

In Chapter 1, the physical case is introduced. First, two different approaches for the description of the nuclear system are described, focusing on the inclusion of three-body forces in the theory. Then the influence of three-body forces in the oxygen isotopic chain is illustrated, with particular interest on the ^{20}O, which represents the study case of this work.

In Chapter 2, the experimental details are presented. The SPIRAL1 complex in GANIL, employed for the production of the radioactive ^{19}O beam, as well as the AGATA-MUGAST-VAMOS setup are presented. In particular, the characteristics and the performances of these detectors and the procedure for the calibration are explained. Moreover, the experimental technique for lifetime measurement is illustrated.

In Chapter 3, the optimization of the apparatus and of the Monte Carlo simulations are illustrated. Realistic parameters are added to the simulation code in order to have better control of the possible systematic errors on the final lifetime results.

In Chapter 4, the results are presented. First, the excited states and the γ-ray transitions are studied and the branching ratios are calculated. Then, the lifetimes of the 2^+_2 and 3^+_1 states are measured. The different procedures that have been followed in order to test the validity of the measurement are presented. At last, the systematic errors of the measurements are estimated.

In Chapter 5, the theoretical results are discussed. First, a short review of *ab initio* calculations is presented. Then, the experimental results are compared to recent *ab initio* calculations and to the results obtained in a previous experiment. New calculations are also introduced. Finally, shell model calculations using the ANTOINE code are presented and the predicted reduced transitions probabilities are compared to those calculated from the lifetimes measured.

In the Conclusions, the experiment and the results are summarized. Moreover, future projects are introduced. In particular, the experiment devoted to the study of ^{16}C and the first preliminary results are presented, as well as the proposal for studying ^{24}Ne. These two experiments, together with the study of ^{20}O, are expected to shed light on the role of three-body forces in *ab initio* calculations for the description of this region.

Contents

1 Nuclear theory

The problem of developing a unified theoretical framework able to describe nuclear systems over the whole nuclear chart is the core of nuclear physics. Over the years, many different theories have been developed and they usually focus either on one region of the nuclear chart or on the description of specific observables. In this chapter, two theories are illustrated: the nuclear shell model and the effective field theory. The basic ideas behind these two methods are explained and then the focus is placed on the prediction capabilities and their limits. These two theories, however, are not to be considered incompatible, but rather two different approaches to the same problem: describing the atomic nucleus and pushing the predictive power to more exotic species, in order to grasp a better comprehension of nuclear forces. To do so, both methods need to consider the inclusion of three-body forces, that over the years have been proven to be a fundamental ingredient in the description of certain regions, such as the neutron-rich oxygen isotopes. The physical interest in this region is presented, as well as the previous experimental measurements and the theoretical calculations. Finally, the study case for the present work is explained in details.

1.1. The nuclear shell model

The atomic nucleus is a complex many-body system composed of two types of nucleons: protons and neutrons. The nucleus can be described using a non-relativistic Hamiltonian [1]

$$H = \sum_{i=1}^{A} t_i + \frac{1}{2} \sum_{i,j=1}^{A} V_{i,j}, \tag{1.1}$$

where the first term represents the kinetic energy of the nucleons and the second term the interaction between them. The wave function of the nucleus can be generalized as a set of wave functions describing the position $\overrightarrow{r_i}$, spin $\overrightarrow{s_i}$ and isospin $\overrightarrow{\tau_i}$ of the nucleons. The problem of the description of the nucleus is reduced to the solution of the Schrödinger equation. However, this approach is feasible only for systems composed of few nucleons, and the computational power required escalates rapidly for heavier systems.

For the solution of this problem, it is useful to re-write the Hamiltonian as [2]

$$H = H_0 + H_{res} \tag{1.2}$$

where $H_0 = \sum_i \{t_i + U_i\}$ is the term describing the motion of nucleons and H_{res} is the residual interaction. Given that the one-body potential U is accurately determined, the solution of the Schrödinger equation will focus on the first term, while the H_{res} part can be treated as a small perturbation.

A natural choice for the description of U is the harmonic oscillator potential $U(r) = \frac{1}{2}m\omega^2 r^2$, similarly to the atomic model. In fact, both the atom and the nucleus are systems of fermions moving in a potential. Each harmonic oscillator can fit $2L+1$ nucleons according to the Pauli exclusion principle, where protons and neutrons, being different particles, fill the shells independently.

When observing the Mendeleev table, the elements of the last column present an ionization energy of the electron significantly higher with respect to their neighbours. These elements, corresponding to $Z = 2, 10, 18, 36, 54, 86$, are known as noble gases and are characterized by having an ionization energy higher with respect to their neighbours, which makes them less reactive from a chemical point of view. A similar pattern is observed in the Segrè chart. From experimental observation of the binding energy, some nuclei appear to be more stable than others, in correspondence to the number of protons Z or neutrons $N = 2, 8, 20, 28, 50, 82, 126$. These nuclei are called *semi-magic* when either N or Z correspond to one of these numbers, and *doubly magic*, when both Z and N correspond to one of these numbers. These nuclei are characterized by having an excitation energy of the first excited state that is higher with respect to the neighbouring nuclei and they typically present a spherical shape.

The harmonic oscillator potential provides an accurate description of the nucleus only for light systems with $Z < 20$ and fails in reproducing the magic numbers for heavier systems. A possible solution was researched in a more realistic potential, such as the Wood-Saxon potential [3]

$$V(r) = \frac{-V_0}{1 + e^{(r-R)/a}}, \tag{1.3}$$

where V_0 is the parameter representing the well depth, optimized in order to reproduce the nucleon separation energies, $R = 1.25A^{\frac{1}{3}}$ fm represents the nuclear radius and a the skin thickness. However, the realistic potential did not predict the magic numbers observed experimentally.

The fundamental ingredient that was missing from this model was the spin-orbit term. The inclusion of this term to the single-particle potential U_i comes from the independent works of Mayer [4] and Haxel, Jansen and Suess [5], inspired by the similarity with the spin-orbit interaction in atomic physics and by experimental evidences coming from scattering experiments. This term can be written as [2]

$$V_{so} = -\frac{2}{\hbar^2}\alpha(r)\widehat{l} \cdot \widehat{s}, \tag{1.4}$$

where $\alpha(r)$ represents the spin-orbit strength. The scalar product has the effect of rearranging the levels with respect to the previous formulation.

If we consider the total angular momentum as $\widehat{j} = \widehat{l} + \widehat{s}$, the scalar product can be written as

$$\widehat{l} \cdot \widehat{s} = \frac{1}{2}(\widehat{j}^2 - \widehat{l}^2 - \widehat{s}^2). \tag{1.5}$$

So written, $\widehat{j}^2$, $\widehat{l}^2$ and $\widehat{s}^2$ form a set of commuting angular operators.

The spin-orbit term has the effect of breaking the degeneracy in the $j = l \pm \frac{1}{2}$ coupling and it modifies the shell closures, now predicted at 28, 50, 82, 126, as observed experimentally. The single-particle levels obtained with this model are shown in Figure 1.1.

This model, also called *independent-particle model*, provides an accurate description of nuclei that are close to shell closures, namely those nuclei where the H_{res} term of the Hamiltonian can be neglected. This approximation is not valid for nuclei that are far from shell closures, where the residual interaction between the nucleons plays an important role in the description of the nucleus. For this reason, a different approach is needed.

1.1.1. The interacting shell model

The *interacting shell model*, or simply shell model, aims at including the effects coming from the nucleon-nucleon interaction in the description of the nucleus in order to extend the formulation to nuclei far from the shell closures. With the increase of the number of nucleons, calculations become more complicated and require more computational power. Hence, to solve the problem some approximation must be considered.

The first fundamental step is the restriction of the calculation to a valence space that is smaller than the Hilbert space. A natural choice, for example, is to restrict the calculations so that only the nucleons outside of the shell closures or sub-closures are considered in the interaction, while the nucleons inside the closed shells behave as an inert core.

Once the valence space has been determined, it is necessary to construct an effective Hamiltonian to solve the Schrödinger equation. The typical procedure starts from nucleon-nucleon (NN) realistic potentials (such as Argonne, Paris, Bonn, N3LO, ...) and then the repulsive part of the NN force is renormalized using different methods (G-matrix computation, $V_{\mathrm{low\,k}}$, ...) [6].

Nowadays, effective Hamiltonians derived from realistic NN potentials still struggle to reproduce both bulk properties (such as binding energies, shell closure, position of the drip lines, charge radii, ...) and spectroscopic features (energy of the states, reduced transition probabilities, ...). However, NN potentials are now considered to be "nearly-perfect" [7]. Moreover, it has been observed that the matrix elements do not depend strongly on the chosen NN potential nor on the normalization method. Hence, the disagreement between theory and experimental observations cannot be connected to the NN interaction and the missing element must come from a deeper level. The solution was searched in the inclusion of three-body forces (3N) in the construction of the effective interaction.

For this purpose, the separation of the Hamiltonian into an unperturbed H_0 and a residual H_{res} part is not convenient anymore. An alternative formulation was provided [8]

$$H = H_m + H_M, \tag{1.6}$$

where H_m represents the *monopole* part, while H_M represents the *multipole* part. The

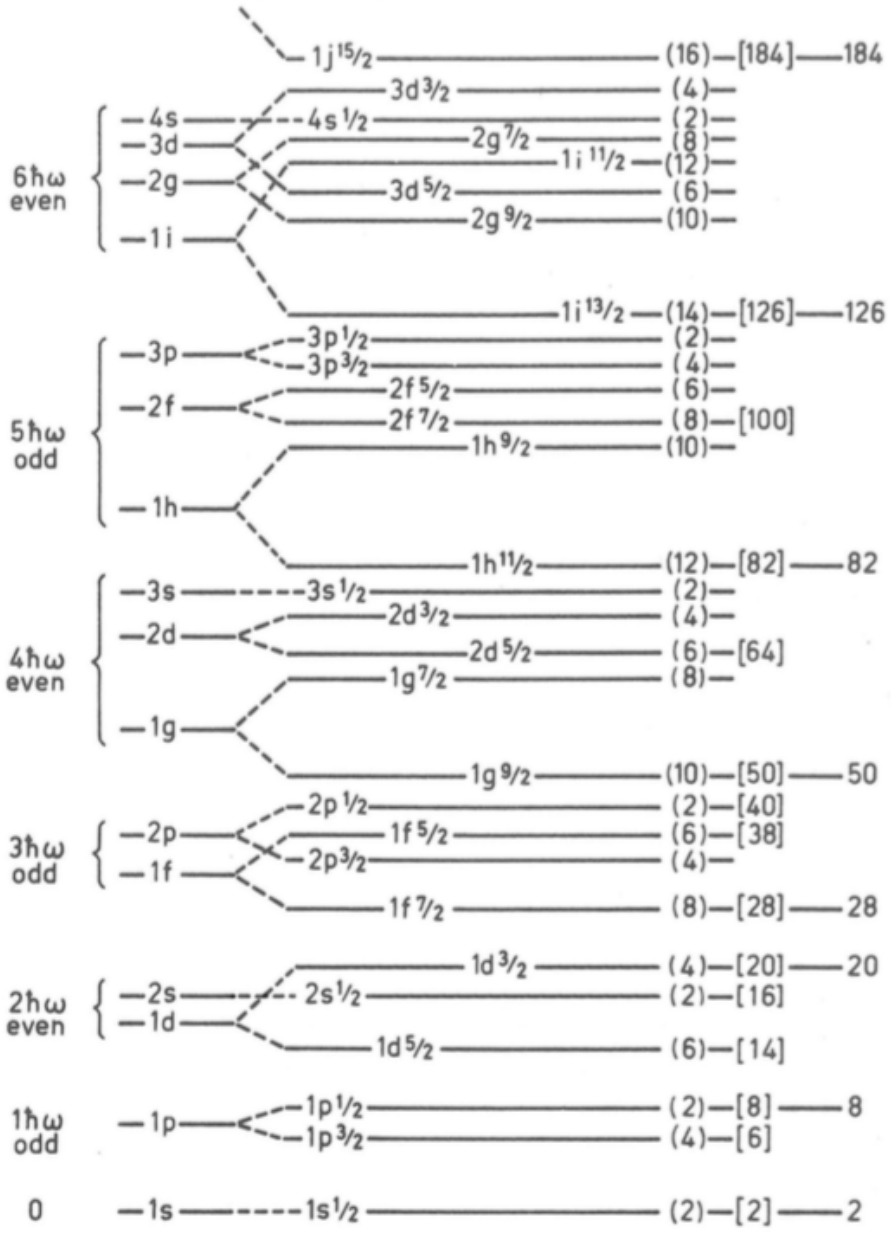

Figure 1.1.: Single-particle spectrum showing the contributions coming from the $l \pm \frac{1}{2}$ splitting due to the spin-orbit interaction. The new shell closures, reported on the right, correspond to the magic numbers observed experimentally. Figure taken from [2].

monopole term refers to the spherical mean-field part and contains the kinetic part of the Hamiltonian, as well as the nucleon interaction. This part is responsible for the global saturation properties and the evolution of the spherical single particle levels towards heavier or more exotic nuclei. The multipole part, instead, includes pairing, quadrupole and other forces that are responsible for the collective behaviour of the nucleus. This second part is well described by a two-body potential [7]. For the purpose of this work, only the monopole term will be treated.

The monopole term of the Hamiltonian can be written as

$$H_{mon} = \sum_i \varepsilon_i n_i + \sum_{i \leq j} a_{ij} n_{ij} + \sum_{i \leq j} b_{ij} T_{ij} + \sum_{ijk} a_{ijk} n_{ijk} + \sum_{ijk} b_{ijk} T_{ijk} \tag{1.7}$$

where n_i and T_i are the number and isospin operators. The first term contains the intrinsic energy of the particle, the second and third terms contains the information on the NN interaction and finally the fourth and fifth are related to the 3N forces. Many studies have observed that the contribution of residual 3N force is much smaller with respect to the 1- and 2-body part [9]. However, in some region such as the *sd* and *pf* shells, these contributions are fundamental to explain the discrepancies between theory and experimental observations.

1.2. Effective field theory

Chiral Effective Field Theory (EFT) is an approach that permits a systematic and model-independent derivation of the nucleon forces starting from the Quantum Chromodynamic (QCD) symmetries and it allows for the study of the properties of hadronic systems, such as the atomic nucleus [10]. Contrary to the shell model, where nucleons were considered as degrees of freedom of the system, in EFT quarks and gluons are the chosen degrees of freedom. Common approaches only consider the light quarks (u, d, s) at the energy scale of the pion mass $Q \sim m_\pi$, where the strong coupling constant α_S is of order 1 and cannot be treated perturbatively.

The interaction between nucleons happens via the exchange of pions and short-range contact interactions, described via Feynman diagram, as shown in Figure 1.2. The contribution of the nuclear forces are separated depending on the expansion in power of Q/Λ_b, where Λ_b represents the breakdown scale, which is around 500 MeV. The calculations start from the leading order (LO) $O(Q^0/\Lambda_b^0)$ and continue with next to leading order (NLO) $O(Q^1/\Lambda_b^1)$ and further expansions. Moreover, EFT allows for the natural inclusion of many-body forces into the calculations, starting from three-, four-body forces.

The derivation of 3N and 4N forces up to N^3LO has been achieved only recently and their inclusion in the calculations is still challenging, since they increase the computational time exponentially. Complete calculations including the contribution of many-body forces, at the moment, have been performed only for small systems ($A \leq 3$), considering N^3LO NN and N^2LO 3N forces [11]. Moreover, the contribution of the NN forces is expected to always be dominant with respect to 3N and 4N forces, as well as the 3N forces contribution is expected to be more important than the 4N. This means that, in cases where the NN forces alone provide a good agreement with experimental data, one is tempted to neglect the many-body parts in the calculations. However, many-body forces have been proven to be fundamental for

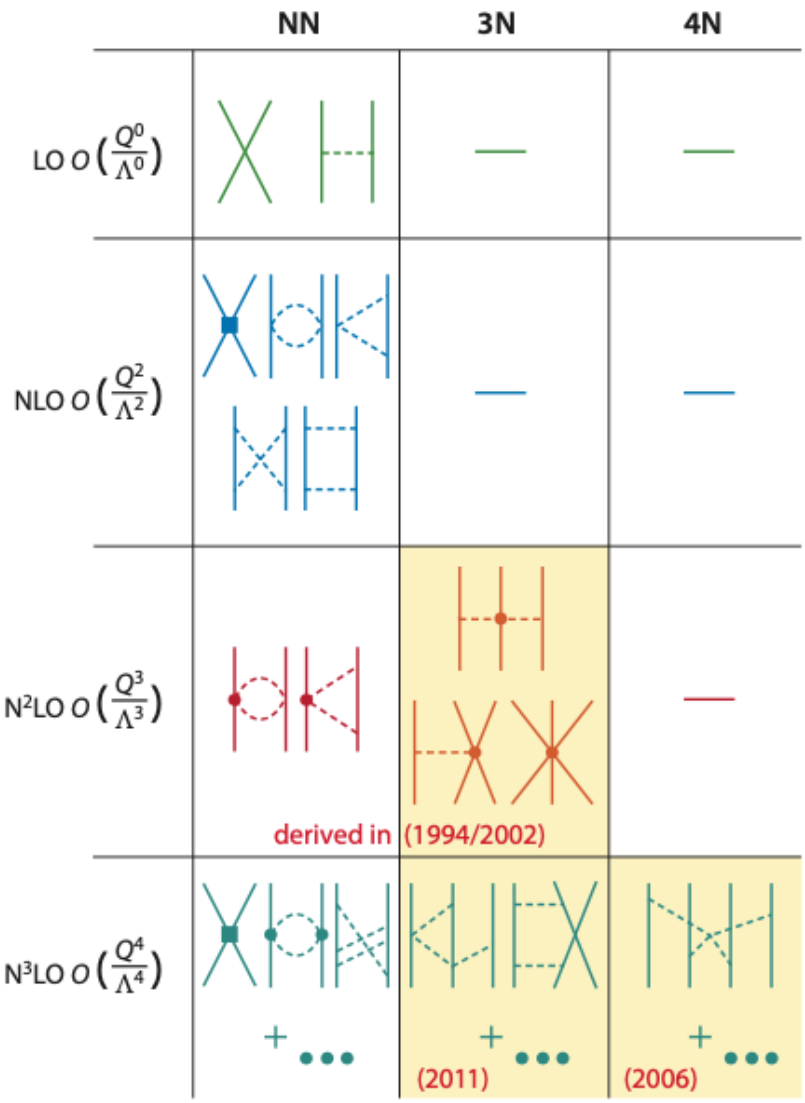

Figure 1.2.: Feynman diagrams representing the chiral effective field theory for nuclear forces, where the nucleons are represented by solid lines while the pions are represented by dashed lines. Highlighted in yellow, the contributions of the many-body forces are presented. Figure taken from [11].

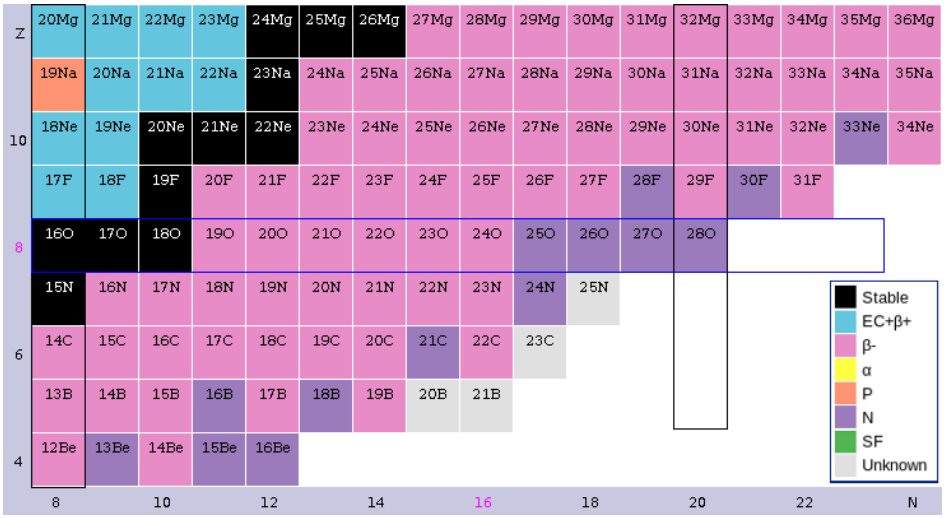

Figure 1.3.: Nuclear chart focused on the neutron-rich region of *sd* nuclei. The color scheme of the chart represents the main decay mode and the legend is reported on the bottom right of the figure. In particular, the nuclei reported purple decay through neutron emission and are unbound. Figure adapted from [12].

the description of nuclei, especially in the study of neutron rich nuclei and in the evolution of shell structure. A striking example of the powerful prediction capabilities of these calculations is provided by the puzzling case of neutron-rich oxygen isotopes.

1.3. The neutron-rich oxygen isotopes

The oxygen isotopic chain is a good study case for exploring the evolution of the nuclear forces in light nuclei and, in particular, the neutron-rich isotopes present some interesting phenomena.

According to standard shell-model calculations, the oxygen neutron drip line is positioned on the ^{28}O nucleus, that is expected to be a doubly-magic nucleus with $Z = 8$ and $N = 20$. The twelve neutrons above the *p*-shell are filling the *sd* shells and the single-particle energies (SPE) of the orbitals $d_{5/2}$, $s_{1/2}$ and $d_{3/2}$ are all expected to be negative. However, experimentally, the ^{24}O was observed to be the heaviest bound oxygen isotope, setting the drip line four neutrons before the shell-model predictions. Moreover, this nucleus has shown the characteristics of a doubly-magic nucleus, shifting the magic neutron number from $N = 20$ to $N = 16$ for the oxygen isotopic chain [13]. This new shell closure was discovered experimentally by Kanungo *et al.* [14], that determined the spherical shape of the nucleus using a one-neutron removal reaction, and by Hoffman *et al.* [15], that instead focused on the excitation energy spectrum and observed the first excited state to be at high energy.

The location of the neutron drip line for oxygen is especially puzzling if we consider that, adding one proton to the system, the drip line is shifted to $N = 22$, namely ^{31}F, which has six neutrons more than the oxygen case (see Figure 1.3). Calculations that consider only NN forces failed to reproduce this anomaly, that can be explained only by including the contribution of 3N forces.

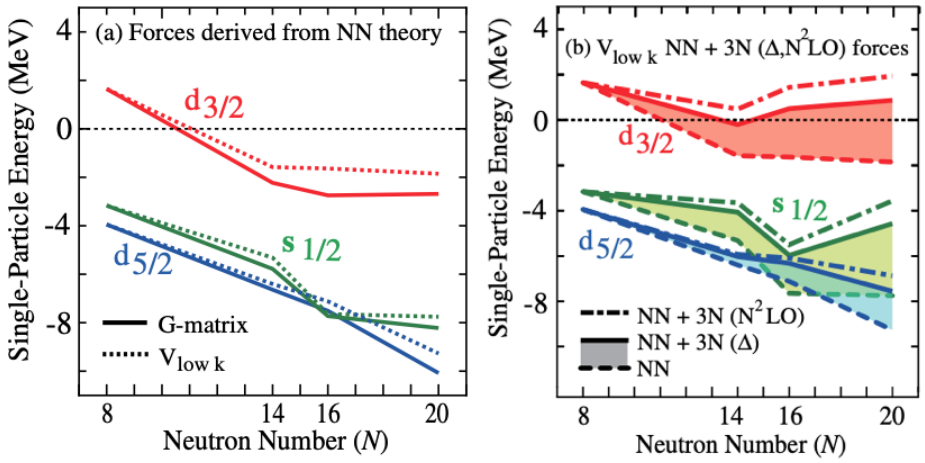

Figure 1.4.: Single-particle energies of the $d_{5/2}$, $s_{1/2}$ and $d_{3/2}$ orbitals as a function of the neutron number in oxygen isotopes calculated using standard calculations derived from NN forces (left) and $V_{\text{low k}}$ NN + chiral EFT 3N interactions at N^{2}LO (right). While the first case places the neutron drip line at ^{28}O, the second case predicts the ^{24}O to be the heaviest bound isotope, in agreement with experimental observations. Figure adapted from [16].

The work of Otsuka *et al.* [16] correctly reproduced the drip line of the oxygen isotopic chain. Standard calculations performed using forces derived by NN theory were compared to calculations that used $V_{\text{low k}}$ NN + chiral EFT 3N interactions at N^{2}LO. The effect of the 3N forces on the position of the SPE of the orbitals is shown in Figure 1.4. In standard calculations, the $d_{3/2}$ orbital has negative SPE for oxygen isotopes with $N > 10$. Thus, the isotopes with $N = 17, 18, 19, 20$, which fill the $d_{3/2}$ orbital, result to be bound. The addition of 3N forces in the calculations has the effect of increasing the gap between the $d_{5/2}$ and $s_{1/2}$ orbitals and the $d_{3/2}$. In particular, the SPE of the latter one are pushed to positive value: the isotopes with $N > 16$ become unbound, as observed experimentally.

The idea that the monopole interaction between the $d_{5/2}$ and $d_{3/2}$ orbitals was too attractive was already suggested by Zuker [17]. The research of a repulsive component that could cancel the contribution of the NN forces was addressed to 3N forces.

Over the years, other approaches have been attempted to describe this region. In particular, numerous *ab initio* many-body calculations have been developed to explore medium-mass nuclei [11]. The different methods can be divided into two different types.

The first type is based on valence-space Hamiltonians, where the degrees of freedom are reduced by considering the many-body system as composed of an inert core and the remaining valence nucleons outside of the closed shell. Calculations using In-Medium Similarity Renormalization Group (IM-SRG) and Coupled-Cluster Effective Interaction (CCEI) methods take the *sd*-shell as valence space, while Many-Body Perturbation Theory (MBPT) extends the space to the shells $sdf_{7/2}p_{3/2}$. These calculations were used to calculate the ground-state energy of oxygen isotopes with respect to the ^{16}O doubly-magic nucleus, and then compared to experimental data. The best agreement with the experimental data was obtained with the MBPT, namely the one with the extended valence space, but the three methods were consistent on the general binding energy trend in the region, as shown in Figure 1.5 (left).

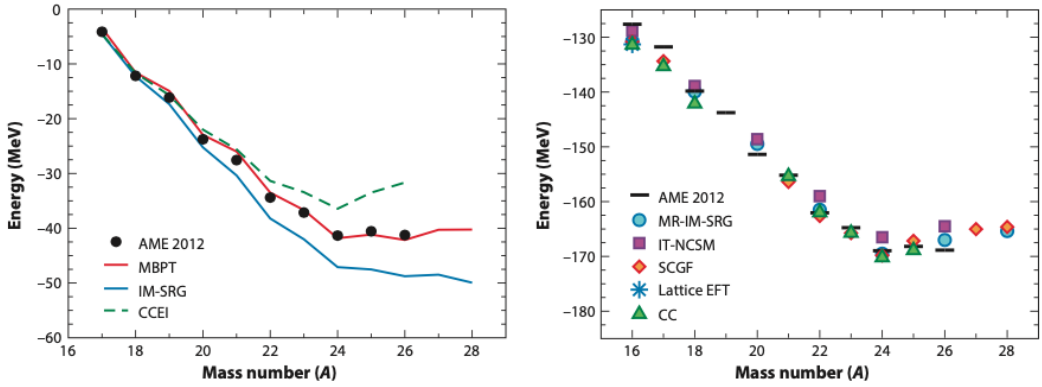

Figure 1.5.: (right) Ground-state energy of the oxygen isotopes with respect to the ^{16}O doubly-magic nucleus. The experimental data are compared to three theoretical calculations: MBPT, IM-SRG and CCEI. (left) Ground-state energy of the oxygen isotopes. The experimental data are compared to three theoretical calculations: CC, (MR-)IM-SRG, SCGF and Lattice EFT. Figure taken from [11].

The second method is obtained in large many-body spaces and it relies on different approximations in order to reduce the computational workload. The ground-state energy of the oxygen isotopes was calculated using different methods: the Coupled Channels (CC), the Multireference IM-SRG (MR-IMSRG), the Self-Consistent Green's Functions (SCGF) and the Lattice EFT methods. Again, these calculations agree with the experimental data and with each other within a few percent, as shown in Figure 1.5 (right).

Nowadays, the importance of the 3N is well established and has been proven for different regions of the nuclear chart. Numerous experiments, devoted to measuring different quantities such as charge radii in calcium isotopes [18], $\beta-$decay lifetimes in tin isotopes [19] and elastic proton scattering on ^{10}C [20] permitted the testing of *ab initio* calculations. However, the quantification of their influence is still to be determined. To do so, new measurements are needed.

Electromagnetic γ decays represent good tools to investigate the influence of 3N forces in *ab initio* calculations. Electromagnetic properties of oxygen and carbon isotopes, in particular, have been proven to be particularly sensitive to the influence of these forces [21] and therefore constitute good study cases.

These nuclei, however, present experimental difficulties, especially when approaching the neutron drip line and extracting electromagnetic properties, such as excitation energies, branching ratios and reduced transition probabilities, is still a difficult task.

1.4. Electromagnetic transitions

In a nuclear reaction, the final nucleus is often created in an excited state. The nucleus then de-excites by evaporating particles, such as protons, neutrons, electrons, α-particles, or by emitting electromagnetic radiations. These processes are not mutually exclusive, and often the second follows the first. When the nucleus de-excites via electromagnetic radiation, it emits γ rays, which are photons produced in nuclear reaction with a typical energy range from hundreds of keV to tens of MeV.

If we consider a nucleus of mass M_A that decays from an excited state of energy E_i to a final state E_f via emission of a γ ray, for the energy conservation law we know that

$$E_\gamma = E_i - E_f - T_R \equiv \Delta E - \frac{E_\gamma^2}{2M_A c^2}, \tag{1.8}$$

where the recoil energy is $T_R = \frac{E_\gamma^2}{2M_A c^2}$. Two solutions exist for the second-order equation (1.8), but only the positive solution has physical meaning and corresponds to

$$E_\gamma = M_A c^2 \left(-1 + \sqrt{1 + \frac{\Delta E}{2M_A c^2}} \right). \tag{1.9}$$

However, since Mc^2 is typically of the order of 10-100 GeV while ΔE is of the order of 0.1-10 MeV, we can assume the recoil energy to be much smaller with respect to ΔE and write the solution as

$$E_\gamma = \Delta E + \frac{(\Delta E)^2}{2M_A c^2}. \tag{1.10}$$

Therefore, by measuring the energy of the γ ray emitted by the nucleus, we can obtain information on the energy of the excited states. Combined with the measurement of the intensity of the γ-ray peaks, angular distribution or with time measurements, it is possible to obtain information on other useful properties of the excited states such as the branching ratios, the multipolarity of the transition or the lifetime of the state. The study of the nucleus from the information carried by the emitted γ ray is called γ-ray spectroscopy.

1.4.1. From classical interpretation to quantum selection rules

The γ rays emitted by the nucleus can have a magnetic or electric character depending on the spacial symmetry of the radiation. A static distribution of charge or current generates a static electric and magnetic field respectively, while a variable distribution generates a radiation field. These fields can then be described in term of their multipolarity L and of their electric or magnetic character.

The case of $L = 1$ is called dipole. In the case of an electric dipole, it is constituted of two opposite charges $\pm q$ separated by a distance $\vec{z}$ and it written as $\vec{d} = q\vec{z}$. A magnetic dipole, instead, is generated by a circular current loop circumscribing an area A and is written as $\vec{\mu} = i\vec{A}$, where $\vec{A}$ corresponds to the normal of the considered area. In particular, if we consider the current as a flux of charges q moving at a velocity v, the dipole can be re-written as $\vec{\mu} = q\vec{r} \times \vec{v}$.

If we consider a parity transformation, we observe that the electric and magnetic dipole behave in different ways. In the case of the electric dipole, $\vec{r} \to -\vec{r}$, and thus $\vec{d} \to -\vec{d}$. For the magnetic dipole, instead, we consider both $\vec{r} \to -\vec{r}$ and $\vec{v} \to -\vec{v}$, and thus $\mu \to \mu$, meaning that it does not change under the parity transformation.

The parity π changes depending on both the multipolarity L of the radiation field and on

its electric or magnetic character as follows:

$$\begin{aligned} \pi(EL) &= (-1)^L \\ \pi(ML) &= (-1)^{L+1} \end{aligned} \tag{1.11}$$

Thus, for the same order of multipolarity, electric and magnetic fields present opposite parity.

A multipole that variates in time with sinusoidal dependence produces a radiation field that propagates in $\vec{E} \times \vec{B}$ direction. The average power radiated by the elecromagnetic field depends on the frequency of oscillation ω, on the amplitude of the moment of the multipole, on the value of L and on the character of the radiation. The radiation power can be generalized as

$$P(\sigma L) = \frac{2(L+1)c}{\epsilon_0 L[(2L+1)!!]^2} \left(\frac{\omega}{c}\right)^{2L+2} [m(\sigma L)]^2 , \tag{1.12}$$

where σ represents the character of the radiation and can be either E or M and $m(\sigma L)$ is the generalized multipole moment.

For a better comprehension of the electromagnetic radiation, a classical interpretation is not sufficient. In fact, in order to describe certain properties, a quantum approach is needed. Let us consider Equation (1.12): by dividing the radiation power for the energy of a single photon $\hbar\omega$, we obtain the probability of emission of a photon. To calculate such a probability, however, it is necessary to write explicitly the generalized multipole moment. This object, in its most generalized form, is complex, so it is useful to restrict the discussion to a single photon emission between two shell-model states. Moreover, the radial part is assumed to be constant. The probability of emission of a single photon can then be written as [22]

$$\begin{aligned} \lambda(EL) &= \frac{8\pi(L+1)}{L[(2L+1)!!]^2} \frac{e^2}{4\pi\epsilon_0\hbar c} \left(\frac{E_\gamma}{\hbar c}\right)^{2L+1} \left(\frac{3}{L+3}\right)^2 cR^{2L} \\ \lambda(ML) &= \frac{8\pi(L+1)}{L[(2L+1)!!]^2} \left(\mu_p - \frac{1}{L+1}\right)^2 \left(\frac{\hbar}{m_p c}\right)^2 \frac{e^2}{4\pi\epsilon_0\hbar c} \left(\frac{E_\gamma}{\hbar c}\right)^{2L+1} \left(\frac{3}{L+3}\right)^2 cR^{2L-2} \end{aligned} \tag{1.13}$$

for electric and magnetic character respectively, where m_p is the proton mass, μ_p is the magnetic moment of the proton and E_γ is the energy of the γ ray emitted in the transition. The relation between the atomic mass A and the radius is $R = R_0 A^{1/3}$.

These estimations are known as *Weisskopf estimates*. Weisskopf estimates are useful to understand the behaviour of a state: in particular, a transition with a probability that is higher than a Weisskopf unit suggests a collective behaviour, while a transition with a probability in the order of the Weisskopf unit or lower typically indicates a single-particle behaviour. The Weisskopf estimate as a function of the different multipolarity L and mass A, for electric and magnetic transitions are reported in Table 1.4.1. Moreover, the Weisskopf estimate for mass $A = 20$ (namely, the one we are interested to study in the present experiment) for the different multipolarities and different character (electric and magnetic) of the transition are reported in Figure 1.4.1. From the figure, it is possible to observe that the probability of

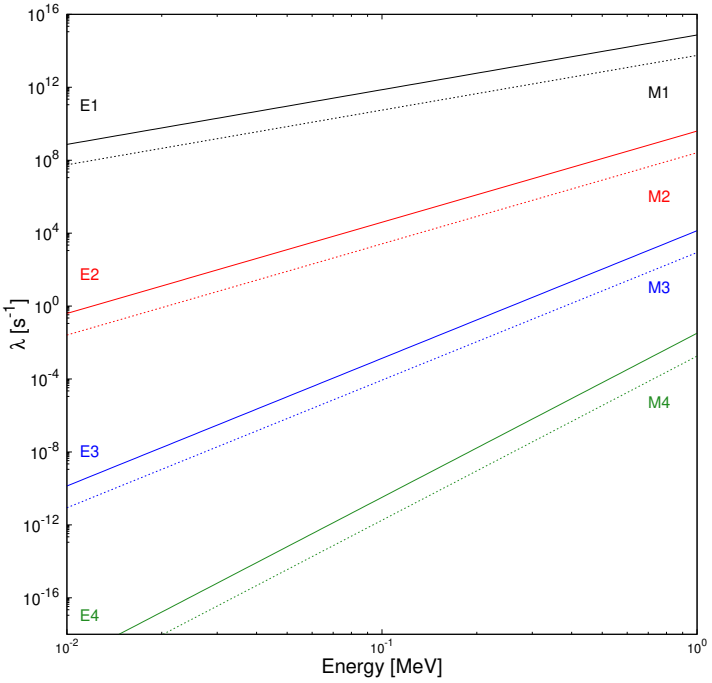

Figure 1.6.: Weisskopf estimates for $A = 20$ for electric (E) and magnetic (M) multipoles, depending on the γ ray energy.

transition presents a strong dependence on the energy of the transition: in particular higher energy corresponds to higher probability. Moreover, the lower multipolarities are more probable than higher multipolarities and electric transitions are more probable than magnetic transitions for the same value of L.

As remarked in the previous section, electromagnetic transitions must conserve the energy and the momentum. If we consider an electromagnetic transition from state ψ_i with angular momentum $\vec{I}_i$ to ψ_f with angular momentum $\vec{I}_f$, since the angular momentum is conserved, this transition must respect the condition

$$\vec{I}_f = \vec{I}_i + \vec{L}\,. \tag{1.14}$$

Electric multipole $[s^{-1}]$	Magnetic multipole $[s^{-1}]$
$\lambda(E1) = 1.0 \times 10^{14} A^{2/3} E^3$	$\lambda(M1) = 5.6 \times 10^{13} E^3$
$\lambda(E2) = 7.3 \times 10^{7} A^{4/3} E^5$	$\lambda(M2) = 3.5 \times 10^{7} A^{2/3} E^5$
$\lambda(E3) = 34 A^{6/3} E^7$	$\lambda(M3) = 16 A^{4/3} E^7$
$\lambda(E4) = 1.1 \times 10^{-5} A^{8/3} E^9$	$\lambda(M4) = 4.5 \times 10^{-6} A^{6/3} E^9$

Table 1.1.: Values of Weisskopf estimates depending on the energy of the transition (E) and the atomic mass (A) for different values of L and for the electric and magnetic transition.

Thus, considering the sum rules from quantum mechanics, the values of the momentum that the emitted photon can carry are [23]

$$|I_i - I_f| \leq L \leq I_i + I_f \,. \tag{1.15}$$

The selection rules of Equation (1.15), together with the rules that determine the change in parity for electric and magnetic transitions depending on the L of Equation (1.11), determine the possible angular momentum and character of the transition. Moreover, as illustrated in Figure 1.4.1, lower multipolarities are more favoured and electric transition are more favoured than magnetic. If we consider a transition from a 2^+ state to a 0^+ state, this transition can only be an electric transition of $L = 2$ (E2). If instead we consider a transition from a 2^+ to another 2^+, this transition will be a mix of E0, M1, E2, M3, E4, where the second and third will be favoured with respect to the others. Finally, transition from 0^+ to another 0^+ can happen only via E0 transition. However, since the photon carries an intrinsic angular momentum $L = 1$, transition with $\Delta L = 0$ are not allowed via the emission of a single γ ray. This kind of transition can happen via internal conversion, pair productions and double γ decay.

1.4.2. Transitions probabilities and lifetime measurements

Obtaining direct information on the wave function of each individual excited state of the nucleus would be the ultimate goal of nuclear structure and would allow a direct comparison to theoretical models. In practice, this is not possible and information must be obtained indirectly from other properties such as mass, spin, parity, excitation energy or transition probabilities between the states. These latter ones are relevant for spectroscopic constraints. For instance, direct reactions, such as (d, p), can be used to probe the L-transfer in the reaction and, when the spin and parity of the mother nucleus is known, to determine the spin, parity and spectroscopic factor from differential cross section (see Appendix A).

Such transition probabilities can also be measured within the same nucleus by measuring the transition probabilities between the excited states. Then, one can determine the overlap between the wave functions of the initial and final states and deduce the reduced transition probabilities from the electromagnetic operators, such as $M1$, $E2$..., according to [23]

$$B(\sigma L; J_i \to J_f) = \frac{|\,\langle J_f|\mathcal{O}(\sigma L)|J_i\rangle\,|^2}{2L+1}, \tag{1.16}$$

where σ indicates the character of the transition (electric E or magnetic M) and L indicates the multipolarity. This spectroscopic information can be experimentally measured and theoretically calculated. Let us consider a pure E2 transition as an example. The reduced transition probabilities and the lifetime of a state are directly related as follows

$$\lambda(E2) = \frac{1}{\tau} \propto \frac{B(E2,\downarrow)E_\gamma^5(1+\alpha)}{BR_\gamma}\,, \tag{1.17}$$

where E_γ is the energy of the transition, α is the internal conversion coefficient and BR_γ is

the branching ratio of the decay.

In some cases, the transition can have different multipolarities, as for example $2_2^+ \rightarrow 2_1^+$ transitions that have both a $E2$ and $M1$ character. In that case, in order to pass from the lifetime to the reduced transition probabilities, it necessary to know the mixing ratio of the transition. The mixing ratio between E2 and M1 can be calculated as [23]

$$\delta^2(E2/M1) = \frac{\Gamma(E2; 2_2^+ \rightarrow 2_1^+)}{\Gamma(M1; 2_2^+ \rightarrow 2_1^+)}, \tag{1.18}$$

where $\Gamma = \hbar T$, where T, the transition rate, is

$$T(\sigma L; J_i \rightarrow J_f) = \frac{8\pi(L+1)}{L[(2L+1)!!]^2} \frac{q^{2L+1}}{\hbar} B(\sigma L; J_i \rightarrow J_f) \tag{1.19}$$

and q can be calculated as

$$q = \frac{\omega}{c} = \frac{E_\gamma}{197\,\mathrm{MeV} \cdot \mathrm{fm}}. \tag{1.20}$$

Therefore, the mixing ratio between $E2/M1$ can be calculated as

$$\delta(E2/M1) = \pm q \frac{\sqrt{3}}{10} \sqrt{\frac{B(E2)}{B(M1)}}, \tag{1.21}$$

where the absorption processes corresponds to the positive sign and the emission processes to the negative sign, according to the Condon-Shortley phase convention [23].

Knowing the mixing ratio and the branching ratio BR_γ of the transition, the relation between the total and the partial widths is

$$\Gamma(M1) = \frac{1}{1+\delta^2} BR_\gamma \Gamma_T = \frac{1}{1+\delta^2} BR_\gamma \frac{\hbar}{\tau} \tag{1.22}$$

and

$$\Gamma(E2) = \frac{\delta^2}{1+\delta^2} BR_\gamma \Gamma_T = \frac{\delta^2}{1+\delta^2} BR_\gamma \frac{\hbar}{\tau} \tag{1.23}$$

where $\Gamma_T = \Gamma(M1) + \Gamma(E2)$ in the case considered.

Lifetimes of the states are hence directly connected to reduced transition probabilities and are useful tools to probe in a model-independent way the wave function overlap between two states, being a highly-sensitive constraint for advanced nuclear model.

There are many different methods to measure the lifetime of a state, depending on the expected range. These methods can be divided into two categories: the indirect methods and the direct methods.

Two of the most common indirect methods, where the lifetime is extracted from the measurement of different quantities, are the Coulomb excitation [24] and the Nuclear Resonance Fluorescence (NRF) [25]. Both these methods have the advantage of populating the low-lying

low-spin states via electromagnetic interaction[1]. In the Coulomb excitation method, the lifetime can be calculated from the reduced transition probabilities, which are extracted from cross section measurements. In the NRF, the decay widths of the states are measured and then the reduced transition probabilities are calculated from them. These methods cover a wide range of lifetimes: from 10^{-8} to 10^{-14} s for the Coulex method and from 10^{-11} to 10^{-17} s for the NRF.

On the other side, the direct methods generally cover smaller ranges; however, they have the advantage of measuring directly the lifetime instead of inferring it from other quantities. Among these methods, two of the most commonly used are the Recoil Distance Doppler Shift (RDDS) method [26, 27] and the Doppler Shift Attenuation Method (DSAM) [28]. Both of these methods are based on the Doppler shift of the γ rays that can be emitted by the nucleus right after the reaction, after an energy loss in a degrader or after the implantation in a stopper, depending on the lifetime of the state of interest. While the RDDS covers a time range typically from 10^{-9} to 10^{-12} s, the DSAM is used for the measurement of lifetimes in the range from 10^{-12} to 10^{-15} s. More details on this latter technique are provided in Section 2.7.

1.5. The ^{20}O study case

In the context of the study of 3N forces in light nuclei, the ^{20}O represents an interesting case. In fact, while the yrast states 0_1^+, 2_1^+ and 4_1^+ are composed of a pure $(d_{5/2})^4$ configuration, the 2_2^+ and 3_1^+ states are dominated by a mixed neutron configuration $(d_{5/2})^3(s_{1/2})^1$, according to shell model calculations [29]. For this reason, these latter states are particularly sensitive to the relative position of the $d_{5/2}$ and $s_{1/2}$ orbitals and possibly to the $d_{3/2}$. The predicted level scheme, with the relative occupation of the orbitals and spectroscopic factors, is presented in Figure 1.7.

As shown in the work of Otsuka *et al.* [16] and reported in Figure 1.4, the 3N forces have the effect of increasing the gap between the orbitals, and an increasing gap results in a shorter lifetime of the states.

Many-body perturbation theory calculations employing chiral NN interactions with and without the addition and 3N interaction show a different scenarios [30]. While the lifetime of the 2_1^+, that does not depend on the position of the $s_{1/2}$ and $d_{3/2}$ orbitals, is consistent with the shell model calculations, the lifetime of the 2_2^+ changes drastically depending on the inclusion of 3N forces. In fact, calculations with only NN forces lead to a lifetime that is 60% longer with respect to 3N calculations, expected in the range of femtoseconds. Therefore, by measuring the lifetimes of these states, it is possible to obtain useful information to quantify the 3N forces.

A previous measurement by Ciemała *et al.* [30], that measured a lifetime of $\tau = 150^{+80}_{-30}$ fs, seems to confirm the necessity of the inclusion of 3N forces in the calculations, proving the ^{20}O to be a good study case for testing *ab initio* calculations. However, the large error bars and the possibility of the influence of feeding transitions still leave open questions.

[1]This is true for Coulomb excitation only under the assumption of maintaining a minimum distance of at least 5 fm between the two nuclear surfaces in the reaction. This condition is also known as Cline's safe energy criterion [24].

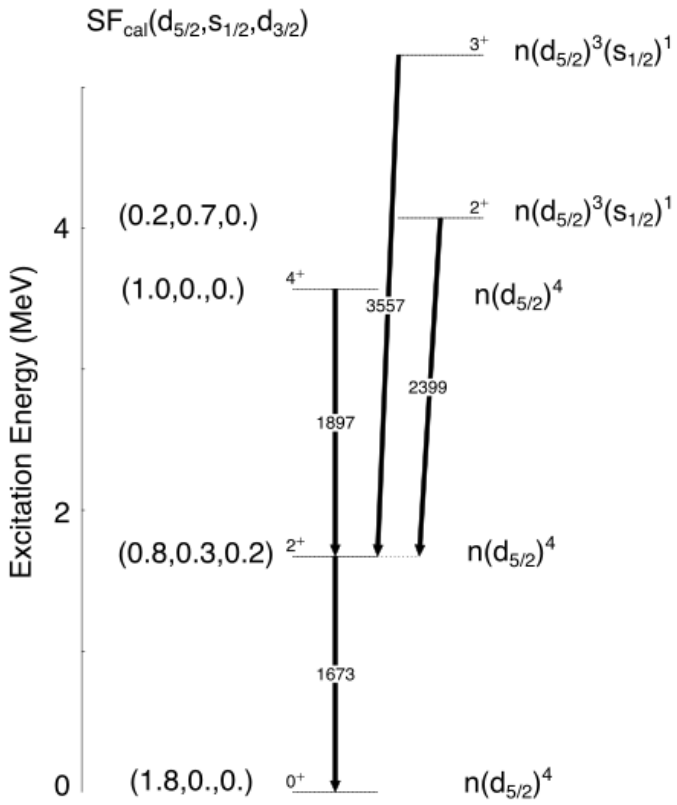

Figure 1.7.: Predicted level scheme of ^{20}O. The occupation of the orbitals and spectroscopic factors are obtained from shell calculations using the USDB interaction [29].

Additional information on the 2_2^+ state and the lifetime measurement of the 3_1^+ state could provide the needed answers.

1.5.1. Populating the ^{20}O

In the past, ^{20}O was populated using many reactions, aimed at studying different features of this nucleus.

Since the Seventies, the nucleus have been studied using (t, p) reactions starting from a triton beam and a target of ^{18}O, with the transfer of two neutrons from the beam to the target. Experiments using these reactions allowed the study of the excited levels of ^{20}O, where the excitation energies and the angular distributions were measured. Moreover, from the angular distributions, spin and parity were assigned to most of the observed states [31–34]. By comparing the experimental results to shell-model calculations, it was possible to obtain a first idea of the structure of this nucleus and in particular to shed light on the nature of the low-lying states. Positive-parity states were observed to have either a $(sd)^4$ character, where the four valence neutrons outside the ^{16}O shell occupied the *sd* shell, or a $(sd)^6(1p)^{-2}$ (six particles-two hole) character. Negative states were expected to present instead a mixing of the $(sd)^5(1p)^{-1}$ (five particle-one hole) and $(sd)^3(fp)^1$ configurations.

An experiment involving a ^{18}O beam at a bombarding energy of 24.5 MeV, impinging on a 100 μg/cm^2-target of Ti-^{3}He, measured the lifetime and the $g-$factor of the 2_1^+ state, yielding to $|g| = 0.352(15)$ and $\tau = 10.7(4)$ ps [35].

Thanks to the development of the accelerator technologies, the ^{20}O was studied via proton scattering in an experiment employing a radioactive beam of ^{20}O impinging on a polypropylene (CH_2) target [36] in an inverse kinematic reaction. In the analysis, the experimental differential cross sections were compared to Coupled Channel Born Approximation (CCBA) calculations for inelastic scattering measurements and the deformation parameters were extracted. In another experiment, the ^{20}O beam impinged on a ^{208}Pb [37, 38] in a direct kinematic reaction. This study focused instead on the 1^- states and measured the B(E1)↑ values.

In the same years, the ^{20}O was populated in a fusion-evaporation reaction using a beam of ^{14}C impinging on a ^{10}Be target [39]. The events of interest were selected by requiring the coincidence of γ rays with one α particle, evaporated in the reaction. This different reaction mechanism enabled to populate and observe five new states below 6 MeV. The comparison between these experimental data and the shell model calculations pointed in the direction of a reduction of the *p-sd* shell gap for oxygen isotopes.

More recently, the nucleus of interest was populated in both direct transfer and deep-inelastic reactions using a ^{18}O beam impinging on a ^{181}Ta target. This experiment was devoted to the lifetime measurement of the 2_2^+ and the state of interest was well populated, leading to a high statistics on the transition of interest, namely the $2_2^+ \rightarrow 2_1^+$ transition measured at 2396 keV. However, in this experiment the control on the population of the states was limited. This control would allow one to select the direct population of the state of interest by applying a gate on the excitation energy spectrum. This gate guarantees a spectrum with a lower background and eliminate the contribution of the feeding transitions coming from higher-energy states that influences the lifetime measurement of the lower states.

One-neutron transfer reactions are perfect tools to study single-particle level and guarantee a strong control on the populations of the states. The ^{20}O was studied using a (d, p) reaction

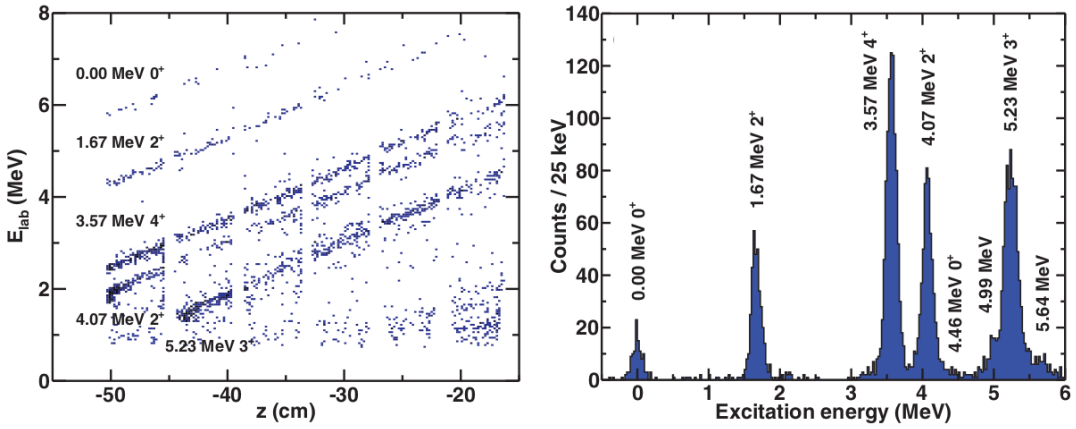

Figure 1.8.: (left) Kinematic lines corresponding to the ^{20}O excited states obtained from the proton distribution measured by the HELIOS magnetic spectrometer. (right) Excitation energy spectrum of the ^{20}O reconstructed using HELIOS. Figure taken from [40].

in Argonne National Laboratories (USA), starting from radioactive beam of ^{19}O provided by the Argonne Tandem-LINAC Accelerator System (ATLAS) and the In-Flight Facility at the beam energy of 6.6 MeV/A [40]. The beam impinged on a deuterated polyethylene (CD_2) 260 μm-thick target, placed inside the HELIcal Orbit Spectrometer (HELIOS). This experiment was devoted to the study of the ^{20}O excited level and their angular distributions.

In the experiment, the excitation energy spectrum of the ^{20}O was reconstructed with a resolution that permitted to well distinguish the levels of interest. In particular the $0^+_{g.s.}$, 2^+_1, 4^+_1 yrast states, as well as the 2^+_2, 0^+_2, 3^+_1 states were observed. Moreover two additional states were observed at 4.99 and 5.64 MeV and were both assigned a tentative spin and parity of 2^+. As showed in Figure 1.8, the state of interest for the lifetime measurement, namely the 2^+_2 and 3^+_1 states at 4.07 and 5.23 MeV, are well populated and separated from the other states.

For these reasons, the ^{19}O(d,p) reaction was chosen to study the ^{20}O nucleus. The experimental apparatus is presented in the following chapter.

2

Experimental Apparatus

In this chapter, the experimental setup is described. The nucleus of interest, ^{20}O, was populated with a transfer reaction using a radioactive beam of ^{19}O that impinged on a deuterated polyethylene (CD_2) target. The beam was provided by the GANIL-SPIRAL1 complex at the kinetic energy of 8 MeV/A and with an average intensity of 4×10^5 particle per second (pps) after the post acceleration process. The CD_2 target was produced with a thickness of 0.3 mg/cm^2 and evaporated on a gold layer with a nominal thickness of 20 mg/cm^2. The γ rays emitted in the process were detected using the AGATA array. For a complete reconstruction of the reaction, the target-like recoils were identified using the MUGAST array, while the beam-like ^{20}O nuclei were detected by the VAMOS++ spectrometer. A scheme of the setup is presented in Figure 2.1.

2.1. GANIL-SPIRAL1 accelerators complex

The Grand Accélérateur National d'Ions Lourds (GANIL) is a facility located in Caen (France) dedicated to the production and acceleration of both stable and radioactive heavy ions beams, aimed at the study of nuclear physics, atomic physics and applications [41]. At the moment, five cyclotrons are operative at GANIL (Figure 2.2):

- C01 and C02 cyclotrons, coupled with the IRRSUD beamline (Energy $<$ 1 MeV/A);
- the CSS1 cyclotron, used for atomic and nuclear physics, biology and solid state physics (Energy 4-13 MeV/A);
- the CSS2 cyclotron, used for nuclear physics and previous applications (Energy $<$ 95 MeV/A);
- the CIME cyclotron, used for the post-acceleration of radioactive beams provided by the SPIRAL1 source (Energy $<$ 20 MeV/A).

SPIRAL1 is a facility for the production of radioactive ion beams using the Isotope Separation On Line (ISOL) technique [42]. With respect to other techniques, like the In-Flight or the fragmentation, the ISOL technique presents several advantages, such as a good optical quality and the possibility of tuning the beam energy in the post-acceleration phase. However,

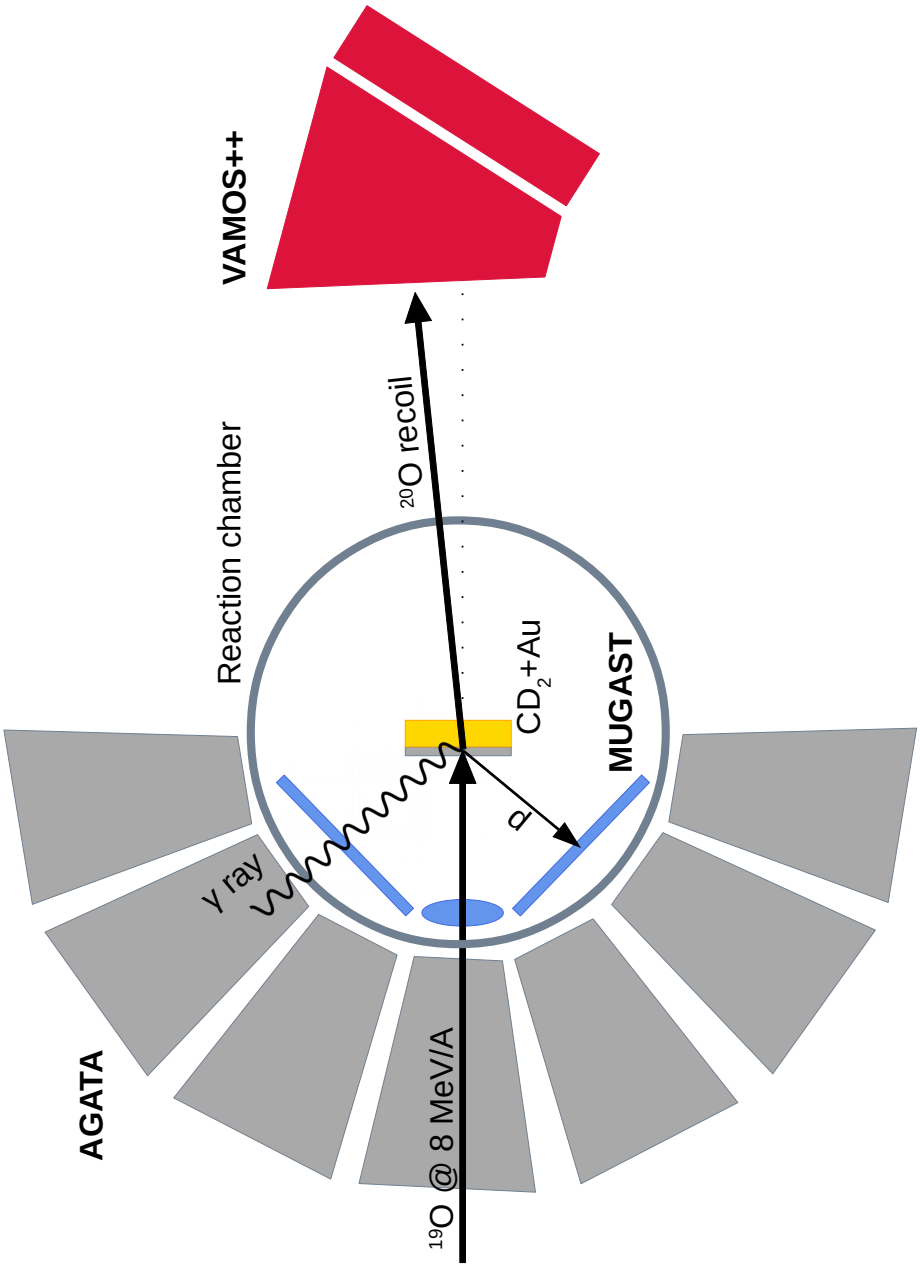

Figure 2.1.: Scheme of the experimental setup. Inside the reaction chamber, at backward angles with respect to the beam direction, the silicon detectors of MUGAST (both trapezoidal and annular detectors, in blue) are placed. Outside of the reaction chamber, at backward angles, the AGATA array (grey) is positioned. At forward angles, the beam-like recoils are detected by the VAMOS++ spectrometer (red). Figure not in scale.

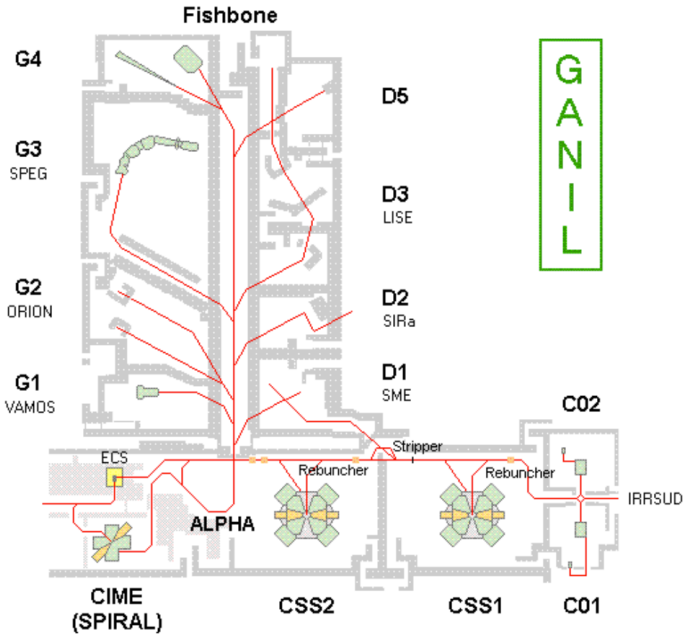

Figure 2.2.: A scheme of the GANIL facility is shown. For the present experiment, the SPIRAL1 facility (bottom left on the map) provided the radioactive beam that was then delivered to the G1 hall, where AGATA and VAMOS++ are located. Figure taken from [41].

due to the longer time required to deliver the beam, the choice of radioactive species must be restricted to the less exotic ones, namely those with a half-life longer than few milliseconds.

Until 2014, the production was limited to beam of gaseous elements. However, after a new upgrade, radioactive beams of condensable elements are now available. For the production, a stable heavy ion beam impinge on a thick graphite target and the fragments generated are diffused from the target to the ion source. Gaseous radioactive beams like nitrogen, oxygen and noble gases are produced using the Nanogan ion source [43]. During the 2014 upgrade, the a new Forced Electron Beam Induced Arc Discharge (FEBIAD) source was implemented, together with a Target Ion Source System (TISS) to connect the target to the source [42]. The FEBIAD source permits to 1+ charge beams of elements with a melting point below 2000 °C, opening to a wider range of elements such as sodium, magnesium, aluminium and others.

The beams are post-accelerated by the CIME cyclotron to energy from a few keV to 20 MeV/A for the lightest nuclei, with an intensity that is highly dependent on the exoticity of the species. Finally, the radioactive beam is delivered to the experimental hall.

For this experiment, a primary beam of ^{22}Ne at 80 MeV/A impinged on a carbon target and the secondary beam of ^{19}O was extracted and re-accelerated at 8 MeV/A with an average intensity of 4×10^5 pps over the whole experiment. The radioactive beam was extremely pure and no trace of contaminants have been detected.

2.2. The AGATA array

2.2.1. Germanium detectors in γ-rays spectroscopy

Since the Sixties, germanium detectors have been proven to be fundamental tools for γ-ray spectroscopy. In fact, their main characteristic is the good resolution that permits to distinguish transitions that are very close in energy, with respect to other detectors previously used such as, for example, sodium iodide scintillators (Na(I)) [44]. Their good resolution is due to the low gap between the valence and conduction band in the semiconductor lattice. In fact, while for typical silicon detectors this gap is 1.2 eV, for germanium detectors it is only about 0.7 eV. This means that in germanium detectors the probability of generating an electron-hole pair is higher, leading to a higher number of charge carriers and resulting in a higher resolution capability. However, this small band gap has a serious drawback: in fact, the leakage current induced by room temperature affects the performances of the detectors. Therefore germanium crystals must be cooled down using liquid nitrogen and the temperature of the crystal must remain in the range of 77-90 K.

In order to efficiently detect the γ-ray radiation, a thick depletion depth is required for these semiconductors detectors. The thickness of the depletion region is given by [44]

$$d = \sqrt{\frac{2\epsilon V}{eN}} \tag{2.1}$$

where ϵ and e are the dielectric constant and the electronic charge respectively, V is the bias voltage and N is the net impurity concentration of the material. Therefore, given an applied voltage, it is necessary to obtain a lower level of impurity concentration in order to reach a greater depletion depth. Two methods have been developed for this purpose. In the first one, the required level of purity is obtained by compensating the residual impurities using an equal concentration of dopant atoms of the opposite type. The lithium ions drifting process has been successfully used with germanium detectors and permits reaching a thickness of about 2 cm. The detectors produced using this approach are called Ge(Li) detectors and they have been commercially available since the 1960s. The second method permits obtaining a higher level of purity by melting the material and, in this way, excluding the impurities. Detectors obtained with this second method are called *High-Purity Germanium* (HPGe) detectors and they can reach depletion depths of several centimetres. They were first developed in the mid-1970s and their lower maintenance costs with respects to the Ge(Li) detectors made them a preferable alternative.

Since the 1980s, an increasing interest in the development of germanium arrays has been manifested, with the goal of reaching a 4π angular coverage. In these arrays, the HPGe detectors are surrounded by a Bismuth Germanate scintillator (BGO) crystal that acts as a Compton shield: whenever a γ ray detected by the germanium detector is in coincidence with a γ ray detected by the BGO, that event is rejected because it does not contain the complete information on the energy of the incident photon. This technique improves significantly the peak-to-total (P/T $\sim$ 55%) ratio in γ-ray spectra, but it limits the angular coverage of the array and consequently the efficiency.

The advent of Radioactive Ions Beams (RIBs), corresponding to lower beam intensity and higher background levels, together with large Doppler broadening, made the experimental

conditions even more challenging. In order to be able to explore the physics of more exotic nuclei, a larger efficiency was needed, which cannot simply be obtained by increasing the number of detectors in the array. Moreover, with the higher energy of the recoils achievable with new accelerators technologies, a better angular resolution was necessary to perform an accurate Doppler correction of the γ rays.

The solution to overcome the limitations was the development of crystal segmentation combined with digital signal processing. These new technologies allowed physicists to measure the energy and position of the interaction points in the crystal and therefore to reconstruct the trajectory of γ rays within the crystals. Segmented arrays permit to achieve a larger efficiency keeping a sufficiently high P/T ratio. Moreover, it allows one to determine with better precision ($\sim 1^\circ$) the emission angle of the γ ray, leading to a reduction of the Doppler broadening and to an improved resolution [45] for in-flight spectroscopy.

The evolution from the first germanium detectors to present-day detectors happened gradually and in many cases the different phases coexisted. It is possible to individuate five phases.

The first generation of germanium array consisted of a few single coaxial detectors arranged together. The TESSA array [46] is a good example of these arrays.

The second generation consisted of single coaxial germanium with AntiCompton (AC) shields and a large number of detectors. GASP [47], EUROGAM [48] and GAMMASPHERE [49].

The third generation is represented by "composite" detectors such as clovers (four crystals in the same cryostat) or clusters (3 or more encapsulated crystals in the same cryostat). An example of clovers is EUROBALL phase II [50] or EXOGAM [51], while an example of clusters is the phase II of GALILEO [52].

The fourth generation consisted of segmented detectors in order to improve the Doppler correction, such as SEGA [53] or MINIBALL [54].

Finally, the fifth generation is represented by composite detectors (clovers or clusters) with no Compton suppression and with the capabilities of performing tracking and pulse shape analysis. Only two arrays have these characteristics: GRETINA [55] and AGATA.

2.2.2. The AGATA project

AGATA (Advanced GAmma Tracking Array) [56] is a European project aimed at the development of a full 4π γ-ray tracking array, similar to its counterpart GRETA [57] in the United States. AGATA has already been successfully employed in numerous in-beam experiments first in its demonstrator phase at LNL [58], then at GSI [59] and finally at GANIL [60], increasing the number of clusters from 5 at LNL, to 7 at GSI, to up to 15 at GANIL, where it was located at the time of the experiment.

In the present configuration, 12 triple clusters, for a total of 36 crystals, are placed at backward angles with respect to the beamline in a compact configuration (18 cm between the target and the endcap) in order to maximize the angular coverage of the HPGe and thus the efficiency. The AGATA detectors are based on closed-end coaxial n-type HPGe crystals with an impurity concentration between 0.4 and 1.8×10^{10} atoms/cm^{-3}. For each cluster, the crystals present three different shapes (presented in Figure 2.3, left) identified with a letter and a colour: A - Red, B - Green, C - Blue. Each crystal is segmented into six rings along the axis, and each ring is subdivided into six sectors, for a total of 36 segments (see Figure

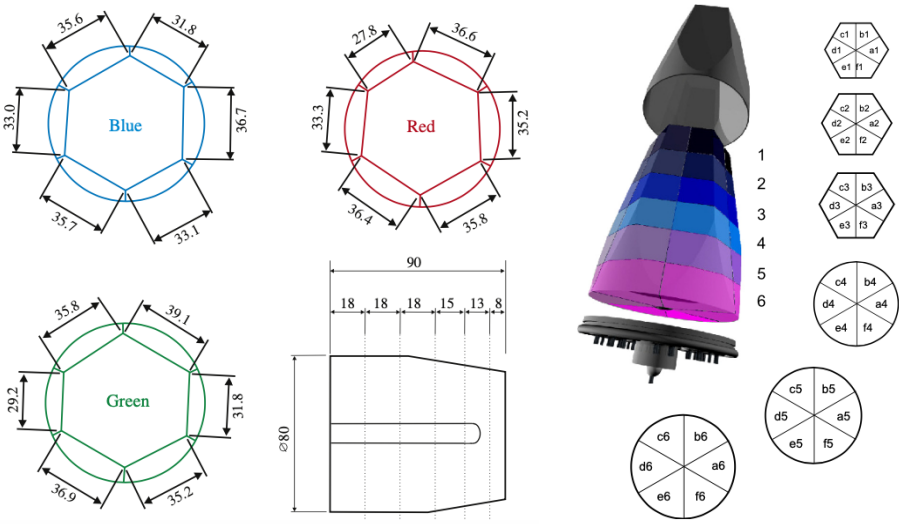

Figure 2.3.: (Left) Three different geometries of AGATA crystals, commonly referred as A - Red, B - Green and C - Blue. (Right) A 3D representation of an AGATA crystal and its segmentation. Figures taken from [56]

2.3, right). A central contact, the core, collects the total energy deposited in the crystal and is used to apply the positive bias voltage. Every segment has its own preamplifier, that must have important characteristics such as a high energy resolution, a short dead time and the capability of sustaining high counting rates. To achieve these requirements, new preamplifiers were developed.

In order to ensure the highest energy resolution, the preamplifier is divided into two parts [61]. A cold part, consisting of a Field Effect Transistor (FET), is placed close to the detector electrodes and operates at cryogenic temperatures in order to reduce the electronic noise. A warm component, instead, operates at room temperature and it is connected to the first part by 15-cm cables. To reduce the dead time and be able to sustain higher counting rates, a new fast-reset technique was implemented. A desaturation circuitry is able to detect saturated signals and to discharge the capacitance, restoring the initial condition. Finally, a new technique employing a time-over-threshold (TOT) algorithm permits to dynamically extend the γ ray energy range up to about 180 MeV. Knowing the quasi-linear relation between the reset time and the amplitude of the signal, this algorithm performs a time-to-amplitude conversion and extends the energy measurement range consequently [62].

AGATA Front-End Electronic

The AGATA Front-End Electronic (FEE) digitizes the signals from each crystal independently at 100 MHz with a 14-bit resolution. For each crystal, the signals from the 36 segments plus low and high gain signals from the core are digitized and sent to the pre-processing electronics at a data bandwidth of about 2 Giga bits per second (Gbps) per channel. Moreover, using the high gain signal of the core, the digitizers are able to generate a fast trigger output that can be used for external coincidence with analog electronics.

The pre-processing electronic is in charge of treating the data coming from the digitizers.

Using Field Programmable Gate Arrays (FPGA), the digitized signal is passing successively into a trigger block (CFD for phase 0 electronic, shaper followed by a leading-edge with a settable threshold for phase 1). For each crystal, the core signal is used to trigger the acquisition of the 36 segments treated as slave. Moving window deconvolution based on a trapezoidal filter is then applied to determine the signal amplitude. For each local trigger, a request is sent to the Global Trigger and Synchronization system (GTS) which can be coupled to a Trigger Processor (TP) to validate events under experiment-driven conditions. Since the counting rate on the AGATA crystals for the present experiment was sufficiently low (about 100 Hz per crystal, for a total of about 4 kHz for the whole array), AGATA ran triggerless, i.e. all the local trigger requests were validated. For each validated event, the FPGA is generating a data frame containing the digital information, e.g. time-stamp, amplitude from the trapezoidal filter, and a fraction of the signal containing the baseline and the rise time of all the signals. The latter will be used during the pulse-shape analysis process to determine the position of the interaction.

Two versions of the FEE were used for the present experiment. In the first type (phase 0), the pre-processing is performed by two carrier cards in the **Advanced Telecommunications Computing Architecture (ATCA)**, each containing four Common Mezzanine Cards (CMC). This electronic is in operation since the demonstrator phase at LNL (2009-). Part of the components that are now obsolete renders the maintenance of this FEE difficult. Moreover, the power needed for each capsule is about 320 W, requiring a complex cooling system.

For this reason, a new kind of pre-processing electronic was developed (phase 1). Similarly to the ATCA, the **Global Gigabit Processor (GGP)** is able to sustain an incoming data rate of 2 Gbps per channel. The GGPs are Peripheral Component Interconnect Express (PCIe) cards that are mounted directly into the computing nodes in charge of the PSA. The board power supply accepts a voltage of 12 V (corresponding to a maximum currents of 1 A) and 5 V (10 A). Hence, the maximum power consumption of the pre-processing electronic is 62 W, five times lower than the previous setup.

In Figure 2.4, the circled crystals have been acquired using the GGP boards while the other ones are read using the ATCA.

2.2.3. Detectors Calibration

The electronic signals coming from the segments and core of the crystals are processed to extract the amplitude using a trapezoidal filter. This information is used for the energy calibration of the detectors. For the calibrations, only events where one and only one segment has fired are selected.

First, a ^{60}Co source is used for a preliminary calibration of the detectors. The calibration is performed for each segment and for the core at two different gains. This procedure is done for each detector, leading to $(36 + 2) \times 36 = 1368$ segments to analyse. Due to this large number, the calibration process is automatized using the program *RecalEnergy* [63]. This program identifies the peaks of the cobalt source, expected at 1173 and 1332 keV, and extrapolates the centroids using a deformed gaussian fit with a left and right tail, the possibility of adding a step to the fit and background subtraction. Then it calculates the linear coefficients to calibrate the segments and the core, fixing the offset to zero. After the automatized procedure, the results of the calibration are checked manually and, when the

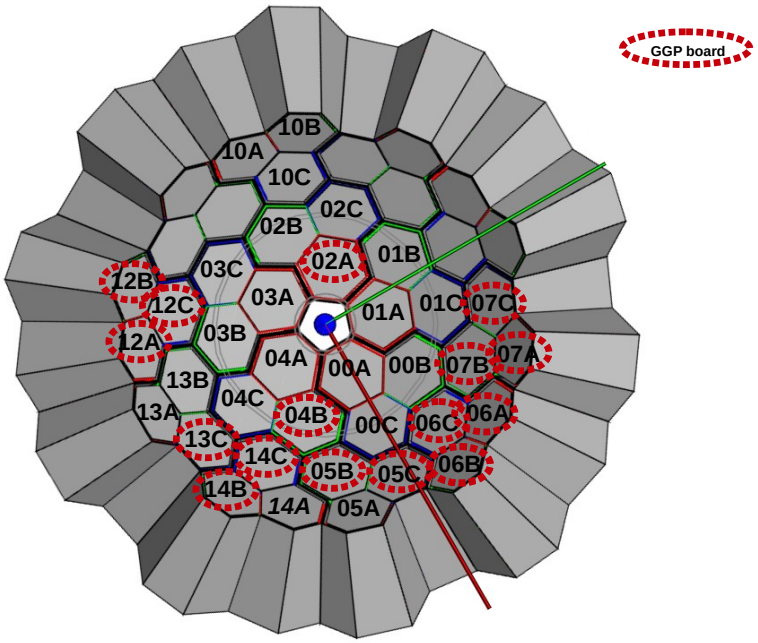

Figure 2.4.: Disposition of the crystals in the AGATA array for the present configuration. The circled detectors have been implemented with the new GGP electronic for the pre-processing.

residual energy between the calibrated peak and the nominal one is more than 1 keV, the coefficient is recalculated manually.

A second calibration is also performed, after the procedures explained in paragraphs 2.2.5, 2.2.6, and 2.2.8, using a source of ^{152}Eu. The program *RecalEnergy* [63] identifies the ten most intense transitions of the spectrum and calculates the linear coefficients, namely the slope and the offset, for the calibration. Then, as in the previous case, the calibration is checked manually by comparing the position of the 1407 keV peak with the nominal one, requiring a residual lower than 0.5 keV.

2.2.4. Cross-talk correction

Electrical cross-talk effects are commonly observed for segmented detectors. In the case of the AGATA crystals, the capacitances of the bulk germanium material create an electronic network that causes these effects. The main consequences of the cross-talk are shifts in the energy of the γ-ray transitions measured by the inner core and outer segments, and a general worsening of the resolution, depending on the multiplicity of firing segments. For example, for the ^{60}Co peak at 1332.5 keV measured with one of the AGATA crystals, a shift of the energy peak position of more than 2 keV per fold to lower energy values and an increase of the FWHM of about 0.5 keV per fold was observed [64].

To retrieve the intrinsic resolution and improve the calibration, a cross-talk correction is needed. In this procedure, the measured energy vector of all the segment signals is converted into a corrected vector. Since the cross-talk propagates in a linear way, the most convenient

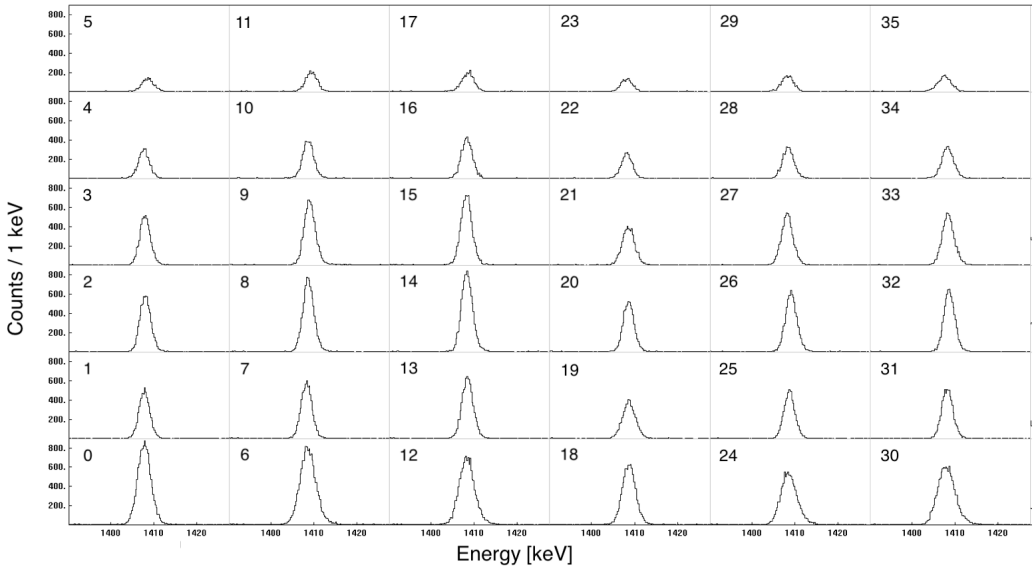

Figure 2.5.: ^{152}Eu source γ-ray energy spectrum for the segments of crystal 02A after the second calibration, expanded around the 1407 keV peak. All the segment are aligned within an energy difference of less than 0.5 keV.

choice for the conversion of the vectors is to use the matrix formalism. The δ_{ij} matrix elements are calculated by selecting events with only one segment j collecting a real energy deposition and then, in coincidence, the baseline shifts of the other segments i are recorded as a function of the energy deposited in segment j. Matrix elements δ_{ij} are expected to be of the order of $\approx 10^{-3}$. Then, by inverting the transformation matrix, it is possible to deduce the true energy deposited in the segments from the distorted measured values.

The cross-talk coefficients are calculated using the program *xTalkSort* [65] and *RecalEnergy* [63], using a ^{60}Co calibration run, as in the first calibration.

2.2.5. Broken and lost segments

The information on the cross-talk can be used for the treatment of problematic segments, classified as either *broken* or *lost*.

A segment is considered broken if the corresponding charge is not regularly collected by its FET and flows to the neighbouring segments. This case is easily recognizable by the presence of ghost peaks in the neighbouring segments.

In case of a lost segment, instead, the charge is normally collected by the FET but the signal is not present in the data. In this second case, no ghost peaks are observed.

There are two different procedures to treat the missing segments. One way is to force the calibration parameter of the segment to zero. The second way is to restore the information on the missing energy released in the segment from the correlation between the energy measured by the core and the sum of the energy measured by the segments. This option is not feasible if more than one segment is missing in the crystal.

In the present experiment, three crystals presented problematic segments: the 00A, the 06A and the 10A. The procedure to deal with these issues is explained in the following.

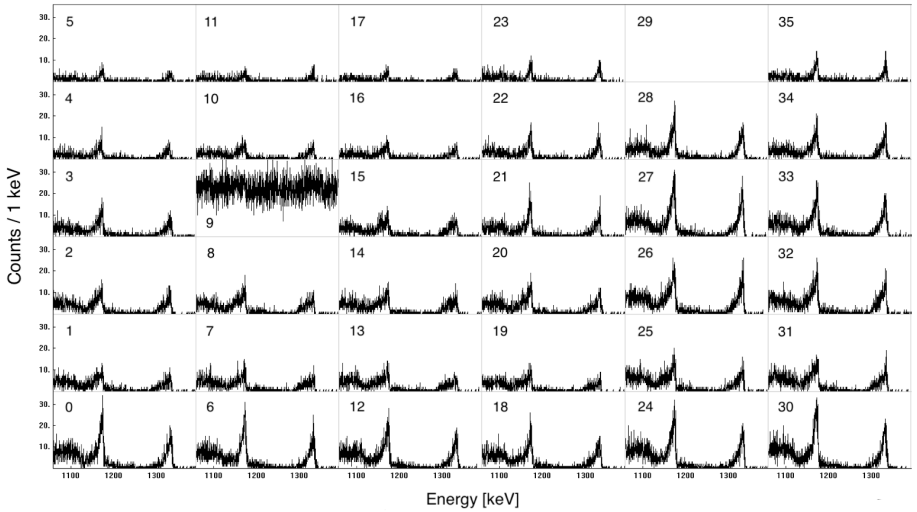

Figure 2.6.: γ energy spectrum of the different segments for crystal 00A. It is possible to notice that segment 9 and 29 present problematic behaviours. In particular, segment 9 is noisy, while segment 29 is completely absent.

- In the case of the 00A crystal, two segments presented a problematic behaviour: the 9 and the 29, as presented in Figure 2.6. In this case, it was not possible to recover the segments and the gain of both segments was fixed at zero.
- Crystal 06A showed issues for segment 3. From the presence of ghost peaks, observed in segment 2 and 4 (see Figure 2.7, top), segment 3 was identified as broken. The coefficients to recover the segment were calculated from the core matrix (Figure 2.7, bottom). The core matrix represents the energy measured in the core as a function of the sum of the segments.
- Crystal 10A showed issues for segment 29. From the absence of ghost peaks, it was identified as lost and the coefficients for the recovery were calculated from the core matrix (see Figure 2.8).

2.2.6. Time alignment

In the AGATA framework, the γ-ray hit time is calculated with respect to the trigger, which is given by the core of each crystal. A leading-edge discriminator is used to be more sensitive to low-energy events. This introduces a dependence on the energy for the trigger. When a crystal is triggered, the trace of the signal for every segment and the core are recorded. The signal consists of 100 samples, 40 before and 60 after the trigger.

The shape of the signals is fundamental for the PSA (see Section 2.2.7). However, the PSA algorithm processes the signals coming from the segments as beginning all at the same time. Therefore, if not previously aligned, the reconstruction of the interaction point can be incorrect and lead to clusterisation patterns.

For this reason, the time alignment of the segments and core of a crystal is extremely important. For the alignment of the segments, the macro *RecalEnergy* [63] is used, requiring

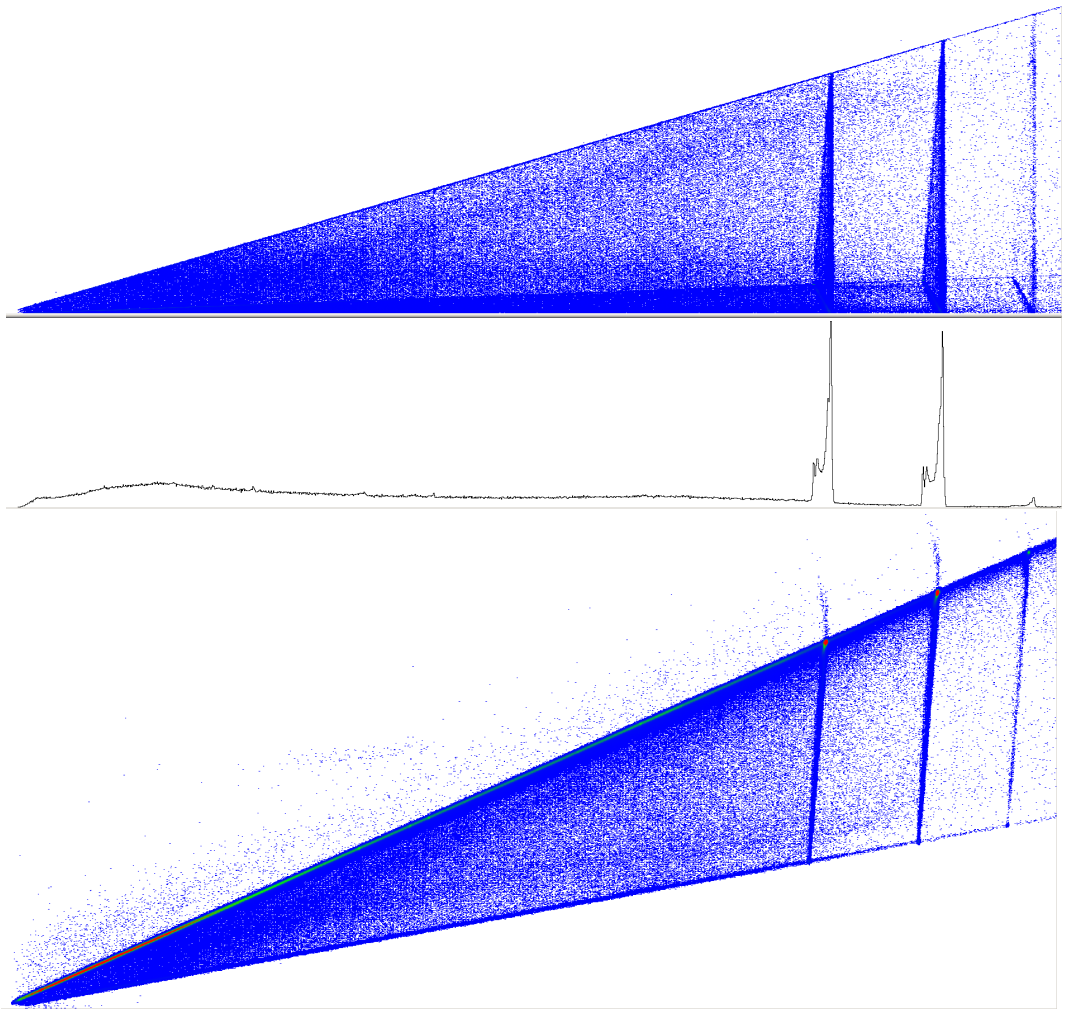

Figure 2.7.: (Top) The energy of the core as a function of the segment 4 (crystal 06A) energy of a ^{60}Co source is presented. The γ-ray energy spectrum for the segment is presented under the matrix. The presence of ghost peaks characterizes segment 3 as broken. (Bottom) The energy of the core as a function of the sum of the segments (core matrix) for crystal 06A is presented.

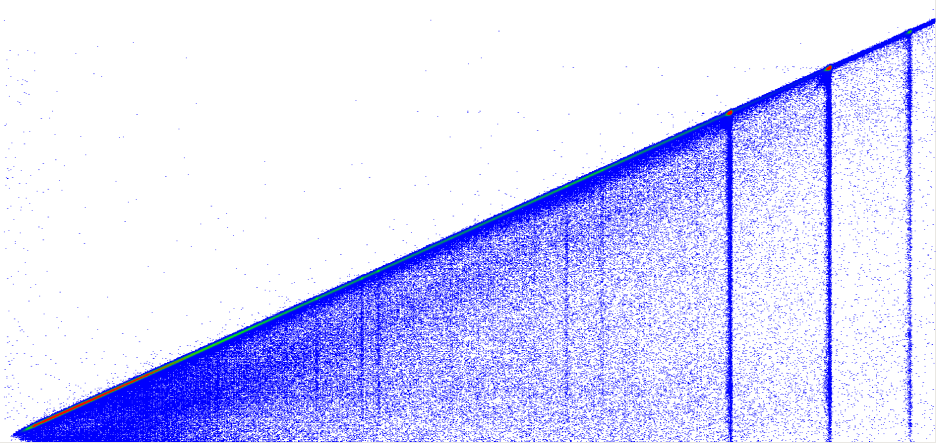

Figure 2.8.: The core matrix for crystal 10A is presented.

all the segments to be aligned at channel 500. In Figure 2.9 an example of the timing of the segments before and after the alignment for crystal 00B.

For the core, a manual procedure is followed. In case the core is not well aligned, in the time spectrum produced by the PSA a second peak will be present, as presented in Figure 2.10 for crystal 00B. In the present case, the second peak was found at channel 468 (red spectrum), therefore a shift of 32 channel is required.

2.2.7. Pulse Shape Analysis

Pulse Shape Analysis (PSA) is a powerful tool in nuclear physics used for different purposes such as time measurements or particle discrimination. In the context of the AGATA project, PSA is used to identify precisely the interaction points of the γ rays inside the segmented crystals and to perform the Neutron Damage correction. At the moment, the accuracy achievable with current algorithms and methods is below 5 mm (FWHM) [56].

Whenever a γ ray hits a segment of the germanium detector, two kinds of signals are created:

- a net charge signal, created in the segment directly hit by the photon;
- a transient signal, created in the neighbouring segments.

An example of these two kinds of signals is shown in Figure 2.11.

The sum of the net charge and transient charge signals are then compared to a set of libraries that permits reconstructing the interaction position of the photon in the germanium crystal. These libraries can be obtained either by direct measurement or via simulation.

The first method requires the usage of a dedicated setup consisting of a high-resolution positioning table, a heavy metal collimator and an intense radioactive source, usually of ^{137}Cs [67]. The heavily collimated source and additional conditions to suppress events with multiple interactions, allow one to obtain a precise experimental set of bases. However, this procedure is time-consuming and, at the moment, a complete set of the pulse shape libraries is still to be obtained.

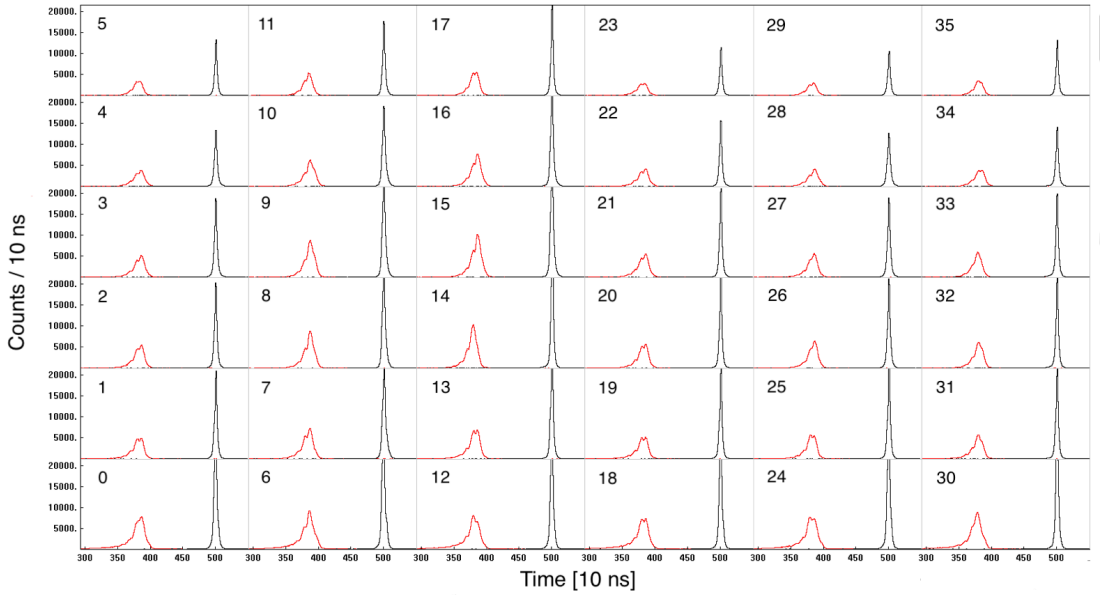

Figure 2.9.: (top) Timing of the segments of crystal 00B before (red) and after (black) of the alignment. All the segments are aligned at channel 500.

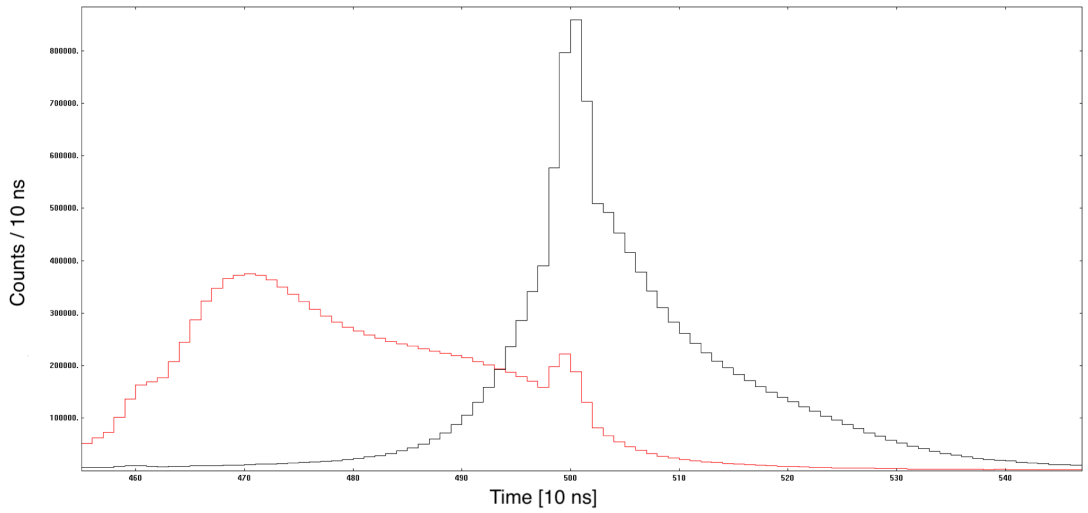

Figure 2.10.: Timing of the core of crystal 00B before (red) and after (black) the alignment. Before the alignment, a second peak around channel 470 is present, while after the alignment only one peak at channel 500 is observed.

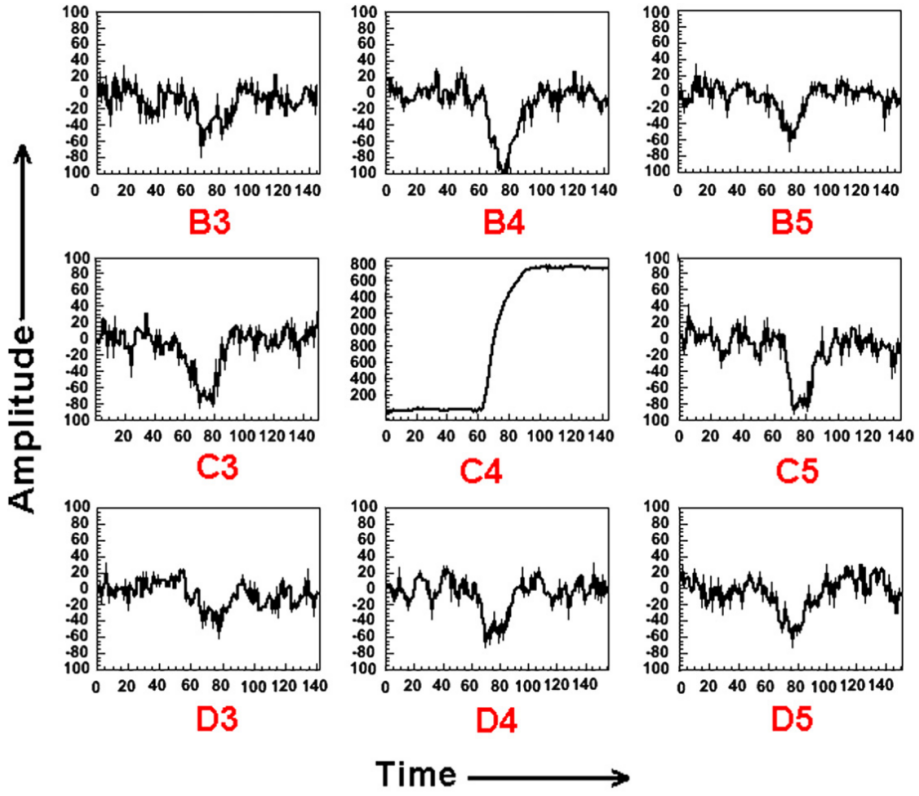

Figure 2.11.: Example of a net charge signal on segment C4 and transient signals in the neighbouring segments of an AGATA crystal. Figure taken from [66].

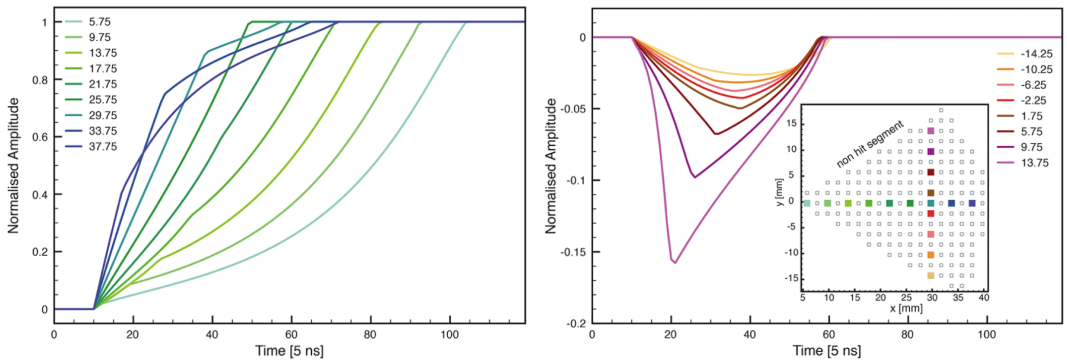

Figure 2.12.: Simulated traces of an AGATA crystal for different positions. (top) The core signal for different values of the radius is shown. (bottom) Transient signals induced in a neighbouring segment are shown. Figure taken from [68].

With the second method, the pulse shape is calculated by simulating a realistic response of the detector hit by a γ ray. Numerous codes have been developed within the AGATA collaboration, among which the AGATA Detector library (ADL), a C-based code used for realistic simulations of semiconductor detectors [68]. Firstly, ADL provides the calculations of the weighting potentials and the electrical field. The volume of the crystal is divided into small cubes called voxels, which can be either an electrode type or an active detector material type. Then, one of the electrode-type voxels is set to 1 V, while all the other electrodes are set to 0 V. The weighting potential is defined by a 3D Poisson solver that iterates over all the voxels. The electric field is obtained from the weighting potential of the core after scaling by the applied bias voltage, to which the space charge distribution field must be summed.

Secondly, a set of bases where each signal shape corresponds to an interaction position must be obtained. When a γ ray hits the crystal, electron-hole pairs are created and then accelerated by the electric field and finally collected to form the signal. Considering that the electric field is not homogeneous within the volume and that electrons and holes have different mobility, the collection time of the charge carriers will vary depending on the position of interaction, leading to different signal shapes. The variety of signal shapes is scanned in a 3D grid with a 2 mm spacing. An example of these signals is shown in Figure 2.12. Since the shape of the signal is also depending on the impurity level of the material, the inverse procedure can be used to determine the presence of neutron damage in the lattice and restore the original shape of the signal, as explained in Section 2.2.8.

Finally, since the PSA base sets are also used for online analysis, it is necessary to develop fast and efficient algorithms to process data at a significant rate. One of the main used algorithms is the Adaptive Grid Search (AGS) [69]. This algorithm compares a set of measured net and transient signals with the signals calculated from a grid of points in the crystal. The residue R is calculated as the sum of the squared difference between the measured and calculated signals over time and segments. The research of a minimum residue is done in two steps. First, the minimum R is evaluated in a wider grid of points in order to determine the voxel where the interaction happened. Then, a second minimization is performed to search for the interaction point within the determined voxel with a full grid search. A full set of reference bases of the simulated signals allows the algorithm to be precise and efficient, characteristics that are fundamental for in-beam experiments and online analysis.

2.2.8. Neutron Correction

HPGe are known to be sensitive to fast neutron irradiation. The fast neutrons can create some defects in the lattice of the crystal. These defects act as electrons and holes trapping, reducing the efficiency of charge collection. The result is that for damaged crystals a left tail on the peak can be observed, which worsens the intrinsic resolution of the detector.

Damaged crystals can be repaired through annealing. This process consists in heating the crystal, typically at temperatures around 120 °C for 72 h, in order to restore lightly damaged detectors. During the process, the cryostat vacuum is guaranteed by an external pump [44]. However, the process of annealing requires time and it is not possible to perform it after each experiment. For these reasons, some correction methods have been developed in order to reduce the effects of the neutron damage and to restore, at least partially, the initial resolution of the detector.

The sensitivity of AGATA detectors was studied in previous works [70, 71]. From these studies, it emerged that holes, being slower than the electrons, are more sensitive to trapping effects. Since segment signals are collected via holes, segments are more sensitive to trapping effects than the core. Moreover, there is a clear dependence of the inefficiency on the path length: therefore, the sensitivity to hole trapping is maximal near the core electrodes, while for the electrons the sensitivity is maximal near the outer segment electrodes.

In order to correct the neutron damages, the paths of the charge collection are reconstructed from the shape of the signals, using the libraries implemented in the ADL simulation code. Then, this path is compared to the nominal one expected for a germanium detector. If the reconstructed path differs from the expected one, the shape of the signal must be corrected to fix the inefficiency in the charge collection. If this procedure is not sufficient, it is possible to recover the initial energy resolution of the crystal by normalizing the sum energy to the energy measured in the core contact, which has been proven to be less affected by the neutron damages.

In Figure 2.13, an example of the effect of neutron damage correction for crystal 04C.

2.3. The VAMOS++ spectrometer

Magnetic spectrometers are widely employed for the identification of heavy ions produced in nuclear reactions from either stable or radioactive ion beams. At energies around the Coulomb barrier, the angular distribution of the reaction products is more spread with respect to fragmentation energies, thus a larger acceptance is required in order to obtain a good efficiency. Moreover, while fragmentation products mainly present a single charge state $Q \sim Z$, at the Coulomb barrier one can have a larger spread (5-10) in charge states per element, depending on the Z. The large $B\rho$ acceptance (20%) allows for the detection of these different charge states.

Large acceptance spectrometers have been widely employed for this aim, often coupled with γ-ray arrays or silicon arrays for light charged particles, as in the case of the present experiment, where the VAriable MOde high acceptance Spectrometer (VAMOS++) is coupled with the γ-ray array AGATA and with the MUGAST silicon array. Other similar spectrometers are PRISMA [72], operating at the LNL, and MAGNEX [73] at LNS.

VAMOS can operate in two different modes: as a zero degree recoil separator, as in the present experiment, or as a dispersive spectrometer at different angles. Moreover, the possi-

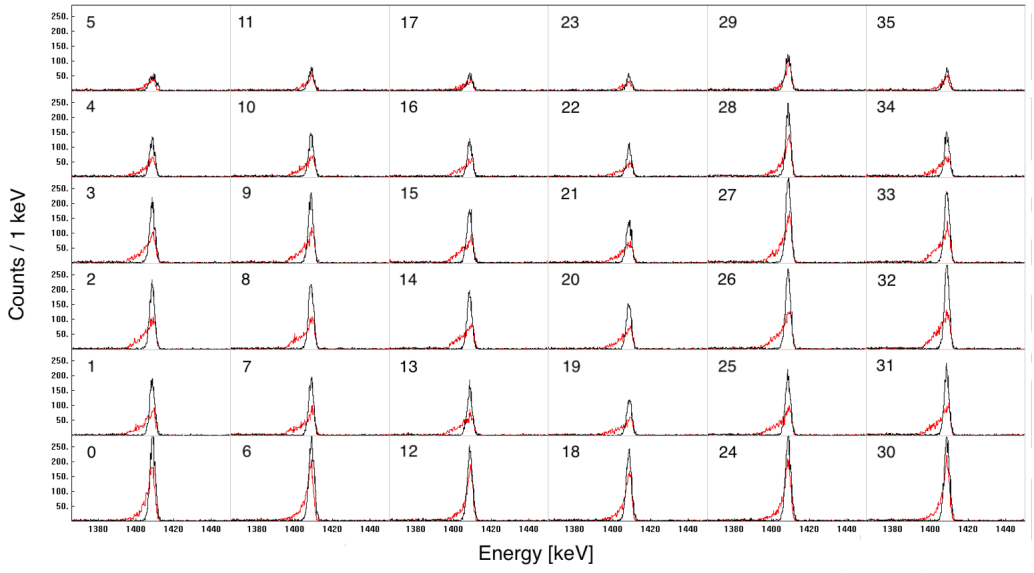

Figure 2.13.: γ-ray spectrum showing the 1407-keV peak coming from a ^{152}Eu source before (red) and after (black) the neutron damage correction. The resolution of the detector improves significantly for all the segments.

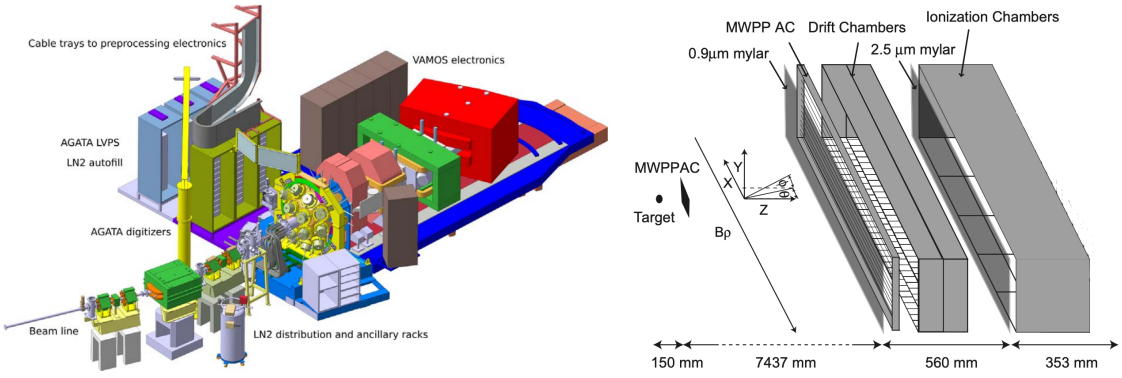

Figure 2.14.: (left) Scheme of the VAMOS++ spectrometer coupled with the AGATA array. Figure taken from [60]. (right) Scheme of the focal plane detectors. Figure taken from [74].

bility of operating VAMOS in gas-filled mode for the detection of fusion products has been successfully tested [75].

The spectrometer consists of a series of optical elements and a detection system [74]:

- large acceptance quadrupoles for the focalization of the beam-like residues;
- a dipole for the dispersion of charged particles;
- an entrance Multi-Wire Parallel Plate Avalanche Counter (MWPPAC) detector;
- a second MWPPAC for Time of flight measurements;
- two drift chambers;
- an ionization chamber.

The Time of Flight (ToF) of the particle is measured between the MWPPAC at the target level and the second MWPPAC while the drift chambers permit the determination of the (x, y) position of the particle. From this information, knowing the optical elements of the spectrometer, it is possible to reconstruct the exact trajectory of the particle on an event-by-event base. The second MWPPAC and the two drift chambers are used to measure the direction of the recoil on the focal plane. This information is compared to a set of simulated trajectories in order to extract most probable. Then, the ionization chamber is used to measure the energy loss ΔE of the charged particle and the residual energy E_r. Knowing v, the ΔE and E_r of the particles, it is possible to reconstruct the mass M, atomic number Z, charge state Q, energy E and angles $(\theta_{lab}, \phi_{lab})$.

Knowledge of the kinematics of the recoil is fundamental for γ-ray spectroscopy. Not only it is possible to gate on a specific nucleus to study its electromagnetic properties (excited states, branching ratios, reduced transition probabilities, etc.), but knowing the three components of the velocity vector of the γ-emitting nucleus, it is possible to perform an event-by-event Doppler correction, obtaining a better energy resolution with respect to the one achievable with a Doppler correction employing an average velocity.

However, due to the high counting rate induced by the beam, it was not possible to use the entrance detector, nor the drift chamber and the ionization chamber for the identification of the ions. Since during the beam diagnostic no contaminants were found in the radioactive beam, it was decided to use only the second MWPPAC of VAMOS for ToF measurement between the MWPPAC and the radiofrequency of the cyclotron and between VAMOS and MUGAST, in order to perform a ToF selection on the events of interest (see Section 3.1.1).

2.3.1. The Multi-Wire Parallel Avalanche Counter

The MWPPAC placed before the drift chamber is characterized by a good time resolution and high counting rate capabilities. The detector is composed of two grounded anodes and one central cathode, polarized at ~ -500 V, each separated by 2.2 mm. The wires are made of gold-coated tungsten and are 150 mm (vertical, cathode) and 1000 mm (horizontal, anode) long, for an active area of 1000×150 mm^2. Moreover, to reduce the capacitance, the cathode is segmented into 20 independent sections, ensuring a fast rise time, essential for a good time resolution. The detector is filled with 6.0 mbar of isobutane (C_4H_{10}) and is isolated from the vacuum of the beam line by an entrance window of 0.9 μm mylar, placed before the MWPPAC.

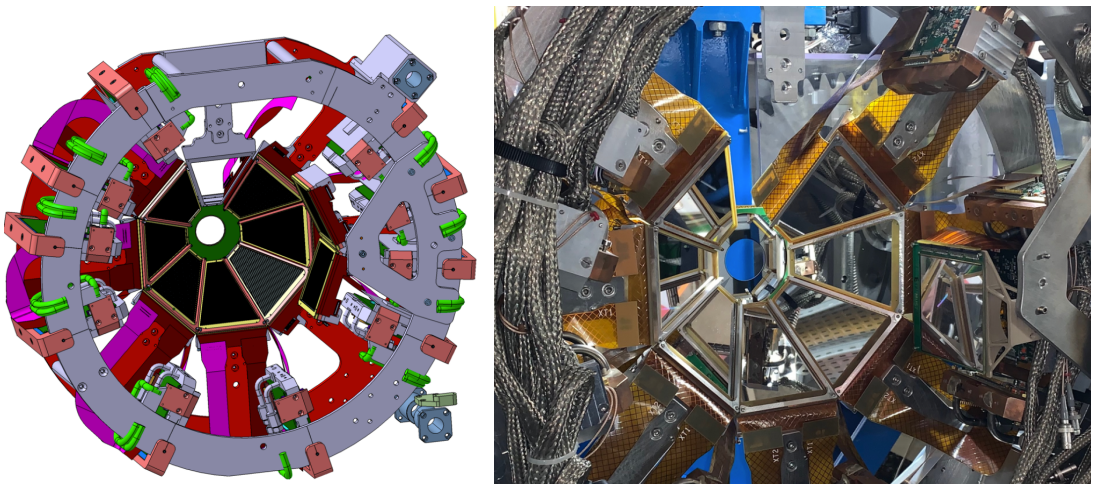

Figure 2.15.: (left) A scheme of the trapezoidal detectors, placed at backward angles. Two square detectors are also present in the figure. (right) A picture of the trapezoidal detectors of MUGAST. In the photograph, one square detector, which was not employed in the present experiment, is also visible. Figures taken from [79].

2.4. The MUGAST array

The GRIT [76] project is a European collaboration aimed at building a highly-segmented 4π Silicon array in order to achieve a better angular and energy resolution in the detection of charged particles for nuclear studies. This project started with the MUST [77] and MUST2 [78] phase, and the third phase, MUGAST [79], is currently operative at GANIL. The GRIT array has been designed to be compatible with the AGATA array.

MUGAST is an array composed of 12 double-sided strip Silicon detectors (DSSD) arranged to fit in a reaction chamber of 18 cm diameter. At backward angles, at 13 cm from the target, seven 500 μm-thick trapezoidal neutron Transmutation Doped (nTD) type DSSDs are placed as shown in Figure 2.15, covering the theta angles between 110° and 150°. The coverage in phi angles is about 70% of the hemisphere in the configuration with 7 trapezoids. Good angular coverage is achieved using a compact configuration where the mechanical part where limited. By comparing the measured efficiency with the simulated one [79], a disagreement was observed around 100° that was attributed to the target frame. In this position, the silicon detectors cover the backward crystals of AGATA. However, the transparency to γ rays is insured by moving the front-end electronic of the silicon detectors to 90°. Each detector is segmented into 128 strips on the front side, 710 μm large, and 128 on the rear side, 760 μm large.

A silicon annular detector covers the angle between 160° and 170°. During the commissioning, the coverage in phi angle was about 80% [79], while in the present experiment the annular detector covered about 50% of phi angle. This detector is divided into four 500 μm-thick quadrants, each of them divided into 16 rings on the front side and four sectors on the rear side.

At forward angles, 4 MUST2 telescopes were placed, covering an angular range between 8° and 50°. The squared detectors consist of four 300 μm-thick DSSDs coupled to 16 CsI

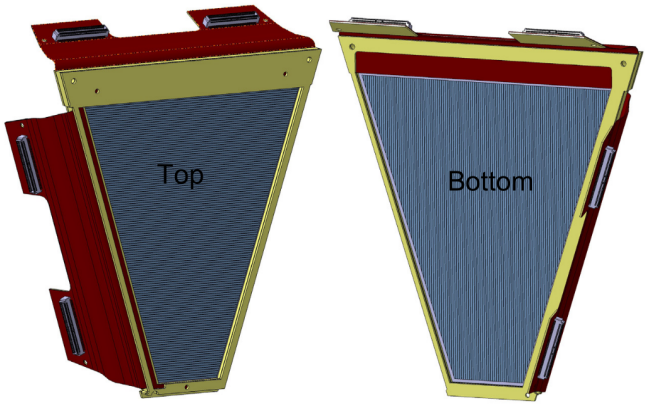

Figure 2.16.: Realistic reproduction of the trapezoidal detectors. The front side, called "top", is segmented horizontally while the rear side, called "bottom", is segmented vertically. Figure taken from [79].

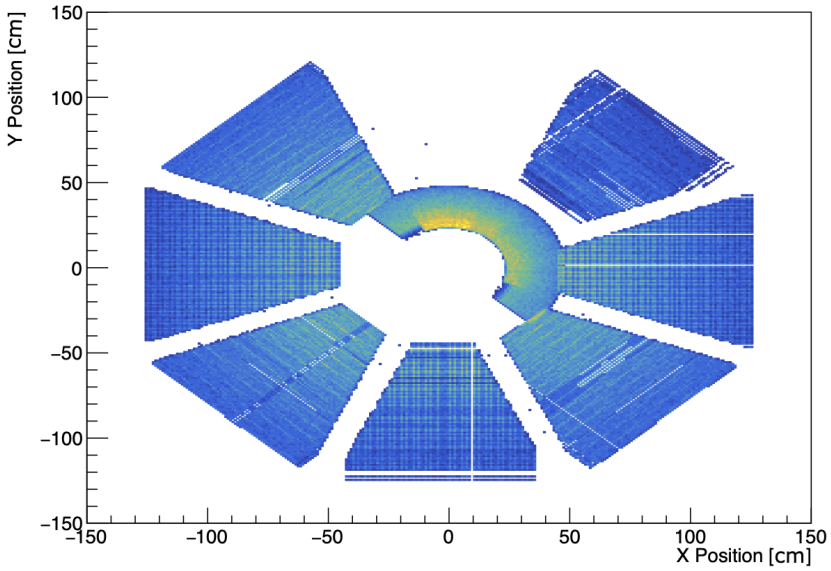

Figure 2.17.: Positions of the MUGAST detector on the X and Y axes, showing the seven trapezoidal detectors and the annular one. The compact configuration guarantees a large coverage of the phi angle. Only half of the sectors of the annular detector were operative during the experiment.

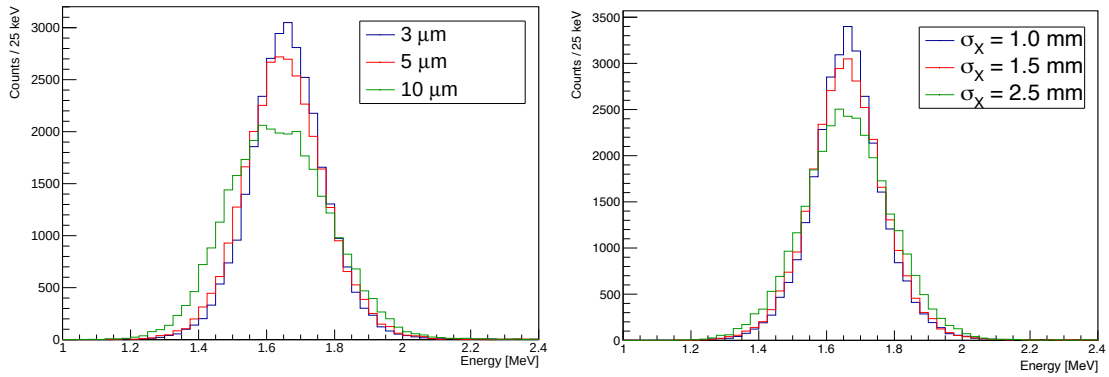

Figure 2.18.: Dependence of the FWHM of the 1.6-MeV peak of ^{20}O on the thickness of the target (left) and the beam spot size in X direction (right) for the silicon detectors of MUGAST, simulated using the NPTool code.

crystal and their photomultipliers. The silicon detectors are segmented into 128 strips on the front and 128 strips on the rear side. Finally, an additional 500 μm 10×10 cm^2 detector, segmented with 128 strips on each side, is placed at 90°. This detector is used to measure the elastic scattering of the beam on the target for normalization purposes.

In the present experiment, only the backward detectors were employed. In fact, the rate of fusion and elastic scattering products on the forward detectors was too high to be sustained and the detectors were removed. Moreover, the proton emitted at forward angles passed through the thick layer of gold, placed after the target, and the straggling in the material affected the energy resolution, when they were not stop inside the degrader.

MUGAST performances

The segmentation of the silicon detectors guarantees a high angular resolution that, for the backward detectors, goes below 0.4°. The position of the detectors inside the reaction chamber is measured with a precision of 0.2 mm.

This precision, together with a good energy resolution, is fundamental for studying angular distributions and reconstructing the excitation energy spectrum of a nucleus, separating states that otherwise would be unresolved.

The elements that typically affect the excitation energy resolution, besides the intrinsic energy resolution of the detector, are the straggling effect in the target and the beam focusing.

Using the NPTool simulation code [80], the effects of target thickness and beam spot size were tested to quantify their influence. Figure 2.18 (left) shows the influence of the target thickness on the resolution of the excitation energy spectrum. With respect to a $3\mu m$-thick target, the FWHM of the 1.6-MeV peak increases by 8% for a $5\mu m$-thick target and by 35% for a $10\mu m$-thick target. In Figure 2.18 (right), instead, the dependence on the beam spot size is shown: with respect to $\sigma_X = 1.0$ mm, the FWHM increases of 7% for a beam spot of $\sigma_X = 1.5$ mm and 28% for $\sigma_X = 2.5$ mm.

In the present experiment, a thin target of 0.3 μm, was employed in order to reduce the straggling effects and to obtain a good resolution. The beam size obtained by the SPIRAL1 optic elements was $\sigma_X = 1.5$ to 1.8 mm and $\sigma_Y = 2.7$ to 3.0 mm. With these elements, the

Nucleus	Energy [MeV]	Intensity [%]
^{239}Pu	5.15659(14)	70.77(14)
	5.11443(8)	17.11(14)
	5.1055(8)	11.94(14)
^{241}Am	5.48556(12)	84.8(5)
	5.44280(13)	13.1(3)
	5.38823(13)	1.66(2)
^{244}Cm	5.80477(5)	76.40(12)
	5.76264(3)	23.60(12)

Table 2.1.: Energies of the alpha source for the calibration of the MUGAST detector.

energy resolution for the 2_1^+ excited state of ^{20}O at 1.67 MeV was measured to be 179 ± 4 keV (FWHM). According to Ref. [79], 22% of the resolution is attributed to the intrinsic resolution of the detectors, while 17% is attributed to the beam spread in energy and position. The main contribution, the 60%, comes from the angular and energy straggling of the protons in the target. The energy resolution obtained with HELIOS for the same state using the same reaction with a slightly thinner target of 0.26 μm is 175 keV (FWHM), comparable with the one obtained with MUGAST.

2.4.1. Calibration of silicon detectors

For the energy calibration of MUGAST detectors, a triple-α source of ^{239}Pu, ^{241}Am and ^{244}Cm (see Table 2.1), placed at the target position, was employed. Each X and Y strip was calibrated independently for the seven trapezoidal detectors and the annular one. The dead layer due to the passivation of the detectors was taken into account when calculating the expected energy of the α particle. Moreover, for the X strip, the different thickness of the dead layer due to the impinging angle was also considered. A dedicated macro individuates the alpha peaks for each strip of each detector and calculates the coefficients for a linear calibration. The calibrations of the strips were then checked one by one and, when not correctly aligned, the linear coefficients were calculated manually. The strips before and after the calibration are shown in Figure 2.19 for Detector 1. A similar procedure was followed for the energy calibration of all silicon detectors.

For the time calibration, a start and stop signals were generated by a pulser. The time between the start and the stop is $t = N \times \tau$ where N is a randomly generated integer number and τ is set to 20 ns, covering a range of 640 ns. The signal is sent to a Time to Digital Coverter (TDC). A dedicated macro individuates the signals registered by each strip and aligns them by using a second order polynomial. The strips before and after the calibration are shown in Figure 2.20 for Detector 2.

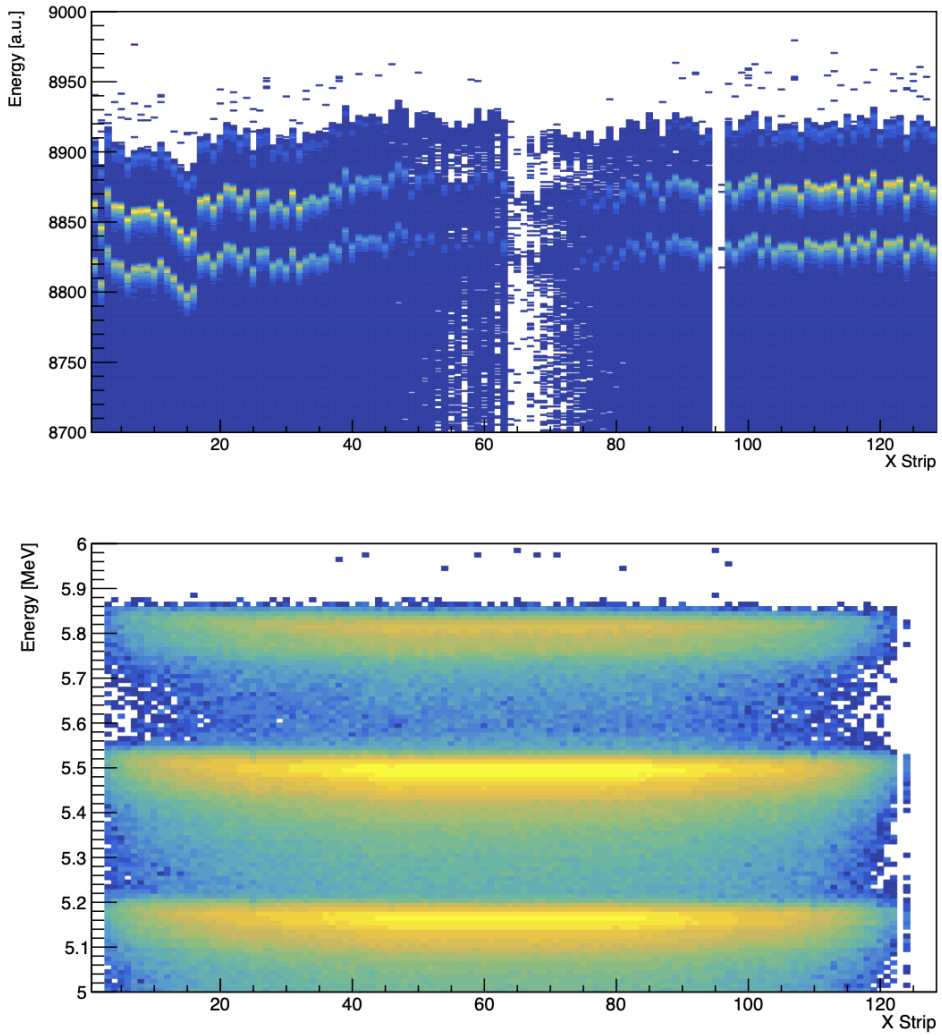

Figure 2.19.: (top) Energy in the DSSDs as a function of the X strips for Detector 1. (bottom) Calibrated energy as a function of the X strips for Detector 1.

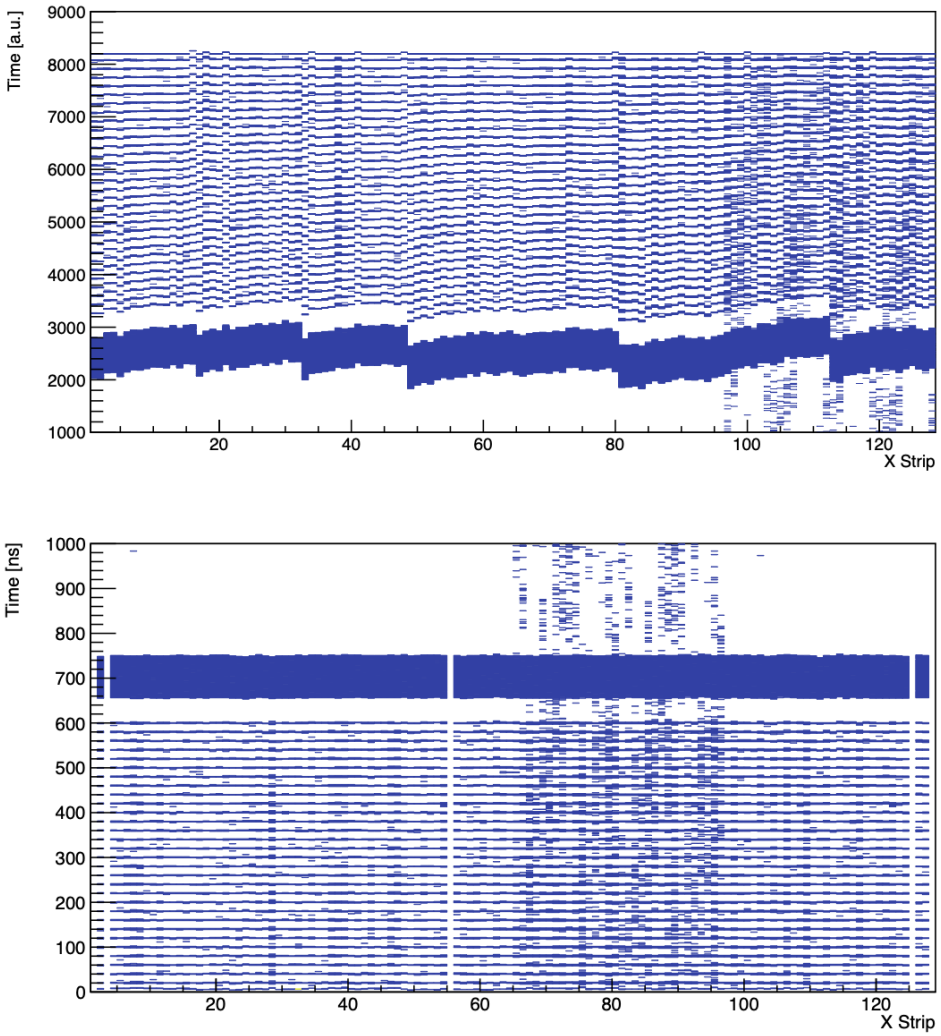

Figure 2.20.: (top) Time in the DSSD as a function of the X strips for Detector 2. (bottom) Calibrated time as a function of the X strips for Detector 2.

2.5. The MUGAST-AGATA-VAMOS configuration

The MUGAST-AGATA-VAMOS configuration was employed for in-beam experiments using radioactive SPIRAL1 beams in GANIL, with energy up to 12 MeV/A. This apparatus is particularly suited for studying direct reactions, since it allows one to obtain a complete reconstruction of the reaction kinematic and a strong control on the direct population of the excited states. During the campaigns, the beam was monitored using CATS [81], consisting of two low-pressure MWPC that allow one to obtain a spatial resolution of about 400 μm with a counting rate up to 1.5×10^5 pps, suitable for experiments with radioactive beams. A good beam diagnostic allows one to know with precision the position of the beam spot and the counting rate. The information on the beam spot is useful to optimize the tracking algorithm and obtain a better reconstruction of the γ-ray interaction in the AGATA crystals, while the counting rate is important to measure the absolute cross section of the reaction. However, the CATS detectors introduce an energy and angular straggling effect in the beam and for the present experiment they were removed from the beamline.

AGATA, MUGAST and VAMOS are running with independent electronics and data acquisition (DAQ) systems. The physical events are reconstructed offline using time stamp information. As mentioned before, AGATA crystals are synchronized using the GTS system, associating a time stamp (AGATA Time Stamp, ATS) to each event. Similarly, an independent GTS tree is used for synchronizing the VAMOS electronics (VAMOS Time Stamp, VTS). To merge the events of the three detectors together, two AGATA VME Adapters (AGAVA) [56] are placed inside the MUGAST electronics, allowing one to correlate the VTS and ATS.

The MUGAST readout is enabled when at least one of the MUGAST detectors is triggered, while VAMOS events are readout only when they are in coincidence with a MUGAST detector, in order to reduce the data flow. The event builder used to correlate VAMOS and MUGAST events is based on the VTS and has a coincidence window of 1 μs when the ToF in VAMOS is expected to be between 100 and 150 ns. Finally, an additional event merger based on the ATS correlates the AGATA data to MUGAST+VAMOS events within a time window of about 1 μs [79].

2.6. The target

Deuterated polyethylene targets, commonly known as CD_2, are vastly used in nuclear physics for studying deuteron-induced reactions, which are perfect tools for probing single-particle states [82]. CD_2 targets can be produced either as self-supporting targets or deposited on a layer of another material.

Many techniques have been developed for the preparation of these targets, including vacuum deposition, hot press and solvent casting. This last technique is the most commonly used. The C_2D_4 powder is dissolved in a solvent (typically xylene) by heating the mixture above its melting temperature (125 °C). When the solvent evaporates, the thin film of plastic is left on the surface. With this kind of technique, targets of thickness from 20μg/cm^2 to 2 mg/cm^2 can be prepared.

For the present experiment, three targets were prepared. The first one was a self-supporting CD_2 target of 300μg/cm^2. This target was used to measure with better precision the energy of the γ-ray transitions of the ^{20}O, as explained in Section 4.1. The second and the third

targets are made of a CD_2 300-μg/cm^2-thick layer deposited on a 20-mg/cm^2 gold support and they have been used to perform the lifetime measurements, as explained in Section 2.7. A scheme of the target placement on the target holder is presented in Figure 2.21.

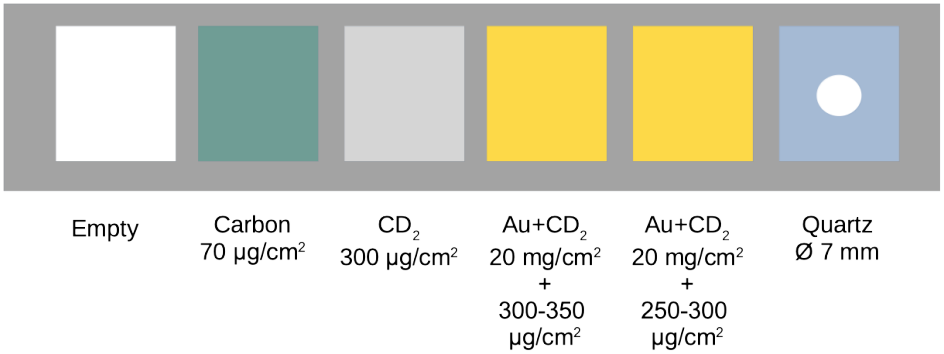

Figure 2.21.: Scheme of the targets disposed on the target holder. The nominal thickness is reported for each target.

It is difficult to determine *a priori* what the thickness of the target will be before the deposition of the material. Thus, after the experiment, the CD_2 targets deposited on the Au layer were analysed using the Focused Ion Beam (FIB) and the Scanning Electron Microscope (SEM), as shown in Figure 2.22. In particular, the FIB was used to create a microscopic hole on the CD_2 layer, while the SEM was used to measure the thickness of deposition. This analysis determined a certain level of inhomogeneity of the plastic layer, highly dependent on the point of measurement. In particular, the presence of bubbles has been observed, as shown in Figure 2.23. These bubbles can affect the measurement by modifying the effective thickness of the target and hence the energy loss. The systematic error related to the different composition of the target is discussed in Section 4.5.

2.7. The Doppler Shift Attenuation Method

The Doppler Shift Attenuation Method is a technique developed in the Fifties by Devons and collaborators [83] for the measurement of short-lived nuclear states in the typical range of femtosecond. The idea behind this technique is to measure the Doppler shift that is observed in the γ rays obtained by slowing down the emitting recoil into a backing placed right after the target. There is a precise relation between the average Doppler shift and broadening, the range of the recoil in the material and the lifetime of the state. Knowing the range of nuclei in the material, it is possible to extract the lifetime of the state from the measurement of the Doppler effect.

The first methods developed for the extraction of the lifetime using the DSAM were based on the radiation effect and on the energy loss of the recoil into the backing material. The Doppler effect shifts the energy of the γ-ray transition to [84]

$$E_\gamma(\theta, t) = E_0 \frac{\sqrt{1-\beta^2(t)}}{1-\beta(t)\cos\theta}, \tag{2.2}$$

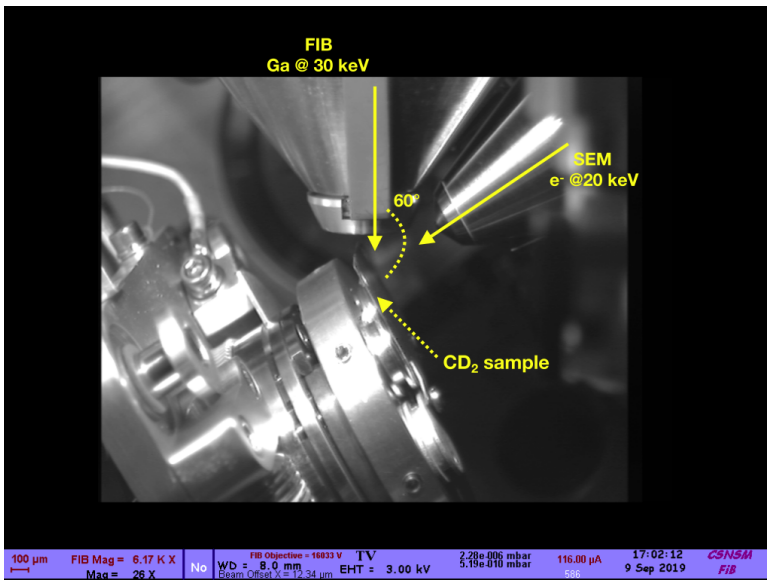

Figure 2.22.: Scheme of the experimental apparatus used for the characterization of the targets.

where E_0 is the real energy of the γ-ray transition, θ is the angle of detection of the γ ray and $\beta = v/c$ is the velocity of the recoil. However, in the case of the DSAM, the velocity varies in time during the process of slowing down from an initial velocity of v_i to $v_f = 0$ in case the degrader thickness is sufficient to stop the recoil. In case of a thinner degrader, $v_f > 0$ and this method is called differential DSAM.

Knowing the velocity function, namely the variation of the velocity as a function of time, is fundamental for this kind of measurement. Many formulations of the problem have been suggested depending on the velocity range of the recoil. In particular, three regions of velocities have been considered:

- low velocity ($\beta \lesssim 0.5\%$): in this range the nuclear scattering of the recoil with the nuclei of the material is predominant in the stopping process;
- medium velocity ($0.5\% < \beta < 2\%$): in this range the electron stopping starts being predominant but the nuclear scattering is not negligible;
- high velocity ($\beta > 2\%$): in this range, the nuclear scattering is negligible.

The first two regions are typically investigated using theoretical calculations, as the experimental data is still scarce. The work of Lindhard et al. [85] is widely accepted for the treatment of slowing-down processes in these ranges of velocity. In the range of high velocity, the analysis is easier and the results are generally more accurate.

The experimental spectrum of a DSAM experiment typically presents a peak where the events are arranged in a continuous distribution $E_\gamma(t)$ ranging from $E_\gamma(0)$ (as defined in Equation 2.2) to $E_\gamma(t \gg t_c)$, where t_c is the time the recoil needs to stop in the stopper or, in case of a differential DSAM experiment, to pass through the degrader. In the first case $E_\gamma(t \gg t_c) = E_0$ ($\beta = 0$). From experimental data on the slowing-down process, it is possible to extract the attenuation factor F, which depends on the lifetime τ of the state and can be

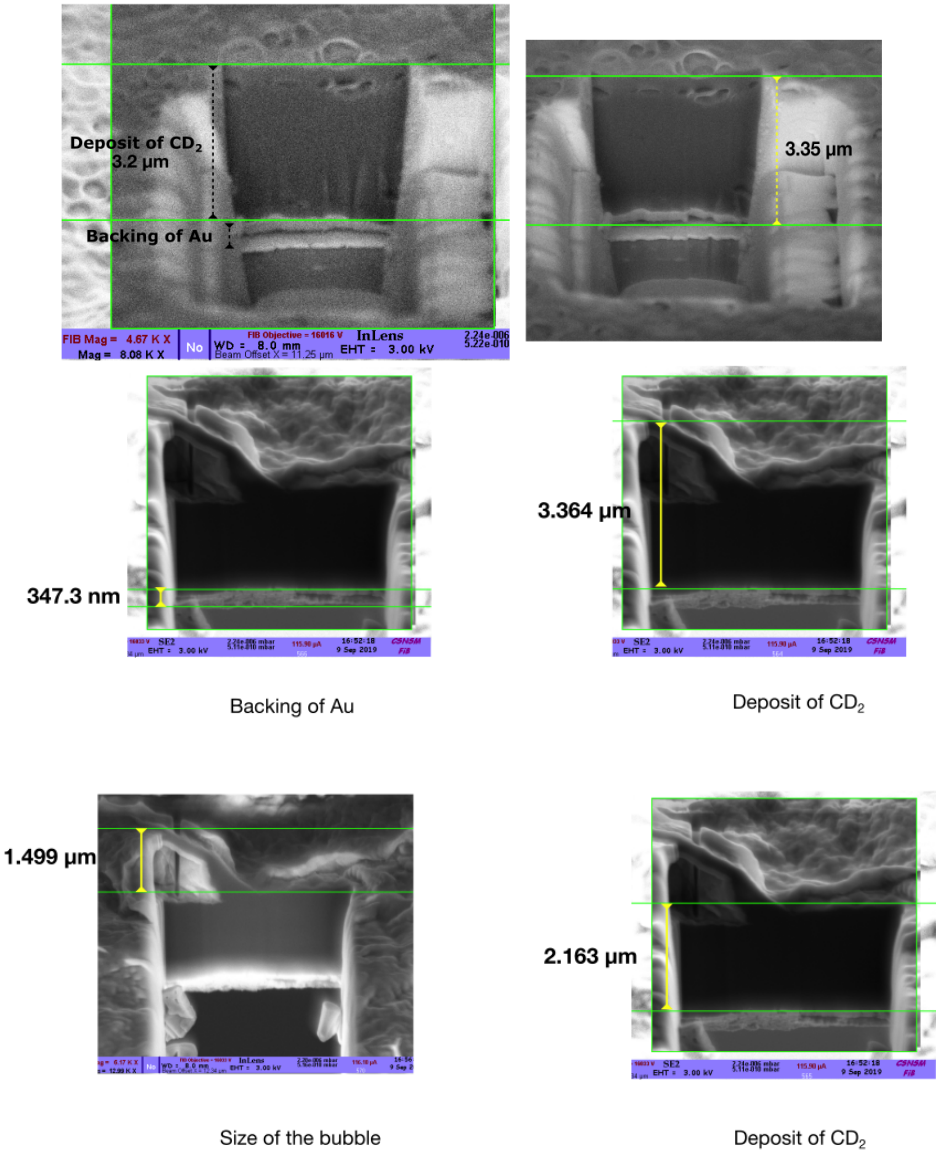

Figure 2.23.: (top) Measurement of the CD_2 target thickness taken on the target frame. (bottom) Measurement of the CD_2 target thickness taken outside of the target frame. The presence of a bubble is observed.

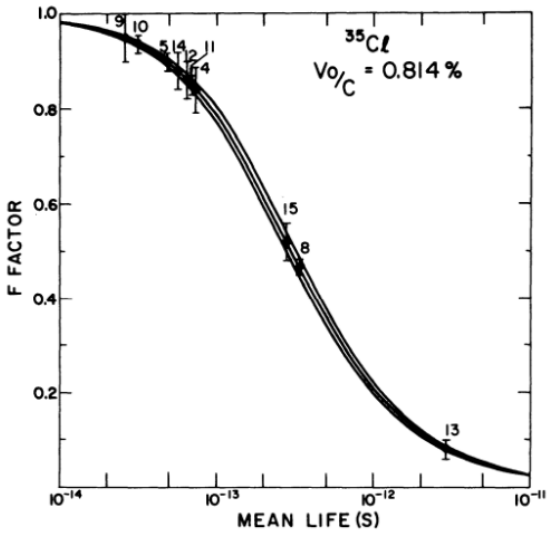

Figure 2.24.: Example of an empirical attenuation factor curve that explicitly shows the dependence of F from τ, allowing the extraction of the lifetime from the measurement of F. This specific curve was obtained for a ^{35}Cl nucleus with an initial $\beta = 0.814\%$. Figure taken from [84].

defined as:

$$F(\tau) = \frac{\langle E_\gamma(\theta)\rangle - E_0}{E_0\beta(0)\cos\theta}. \tag{2.3}$$

Knowing the exact velocity function, is is possible to re-write the attenuation factor as

$$F(\tau) = \frac{1}{v_i\tau}\int_0^\infty v(t)e^{-t/\tau}dt, \tag{2.4}$$

where v_i is the initial velocity, namely the velocity at which the recoil is produced in the reaction. Numerous experimental curves representing the dependence of F on τ have been calculated (an example can be seen in Figure 2.24), allowing one to extract the lifetime of a state from the measurement of the attenuation factor. In case of $F(\tau) \approx 1$ or $F(\tau) \approx 0$, it is not possible to extract the lifetime, but only an upper or lower limit is given respectively. These cases correspond to a lifetime that is $\tau \ll t_c$ or $\tau \gg t_c$, which means that the lifetime is outside the range of sensitivity of the DSAM experiment.

This method has been used extensively in the past to extract lifetimes in different regions of the nuclear chart. However, it relies on many approximations and assumptions, and the $F(\tau)$ curves do not take into account several factors such as:

- the scattering of the slowing ions;
- the finite size of the γ-ray detectors;
- the initial velocity distribution;
- the angular distributions of the recoils;

- the feeding from other states.

For medium-low velocities of the recoil, in experiments where the Doppler shift is comparable to the resolution of the detectors, the lifetime extracted from the centroid shifts using the attenuation factor curves can still be considered accurate. However, for experiments where the recoils are faster and the Doppler shift is significantly larger than the detector resolution, a more accurate result is obtained using the lineshape analysis.

2.7.1. Lineshape analysis and Monte Carlo method

The lineshape analysis compares the experimental spectrum with lineshapes calculated for different lifetime values. The lifetime of the state is extracted based on how well a curve reproduces the experimental peak lineshape. With respect to the centroid shift method, the lineshape contains the complete information on the velocity distribution and the results are generally more accurate and less affected by systematic errors.

The most used method to compute lineshapes, which are then compared to the experimental data, is the Monte Carlo calculations. The Monte Carlo method treats the nuclear scattering as a random process: each ion proceeds inside the target and the backing through random collisions until a γ ray is emitted. Then, depending on the thickness of the stopper, the ion is stopped inside or exits the backing with a velocity determined by the path that it followed inside the material. Random number generators are used to determine:

- the time of emission of the γ ray;
- the initial velocity of the ion;
- the position of the reaction within the target;
- the number of collisions inside the material;
- the scattering angle after each collision;
- the angle of entry in the detector.

In order to achieve more accurate results and reduce the sources of errors, it is possible to optimize the Monte Carlo simulation taking into account different factors that influence the lineshape of the peak, including the angular distribution, the resolution of the detectors and the geometrical efficiency of the apparatus. A more exhaustive list of these factors and how they influence the lifetime measurement has been discussed in detail in Chapter 3.

2.7.2. Effect of the feeding from higher levels on the lifetime measurement

In nuclear reactions, it is common to populate more than one state of the nucleus of interest. It is possible that the state we intend to study is not directly populated (or only partially) in the reaction, but rather another state at higher energy decays on the state of interest, populating it. In these cases, if the lifetime of the feeding state is comparable to the lifetime of the state of interest or longer, it can significantly affect the measurement of the lifetime.

Let us consider a simple level scheme as presented in Figure 2.25, where we are interested in measuring the lifetime τ_1, whose measurement is influenced by the feeding transitions coming

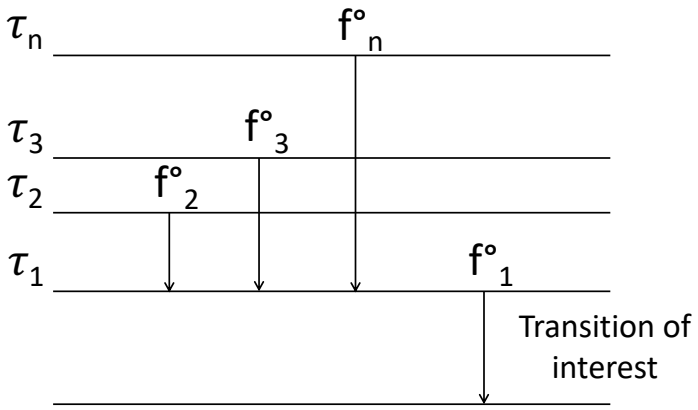

Figure 2.25.: Level scheme of a nucleus where more states are populated.

from the levels 2, 3 and n with lifetimes of τ_2, τ_3 and τ_n of the same order of magnitude of τ_1. Then the fraction of events decaying from level 1 to level 0 is:

$$f_1(t) = \frac{1}{\tau_1}\left[f_1^0 e^{-t/\tau_1} + \sum_{i=2}^{n} f_i^0 \frac{\tau_1}{\tau_i - \tau_1}(e^{-t/\tau_i} - e^{-t/\tau_1})\right]. \tag{2.5}$$

where f_1^0 is the fraction of the nuclei directly populated in the state i. The attenuation factor for the case of feeding transitions is now dependent on the different lifetimes and attenuation factors:

$$\begin{aligned} F(\tau_1, \ldots, \tau_n) &= \int_0^\infty \left[f_1^0 e^{-t/\tau_1} v(t) + \sum_{i=2}^{n} \frac{e^{-t/\tau_i} - e^{-t/\tau_1}}{\tau_i - \tau_1} v(t)\right] \\ &= f_1^0 F(\tau_1) + \sum_{i=2}^{n} \frac{\tau_i F(\tau_i) - \tau_1 F(\tau_1)}{\tau_i - \tau_1} f_i^0. \end{aligned} \tag{2.6}$$

Hence, if τ_i (with $i = 2, \ldots, n$) and f_i^0 (with $i = 1, \ldots, n$) are known, it is possible to extract the lifetime τ_1 both using the centroid shift method and the lineshape analysis. However, in these cases the measurement of τ_1 depends on the measurement of the other τ_i and f_i^0 and a wrong measurement of one of these quantities would affect the final result.

For this reason, when possible, it is preferable to select the events that directly populate the state of interest and eliminate the contribution from the feeders, either by choosing a selective reaction that populates only the state of interest or by requiring an energy gate on the excitation energy of the nucleus. In this way, the measurement of the state of interest is independent of the measurement of the other states.

This second procedure has been employed for the present analysis, where the excitation energy of the ^{20}O reconstructed using MUGAST allowed for a selective energy gate on the direct population of the state, as seen in the previous section. Therefore, the feeding from the 3_1^+ state or other higher-lying states do not affect the measure of the 2_2^+ lifetime.

2.7.3. Target and backing preparation for DSAM measurements

In order to perform a measurement using the DSAM, the target is deposited on a backing that acts as a degrader, contrary to the RDDS method, where a series of different distances between the target and the degrader or stopper is needed to perform the measurement. Therefore, while with the RDDS method we expect two distinct peaks corresponding to two velocities, in the DSAM we expect one continuous distribution that varies depending on the initial velocity of the recoil, the thickness of the degrader and lifetime of the state.

Typically, in DSAM measurements, a thin target is deposited on the backing material. A thin target guarantees a better energy resolution of the excitation energy spectrum and a smaller velocity spread, making the lineshape analysis more accurate.

Thin targets, however, present numerous downsides. First of all, when evaporating the material on the backing, the formation of microcavities can happen. Microcavities have the effect of changing the density of the target and influencing the path of the ions inside the target. This might affect the final lineshape of the peak. Another problem of thin films is the dishomogeneity of the deposit on the backing material. If the deposit is not homogeneous, the thickness of the target changes depending on the point of interaction of the beam. Thus, it is important to ensure that the part of the target corresponding to the beam spot is as homogeneous as possible. Finally, it is important to ensure that the contamination due to other elements, as for example oxygen or carbon, is under control.

In order to overcome these problems, several solutions have been suggested. The quality of the film deposit depends on the surface of the backing material, which must be clean and homogeneous. It has also been observed that, in case of evaporation of plastic on metal, the film presents a better adherence and a more homogeneous deposit for slow cooling-down processes. This might be due to the fact that the materials of the target and the backing typically have different dilatation coefficients.

Finally, after the experiment is performed, an analysis using an electronic microscope, such as the Scanning Electron Microscope (SEM), allows one to control the level of homogeneity and the presence of microcavities and determine the overall quality of the target.

The choice of the backing material is also important. The most commonly used materials are metals, with particular attention to those that are less affected by oxidation. Natural gold is a typical choice. The thickness of the backing must be chosen taking into account the expected range of lifetimes that one intends to measure, to ensure that the stopping time or the time spent to cross the backing (t_c) is of the same order of magnitude of the expected lifetime.

Depending on the experiment, the backing thickness can be chosen to stop the recoil in the backing (in this case, a stopper) or only to significantly change the velocity of the recoil, that exits the backing with a velocity $\beta > 0$ (in this case, a degrader). The advantage of using a degrader is that the recoil can be detected after the energy loss. The detection of the recoil allows one to obtain more information, depending on the detector used for the measurement. For example, by using a magnetic spectrometer, it is possible not only to select the events in coincidence with the nucleus of interest, hence cleaning the spectrum from the contribution of parasite reaction channels, but also by measuring the energy and the position of the recoil, it is possible to reconstruct the velocity vector of the nucleus and use this information to perform an event-by-event Doppler correction.

The nominal thickness of the backing can differ from the real one even up to a 10-20%. This method, however, does not take into account the possible inhomogeneity of the backing.

Another method is to measure the energy loss of a particle in the foil. Depending on the thickness of the material, it is possible to use a collimated α-particle source or an accelerated beam. This second method is more precise with respect to the previous one; however, it is affected by the straggling of the particle inside the target.

The most precise method is the Rutherford Backscattering method, where a collimated ion beam, typically α particles, impinges on a target and the backscattered ions are measured at a fixed angle. Depending on the energy of the backscattered particle it is possible to extract the thickness of the target. This same method is also useful to determine the presence of contaminations.

3 Analysis and optimization

The AGATA and MUGAST arrays are powerful tools for nuclear experiments. With their high energy and position resolution, they constitute the state-of-the-art of segmented germanium and silicon detectors, respectively. However, in order to push their capabilities to their limits, a thorough optimization is required. The characteristics of AGATA and MUGAST, such as the position, the resolution and the efficiency, were studied in detail. The capabilities of the two arrays were combined to entail a better Doppler correction, fundamental for Doppler Shift Attenuation Method (DSAM) analysis. Moreover, in order to extract the lifetime of the 2_2^+ and 3_1^+ states, a series of realistic parameters must be added to the Monte Carlo simulation in order to ensure the accuracy of the result. These parameters and their influence on the simulations have been studied.

3.1. Optimization of the apparatus

The AGATA and MUGAST arrays have been optimized for the present analysis. The time gate for the selection of the events of interest has been chosen. The nominal position of the AGATA array, as well as the stability of the crystals has been verified. The parameters of the tracking algorithm have been chosen to maximize the P/T and the number of events reconstructed, then the efficiency and the resolution of the array have been studied. The kinematic reconstruction of the ^{20}O recoils has been obtained from the information of the detected protons and the procedure is explained in detail. Finally, the thickness of the gold degrader has been investigated.

3.1.1. Optimization of the time gate

As stated in Chapter 2, the drift and ionization chambers of the VAMOS++ spectrometer are usable with counting rates up to 100 kHz, while they become inefficient for higher beam intensities. The MWPPAC placed at the focal plane of the spectrometer was used to measure two times of flight: the one between the radiofrequency of the cyclotron and VAMOS (VAMOS-HF) and the one between MUGAST and VAMOS (VAMOS-MUGAST). These two ToF measurements were used to perform a time gate and select the events of interest, in order

to clean the spectrum from background events, such as the reaction on the gold backing or the scattering on carbon nuclei of the target.

The ToF between MUGAST and VAMOS, however, presented some issues. In Figure 3.1.1 (top) it is possible to observe a different ToF for the MUGAST detectors. This misalignment is due to a delay caused by the cables. The detectors were aligned with respect to the annular detector (Detector 11) by adding an offset to the time measurement. The result of this alignment is shown in Figure 3.1.1 (bottom).

To decide the size of the gate, two quantities were considered: the number of events on the $2_1^+ \rightarrow 0_1^+$ peak of the ^{20}O and the P/T ratio. Different gates have been tested by changing the upper value of the VAMOS-HF Time of flight in a range from 12900 to 13500 by steps of 20. Figure 3.2 shows how the number of events on the analysed transition increases as the gate increases and then saturates around 13300. However, when looking at the P/T ratio, it is clear that a larger gate only increases the background. The upper value of the VAMOS-HF ToF for the gate has been set to 13320. The chosen gate for the dataset using the CD_2+Au target is presented in Figure 3.3.

3.1.2. Optimization of the AGATA array position

The AGATA infrastructure allows the array to translate in the beam direction and also to rotate along the same axis. For the present experiment, the nominal *z-offset* of the array was 49.0 mm, corresponding to a distance of 183 mm between the target position and the endcap, and the ϕ rotation was 265° with respect to the MUGAST reference. The relative position between MUGAST and AGATA is crucial for a correct computation of the angle between the recoil and the γ ray, which is later used for the event-by-event Doppler correction. An improper setting of the position leads both to a worsening of the resolution and an improper Doppler correction. In particular, the z-offset influences the calculation of the θ angle for the Doppler correction, leading to an incorrect estimation, while the ϕ angle uncertainty increases the Doppler broadening. In order to estimate the correct position of the array, different values of the z-offset and ϕ angle were used to calculate the correct angles used for the Doppler correction. The z-offset values were scanned in a range between -10 and 10 mm using a step of 1 mm around the nominal offset of 49.0 mm, while the ϕ angle was scanned for the whole 2π with respect to the nominal 0° position. The corresponding Doppler corrected γ-ray spectra for the runs with the CD_2-only target were produced for each configuration. For each spectrum, the centroid and the FWHM of the $2_1^+ \rightarrow 0_1^+$ transition of ^{20}O at 1674 keV were extracted. Then, the residuals with respect to the nominal value were plotted as a function of the z-offset, in order to find the position at which the residual was minimized, as presented in Figure 3.4 (left). Similarly, the FWHM of the peak was plotted as a function of the ϕ angle in order to find the minimum, as presented in Figure 3.4 (left). The z-offset and ϕ values that minimized the residual and FWHM respectively were -0.63 mm and 263.3°.

3.1.3. Stability of the crystals

In measurements where the energy precision is of fundamental importance, as in the case of the lineshape analysis, the stability of the detectors is carefully accounted for. The present dataset was collected through ten days of beam time, during which any modifications of the electronics or other external factors (e.g. temperature, humidity, etc.) could affect the

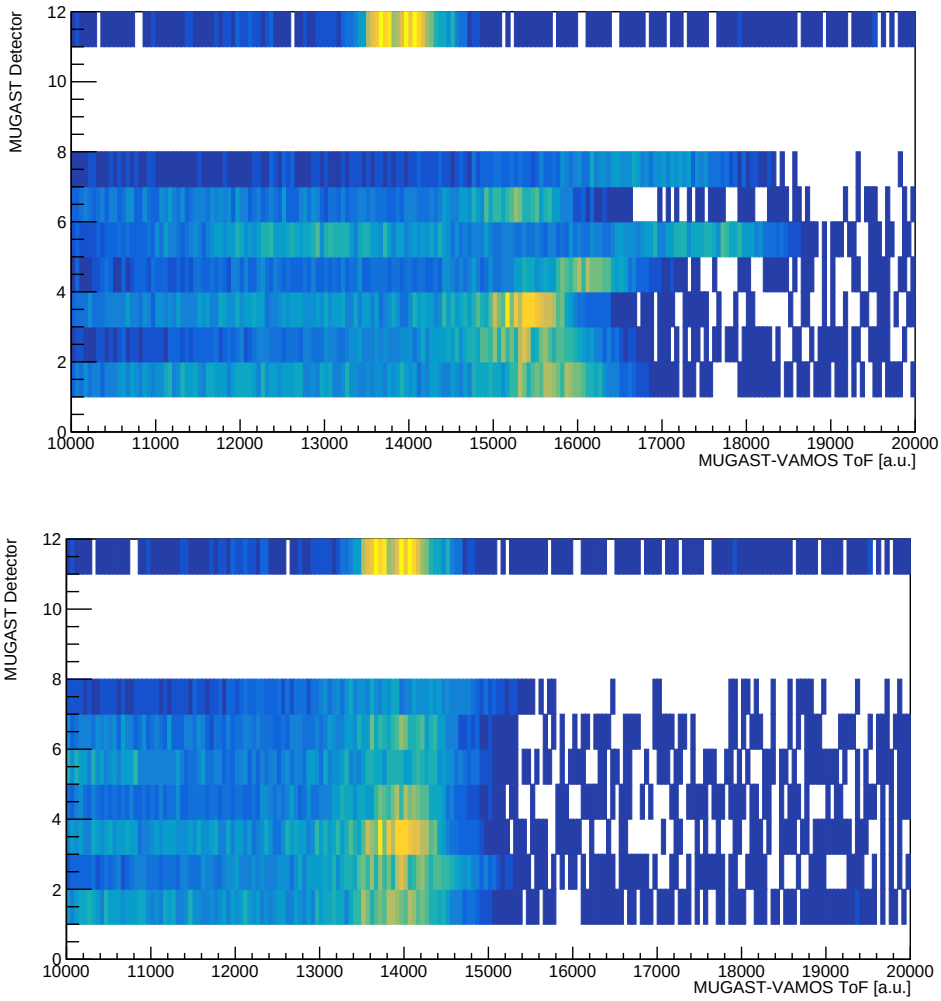

Figure 3.1.: (Top) The Time of Flight between VAMOS and MUGAST for the different detectors of MUGAST. (Bottom) By adding an offset, the Time of Flight of the detectors was aligned with respect to the annular detector.

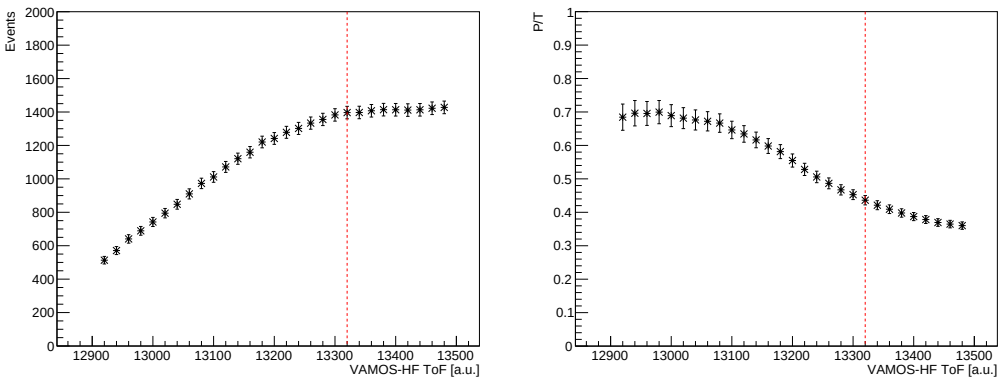

Figure 3.2.: (left) Number of events on the 1674-keV peak as a function of the time gate. At 13320 channel the number of events saturate. (right) P/T ratio as a function of the time gate.

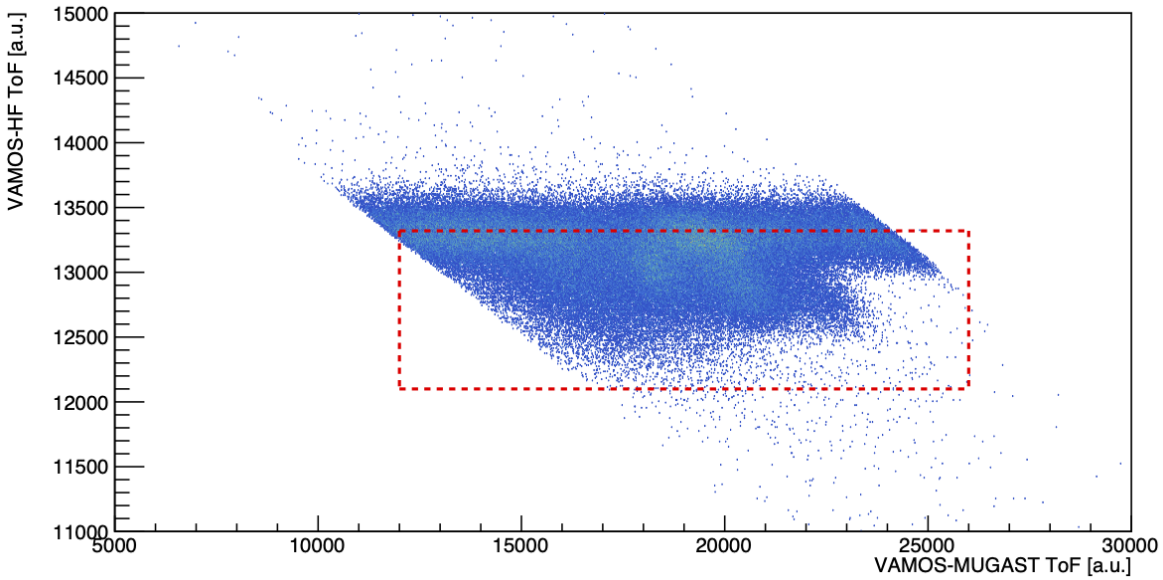

Figure 3.3.: Number of events as a function of the VAMOS-HF ToF and the MUGAST-VAMOS ToF. The chosen gate is marked in red.

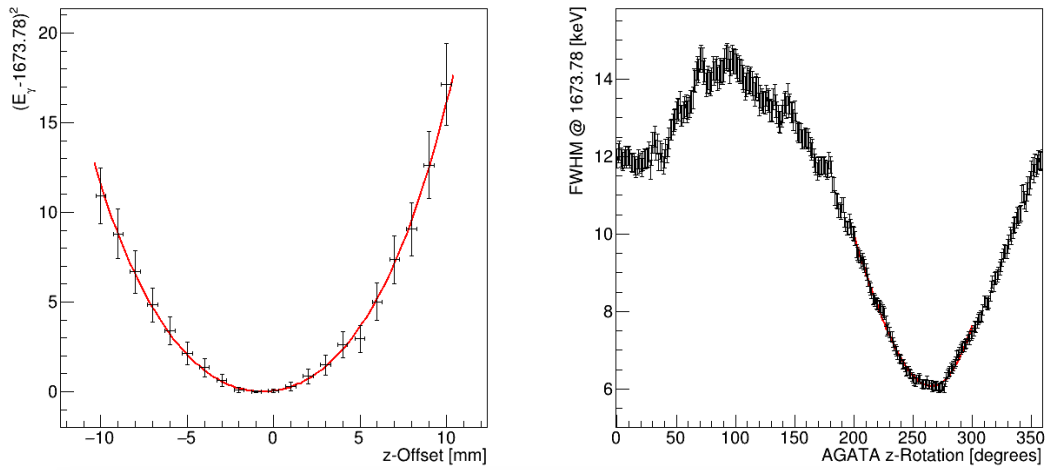

Figure 3.4.: Optimization of the z-offset (left) and the ϕ position (right) of the AGATA array.

resolution of the detectors. By quantifying the stability of the crystals, it is also possible to estimate the confidence in the energy measurement and compute the error.

In order to verify the stability, three peaks were chosen in the γ-ray energy spectrum: the 197.1-keV and 1356.8-keV transitions coming from the β decay of ^{19}O after the implantation of the beam in the reaction chamber and the 2614.5-keV transition of the ^{208}Pb coming from background radiation. These three peaks, being located in three different energy ranges of the spectrum, provide information on the stability of the array at low, medium-high and high energy. For the present experiment, we are particularly interested in the high-energy part of the spectrum, since the transition of interest for the lifetime measurement are found around 2395 keV and 3552 keV.

A dedicated macro fits the three peaks for every run, extracted the centroid and the sigma, and calculates the residual with respect to the average measured value. The results are presented in Figure 3.5 for Crystal 01A. At low energy, the crystals are observed to be extremely stable, in a range of about 0.1 keV. At medium-high and high energy, the range increases to about 0.5 keV and 0.7 keV respectively. However, this value is still below the intrinsic resolution of the crystals. The fluctuations observed appear to follow a random distribution and do not show any particular trend.

3.1.4. Tracking

The real innovation of segmented HPGe arrays like AGATA or GRETINA with respect to non-segmented ones is that it is possible to reconstruct the path of the photon inside the crystal. The idea behind this new technology is to increase the angular coverage of the array by eliminating the anti-Compton shields. At the same time, in order to maintain a good P/T ratio on the γ-ray spectrum, it is necessary to reconstruct the trajectories of the photons inside the array [56]. This is possible thanks to the segmentation of the detectors, the determination of the interaction point through PSA and the tracking algorithm. The reconstruction of the path of the photon allows one to obtain a better angular resolution, which means a better Doppler correction and a better energy resolution.

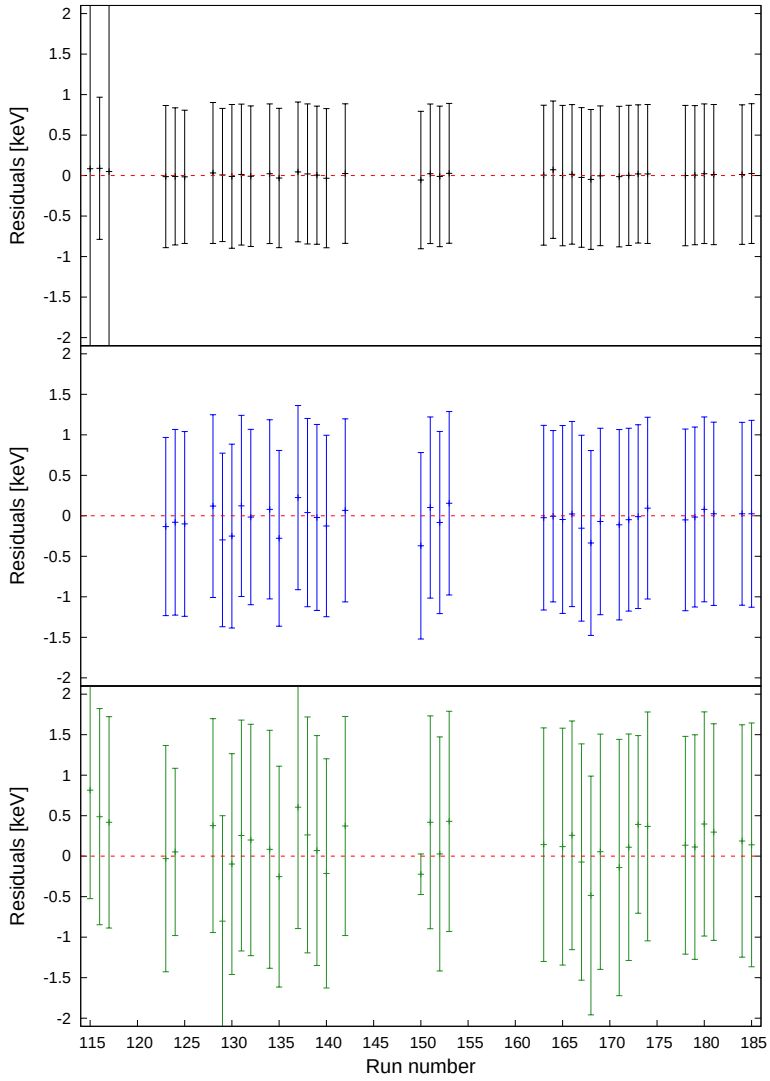

Figure 3.5.: Residual of the measured energy with respect to the average value for the 197.1 (a), 1356.8 (b) and 2614.5 keV (c) transitions for Crystal 01A, over a beam time of about ten days. The error bars represent the measured sigma of the peaks. Run where the statistic was too low were excluded from the analysis.

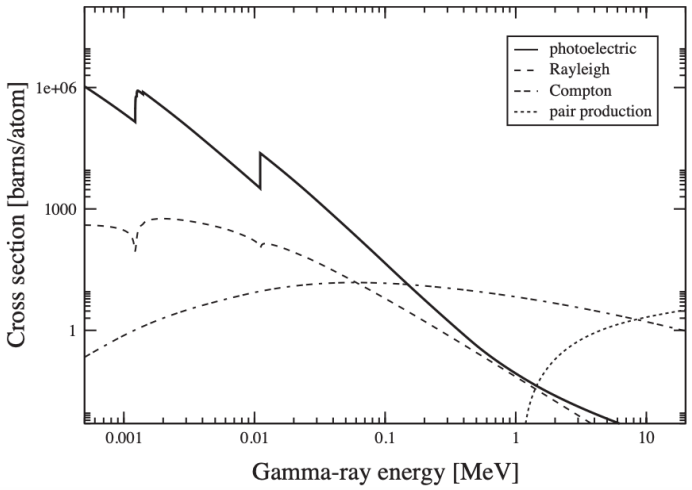

Figure 3.6.: Cross section of different interaction mechanisms of photons with matter depending on the energy of the incident photon.

As illustrated in Section 2.2.7, the PSA is used to determine the energies and the positions of the interaction points of the photons in the crystal. The aim of the tracking algorithm is to reconstruct the scattering sequence of the photons inside the detectors. Photon interactions in the matter can be divided into four main mechanisms: the Rayleigh scattering, the photoelectric absorption, the Compton scattering and the pair production. These mechanisms have different cross sections depending on the energy range of the photons, as shown in Figure 3.6. Low-energy γ rays are characterized by single-point interaction where the total energy of the photon is transferred via photoelectric absorption. In the range from hundreds of keV to MeV, γ rays typically transfer energy through multiple Compton scatterings and a final photoelectric absorption. Finally, above the threshold of 1022 keV, corresponding to $2m_e$, the pair production must be taken into account.

Tracking algorithms can be divided into two main categories: back-tracking and forward-tracking [86]. The characteristic of the back-tracking algorithm is that it starts reconstructing the photon path from the photoelectric interaction, which is expected in the range of $100-200$ keV independently from the energy of the incident photons.

The forward-tracking, instead, aims at identifying the first interaction point in the crystal. The first step is the clusterization of the interaction points in the (θ, ϕ) space. Given an interaction point i, a second interaction point j will be assigned to the same cluster if they are within an angular range α. The same calculation will be repeated for all the other interaction points. If none of them is found in the angular range determined by α, then the initial point will be assigned to a single interaction cluster. This procedure is repeated for different values of α in a range from 0.15 to 1 rad with a step of 0.1 rad. For each value of α, there will be n clusters composed of 1 to 6 interaction points and the total energy of the incident photon E_{tot} corresponds to the sum of the interaction points energies.

The scattering sequence always begins at the source point, which typically corresponds to the centre of the target. Then, considering a first interaction point i and a second j in the cluster, the scattering energy after interaction i is $E_{s,e} = E_{tot} - e(i)$ where the energy before the scattering is $E_t = E_{tot}$. From the Compton scattering formula we expect the remaining

energy after the interaction i to be:

$$E_{s,p} = \frac{E_t}{1 + \frac{E_t}{m_e c^2}(1 - \cos\theta_p)} \tag{3.1}$$

where θ_p is the angle between the direction from the source to point i and the direction from i to j. The figure of merit to quantify the goodness of point i as the first interaction point is defined as:

$$F_E = \exp\left(-2\frac{(E_{s,p} - E_{s,e})^2}{\sigma_e^2}\right) \tag{3.2}$$

where σ_e is the uncertainty on the energy measurement. If the cluster contains only two points then the statistic for the sequence is defined as:

$$F_{s\to i\to j} = P(E_t)_{Comp} P(r_{s\to i}) P(E_{s,e})_{Photo} P(r_{i\to j}) F_E \tag{3.3}$$

otherwise, the procedure will continue considering a third interaction point k. The scattering energy after interaction j will be $E_{s,e} = E_t - e(i) - e(j)$ where now $E_t = E_{tot} - e(i)$ and $E_{s,p}$ is calculated using Equation (3.1) with E_t redefined as before and θ_p being the angle between the i-j direction and the j-k direction. The figure of merit is calculated as in Equation (3.2) but without the factor 2. The factor 2 in Equation (3.2) is present only for the first interaction since the position of the source is known with better precision than the interaction points. This calculation is repeated for all the interaction points in the cluster. The accepted sequence for the cluster is the one that maximizes the figure of merit:

$$F_{tot} = (F_{s\to i\to\ldots\to k})^{1/(2n-1)} \tag{3.4}$$

where n is the number of interaction points in the cluster and can vary from 2 to 6. In case of cluster composed of a single interaction point, the assigned figure of merit is F_{sing}.

This same procedure is done for all the clusters. Finally, the clusters are sorted according to decreasing figures of merit.

The performances of the two algorithms were compared using 1332-keV photons coming from a ^{60}Co source [86]. The forward-tracking algorithm showed not only a better photopeak efficiency with respect to the back-tracking one, but also a better P/T ratio and a lower summing probability for all the event multiplicity.

In the context of the AGATA collaboration, two forward-tracking algorithms have been developed: the Mars Gamma-Ray Tracking [87] and the Orsay Forward Tracking codes [86]. For this thesis, the latter one was employed.

Determination of the parameters

The Orsay Forward Tracking (OFT) code is based on the optimization of three parameters that must be chosen in order to optimize the performances of the tracking algorithm in agreement with the need of the experiment:

- **MinProbTrack**: this parameter defines a minimum probability threshold for the figure

of merit accepted by the tracking algorithm;

- **MinProbSing**: similarly to the previous one, this parameter defines a minimum probability threshold for the calculation of the figure of merit for single interaction clusters. It takes into account the probability to reach a certain depth in the crystal and the probability of photoelectric absorption in the energy range of interest. This threshold reject background events;
- **SigmaTheta**: this parameter determines the position resolution of the interaction points.

These parameters need to be optimized in order to maximize the peak efficiency and the P/T ratio. For this procedure, the $2_1^+ \rightarrow 0_1^+$ transition of ^{20}O at 1674 keV of the CD_2-only target dataset was used. The tracked γ-ray spectrum was produced starting from the hit information. An event-by-event Doppler correction was applied using the reconstructed kinematics of the ^{20}O obtained with MUGAST (see Sections 3.1.8 and 3.1.9). Moreover, the z-offset and ϕ rotation correction determined in Section 3.1.2 was also taken into account.

The MinProbTrack parameter was scanned in a range from 0.01 to 0.99, while the SigmaTheta parameter was scanned in a range from 0.50 to 1.50, both with a 0.01 step. The results are shown in Figure 3.7. The MinProbTrack parameter was set at 0.05, the SigmaTheta was set at 1.30, while the MinProbSing was fixed at 0.15. The comparison between the AddBack spectrum and the one obtained with the tracking algorithm is shown in Figure 3.8. In the tracked spectrum it is possible to observe an improvement in the efficiency but also a reduction in the resolution of the peak.

3.1.5. Efficiency

The efficiency of germanium detectors presents a strong dependence on the energy range of the detected γ rays. Low-energy γ rays below 100 keV are typically suppressed by the energy threshold or absorbers, used for the rejection of background events and electronic noise. The region where detectors have the highest efficiency is between 200 and 300 keV, depending on the absorbers placed in front of the detectors, then the efficiency decrease at higher energy. The reason for this dependence is that at higher energy the probability that a photon exits leaves the crystal without losing its entire energy is larger.

For the measurement of the efficiency a ^{152}Eu source was used. The efficiency was calculated as

$$\varepsilon(E_\gamma) = \frac{I(E_\gamma)}{BR(E_\gamma) \times A \times \Delta t} \tag{3.5}$$

where $I(E_\gamma)$ is the integral of the peak, $BR(E_\gamma)$ is the branching ratio of the transition, A is the activity of the source at the time of the calibration and Δt is the acquisition time.

The function used to study the efficiency is the Radware function [88] that is defined as

$$\varepsilon(E_\gamma) = \exp\left\{\left[A + B\ln\frac{E_\gamma}{100\,keV}\right]^{-F} + \left[C + D\ln\frac{E_\gamma}{1\,MeV} + E\ln\frac{E_\gamma}{1\,MeV}\right]^{-F}\right\}^{-1/F} \tag{3.6}$$

where A, B, C, D, E and F are fitting parameters.

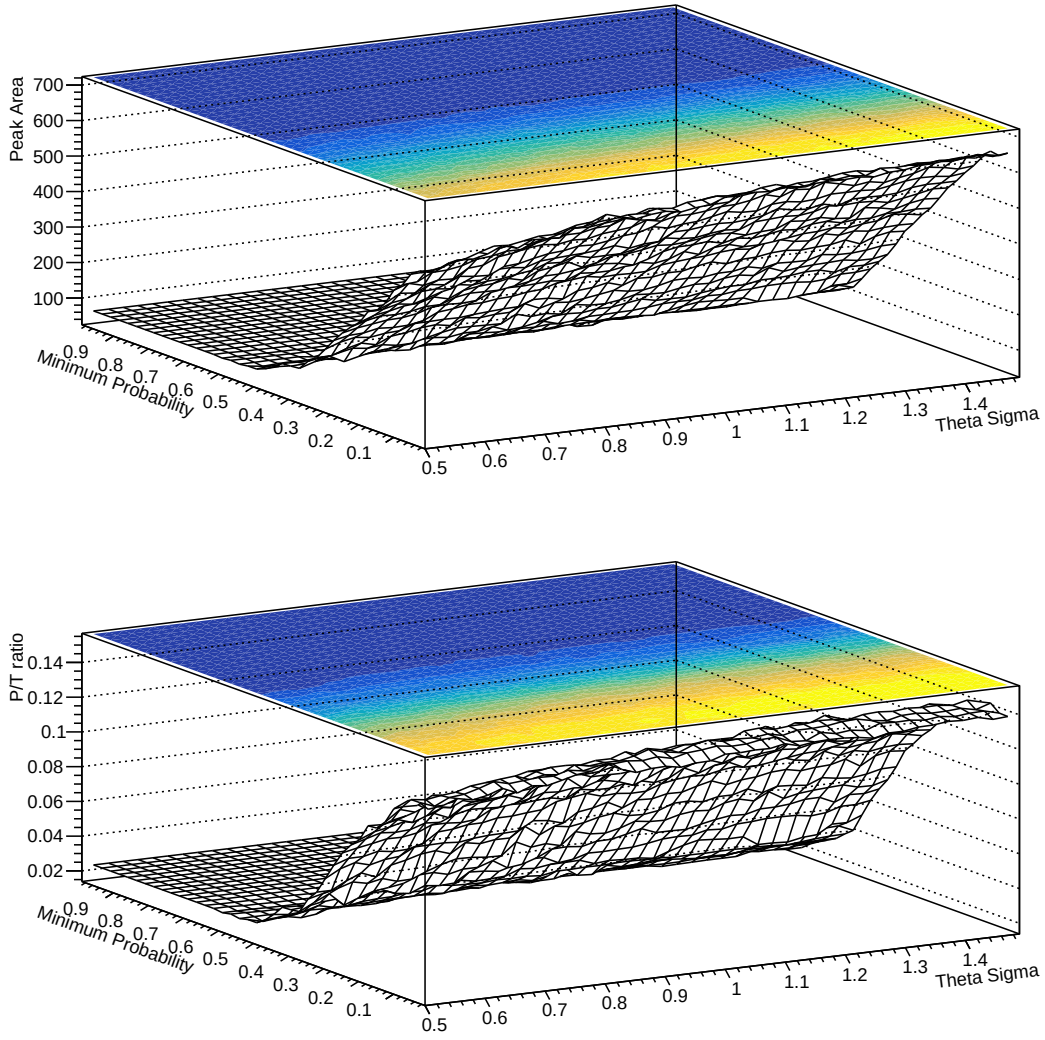

Figure 3.7.: Peak area (top) and Peak to Total ratio (bottom) of the $2_1^+ \rightarrow 0_1^+$ transition at 1674 keV as a function of the MinProbTrack and SigmaTheta parameters. The MinProbSing was fixed at 0.15.

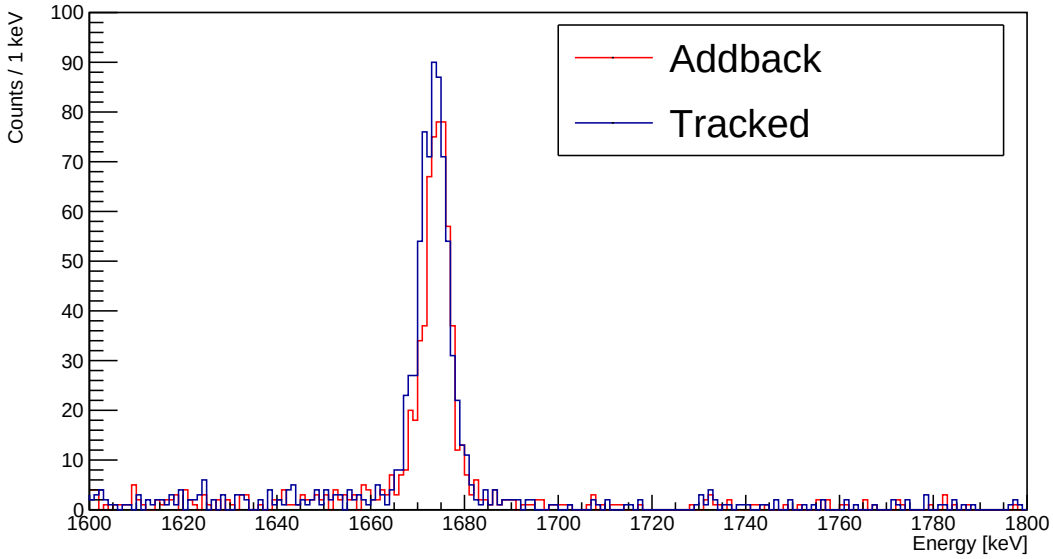

Figure 3.8.: Comparison between the AddBack and tracked γ-ray spectra for the $2_1^+ \rightarrow 0_1^+$ transition at 1674 keV.

The efficiency has been calculated both for the AddBack and tracked spectra and reported in Figure 3.9. In the AddBack procedure, the energy signals of the core from neighbouring crystals is summed and as first interaction the hit with highest energy according to the PSA is chosen. The tracking algorithm is less efficient at lower energy, below 1200 keV, while it becomes comparable to the AddBack at higher energy. Below 100 keV, in particular, because small signals are difficult to process for the PSA and they are rejected by the tracking algorithm, reducing the efficiency in this range of energies [89]. Because of the lacking of high-energy calibration sources it is not possible to study how the efficiency evolves in the range above 1.5 MeV, which is the region of interest.

3.1.6. Resolution

One of the compelling characteristics of the AGATA array is its high resolution, which makes measurement that requires a high energy precision, as the present experiment, feasible. For the study of the resolution, a ^{152}Eu source was used. Moreover, to study the resolution at high energy, in the region of interest for this experiment, the 2614-keV transition of the ^{208}Pb coming from the background radiation was also used.

The resolution is expected to worsen at higher energy according to the following empirical expression

$$FWHM = \sqrt{a + bE_\gamma + cE_\gamma^2}, \tag{3.7}$$

where a, b and c are fitting parameters. The comparison between the tracked and AddBack spectra is shown in Figure 3.10 and the resulting fitting parameters are shown in Table 3.1. In this case, the AbbBack presents a better resolution with respect to the one obtained with

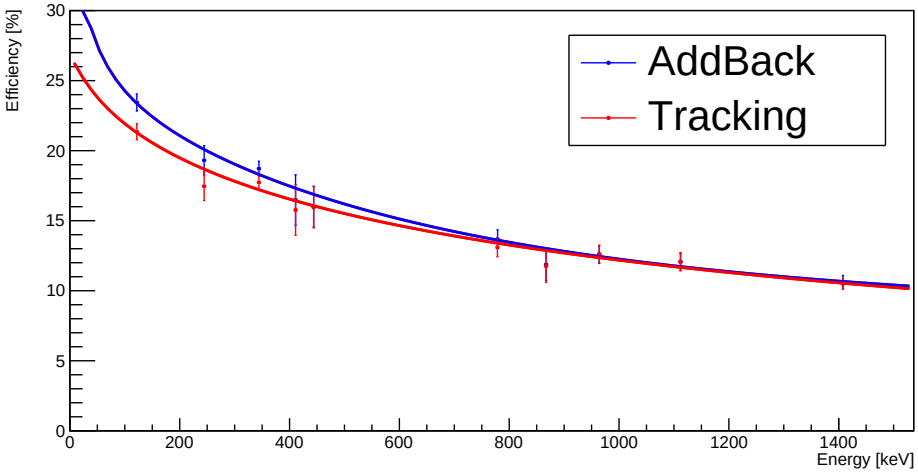

Figure 3.9.: Efficiency of the AGATA array as a function of the γ-ray energy for the AddBack (blue) and tracked (red) spectra. The respective fitted Radware functions are also plotted.

Parameter	a [MeV^2]	b [MeV]	c
Tracking	5.46 ± 0.03	$(4.6 \pm 0.1) \times 10^{-3}$	$(2.17 \pm 0.06) \times 10^{-6}$
AddBack	4.97 ± 0.03	$(3.80 \pm 0.01) \times 10^{-3}$	$(2.1 \pm 0.1) \times 10^{-6}$

Table 3.1.: Fitted parameter for the resolution of AGATA obtained from Equation (3.7).

the tracking algorithm. This result is due to the fact that the AddBack algorithm takes the energy measured in the core, while the tracking algorithm takes the sum of the energies measured in the segments. As illustrated in Section 2.2.3, the crystal segments are calibrated independently and, when summed, it results in a lower resolution compared to the core, due to the standard deviation of the energy.

3.1.7. Kinematic lines

The first part of the analysis concerning the MUGAST array consisted in checking the kinematic lines expected from the reaction. To do so, the expected kinematic lines were plotted over the matrix representing the energy of the protons as a function of the angle in the laboratory frame. A mismatch between data and calculation was observed, that varied depending on the detector.

A possible mismatch in the energy calibration was evaluated. To do so, the energy calibration of the MUGAST detectors was checked by controlling the thickness of the passivation layer of the silicon detector. When performing the calibration, the expected energy for the peak is reconstructed considering the energy loss of the α particle in the aluminium layer. Then, that same energy loss is considered for the particle that is being measured, namely the proton for the present experiment. An incorrect estimation of the passivation layer can lead

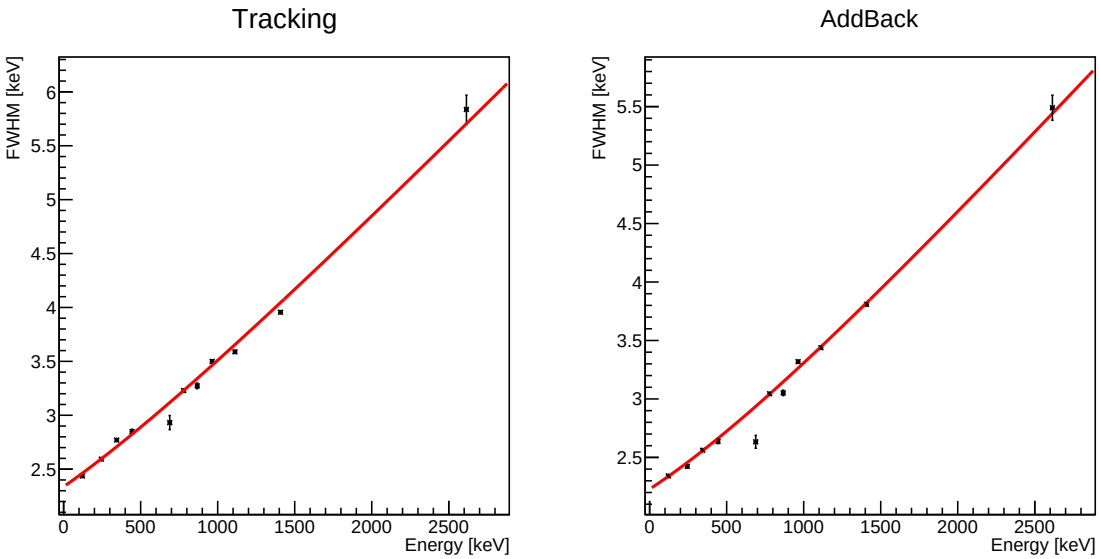

Figure 3.10.: Resolution for the tracked and AddBack spectra obtained using a ^{152}Eu source and the 2614-keV transition of the ^{208}Pb coming from background radiation.

to an incorrect calibration that will be reflected on the final energy spectrum. To verify the goodness of the calibration and the correct estimation of the passivation layer thickness, the α source calibration run has been sorted using the same NPTool code used for the analysis. The effect of the passivation layer thickness is shown in Figure 3.11, where the calibration spectra for three different values of thickness are shown. The final value for the thickness has been estimated to be 0.35 μm for the trapezoidal detectors and 0.32 μm for the annular detector. These values are coherent with typical passivation layers for silicon detectors.

After checking the energy calibration of the MUGAST detectors, two hypotheses were proposed to explain this shift of the kinematic lines. The first possibility was that the beam position on target had been miscalculated, causing a shift in the θ angle reconstruction that depended on the detector position. In this case, there must be a beam spot position for which the θ offset is fixed for all the detectors. The second possibility was that the mismatch was caused by a misalignment caused during the assembly of the array. In this case, every detector can have a different offset independently from the other detectors.

To verify the first hypothesis, the code for the analysis was modified in order to add the possibility of scanning the beam spot position within a range of ± 1 cm in vertical and horizontal directions with a 1 mm step, for a total of $21 \times 21 = 441$ possible positions. This offset in the beam spot changed the calculation of the θ angle for the protons emitted from the target and therefore the position of the kinematic lines. For each position of the beam spot, the excitation energy was calculated. A dedicated macro determined the centroid position of the ground-state excitation energy peak, and calculated the residual with respect to zero. Then the residuals were plotted as a function of the beam spot position in the range scanned. The results for each detector are presented in Figure 3.12.

For each detector, the position that minimizes the residual is represented by a straight line. However, there is not a single position that would minimize the residual for all the detectors.

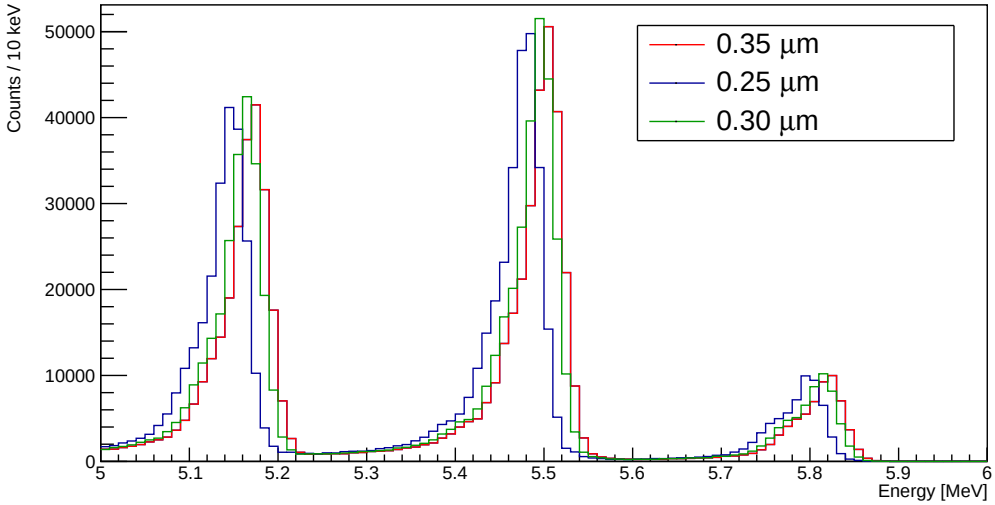

Figure 3.11.: Effect of the passivation layer of the silicon detectors on the energy calibration.

While the position $(-4, 0)$ mm minimizes the residuals for detectors 1, 2, 3, 4, 5, that is not the case for detectors 6 and 7. Therefore this first hypothesis was rejected.

A θ offset in the range of $\pm 1^\circ$ has been added to the nominal orientation of each detector. The resulting kinematic lines were compared to the theoretical ones in order to verify the correct reconstruction of the proton emission θ angle. The results are shown in Figure 3.13.

3.1.8. Reconstruction of the reaction kinematics

For the present experiment, the MUGAST array was used for the detection of the protons emitted in the transfer reaction. Since the ^{20}O was populated using a two-body reaction, by measuring the target-like recoils it was possible to reconstruct the velocity vector of the beam-like recoil, as well as the excitation energy.

In particular, the energy, θ and ϕ angles of the protons were measured, allowing to reconstruct the Lorentz vector of the target-like partner[1]:

$$\vec{p_3} = \begin{pmatrix} p_3 \sin\theta_3 \cos\phi_3 \\ p_3 \sin\theta_3 \sin\phi_3 \\ p_3 \cos\theta_3 \\ E_3 + m_3 \end{pmatrix} \tag{3.8}$$

where $p_3 = \sqrt{E_3^2 + 2m_3E_3}$, and E_3, θ_3 and ϕ_3 are measured quantities while m_3 is the proton mass. From this information, it is possible to reconstruct the $\vec{p_4}$ vector using the momentum conservation:

[1]For the present notation, the number 1 will refer to the beam (^{19}O), 2 to the target (^{2}H), 3 to the target-like (^{1}H) and 4 to the beam-like (^{20}O).

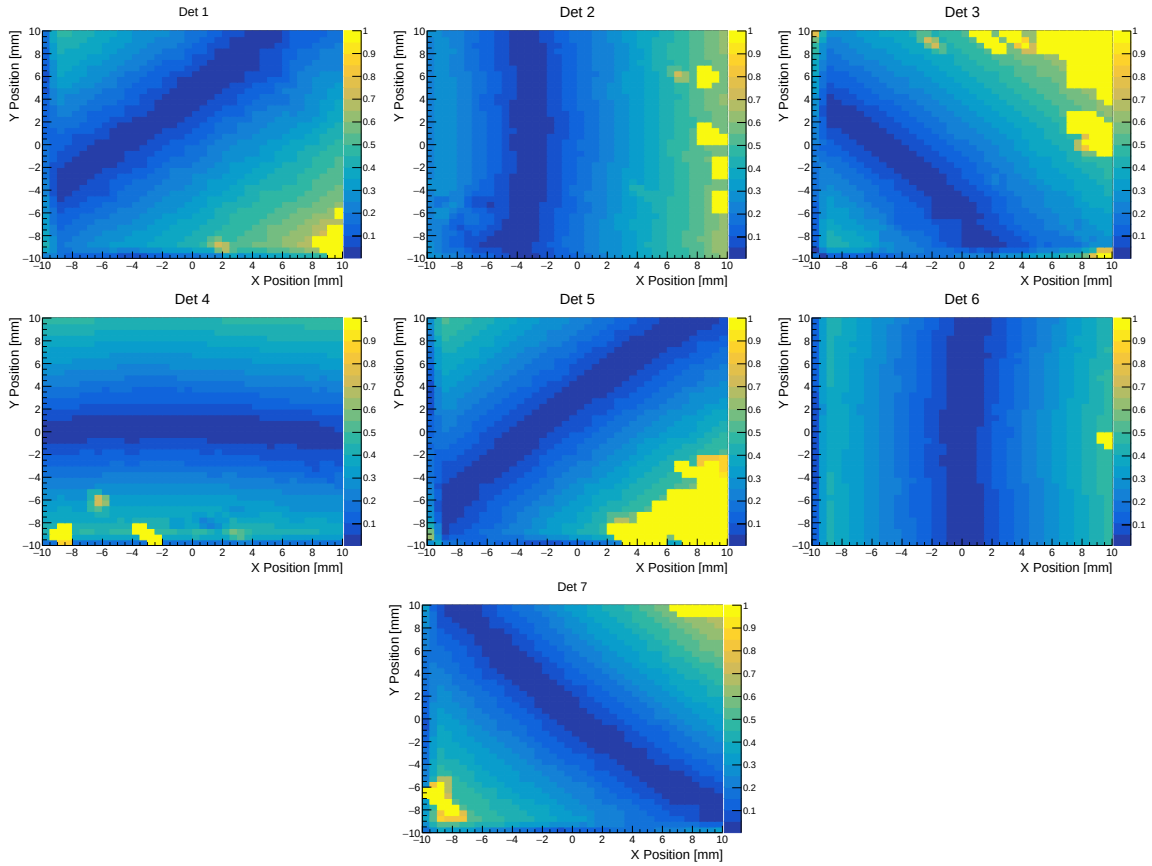

Figure 3.12.: Residual of the 0_1^+ peak measured with MUGAST for different value of beam position in a range from ± 1 cm in the X and Y directions with a pace of 1 mm. While for detectors 1, 2, 3, 4, and 5 the position $(-4, 0)$ minimize the residual, it is not observed for detector 6 and 7.

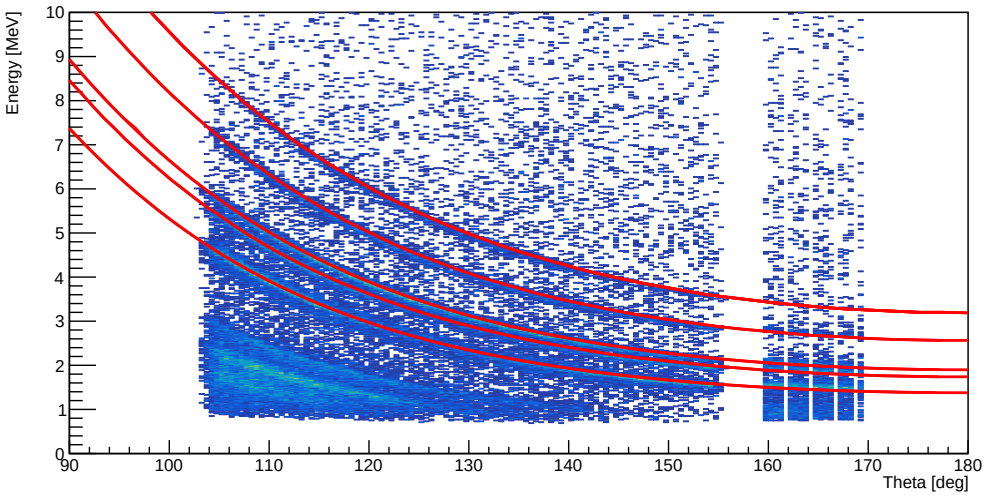

Figure 3.13.: Kinematic lines measured using MUGAST, obtained by plotting the proton energy as a function of the θ angle. The simulated lines of the 0^+_1, 2^+_1, 4^+_1, 2^+_2 and 3^+_1 states are shown in red.

$$\vec{p}_4 = \vec{p}_{TOT} - \vec{p}_3 \tag{3.9}$$

where $\vec{p}_{TOT} = \vec{p}_1 + \vec{p}_2$. In this context, $\vec{p}_1$ is the vector of the incident beam while $\vec{p}_2$ is the vector of the target, therefore $\vec{p}_{TOT}$ can be written as:

$$\vec{p}_{TOT} = \begin{pmatrix} 0 \\ 0 \\ \sqrt{E_1 + 2E_1 m_1} \\ E_1 + m_1 + m_2 \end{pmatrix}, \tag{3.10}$$

where E_1 is the beam energy 152 MeV minus the energy loss in half of the target, and m_1 and m_2 are the mass of the beam ion and target respectively. Using Equations (3.8), (3.9) and (3.10), $\vec{p}_4$ results to be:

$$\vec{p}_4 = \begin{pmatrix} -p_3 \sin\theta \cos\phi \\ -p_3 \sin\theta \sin\phi \\ \sqrt{E_1 + 2E_1 m_1} - p_3 \cos\theta \\ E_1 + m_1 + m_2 - E_3 - m_3 \end{pmatrix}. \tag{3.11}$$

The information on the reconstructed $\vec{p}_4$ will be used for the Doppler correction, presented in the following section. The excitation energy of the ^{20}O is calculated with the following equation:

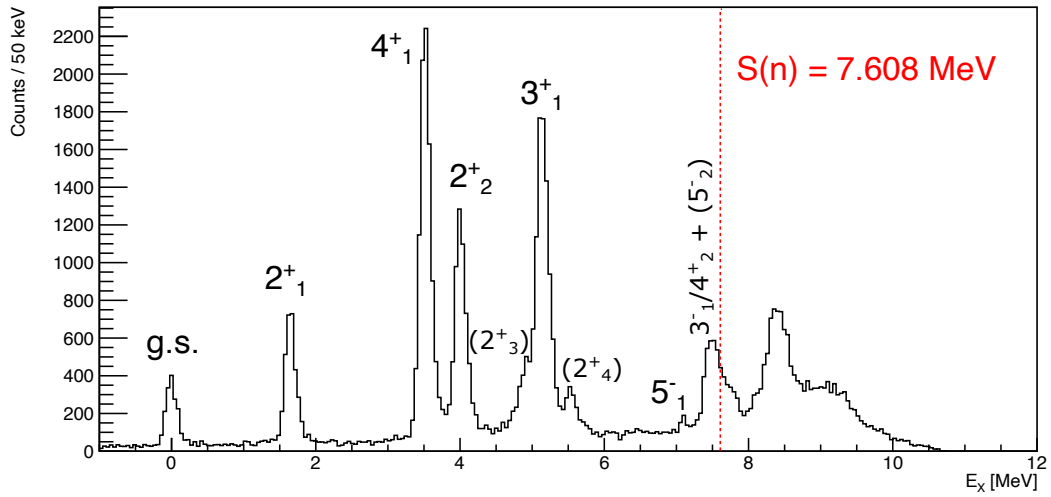

Figure 3.14.: Reconstructed excitation energy spectrum with the identified states and the neutron separation energy (red dashed line) reported. The absence of events above 11 MeV is related to the energy threshold of MUGAST.

$$E_X = M - m_4. \tag{3.12}$$

where $M = (E_1 + E_2)^2 - \|\vec{p}_1 + \vec{p}_2\|$ is the invariant mass. The resulting excitation energy spectrum is shown in Figure 3.14. It is possible to identify the 0^+_1 state, the 2^+_1 at 1.6 MeV, the 4^+_1 at 3.6 MeV, the 2^+_2 at 4.1 MeV and the 3^+_1 at 5.2 MeV.

Below the neutron emission threshold at 7.6 MeV, it is possible to observe two additional peaks at 4.9 MeV and 5.5 MeV. This two states may correspond to a possible 2^+_3 and 2^+_4 at 5.0 MeV and 5.6 MeV respectively observed by Hoffmann *et al.* [40]. In the same paper, a 0^+ state at 4.46(2) MeV was also observed. However, the presence of the tails of 2^+_2 and 3^+_1 states did not allow for the identification of this state. Another state can be observed in the spectrum at 7.2 MeV. This state was also observed in Ref. [32] and it has been assigned a spin and parity of 5^-.

At and above the neutron separation energy and below 8 MeV, a structure can be observed. This structure might correspond to the unresolved 7.6-MeV and 7.8-MeV states observed in Ref. [32] that were assigned a spin and parity of 3^- and 4^+ for the first state and a tentative (5^-) for the second. Above 8 MeV, three peaks can be observed: one at 8.2 MeV, one at 8.5 MeV and one at 9.2 MeV. The absence of events above 11 MeV is connected to the energy threshold of MUGAST that was set at 1 MeV, as shown in Figure 3.13.

More information on the states is presented in the spectroscopic study of the γ rays emitted in coincidence with the protons 4.1 and in the study of the angular distributions.

3.1.9. Doppler Correction

For the present experiment, the average velocity at the reaction point was about $\beta \approx 12.6\%$. At this velocity, an accurate Doppler correction is necessary to study the γ-ray spectrum. The γ ray emitted by the ^{20}O recoil in-flight is shifted according to

$$E_\gamma = E_0 \frac{\sqrt{1-\beta^2}}{1-\beta\cos\theta} \tag{3.13}$$

where E_γ is the energy measured by AGATA, E_0 is the expected transition energy, β is the velocity of the recoil and θ is the angle between the recoil and the detected γ ray.

For the present experiment, the beam-like recoils were emitted in a small forward-boosted cone ($\pm 5°$) and with a small velocity spread ($12.4 - 12.6\%$). Therefore, it is possible to reconstruct the γ-ray spectrum with an average-velocity Doppler correction and considering only the angle measured by AGATA with respect to the beam axis, hence assuming a small angle of emission for the beam-like recoil.

However, for lineshape analysis, as in the present work, it is extremely important to have a good resolution in order to be more precise when extracting the lifetimes and this can be obtained with an event-by-event Doppler correction. The velocity and the direction of the recoil are usually reconstructed using a spectrometer at forward angles, like VAMOS. However, for the present experiment the counting rate on VAMOS was too high and the efficiency of the drift and ionization chamber was reduced. Therefore, the kinematics of the ^{20}O was reconstructed from the information provided by the protons measured by MUGAST, as explained in the previous section, allowing an event-by-event Doppler correction that takes into account the reconstructed velocity and the angle between the recoil and the γ ray measured by AGATA.

Figure 3.15 shows the spectrum obtained with an average-velocity Doppler correction compared to the spectrum obtained with an event-by-event Doppler correction for the 1674-keV $2_1^+ \rightarrow 0_1^+$ transition. For the comparison, the dataset obtained using the CD_2-only target was chosen, in order to minimize the lifetime effect on the peak shape. The FWHM of the 1674-keV peak obtained with the average velocity is 9.1(4) keV, while the FWHM obtained with the event-by-event Doppler correction is 6.5(3) keV. Considering that the calculated intrinsic resolution of AGATA crystals at 1.6 MeV is 4.2(3) keV (according to Equation (3.7) using the fitted parameters), the event-by-event Doppler correction allows one to retrieve a comparable resolution with an average $\beta = 12.6\%$.

The accuracy of the event-by-event Doppler correction, and in particular the reconstruction of the correct angles and velocity, is verified. In Figure 3.16, the energy of the γ-ray transitions obtained from the CD_2-only dataset is plotted as a function of the θ angle in the laboratory frame. The expected energy of the transitions is also plotted (dashed red lines). The energy results to be correctly reconstructed using this Doppler correction.

3.1.10. Indirect measurement of the degrader thickness

In order to perform a DSAM measurement, the target was deposited on a backing of gold of a nominal thickness of 20 mg/cm^2. However, it was not possible to directly measure the effective thickness of the gold backing neither with Scanning Electron Microscope technique

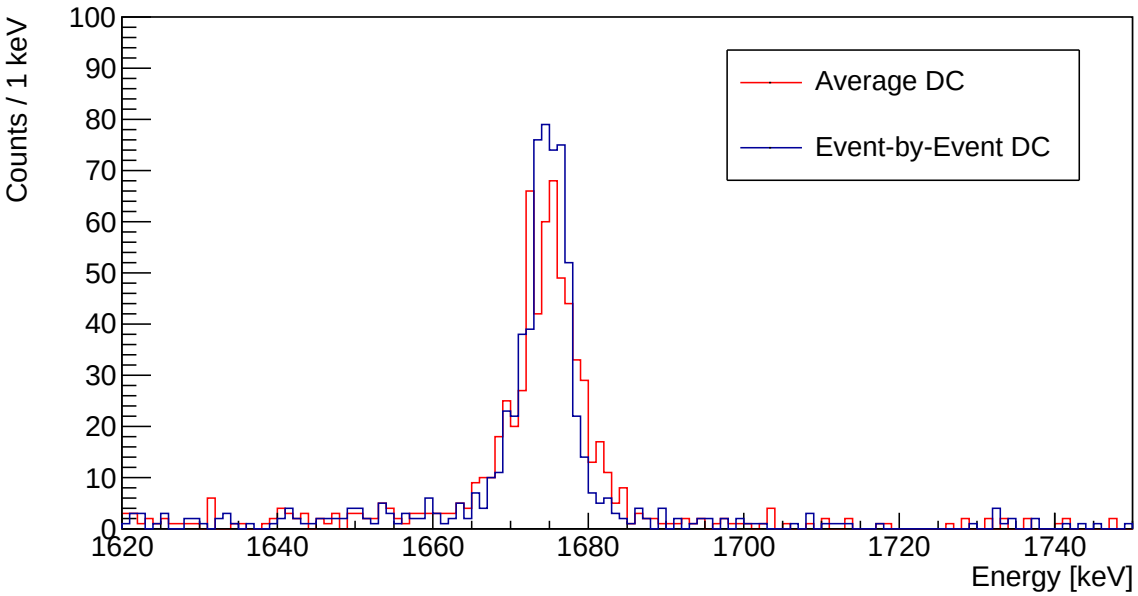

Figure 3.15.: A comparison the 1674-keV peak of the $2_1^+ \rightarrow 0_1^+$ transition obtained using the average-velocity Doppler correction (red) and the event-by-event one (blue). The event-by-event Doppler correction improves significantly the resolution.

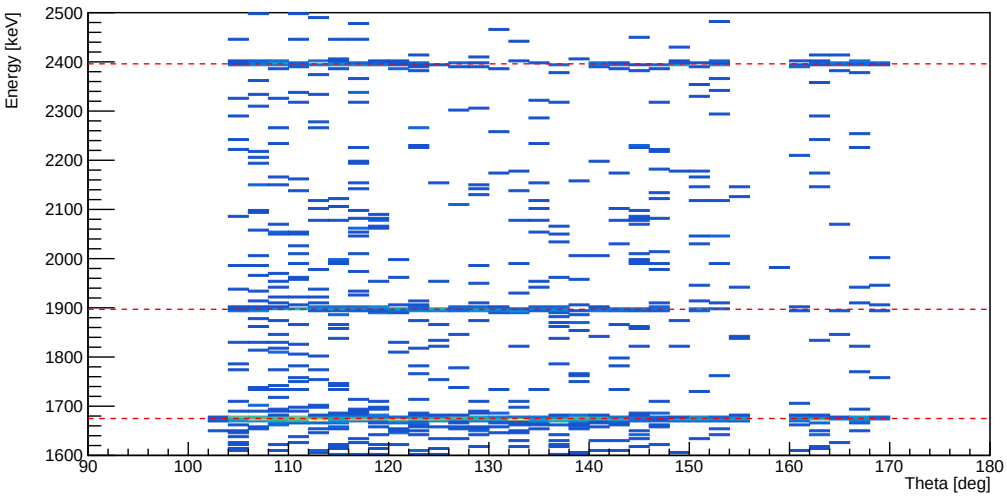

Figure 3.16.: Doppler-corrected energy of the $2_1^+ \rightarrow 0_1^+$, $4_1^+ \rightarrow 2_1^+$ and $2_2^+ \rightarrow 2_1^+$ transitions as a function of the θ angle in the laboratory frame. The expected energies of the transitions, 1674, 1897 and 2396 keV respectively, are also shown (red dashed lines).

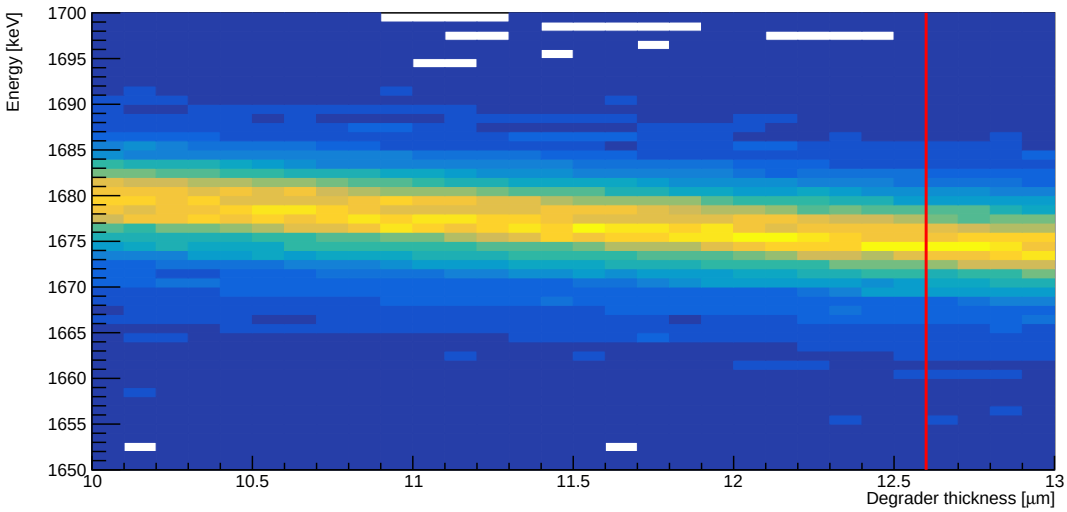

Figure 3.17.: Energy of the $2_1^+ \rightarrow 0_1^+$ transition as a function of the backing thickness. The correct thickness of the backing was estimated as 12.6 μm, corresponding to 24.4 mg/cm^2.

nor by measuring the energy loss of particles in the layer of gold by using radioactive sources or an accelerator. An estimation of the thickness of the gold layer was possible by using the Doppler correction.

The energy of the $2_1^+ \rightarrow 0_1^+$ transition is well known in literature and has been measured by previous experiments and in this same experiment. The lifetime of the 2_1^+ state has also been measured by previous experiments and resulted to be 10.5(4) ps [12]. Such a lifetime guarantees that the 2_1^+ state decays mostly after passing through the gold degrader, as the estimated time necessary for the ^{20}O nucleus to cross the gold is about 0.5 ps. Therefore, the $2_1^+ \rightarrow 0_1^+$ transition peak is expected at the energy of 1674 keV when the Doppler correction is performed by using the reconstructed velocity after the gold layer.

In the present experiment, it was not possible to measure this velocity of the ^{20}O after the energy loss. The velocity of the beam-like recoil at the reaction point was reconstructed from the measurement of the emitted proton, as explained in Section 3.1.8. The velocity of the recoil after the gold is obtained by calculating the energy loss of the recoil in the gold layer. Therefore the Doppler corrected peak energy of the $2_1^+ \rightarrow 0_1^+$ transition is expected at 1674 keV only if the energy loss is correctly calculated.

The Doppler corrected spectrum was calculated for different values of the gold layer thickness in a range from 10.0 μm to 13.0 μm (corresponding to 19.3 mg/cm^2 and 25.1 mg/cm^2) with a step of 0.1 μm. The correct energy of the peak was found for 24.4 mg/cm^2, corresponding to 12.6 μm, which is taken as the real thickness of the degrader. The dependence of the peak energy from the layer nominal thickness is shown in Figure 3.17.

3.2. Simulation

In the present work, the lifetime of the 2_2^+ and 3_1^+ states is extracted by comparing the lineshape of the experimental peaks to realistic Monte Carlo simulations, performed using the Geant4 code [90]. In these simulations, the geometry of AGATA and MUGAST in the present configuration, as well as the measured thickness of target and degrader, are included, in order to correctly reproduce the experimental setup. In order to ensure the best agreement between the experimental data and the simulation, the latter has been optimized by adding realistic parameters such as the measured resolution of the AGATA detectors, the proton angular distribution for the states populated in the reaction, energy losses in the target and backing, beam spot size on the target, smearing of both recoils and γ rays, background estimation. By having control over all the possible sources of systematic error, it is also possible to estimate the accuracy of the method, which will be discussed in the next chapter.

3.2.1. Resolution

For the present analysis, a realistic resolution is crucial for extracting an accurate lifetime, which depends on the shape of the peak. The resolution of detectors depends on the energy of the γ ray following Equation (3.7) and the FWHM is expected to increase at higher energy. The parameters measured in Section 3.1.6 were inserted in the simulation code in order to retrieve the same energy dependency. Then a ^{152}Eu source was simulated using the realistic resolution measured before the experiment and studied in Section 3.1.6. Moreover, a single transition at 2614 keV of ^{208}Pb has been added to the simulation to study the resolution at high energy, which corresponds to the range of interest for the present experiment.

The FWHM of the peaks were measured and fitted using the same empirical equation. The extracted parameter were $a = 5.60(4)$, $b = 3.2(1) \times 10^{-3}$ and $c = 2.64(9) \times 10^{-6}$. The comparison between the experimental tracking data and the simulation is presented in Figure 3.18.

3.2.2. Strips check

As stated in Chapter 2, the trapezoidal detectors of MUGAST are segmented into 128×128 stripes, while the annular detector is composed of 4 sectors, each of them segmented into 16×4 stripes. However, not all the strips were active during the experiment because of geometrical inefficiency or electronic problems. When simulating event distributions using the NPTool code it is important to consider the strips that are deactivated, in order to have a realistic geometric efficiency in the whole range.

For this reason, the strips that were not working during the experiment were disabled in the simulation as well. The X and Y strips were checked for each detector. On average, 5 strips per detector needed to be disabled, and in particular the strips on the border presented more problems than those at the center of the detectors. Detector 7 was the one with the highest number of strips that were not working: 26 for the X side and 38 for the Y side. This large number of disabled strips has the effect of lowering the efficiency of detector 7 with respect to the other trapezoidal detectors. Figure 3.19 shows the energy measured by each X-strip of detectors 7 for both data and NPTool simulation.

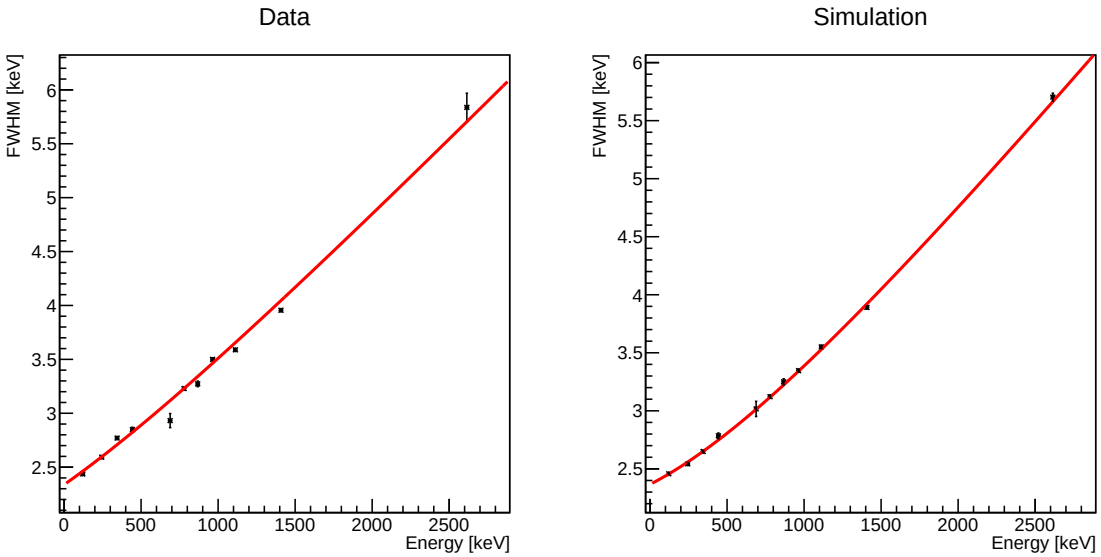

Figure 3.18.: Resolution for the tracked data and simulation spectra obtained using a ^{152}Eu source and the 2614-keV transition of the ^{208}Pb coming from background radiation.

3.2.3. Angular distribution and velocity comparison

The MUGAST array, being segmented in both X and Y directions, allows for a good angular resolution in both θ and ϕ angles. The array was used for the detection of the emitted protons and hence for the reconstruction of the ^{20}O kinematics. The angular distributions of the states populated in the present experiment were studied in a previous experiment employing the same reaction and a similar energy [40]. In this latter work, the cross sections of the states and the spectroscopic factors were calculated. The angular distributions of the states were observed to differ from each other depending on the excitation energy and the L-transfer.

The different angular distributions of the states influence the recoil momentum in angle and velocity and hence the Doppler correction. Therefore, the observed distribution for each excited state must be included in the simulation individually. The distributions in the centre of mass were normalized on the geometrical efficiency of MUGAST, obtained by simulating a uniform distribution of protons at the energy corresponding to the excited state. The geometric efficiency of MUGAST in the present configuration was calculated by simulating a uniform distribution of protons for each of the corresponding excited states of the ^{20}O.

The dependence on the L-transfer and the different excitation energy of the states is reflected in the distribution of the velocity of the ^{20}O nucleus for the different excited states, as observed in Figure 3.20. The realistic simulation of the recoil velocity is fundamental to ensure a proper Doppler correction of the γ rays. The normalized angular distributions, measured in the experiment were used as input parameters for the Monte Carlo simulations. In this way, a good matching between the experimental velocity distribution and the simulated ones is achieved. As expected, the velocity distributions of the ^{20}O vary depending on the excited states, as shown in Figure 3.21 for 2^+_1 and 2^+_2 states. The 2^+_1 state, corresponding to

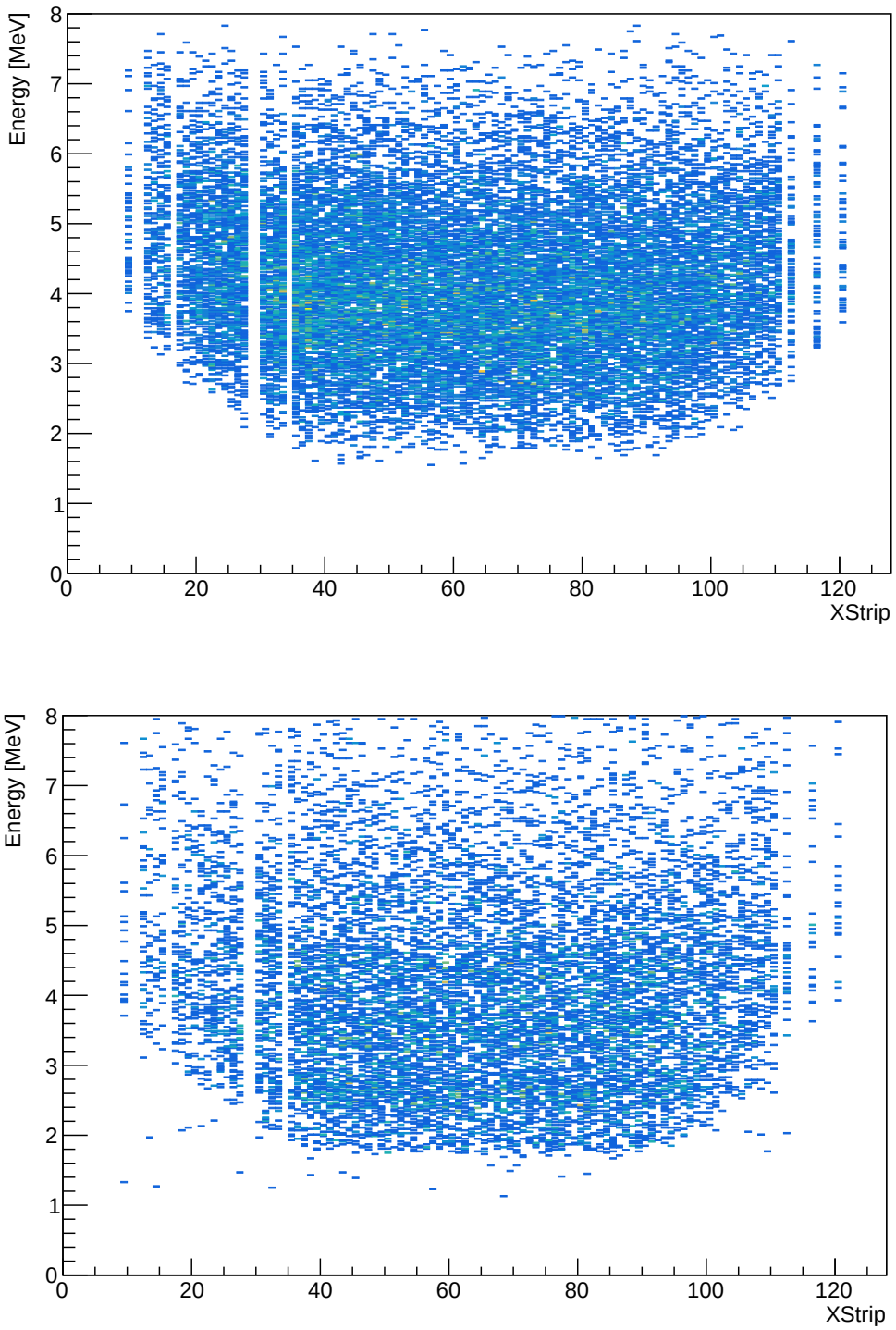

Figure 3.19.: Comparison between energy measured by X-strip of detector 7 for data (top) and NPTool simulation (bottom).

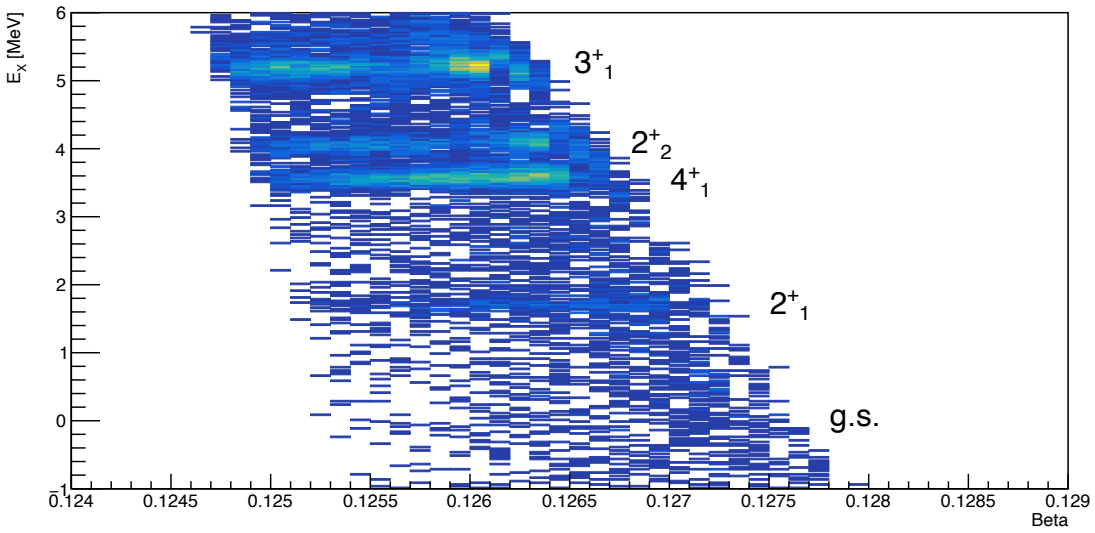

Figure 3.20.: Velocity of the ^{20}O at reaction point, reconstructed with the MUGAST array, for the different excited states of the nucleus. As expected, the average velocity of the states at higher energy is lower.

lower excitation energy, presents slightly higher values of β, as expected. This correspondence ensures a realistic reconstruction of the Doppler correction of the γ ray spectrum.

3.2.4. Particle and γ ray smearing

The same tracking algorithm that is employed to analyse the experimental data coming from the AGATA array is also employed for the analysis of the simulated spectrum. This procedure guarantees the best agreement between the experimental and simulated spectra.

The program uses a source position of (0,0,0), placed at the target position. The energy threshold on the interaction point energies is 5 keV as default. The program requires the user to provide nine arguments:

- name of the output file;
- incident photon multiplicity;
- number of incident photons;
- packing of interaction points within 5 mm or otherwise;
- packing points in segments at the energy weighted barycenter or otherwise;
- packing points at the centre of the segment or otherwise;
- smearing of the position with an energy-dependent formula;
- smearing of the γ-ray energies;
- presence of background.

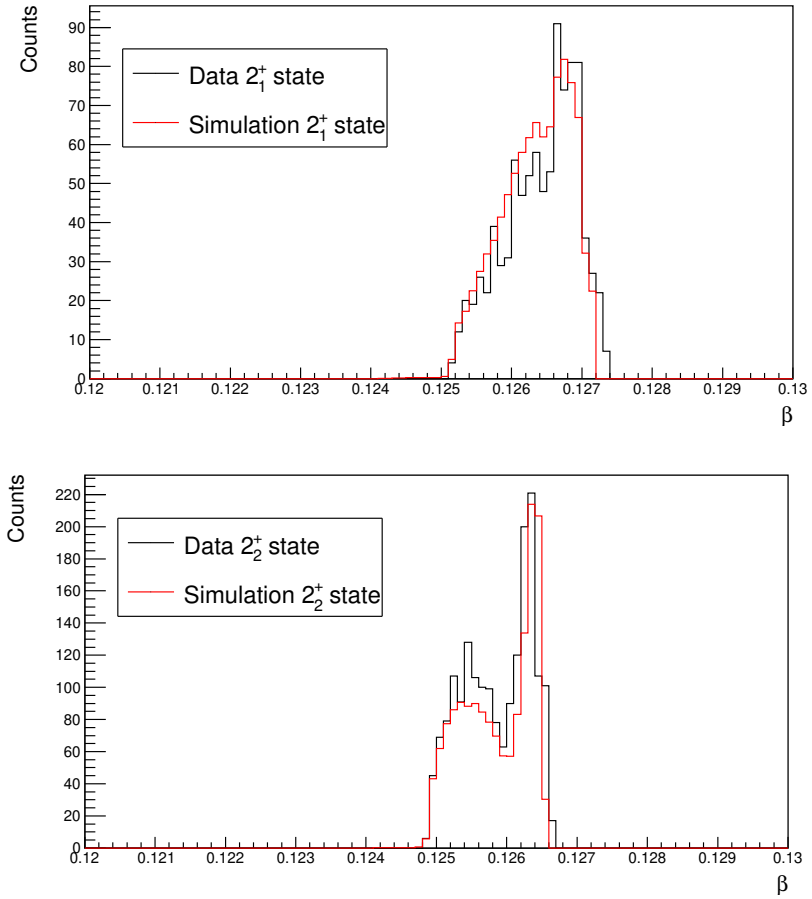

Figure 3.21.: The experimental (black) and simulated (red) velocity distributions of 2_1^+ (top) and 2_2^+ (bottom) states of ^{20}O nucleus are shown. The different shapes of the peaks reflect the convolution between the different L-transfer (L=2/0 for 2_1^+ state and L=0 for 2_2^+, according to Ref. [40]) and the angular coverage of the detectors.

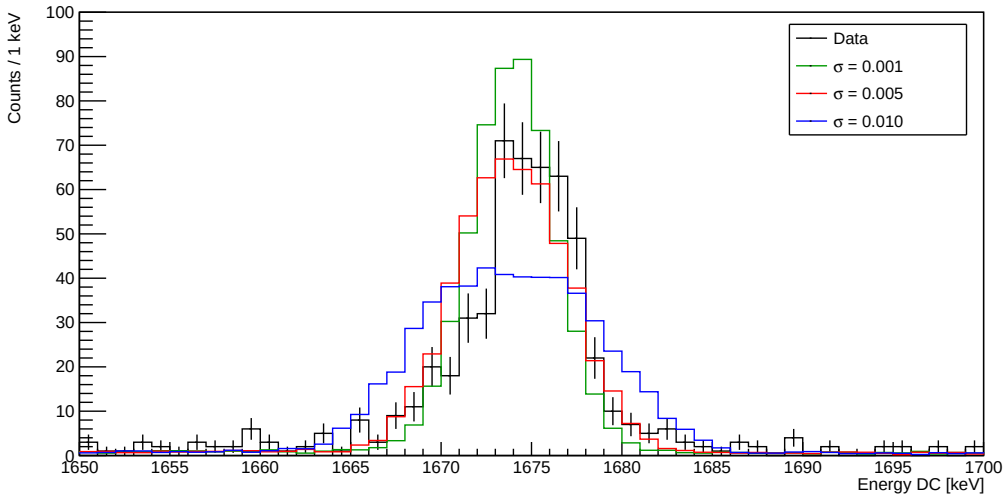

Figure 3.22.: Effect of different level of smearing of the recoil velocity on the γ-ray simulated spectrum.

For the present work, the required multiplicity for the simulated photons (argument 2) was at least one. The packing of the interaction points has been performed within 5 mm (argument 4) and the position of interaction have been chosen as the energy weighted barycentre (argument 5) instead of picking the centre of the segment (argument 6). Both the position and the energy of the γ rays have been smeared in order to retrieve the experimental conditions. The background has also been included in the simulation, as explained in Section 3.2.5.

In addition to the smearing on the photons included in the tracking code, the smearing of the proton energies was added to the code used for the analysis of the simulation in order to reproduce the realistic straggling and energy resolution of the protons in the target and in the passivation layer of the MUGAST detectors. In the code, the velocity reconstructed from the proton Lorentz vector is smeared according to equation

$$\beta_{\text{smear}} = \beta + (\xi - \frac{1}{2})\sigma_\beta \tag{3.14}$$

where ξ is a random number in an uniform distribution from 0 to 1 and σ_β is a factor that quantify the smearing of the velocity.

Different values of σ_β in a range from 0.001 to 0.010 have been tested by comparing the simulated $2_1^+ \rightarrow 0_1^+$ transition to the experimental one. For this comparison, the dataset using the CD_2-only target was employed, in order to eliminate the influence of the lifetime of the state on the lineshape. The simulation has been normalized to the experimental data in the range from 1650 to 1700. After evaluating different smearings, a $\sigma_\beta = 0.005$ was chosen. The effects of the smearing of the velocity on the lineshape of the γ-ray transition are presented in Figure 3.22.

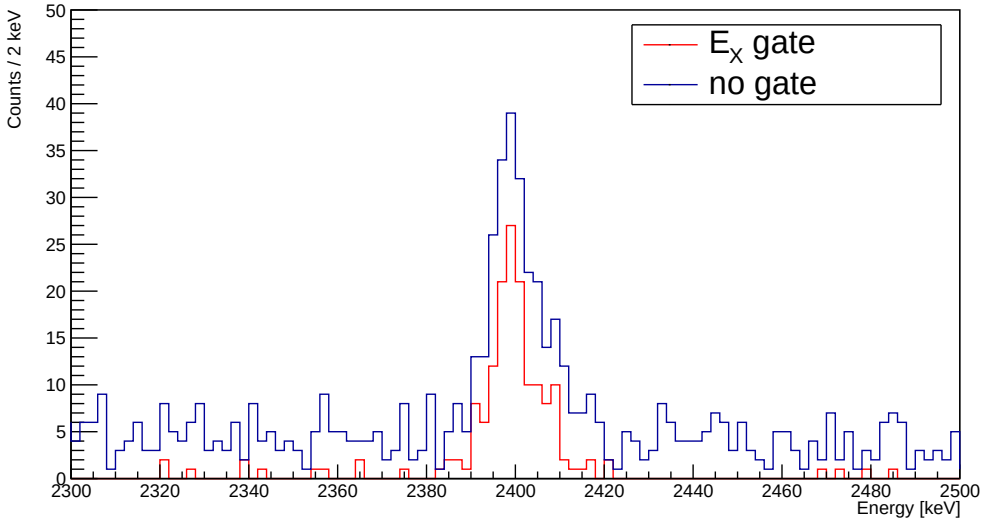

Figure 3.23.: Comparison between the spectra obtained with (red) and without (blue) the gate on the 2_2^+ excited state.

3.2.5. Background

For the present experiment, a time gate between VAMOS-MUGAST and HF-VAMOS was required in order to clean the spectra from fusion-evaporation and scattering events, as illustrated in Section 3.1.1. This time gate guarantees a good selection of the events corresponding to ^{20}O. However, for lifetime measurements it is important to select only the γ rays coming from the direct population of that state and to eliminate the contribution coming from feeders. This additional selection has also the effect of further cleaning the spectrum. Figure 3.23 shows the comparison between a spectrum obtained by requiring the coincidence between protons and γ rays, and the spectrum obtained by requiring a selection on the 2_2^+ state at 4.1 MeV in a range from 3.7 MeV to 4.5 MeV. The spectrum is expanded around 2.4 MeV to better observe the $2_2^+ \rightarrow 2_1^+$ transition at 2396.6 keV, which is used for the lifetime measurement of the state. The spectrum obtained with the gate in excitation energy not only shows a different shape, due to the elimination of the feeder ($3_1^+ \rightarrow 2_2^+$ transition at 1155 keV), but also a lower level of background before and after the peak of interest can be observed.

For the Monte Carlo simulations, the background of the spectrum was reproduced. As input parameters, it is possible to select the number of background events for each event of interest and the dependence of the number of background events from the energy. The background obtained with the simulation was compared to the background of the experimental data. In particular, the number of counts in a range before and after the transition of interest has been measured. The simulated spectrum was normalized with respect to the range of the transition of interest, as will be explained in Section 4.2.

The ranges from 2280 and 2380 keV and from 2440 and 2540 keV were considered for the comparison. The experimental background was 11 in the first range and 9 in the second, while the normalized simulation counted 13 in the first and 8 in the second. The experimental data and the simulation are in agreement within the statistical uncertainties.

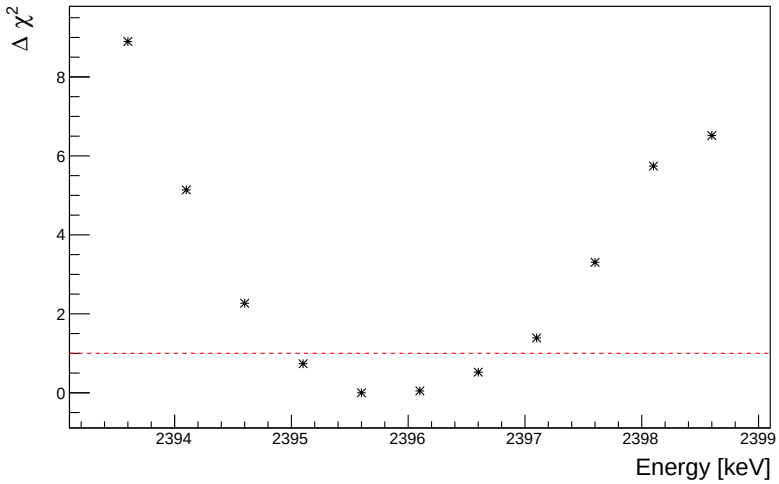

Figure 3.24.: $\Delta\chi^2$ as a function of the transition energy for the $2_2^+ \rightarrow 2_1^+$ transition. The minimum is found around 2396 keV, while the energy range determined by the $\Delta\chi^2 = 1$ condition (red dashed line) is between 2395 and 2397 keV.

3.2.6. Energy tuning

The dataset obtained using the CD_2-only target was employed to tune the energy of the transitions that were chosen for the lineshape analysis. This dataset, contrary to the one using the CD_2+Au target, is not affected by the energy shift of the peak due to the energy loss in the degrader. By comparing the simulation to experimental data it is possible to determine the confidence level for the transition energy and set the boundaries on the energy range. This procedure is important in the case of the present nucleus, as the energy of the transitions of interest is known with an accuracy above 1 keV.

The tuning for the $2_2^+ \rightarrow 2_1^+$ transition at 2395(1) keV is shown as an example. The comparison between the experimental and simulated spectra was performed using the least-χ^2 method. More details about the χ^2 test and the estimation of uncertainties are given in Section B.1. The range for the normalization of the simulation to experimental data was chosen between 2386 and 2410 keV.

The $\Delta\chi^2$ as a function of the transition energy is presented in Figure 3.24. The energy range was investigated between 2393.6 and 2381.6 keV with a step of 0.5 keV. The minimum is found around the transition energy of 2396 keV while the $\Delta\chi^2 = 1$ condition determined uncertainties between 2395 and 2397 keV. The uncertainties provide information on the energy range that will be used to determine the lifetime of the state.

The same procedure was performed for the $3_1^+ \rightarrow 2_1^+$ transition around 3553 keV in a range from 3550.3 to 3554.3 keV with a step of 0.5 keV. The range for the normalization was chosen between 3536 and 3570 keV. The minimum was found around 3552.3 keV while the $\Delta\chi^2 = 1$ condition fixed the uncertainties between 3550 and 3554 keV.

The comparison between the experimental and simulated spectra for the different transition energies is presented in Figure 3.25 for the $2_2^+ \rightarrow 2_1^+$ transition and in Figure 3.26 for the $3_1^+ \rightarrow 2_1^+$ transition.

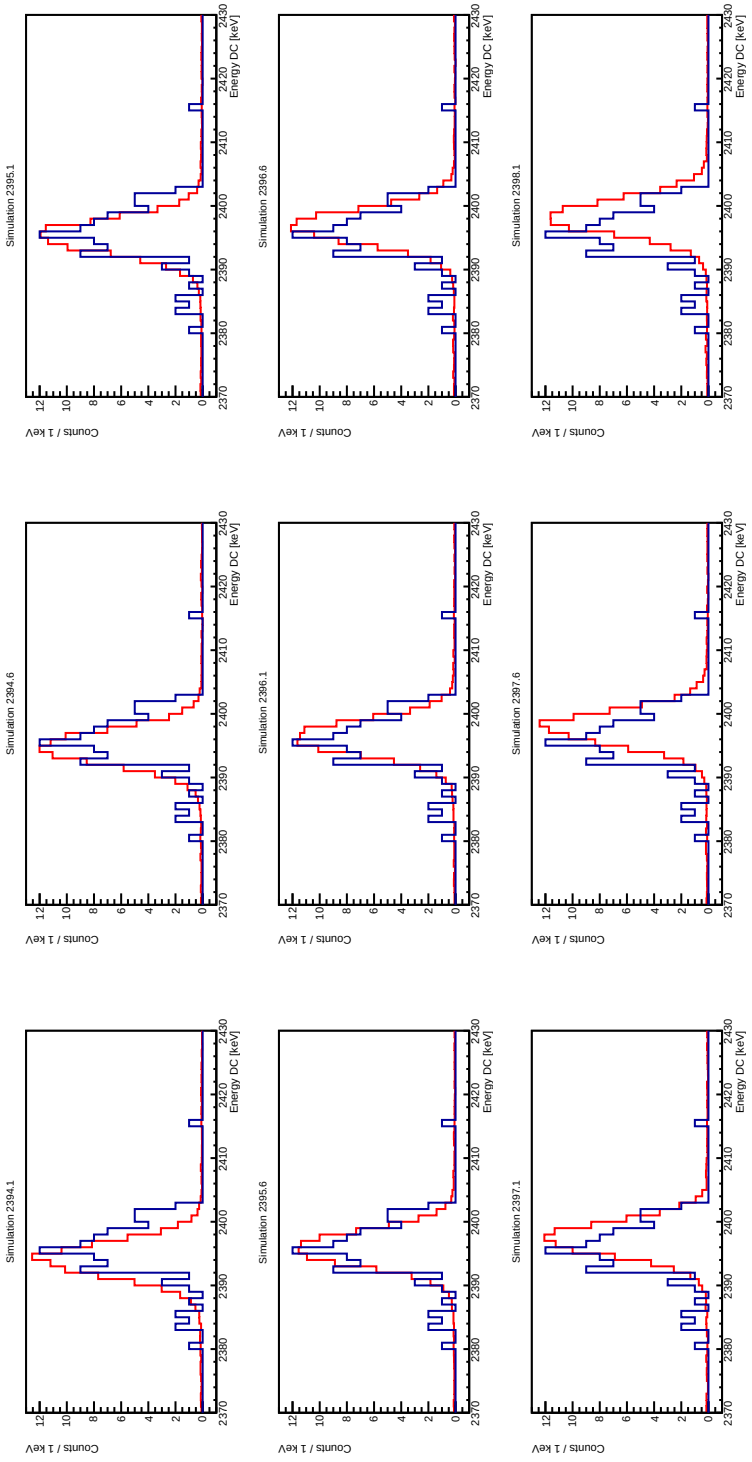

Figure 3.25.: Comparison between the experimental (blue) and simulated (red) spectra for different transition energies for the $2_2^+ \rightarrow 2_1^+$ transition.

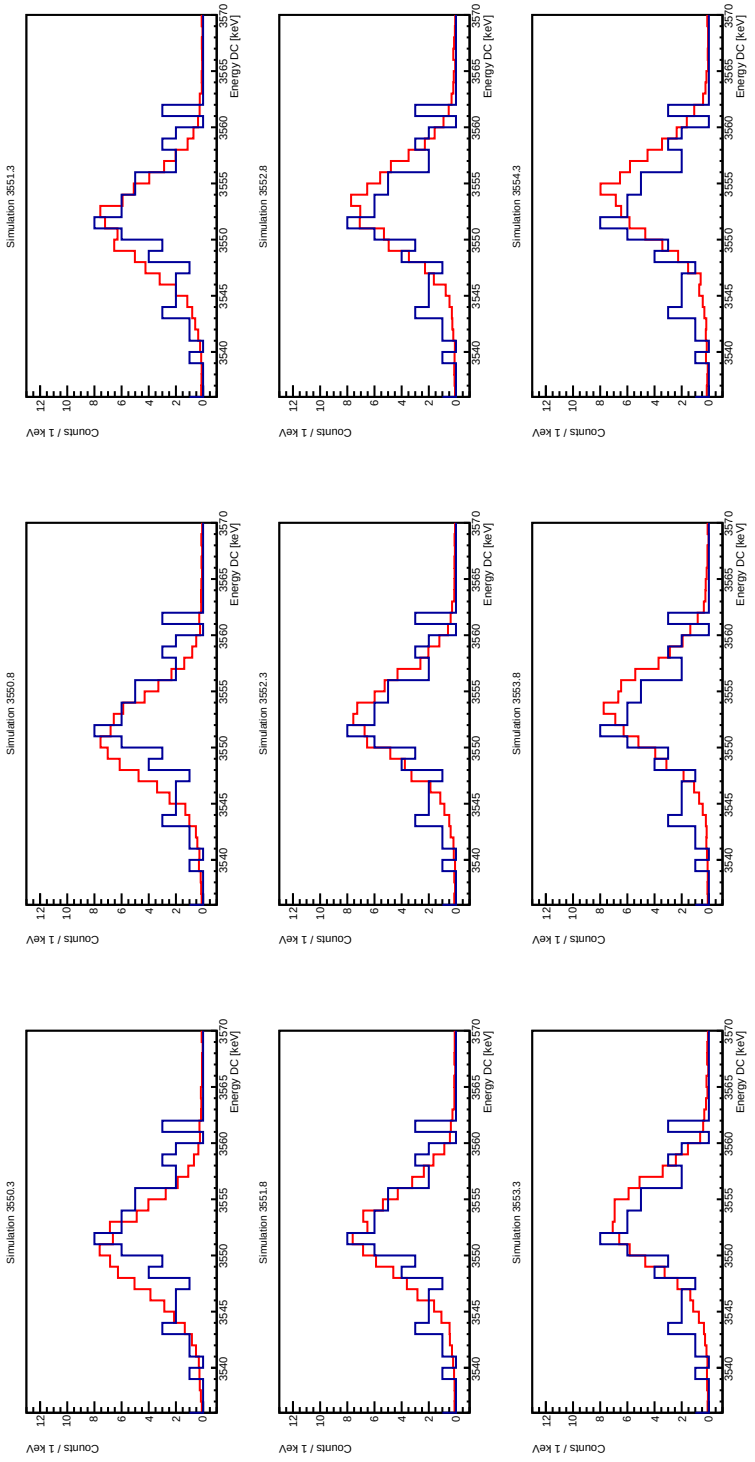

Figure 3.26.: Comparison between the experimental (blue) and simulated (red) spectra for different transition energies for the $3_1^+ \rightarrow 2_1^+$ transition.

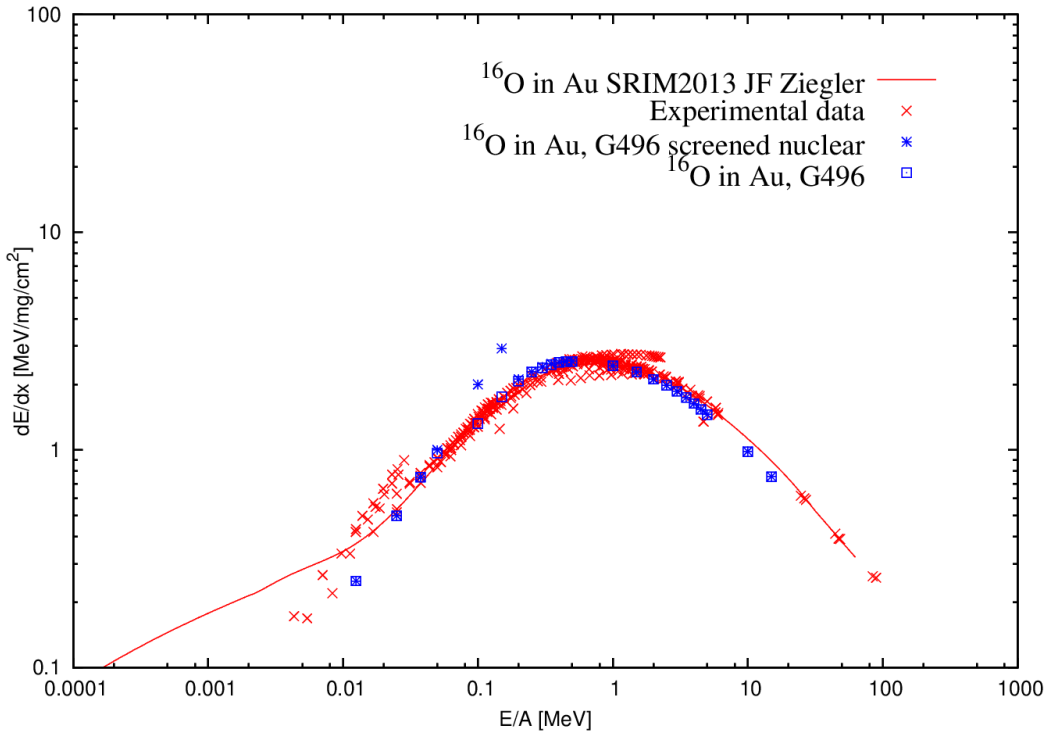

Figure 3.27.: Energy loss of oxygen ions in gold for different calculations. The experimental data are taken from [93].

3.2.7. Energy loss test

The calculation of the energy loss of the ion in the target and in the degrader is important in order to reconstruct the correct velocity of the recoil for the Doppler correction. Different codes, such as Geant4, SRIM [91] or LISE++ [92], employ different calculations that, because of different assumptions, might differ in certain energy regions. The energy loss of oxygen ions in gold is presented in Figure 3.27 using different codes. Despite some differences, there is a general agreement between the calculations.

In the Monte Carlo simulation performed for the present analysis, the nuclear stopping power is also considered in addition to the electronic stopping power. Nuclear stopping power is negligible at high velocity, while when the ion slows down the probability of interacting with the nuclei of the material is higher.

The target thickness was measured after the experiment and resulted to be around 0.3 mg/cm^2, as presented in Section 2.6. It was not possible to directly measure the thickness of the degrader; however, it was tested in Section 3.1.10 and resulted to be 24.4 mg/cm^2. These values were used as input parameters in the simulation and the results were compared to experimental data to test the energy loss table employed for the simulation. Figure 3.28 shows the $2_1^+ \rightarrow 0_1^+$ transition of ^{20}O at 1674.38 keV without Doppler correction. The Doppler shift observed in the simulation is in agreement with the one observed in the experimental data.

In the experiment and in the simulation, the velocity of the ^{20}O is reconstructed from the target-like partner, namely the proton. In order to know the velocity of the recoil after the

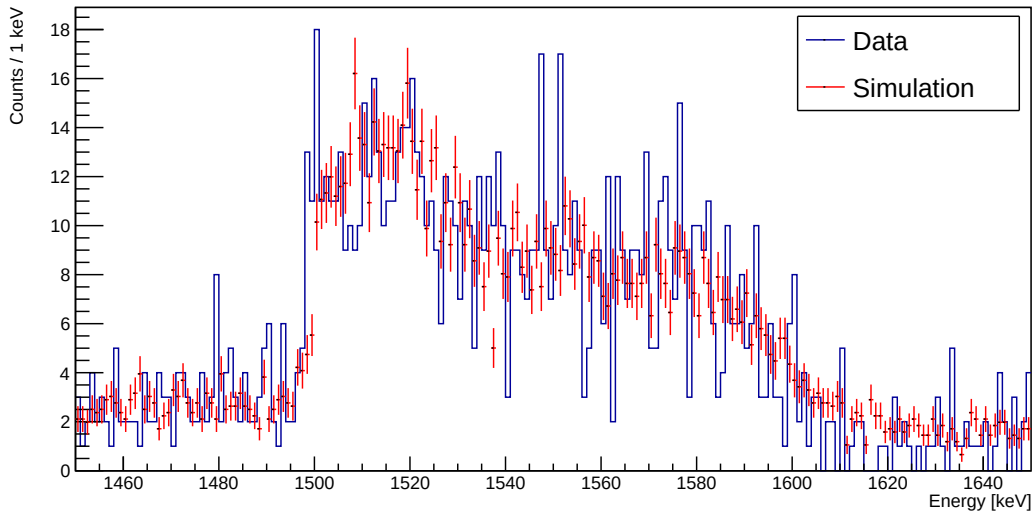

Figure 3.28.: Comparison between the experimental (blue) and simulated (red) spectra for the $2_1^+ \rightarrow 0_1^+$ at 1674.38 keV. No Doppler correction has been applied.

degrader, the energy loss of the ^{20}O in the gold is calculated. The Doppler correction using the velocity after the energy loss is tested by comparing the experimental spectrum to the simulated one, as presented in Figure 3.29. The two spectra present a good agreement and the broadening caused by the straggling in the target and in the degrader is well reproduced. Both peaks are at the expected energy around 1674 keV.

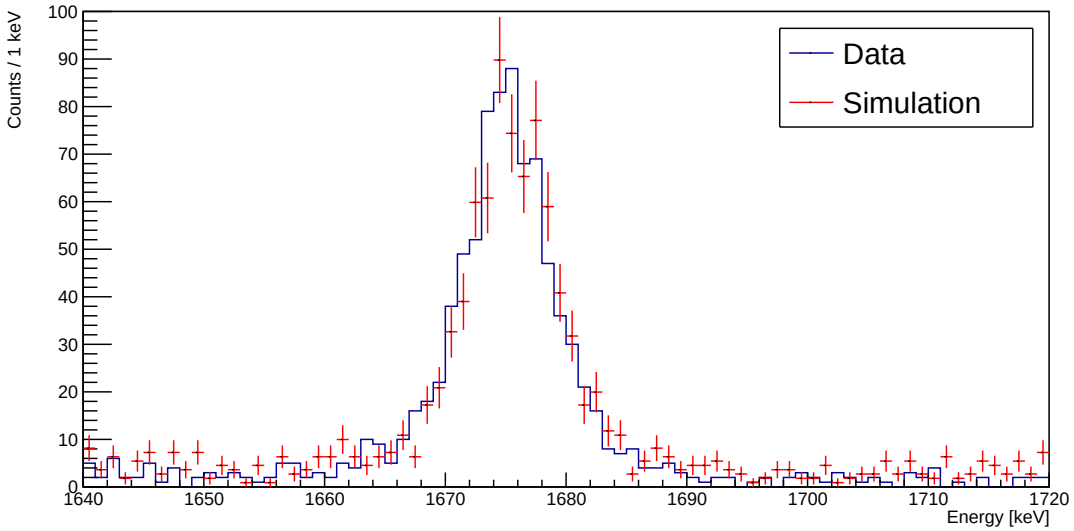

Figure 3.29.: Comparison between the experimental (blue) and simulated (red) spectra for the $2_1^+ \rightarrow 0_1^+$ at 1674.38 keV. An event-by-event Doppler correction using the reconstructed velocity after the energy loss in the gold degrader is applied.

4 Results

After calibrating the AGATA and MUGAST detectors and optimizing the apparatus and the simulations, the results of the present experiment are presented. First, the γ-ray spectra using different gates on the excitation energy have been analysed to determine the energy of the transitions and the branching ratios. Using γ-particle coincidences, the level scheme of ^{20}O has been reconstructed. Then, the lifetime of the 2_2^+ and 3_1^+ states have been measured and the statistical errors have been computed. Different approaches have been attempted and the obtained values have been compared in order to verify the validity of the results. Finally, the systematic errors for the lifetime measurements have been estimated.

4.1. Spectroscopic study

Combining the information on the excitation energies obtained thanks to the MUGAST array with the photons detected by the AGATA array, it is possible to study the level scheme of the present nucleus by gating on the excited states of ^{20}O and observing the γ rays emitted in coincidence.

Due to the fact that γ-rays are emitted in-flight, the lifetime of the states influences the shape and the position of the γ-ray peaks. For this reason, for spectroscopic studies the dataset obtained with the CD_2-only target is preferable, in order to obtain more reliable information on the energy of the transitions. Figure 4.1 shows the γ rays as a function of the reconstructed excitation energy of the ^{20}O. The 2_1^+, 4_1^+, 2_2^+ and 3_1^+ states are distinguishable.

Figure 4.2 shows the γ-ray spectra obtained by gating on the excitation energy of the aforementioned states. The gate on the 2_1^+ is taken from 1.55 to 1.95 MeV. As expected, only one peak is observed at 1674.5(4) keV, corresponding to the $2_1^+ \rightarrow 0_1^+$ transition, and is in agreement with literature values [12].

The gate on the 4_1^+ is taken from 3.35 to 3.75 MeV. The $2_1^+ \rightarrow 0_1^+$ transition is observed at 1674.2(3) keV, confirming the previous measurement while the $4_1^+ \rightarrow 2_1^+$ transition is observed at 1897.7(3) keV. This measurement places the 4_1^+ excited state at 3571.9(9) keV, in agreement with what measured using MUGAST.

The gate on the 2_2^+ is taken from 3.95 to 4.35 MeV. This state decays via two transitions: the $2_2^+ \rightarrow 2_1^+$ transition of 2396.0(4) keV and the $2_2^+ \rightarrow 0_1^+$ transition of 4071(1) keV. Summing the $2_2^+ \rightarrow 2_1^+$ and $2_1^+ \rightarrow 0_1^+$ transitions we obtain 4071(1) keV, compatible with the $2_2^+ \rightarrow 0_1^+$

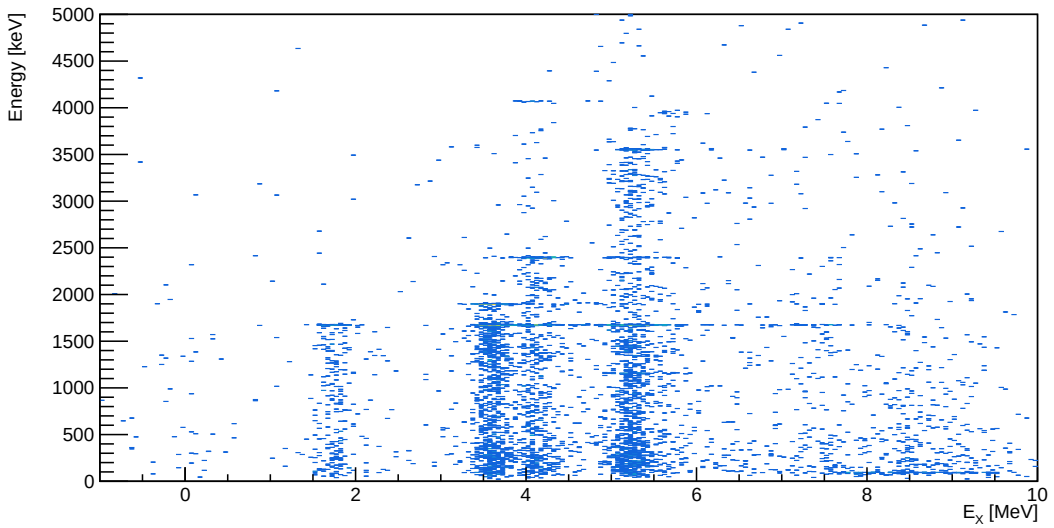

Figure 4.1.: Energy of γ rays measured with AGATA as a function of the ^{20}O excitation energy, reconstructed using MUGAST.

transition and the measurement obtained with MUGAST for the 2_2^+ state.

Finally, the gate on the 3_1^+ state is taken from 5.10 to 5.50 MeV. A peak was observed at 1156.0(8) keV, corresponding $3_1^+ \rightarrow 2_2^+$ transition, as well as a peak at 2397(1) keV, corresponding to the $2_2^+ \rightarrow 2_1^+$. The peak at 3552.6(6) keV corresponds to the $3_1^+ \rightarrow 2_1^+$ transition. The sum of the energies of the $2_2^+ \rightarrow 2_1^+$ and $3_1^+ \rightarrow 2_2^+$ transitions is compatible with the energy of the $3_1^+ \rightarrow 2_1^+$. The $2_1^+ \rightarrow 0_1^+$ transition is also measured at 1674.7(3) keV. Again, the sum of the γ-ray transition energies confirms the MUGAST measurement of the 3_1^+ excited state.

As stated in Section 3.1.8, two additional peaks are observed in MUGAST. These states present a low statistic and no γ-ray peaks are observed in the dataset using the CD_2 only target. However, using the dataset with the CD_2+Au target, which has higher statistics, it is possible to gate on these states and observe some γ-ray transitions. The γ-ray spectra are presented with two Doppler corrections: the one with the velocity of the ^{20}O nucleus at the reaction point (fast DC) and the one that considers the energy loss in the Au degrader (slow DC).

The gate on the 4.9 MeV state is taken from 4.75 to 5.15 MeV. This state has already been observed by Hoffman et al. [40] at 4.99(2) MeV and a tentative spin 2 and positive parity was assigned. Being close to the 3_1^+ state at 5.2 MeV, it is possible to observe the presence of the $3_1^+ \rightarrow 2_1^+$ transition around 3.5 MeV and the $3_1^+ \rightarrow 2_2^+$ transition around 1.2 MeV, marked in blue in Figure 4.3. Despite the low statistics, it is possible to notice a peak at 3329(2) keV (fast DC), which has its counterpart at 3291(5) keV in the slow DC spectrum. This peak might be attributed to the $(2_3^+) \rightarrow 2_1^+$ transition. The sum of the energy of this peak and the 2_1^+ excitation energy is compatible with the energy of the (2_3^+) excited state measured by Hoffman *et al* and the measured with MUGAST in the present work. The first measurement (fast DC) would place the excitation energy of the (2_3^+) state at 5003(2)

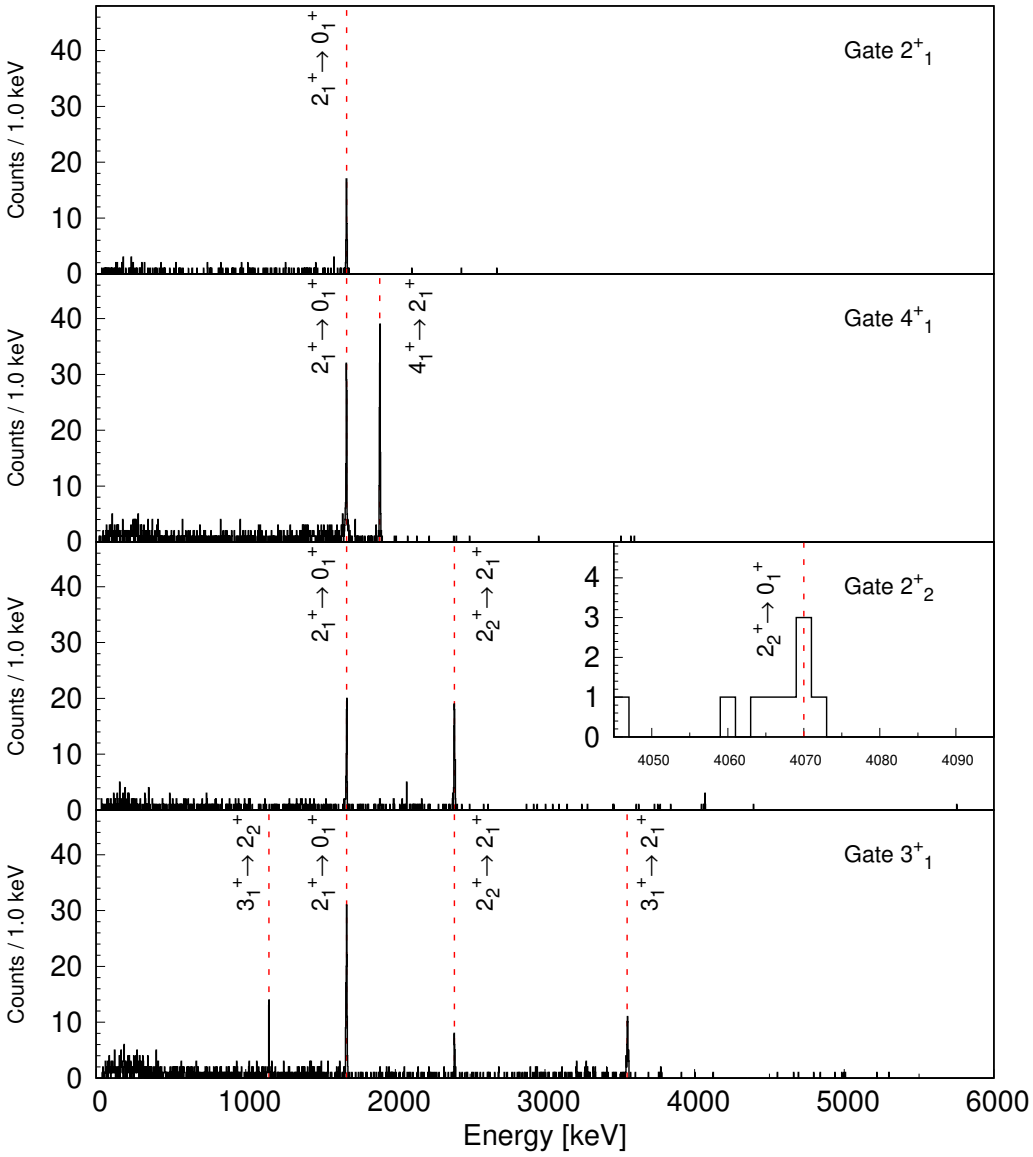

Figure 4.2.: γ-ray spectra obtained using the CD_2-only dataset with different gates on the reconstructed excitation energy obtained with MUGAST. The identified γ-ray transitions are reported.

keV, while the second one (slow DC) would place it at 4965(5) keV. The fact that the peak appears to be broader in the slow DC spectrum seems to imply that this state is depopulated before the energy loss in the degrader, suggesting a lifetime in the range below hundreds of femtoseconds, rather than in the range of picoseconds as in the case of the 2_1^+ state. This would validate the hypothesis of a (2_3^+) state at 5003(2) keV.

A peak at 933(2) keV is also observed (fast DC), that has its counterpart at 922(2) keV (slow DC). This peak might correspond to the $(2_3^+) \rightarrow 2_2^+$ transition. In fact, this measurement summed to the energy of the 2_2^+ state, measured at 4071(1) keV, is again compatible with the measurement of the excited state (Ref. [40] and this work). This measurements would place the (2_3^+) state at 5004(2) keV (fast DC), compatible with the measurement obtained with the 3329(2)-keV transition, or at 4993(2) keV (slow DC). From the comparison between the two spectra, the transition observed in the fast DC seems to be broader, suggesting a longer lifetime of the corresponding state. If this hypothesis is correct, the state from which this transition decay cannot be the same suggested in the previous paragraph, that seemed to indicate a shorter lifetime. However, since the statistics on the transition at 900 keV is too low, it is not possible to make conclusions on the lifetime of the state and on whether the transition comes from the short-lived (2_3^+) state or from another previously unknown state. For this reason, the transition has been excluded from the final level scheme. The observed peaks for the two spectra are shown in Figure 4.3.

The gate on the 5.6 MeV state was taken from 5.45 MeV to 5.85 MeV. This state has also been observed by Hoffman et al. [40], who assigned a tentative spin 2 and positive parity. Similarly to the previous case, being close to the 3_1^+ state it is possible to observe the presence of transitions coming from the depopulation of the latter, marked in red in Figure 4.4. In the fast DC spectrum, a transition at 3954(5) keV is observed and is attributed to the $(2_4^+) \rightarrow 2_1^+$. This hypothesis is supported by the sum of the energy of the observed transition with the energy of the $2_1^+ \rightarrow 0_1^+$ transition: the result is compatible with the energy of the (2_4^+) state measured at 5.64(2) MeV by Hoffman *et al.* The $(2_4^+) \rightarrow 2_1^+$ transition is also observed in the slow DC spectrum at 3903(3) keV. Similarly to the (2_3^+) state, this result suggests a lifetime in a range below hundreds of femtoseconds.

The results are summarized in Table 4.1 and the level scheme is presented in Figure 4.5. The complete γ-ray spectra using the two datasets are presented in Figure 4.6. The shift in energy observed for the $2_1^+ \rightarrow 0_1^+$ and $4_1^+ \rightarrow 2_1^+$ transitions around 1.7 and 1.9 MeV respectively is caused by the lifetime effects. The same shift is not observed for the 2_2^+ and 3_1^+ states, suggesting a shorter lifetime, in the range of femtoseconds.

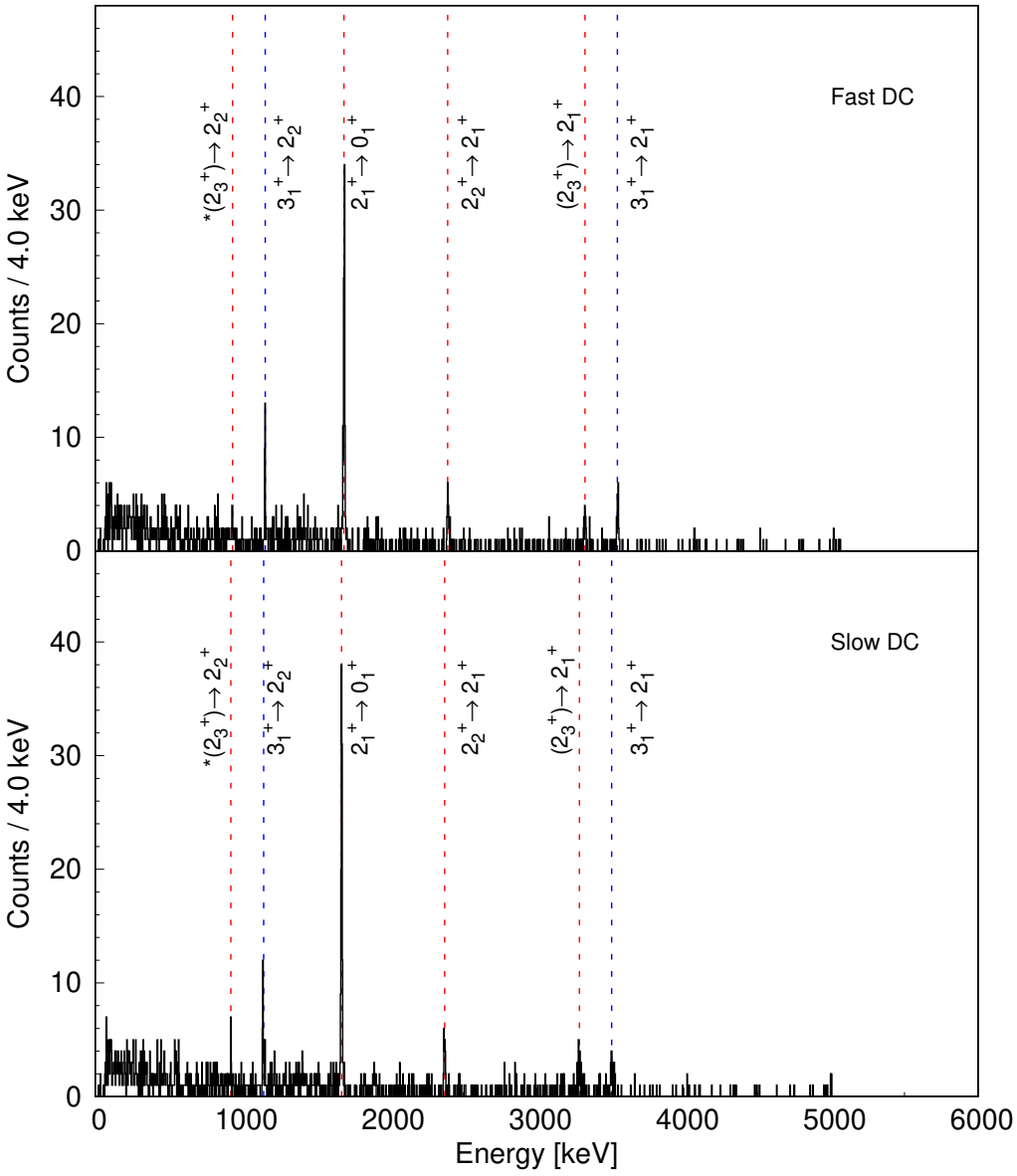

Figure 4.3.: γ-ray spectrum obtained using the CD_2+Au dataset for the Doppler correction at the reaction point (top) and after the energy lost in the degrader (bottom). A gate on the excitation energy of the ^{20}O between 4.75 and 5.15 MeV is applied. The transitions attributed to the state at 4.9 MeV are marked in red, while the transitions attributed to the contamination from the 3_1^+ state at 5.2 MeV are marked in blue. The attribution of the transition around 900 keV to the $(2_3^+) \rightarrow 2_2^+$ transition is only tentative.

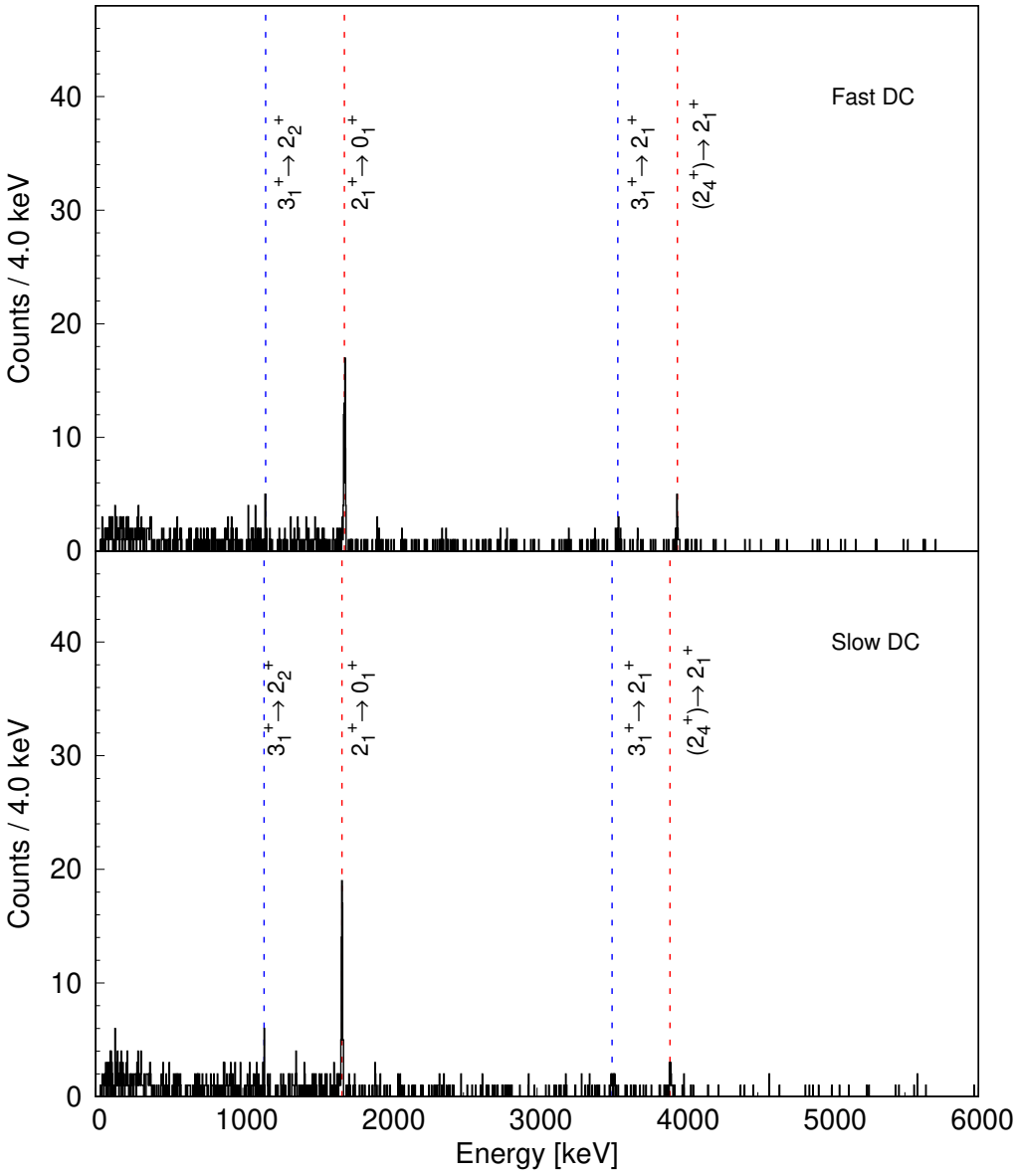

Figure 4.4.: γ-ray spectrum obtained using the CD_2+Au dataset for the Doppler correction at the reaction point (top) and after the energy lost in the degrader (bottom). A gate on the excitation energy of the ^{20}O between 5.45 and 5.85 MeV is applied. The transitions attributed to the state at 5.6 MeV are marked in red, while the transitions attributed to the contamination from the 3_1^+ state at 5.2 MeV are marked in blue.

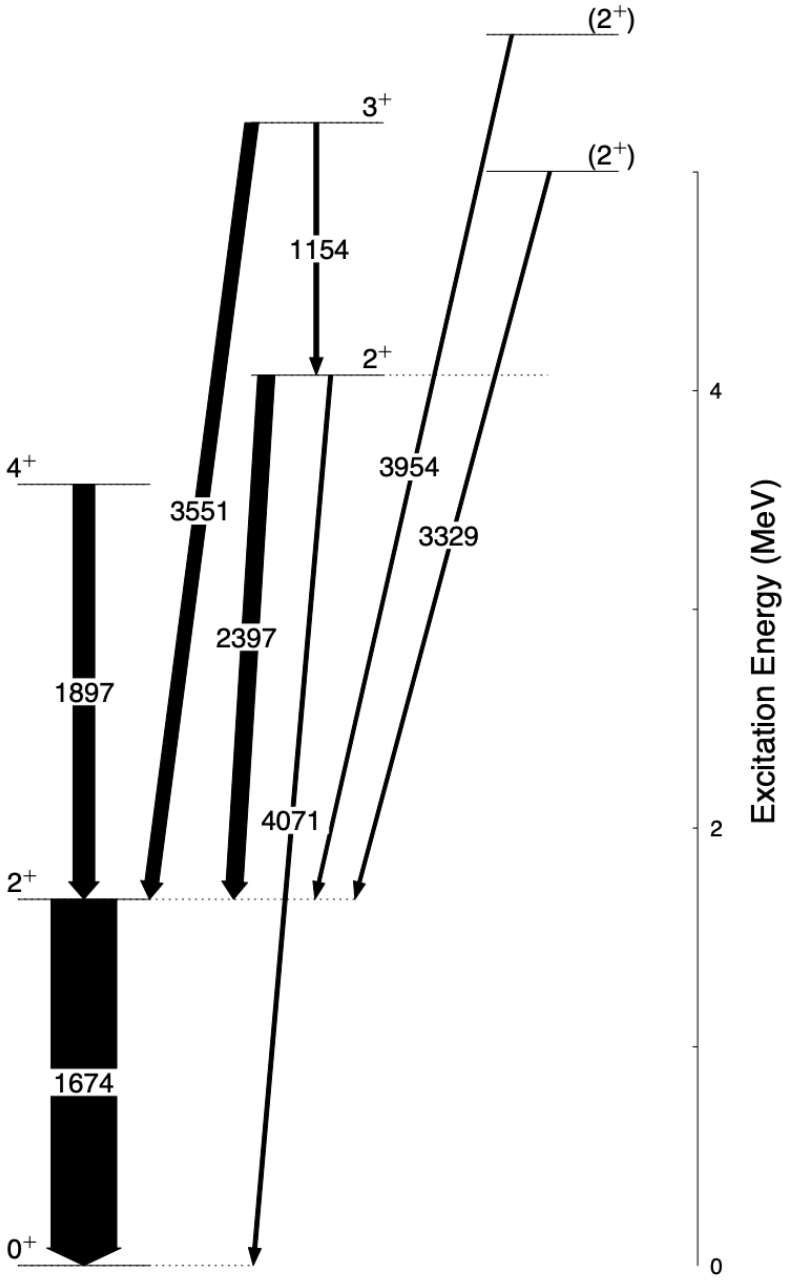

Figure 4.5.: Reconstructed level scheme of the ^{20}O. The width of the transitions is proportional to the number of counts observed in the spectra corrected for the relative efficiency of the germanium detectors.

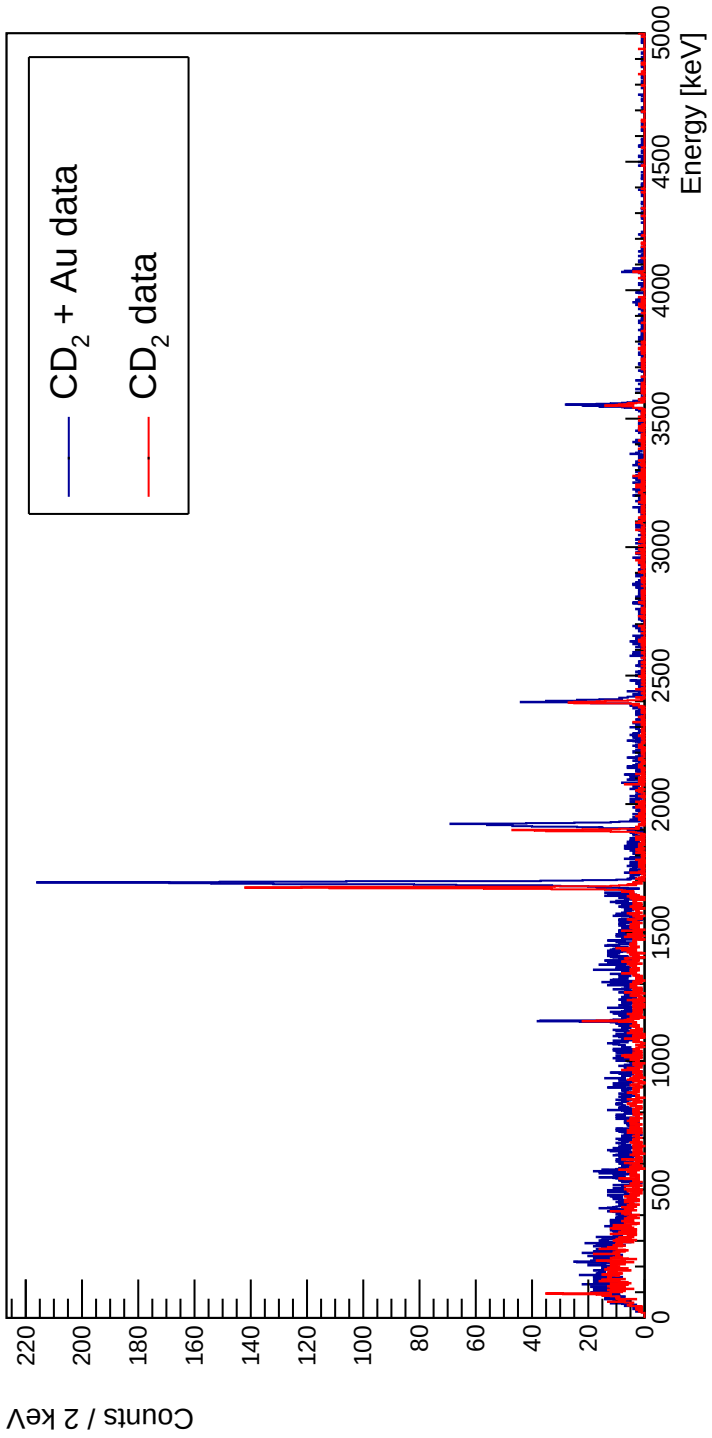

Figure 4.6.: Comparison between the γ-ray spectra obtained using the CD_2-only (red) and the CD_2+Au (blue) datasets. In the case of the CD_2+Au dataset, the fast DC was employed.

J_i	E_X [MeV]	J_f	E_γ [keV]
2_1^+	1.675(1)	0_1^+	1674.5(4)
4_1^+	3.572(1)	2_1^+	1897.7(3)
2_2^+	4.071(1)	2_1^+	2396.1(2)
		0_1^+	4071(1)
(2_3^+)	5.004(2)	2_1^+	3329(2)
3_1^+	5.228(1)	2_2^+	1156.0(8)
		2_1^+	3552.6(6)
(2_4^+)	5.629(5)	2_1^+	3954(5)

Table 4.1.: γ ray transitions identified in the spectroscopic study of ^{20}O using both the CD_2-only and the CD_2+Au dataset.

4.1.1. Branching ratio calculation

Following the spectroscopic study of the γ ray spectra, the branching ratios of the transitions depopulating the 2_2^+ and 3_1^+ states have been calculated, after gating on the direct population of the states. Branching ratios are necessary for the calculation of the reduced transition probabilities and hence for comparing the experimental lifetimes to theoretical calculations.

The 2_2^+ state has two branches: the $2_2^+ \rightarrow 2_1^+$ transition at 2396 keV and the $2_2^+ \rightarrow 0_1^+$ transition at 4071 keV. The branching ratio has been calculated using both the AddBack and the tracked spectra and using both the CD_2-only and the CD_2+Au dataset and the results have been compared. The efficiency of AGATA for the AddBack and tracked array at the energy of the considered transitions as measured in the present experiment has been taken into account. The efficiency at 2396 keV is 8.4% for the AddBack method and 8.1% for the tracked method, while the efficiency at 4071 keV was 6.4% and 6.0% for the two methods respectively.

The branching ratio calculated using the CD_2-only dataset resulted to be 86(8)% for the $2_2^+ \rightarrow 2_1^+$ transition and 14(1)% for the $2_2^+ \rightarrow 0_1^+$ transition both using the AddBack and the tracked spectrum. The branching ratio calculated using the CD_2+Au dataset, instead, provided different results for the AddBack and the tracked spectra: in the first case, the branching ratio resulted to be 88(6)% and 12(1)%, while in the second case it resulted to be 91(7)% and 9(1)%. These values differ significantly from the values of Ref. [39] and [30]. However, the two dataset and the two methods are in agreement within the error bars and the weighted average resulted to be 88(1)% and 12(1)%.

The 3_1^+ states presents two branches: the $3_1^+ \rightarrow 2_2^+$ transition at 1156 keV and the $3_1^+ \rightarrow 2_1^+$ transition at 3553 keV. The efficiency of AGATA at 1156 keV is 11.7% for the AddBack and 11.5% for the tracked spectrum, while at 3554 keV the efficiency is 6.9% and 6.5% for the AddBack and tracked spectra respectively.

The branching ratio calculated using the CD_2-only dataset with the AddBack spectrum resulted to be 28(1)% for the $3_1^+ \rightarrow 2_2^+$ transition and 72(6)% for the $3_1^+ \rightarrow 2_1^+$ transition, while using the tracked spectrum it resulted to be 34(2)% and 66(6)%. Finally, the branching ratio calculated using the CD_2+Au dataset resulted to be 29(1)% and 71(5)% for the AddBack spectrum and 30(1)% and 70(4)% using the tracked spectrum.

The results for both datasets and both methods are presented in Table 4.2. The weighted

$J_i \to J_f$	E_γ [keV]	ε [%]	Dataset	BR	Average	Lit.
$2_2^+ \to 2_1^+$	2396	8.4 %	CD_2	0.86(8)	0.88(1)	0.72(8)
			CD_2+Au	0.86(8)		
		8.1 %	CD_2	0.88(6)		
			CD_2+Au	0.91(7)		
$2_2^+ \to 0_1^+$	4071	6.4 %	CD_2	0.14(1)	0.12(1)	0.28(8)
			CD_2+Au	0.14(1)		
		6.0 %	CD_2	0.12(1)		
			CD_2+Au	0.09(1)		
$3_1^+ \to 2_2^+$	1156	11.7 %	CD_2	0.28(1)	0.30(1)	
			CD_2+Au	0.34(2)		
		11.5 %	CD_2	0.29(1)		
			CD_2+Au	0.30(1)		
$3_1^+ \to 2_2^+$	3556	6.9 %	CD_2	0.72(6)	0.70(1)	
			CD_2+Au	0.66(6)		
		6.5 %	CD_2	0.71(5)		
			CD_2+Au	0.70(4)		

Table 4.2.: Branching ratio of the transitions decaying from 2_2^+ and 3_1^+ states using the AddBack and tracked spectra and the CD_2-only and CD_2+Au datasets. Literature values taken from [39].

average of the results obtained using the four different method is also reported and, when present, compared to literature value.

4.2. Lifetime measurement of the 2_2^+ via lineshape analysis

The lifetime of the 2_2^+ state is extracted from the $2_2^+ \to 2_1^+$ transition at 2396 keV. Another peak at 4071 keV, corresponding to the $2_2^+ \to 0_1^+$ transition, was observed in the spectrum; however, due to the smaller branching ratio and to the lower efficiency of AGATA at the latter energy, the statistics was not sufficient to perform a lineshape analysis. In the spectroscopic study of the ^{20}O, the 3_1^+ state has been observed to decay via two transitions at 3551 keV and 1156 keV, corresponding to $3_1^+ \to 2_1^+$ (BR= 70%) and $3_1^+ \to 2_2^+$ (BR= 30%) respectively. This second transition is particularly concerning because, by feeding the 2_2^+ state, it influences the lifetime measurement of it. For this reason, an additional gate on the 2_2^+ state is required, by selecting the corresponding excitation energy of the state. This selection also reduces the background in the proximity of the peak, allowing to obtain a cleaner spectrum.

As explained in Chapter 2, the energy of the γ rays detected by AGATA can be reconstructed using two methods: the AddBack and the tracking. Since this experiment presents a low multiplicity and a low counting rate, the tracking does not result convenient with respect to the AddBack method. In fact, when comparing the spectra obtained with the two method, the AbbBack one has a larger number of events in the range of interest (167) with respect to the tracked spectrum (144) in the same range. The comparison between the two spectra is shown in Figure 4.7. However, the simulated spectrum is obtained by using the same

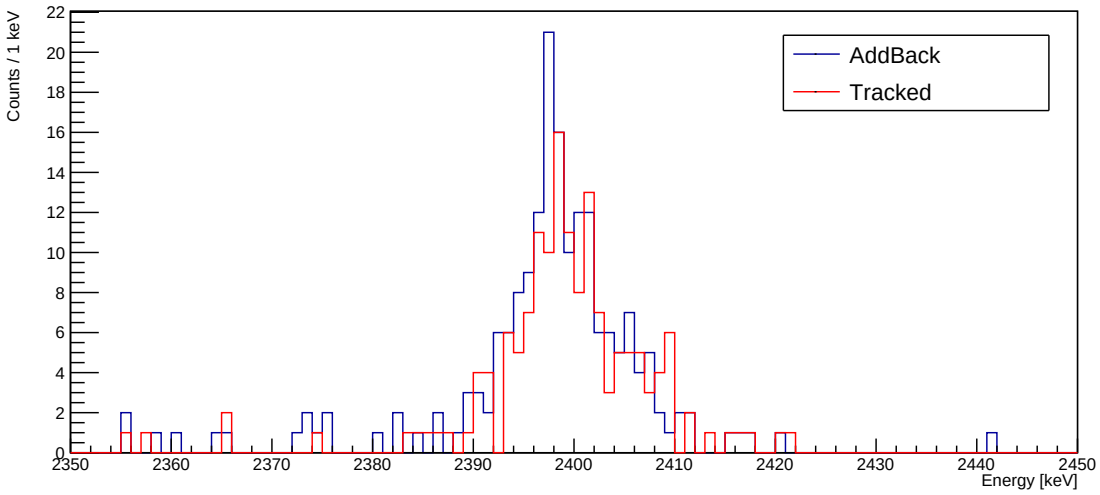

Figure 4.7.: Comparison between the experimental spectra obtained using the AddBack (blue) and tracking (red) method.

tracking algorithm that has been used for the analysis of the data. The tracking algorithm could, in principle, add biases to the spectrum. Since we are interested in the comparison of the experimental and simulated spectra, by using the tracked spectrum the effect of these biases would be compensated. For these reasons, the analysis was carried out using both the AddBack and the tracked spectra for the experimental part.

The Monte Carlo simulations have been performed using the AGATA simulation code [94]. In the simulation, only the state of interest, namely the 2_2^+, has been populated using the experimental particle angular distribution measured in the present experiment. The Doppler correction has been performed using the velocity reconstructed from the protons emitted in the reaction. In the velocity reconstruction, the energy loss in the target has been taken into account, as well as the angle of emission of the protons and of the oxygen recoil. The agreement between the experimental and simulated velocities has been verified, as illustrated in Chapter 3.

For the comparison of the simulated and experimental spectra using the χ^2 method, a range of integration must be chosen. In fact, in order for the method to be effective, it is important to compare only the region of interest. On the other hand, a too narrow range could exclude from the analysis portions of the spectrum that are sensitive to the lifetime effect.

In order to understand what the region of sensitivity is, two simulations of the 2_2^+ have been performed: in the first one a very short lifetime, below the sensitivity of the DSAM method, was assumed, while in the second one a very long lifetime, long enough to ensure that the decay would happen after the gold degrader, was assumed. The resulting spectra, Doppler corrected using the β value at the reaction point, are shown in Figure 4.8. The spectrum corresponding to a lifetime of 1 fs has its centroid at 2395 keV, while the left part of the peak begins at 2386 keV. The spectrum corresponding to a lifetime of 10 ps presents a peak around 2425 keV and the right part of the peak ends around 2440 keV. This means that the lifetime of the 2_2^+ influences the position of the peak only in a range from 2386 keV to 2440 keV. For this reason, the region of integration for the calculation of the χ^2 has been

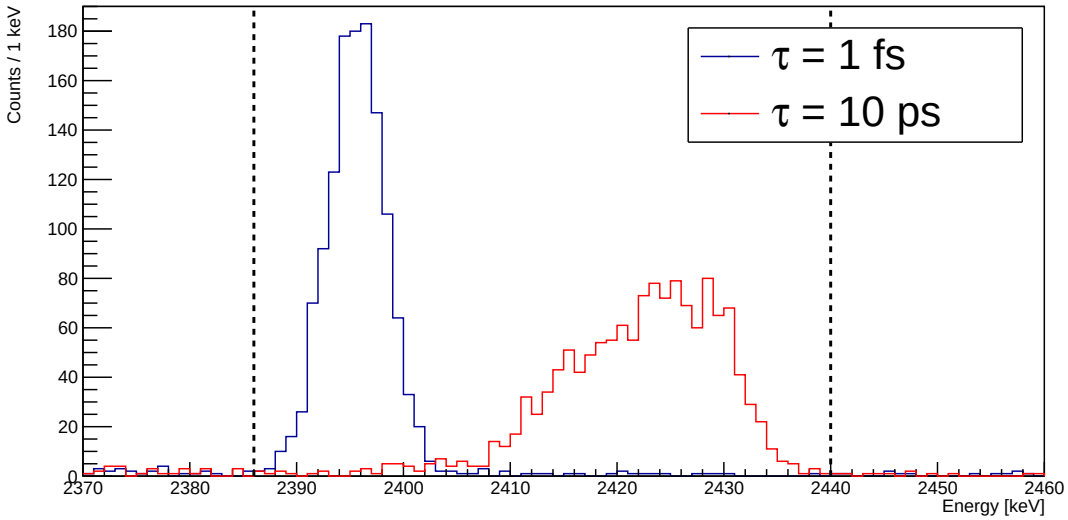

Figure 4.8.: Simulated spectra corresponding to a lifetime of 1 fs (blue) and 10 ps (red). The lifetime of the 2_2^+ state influences the peak position in a range from 2386 keV to 2440 keV.

chosen between 2386 keV 2440 keV.

For every simulation, 10^6 events have been simulated. Considering the efficiency of the apparatus and the angular distribution of the state, in the simulation only $(131 \pm 1) \times 10^2$ events on average are observed in the range of interest, corresponding to a scaling factor of 1.09(1)%. In order to guarantee the condition of $N = N_0$ required by the multinomial problem (see Appendix B), the normalization has been adjusted for the number of events in the range of interest of each simulation. The variation of the scaling factor was below 1%. The stability of this value is an additional evidence of the validity of the range of integration chosen for the normalization and the χ^2 analysis.

A first series of simulations have been performed, in order to obtain a first estimation of the lifetime. In this series, two parameters have been investigated: the energy of the transition and the lifetime of the state. The scan in energy was performed between 2394.5 keV and 2398 keV with a step of 0.5 keV. This step is already below the resolution of the detectors and a finer step would lead to statistical fluctuation. The initial constraints for the energy values have been provided by the spectroscopic measurement and the energy tuning performed using the data obtained with the CD_2 target and measured the transition to be between 2395 and 2397 keV. The scan in lifetime was done in a range between 40 and 175 fs with a step of 15 fs. The experimental and simulated spectra have been compared using the least-χ^2 method for the histograms comparison. In particular, both the Neyman's and the Pearson's statistics, defined in Equation B.4 and B.3, have been used.

In order to use the least-χ^2 method for the comparison, a rebinning procedure is needed. The χ^2 method can be used under the assumption of random Gaussian independent variables. In the case of histograms comparison, the Gaussian condition is guaranteed only if the bins of the histograms contain at least ten events. Having at least ten events per bin reduces the errors due to random fluctuations that can happen when the statistics is low, as in the case of the present experiment. The experimental histogram has been rebinned with the condition

of having at least ten events per bin. The resulting histogram has bins of different widths: in particular, in the range where the main peak is present, the bin results to have a typical range of about 1 or 2 keV, while at higher energy, where the tail of the peak is expected, the width of the bins increases. In particular, all the events corresponding to the tail are collected in the last bin.

This rebinning procedure has been applied both on the AbbBack and the tracked histograms. The first histogram is divided into 13 bins of different widths, while the second histogram into 12 bins. For the comparison, the simulations have been rebinned using the same binning as the experimental data.

From this first preliminary analysis, the χ^2 was minimized around 65 fs. The results coming from the two different histograms and the two different statistics were all in agreement within the range of confidence.

Then, after determining the region of interest, a second series of simulations was performed. The lifetime was scanned in a range from 35 to 100 fs with a step of 1 fs, while the energy of the transition has been studied from 2395 keV to 2397.5 keV with a step of 0.5 keV.

The χ^2 has been calculated using two classical forms: the Neyman's χ^2 (see Equation (B.4)) and the Pearson's χ^2 (see Equation (B.3)). These two forms differ for the kind of weight that is used in the quadratic sum: while the Neyman's χ^2 uses the experimental uncertainties, corresponding to the number of events, the Pearson's χ^2 uses the theoretical ones, in this case the events of the bin in the simulated histogram. More details are given in Appendix B.

For the tracked spectrum, the minimum is found at $\tau = 63$ fs (Neyman's) and $\tau = 66$ fs (Pearson's). For the AddBack spectrum, the minimum is found at $\tau = 66$ fs (both Neyman's and Pearson's χ^2). The χ^2 distributions are presented in Figure 4.9

As explained in Section B.1, the least-χ^2 method can be used to determine the confidence limit of the parameters. In particular, one standard deviation of the parameter corresponds to a $\Delta\chi^2 = \chi^2 - \chi^2_{\text{min}} = 1$ with respect to the minimum χ^2 [95]. For the tracked spectrum, the confidence limits were found between 48 and 92 fs (Neyman's) and between 56 and 95 fs (Pearson's). Hence the measurements are $\tau = 63^{+28}_{-16}$ fs and $\tau = 66^{+29}_{-12}$ fs. For the AddBack measurement, the results are $\tau = 66^{+20}_{-20}$ fs (Neyman's) and $\tau = 66^{+19}_{-20}$ fs (Pearson's). The results obtained with the different methods are consistent both on the value of the lifetime and the statistical errors. The comparison between the experimental and simulated spectra for the Neyman's statistic and tracked spectrum is presented in Figure 4.10.

This estimation takes into consideration only the statistical errors of the measurement, while it does not consider the systematic errors that come from the methodology and the *a priori* assumptions. The estimation of the systematic errors is discussed in Section 4.5.

Influence of the rebinning on the lifetime value

In order to reduce the effect of statistical fluctuation due to low statistics, the histogram has been rebinned requiring at least 10 events per bin. However, this is an arbitrary number and the rebinning could be done requiring a larger number of events. A possible correlation between the minimum number of events per bin and the lifetime measurement has been investigated. The least-χ^2 has been calculated for four additional binnings, from 11 events per bin to 15 events per bin. The results are shown in Figure 4.11.

The lifetime measurements obtained with the new binning procedures are all compatible to each other, both for the Pearson's and Neyman's statistics. Moreover, no specific trend

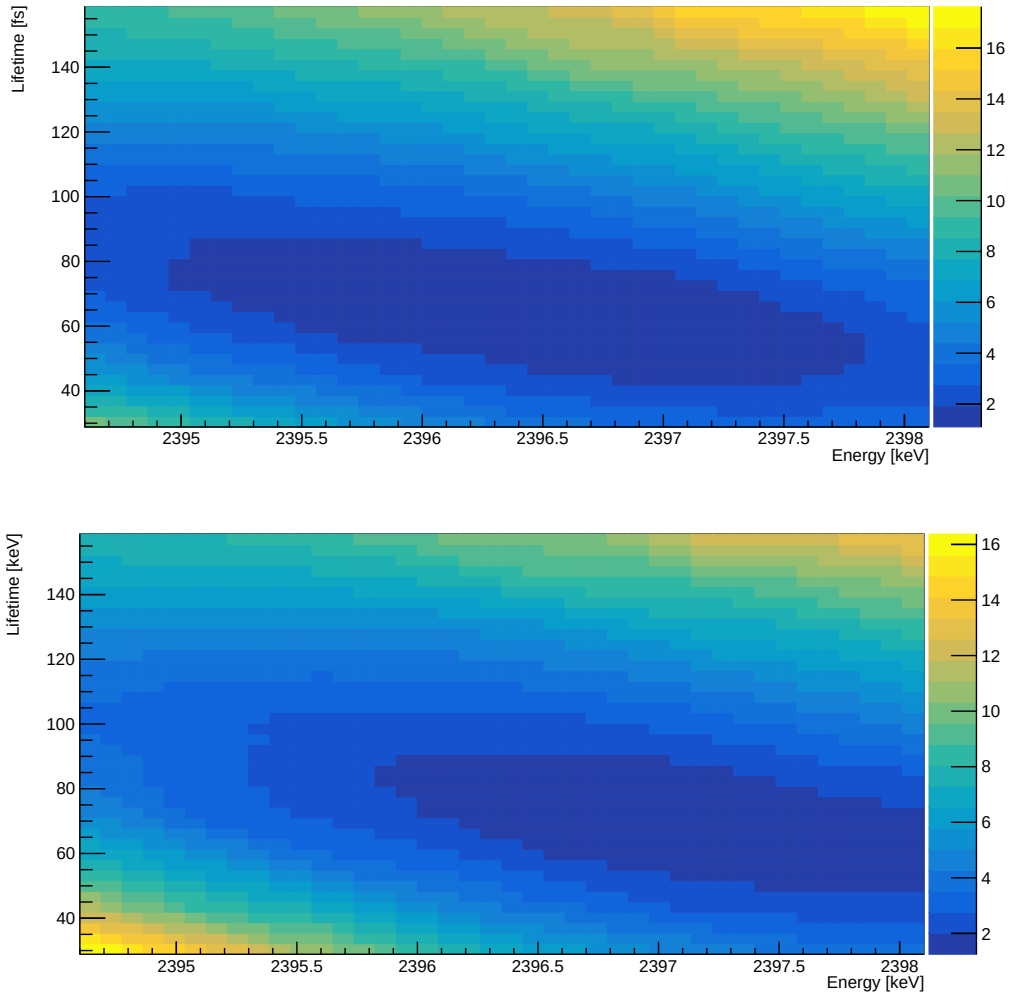

Figure 4.9.: χ^2 distribution depending on two parameters, the lifetime of the 2_2^+ and the energy of the $2_2^+ \rightarrow 2_1^+$ transition, for the AddBack (top) and tracked (bottom) spectra using the Neyman's χ^2.

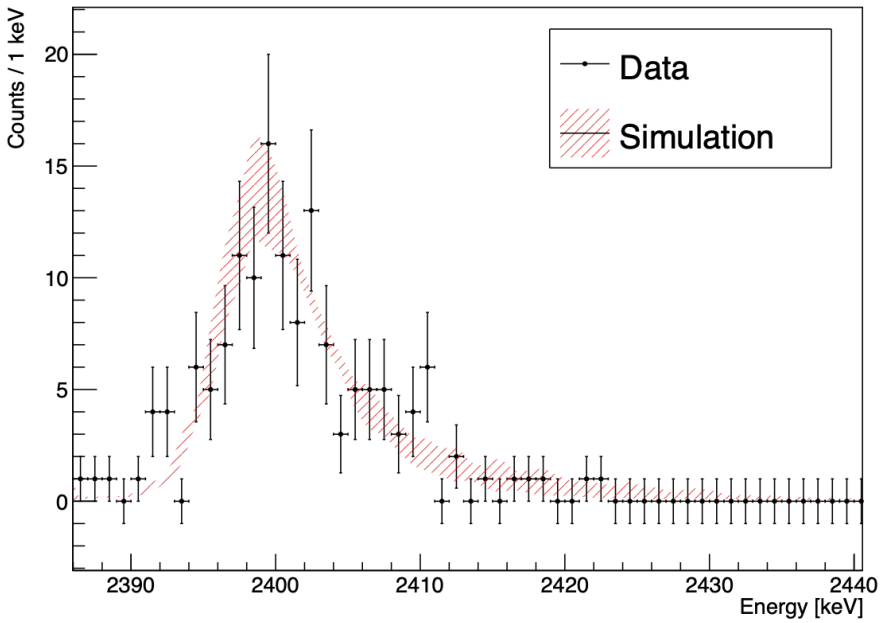

Figure 4.10.: Comparison of the experimental histogram and the simulated one for lifetimes corresponding to confidence range given by the $\Delta\chi^2 = 1$ at the transition energy of the 2396.6 keV for Neyman's χ^2 and tracked spectrum.

can be observed and the fluctuations of the results are random. Similarly, the error bars do not increase or decrease significantly depending on the chosen binning. Therefore, it is possible to conclude that for this analysis the binning does not influence the lifetime or the error calculations of the state.

4.2.1. Lifetime measurement using the reconstructed velocity

An additional test was performed by investigating the lineshape of the $2_2^+ \rightarrow 2_1^+$ transition Doppler corrected using the velocity of the recoil after the energy loss in the gold instead of the one directly extracted from MUGAST as previously discussed.

The reaction is assumed to take place in the centre of the target, therefore the energy loss is calculated for half of the target thickness and for the degrader thickness. The angle of emission of the ^{20}O recoil, calculated from the information on the proton as explained in Section 3.1.8, has been taken into account. The energy loss was calculated using the Geant4 tables for oxygen in CD_2 and in gold. The validity of the energy loss tables employed in the experiment has been discussed in Section 3.2.7.

The same Doppler correction has been applied for both the experimental data and the simulation using the NPTool code. The range for the normalization and the histogram comparison was chosen between 2350 and 2420 keV, where the AddBack spectrum counted 175 events and the tracked 147 events. The scaling factor resulted to be around 0.126 for the AddBack spectrum and 0.106 for the tracked spectrum.

Then the experimental and simulated histograms have been compared using the least-χ^2 method, requiring at least 10 events per bin. The events were collected into 15 and 12 bins

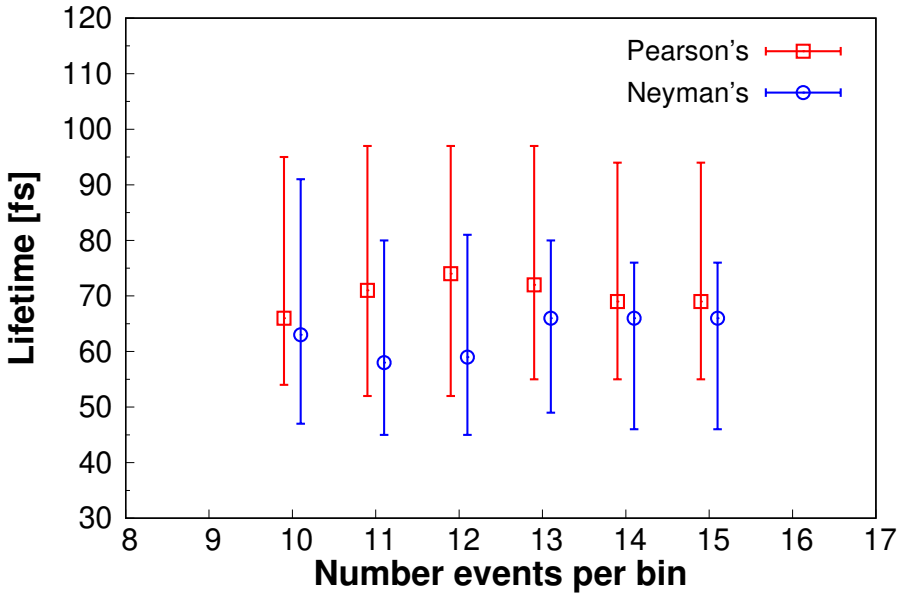

Figure 4.11.: Lifetime results and corresponding error bars using the χ^2 Pearson's (red) and Neyman's (blue) statistics with different binning. The results fluctuate within the error bars of the measurement and no trend is observed.

for the AddBack and tracked spectra respectively.

The least-χ^2 method leads to different results for the AddBack and tracked spectrum, using the Neyman's χ^2. In particular, for the AddBack spectrum the χ^2 is minimized for $E_\gamma = 2395$ keV and for $\tau = 69$ fs. The lower and upper limits, determined by the condition $\Delta\chi^2 = 1$, correspond to 42 and 93 fs. With the tracked spectrum, on the other side, the χ^2 is minimized at the same E_γ for $\tau = 81$ fs and the lower and upper limits are 54 and 110 fs. The results are presented in Figure 4.12.

4.2.2. Lineshape analysis using the maximum likelihood method

An additional test has been performed in order to measure the lifetime of the 2_2^+ state using the maximum likelihood method (see Appendix B.2). One advantage of this method is that it does not require a rebinning of the histograms to have at least 10 events per bin.

The same Monte Carlo simulations produced for analysis using the least-χ^2 have been used for the present test. Both histograms have the same binning with a bin width of 1 keV.

From the analysis of the maximum likelihood method, the AddBack and the tracked spectra gave different results. In particular, the analysis using the tracked spectrum suggests a lifetime around 86 fs, which is longer than what measured using the least-χ^2 method but still in agreement within the error bars. The analysis that instead relies on the AddBack spectrum seems to suggest a shorter lifetime around 57 fs, again in agreement with the least-χ^2 measurement within the error bars. The results are shown in Figure 4.13.

The difference between the result obtained with the AddBack and tracked spectra are related to the shape of the spectra, which can be observed in Figure 4.7. In particular, the AddBack spectra shows a higher concentration of events in the peak. A distribution with

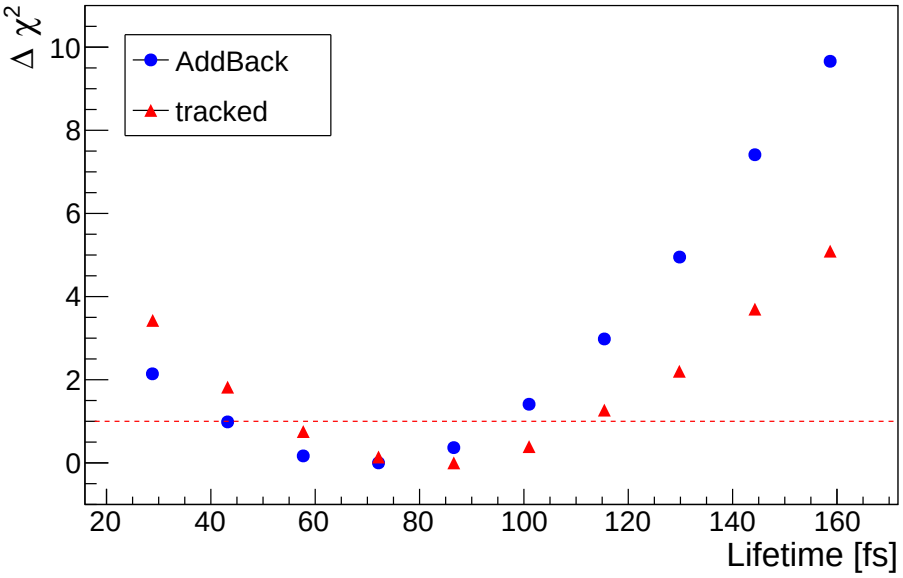

Figure 4.12.: $\Delta\chi^2$ as a function of the lifetime for the AddBack (blue) and tracked (red) spectra, Doppler corrected using the reconstructed velocity of the recoil after the energy loss in the gold degrader.

more events in the peak rather than in the tail leads to a shorter lifetime, which would explain the difference between the results obtained with the two different spectra.

The different results obtained using the least-χ^2 and the maximum likelihood methods can be explained by the rebinning procedure. In fact, the binning required by the least-χ^2 method collects the events of the tail in the last bin. As the tail is the most sensitive part to the lifetime, this might influence the final result. However, all the different approaches lead to values of lifetime that are compatible, proving the solidity of the measurement.

4.3. Lifetime measurement of the 3_1^+ via lineshape analysis

The lifetime of the 3_1^+ state has been extracted using the same methodology as for the 2_2^+ state. The analysis focused on the $3_1^+ \rightarrow 2_1^+$ transition at 3556 keV. This transition presents higher statistics with respect to the $3_1^+ \rightarrow 2_2^+$ one at 1156 keV. Moreover, being at higher energy, the Doppler shift is more prominent and the background is lower. In the case of the 3_1^+ state, no transition has been observed to decay on this state, influencing the lifetime measurement. However, the gate on the excited state was required to clean the spectrum. Moreover, this procedure ensures the elimination of contributions coming from unobserved feeding transitions.

Similarly to the case of the 2_2^+ analysis, in the simulations only the 3_1^+ state has been populated, assuming the angular distribution measured in this experiment for that state. For each simulation, 10^6 events have been simulated. The normalization range has been chosen between 3540 keV and 3600 keV, which corresponds to the maximum variation range of the peak under the influence of the lifetime.

In this range, the experimental histogram has been rebinned by requiring at least ten events

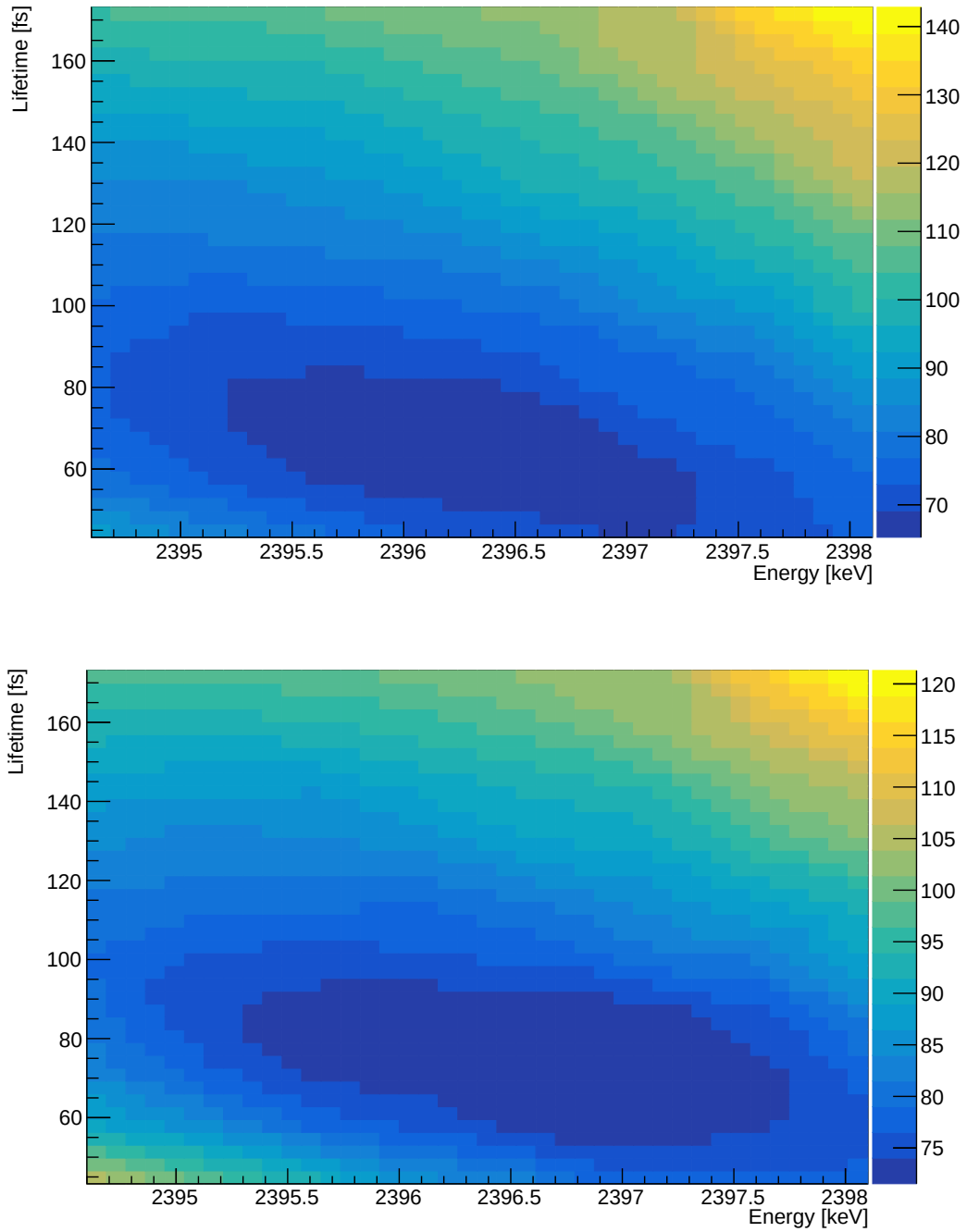

Figure 4.13.: Lineshape analysis of the $2_2^+ \rightarrow 2_1^+$ transition using the maximum likelihood method to compare the AddBack (top) and tracked (left) spectra to the Monte Carlo simulations. In the figure, for practical reasons, instead of plotting the likelihood $\mathcal{L}$, the $-\ln(\mathcal{L})$ is plotted.

per bin. In this case, the AddBack histogram has been divided into 12 bins of different width, while the tracked histogram into 11 bins.

In the first series of simulations, the energy of the transition has been investigated in a range between 3549 keV and 3553 keV with a step of 0.5 keV. The lifetime values have been scanned from 30 to 86 fs with a step of about 7 fs.

After a preliminary analysis, the least-χ^2 has been found for a lifetime of about 50 fs. The analysis using the two spectra (AddBack and tracked) and the two χ^2 methods (Neyman's and Pearson's) were in agreement within the confidence limits.

A second series of simulations have been performed. In this case, the lifetime has been investigated with a step of about 1 fs. Both the AddBack and tracked spectra have been analyzed using the Neyman's and Pearson's statistics as defined in Equation (B.4) and (B.3), respectively. The confidence limits of the measurements have been taken as those corresponding to $\Delta\chi^2 = 1$. The AddBack spectrum suggested a lifetime of 61^{+17}_{-18} fs and 52^{+27}_{-12} fs for the Neyman's and Pearson's χ^2 respectively. The tracked spectrum suggested a lifetime of 55^{+16}_{-18} fs and 48^{+17}_{-12} fs. The simulations presented the best agreement with the tracked spectrum, as expected. All the results obtained with the two spectra and the two statistics are compatible within the confidence limits.

Similarly to the case of the lifetime measurement of the 2_2^+ state, the lifetime of the 3_1^+ state has been measured using also the maximum likelihood method, comparing the experimental spectra to the Monte Carlo simulations described in the previous section. In this case, the AddBack and the tracked spectra lead to the same value of lifetime, with the likelihood being maximized at $\tau = 57$ fs.

4.3.1. Influence of the feeder

The lifetime measurement of a state is influenced by the presence of feeding transitions coming from higher energy states. The influence of the feeders has been discussed in Section 2.7.2. In particular, the influence depends on the branching ratio of the feeding transition, on the population of the higher-lying state and on its lifetime. The lifetime of the 3_1^+ state has been measured to be comparable to the lifetime of the 2_2^+. According to the excitation energy spectrum (see Figure 3.14), the 3_1^+ state is more directly populated in the reaction compared to the 2_2^+ state and a feeding transition $3_1^+ \rightarrow 2_2^+$ has been observed at 1156 keV, with a branching ratio of 30%. Hence, it is reasonable to assume that if not excluded from the analysis, the 3_1^+ state influences the lifetime measurement of the 2_2^+.

The influence of this state has been verified experimentally, by measuring the lifetime of 2_2^+ with a gate that includes the 3_1^+ state and other less intensely populated states close to the 3_1^+ state. The $2_2^+ \rightarrow 2_1^+$ transition has been used for this test. The spectrum has been obtained by requiring a time gate and an excitation energy gate between 3.7 and 5.5 MeV, hence including both the 2_2^+ and 3_1^+ states, as well as the state at 4.9 MeV. Then the histogram has been rebinned using the same criterion as in the previous 2_2^+ and 3_1^+ measurement, requiring at least 10 events per bin, obtaining bins of different width.

The first series of simulations used for the 2_2^+ measurement has been used to determine the systematic error coming from a feeder. The simulated histograms have been rebinned using the same binning as the experimental ones. The same range of integration has been chosen to be the same as the 2_2^+ analysis, between 2386 keV and 2440 keV, in order to take into account the whole range of sensitivity.

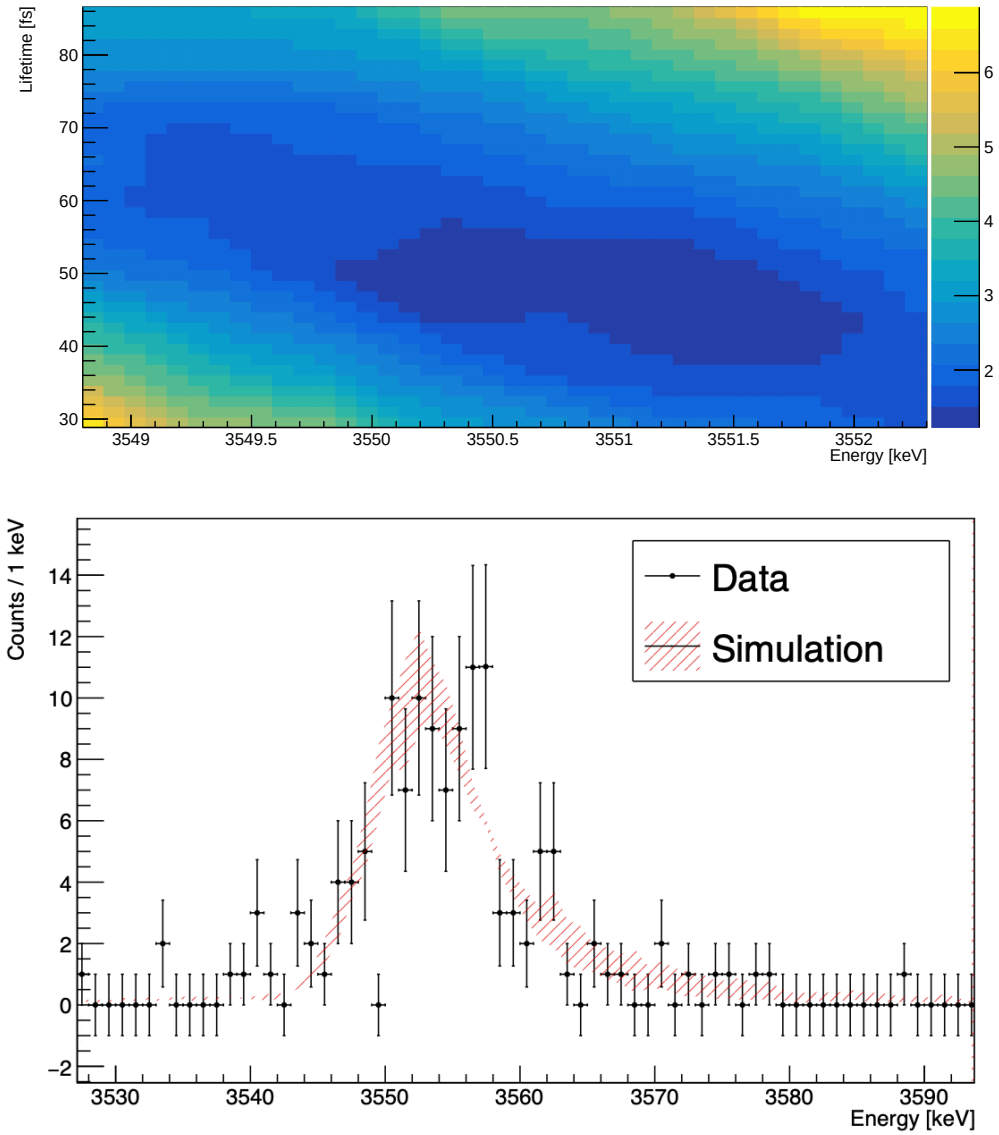

Figure 4.14.: (Top) χ^2 distribution depending on two parameters, the lifetime of the 3_1^+ and the energy of the $3_1^+ \to 2_1^+$ transition, for the tracked spectrum using the Neyman's χ^2. (Bottom) Comparison of the experimental histogram and the simulated one for lifetimes corresponding to confidence range given by the $\Delta\chi^2 = 1$ at the transition energy of the 3550.8 keV for Neyman's χ^2 and tracked spectrum.

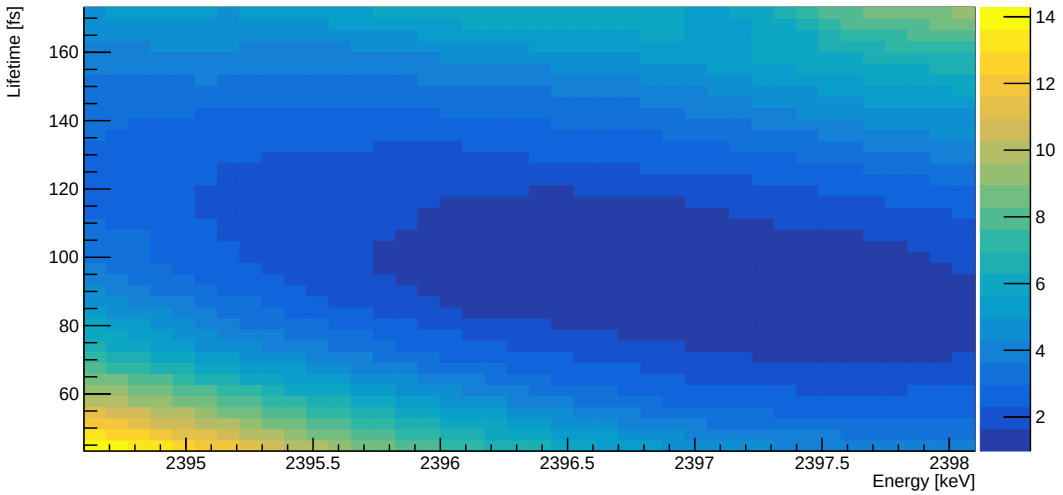

Figure 4.15.: Least-χ^2 results for the lifetime measurement of the 2_2^+ state (tracked spectrum, Neyman's χ^2) when the contribution of the $3_1^+ \rightarrow 2_2^+$ feeding transition is not under control. A longer lifetime is observed.

The experimental histograms have been compared to the simulated ones using the two statistics of the χ^2. The lifetime of the 2_2^+ obtained without removing the influence of the 3_1^+ feeder state is longer than the one obtained with an appropriate gate. In particular, the AddBack histogram suggests a lifetime of 100^{+30}_{-31} fs using the Pearson's χ^2 and 87^{+27}_{-30} fs using the Neyman's χ^2. The tracked histogram suggested a lifetime of 100^{+40}_{-23} fs and 87^{+38}_{-14} fs with the Pearson's and Neyman's χ^2 respectively.

This test confirms the influence of the feeder in the present experiment. In fact, without an appropriate gate to select only the event where the state of interest is directly populated, the systematic error leads to a lifetime of the 2_2^+ about 30% longer than the real one.

4.4. Summary

The results for the lifetime measurement of the 2_2^+ obtained using the different analysis approaches (least-χ^2, Likelihood, rebinning procedures) and different spectra (tracking, AddBack, low beta). The different values that resulted are summarized in Figure 4.16.

The different approaches lead to similar results, where the extracted values are always compatible within the error bars of the measurement. The two most noticeable differences are the result obtained from the tracked spectrum using the velocity after the energy loss and the result obtained using the maximum likelihood method for the tracked spectrum. This might be explained by the shift in energy of about 1 keV of the centroid (see Figure 4.7) for the tracked spectrum. Moreover, the tracked spectrum seems to present a more important tail compared to the AddBack spectrum. However, due to the low statistics and the large uncertainties on the events number, these differences are mostly absorbed in the rebinning procedure, which explains why these differences are not observed in the first results.

In the end, the tracked spectrum is considered more accurate with respect to the AddBack

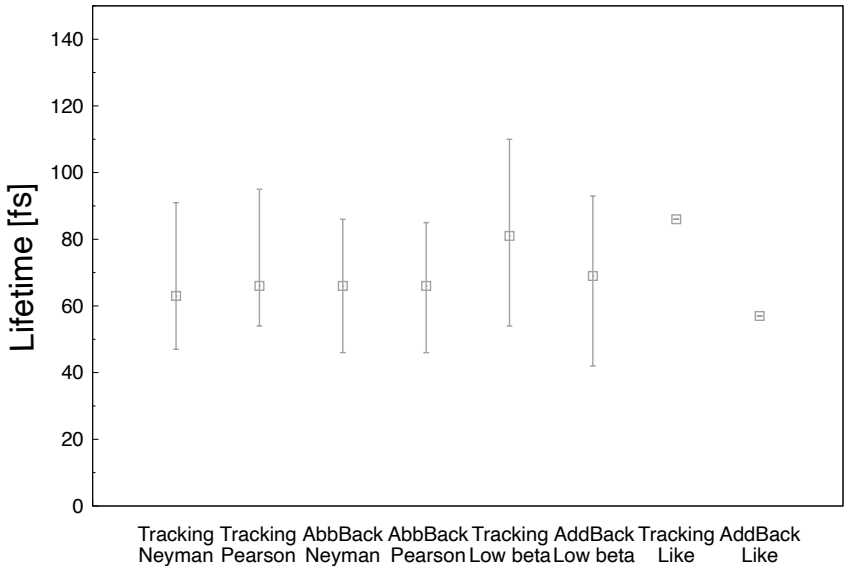

Figure 4.16.: Summary of the experimental results for the lifetime of the 2_2^+ state using different approaches. All the values result to be compatible within the error bars.

spectrum, since the simulation follows the same algorithm for sorting data and it is considered more accurate. The Neyman's χ^2 is considered preferable with respect to the Pearson's, since the experimental uncertainties are used instead of the simulated ones, that are normalized. Finally, the comparison obtained using the velocity at the reaction point is preferable to the one obtained with the velocity after the energy loss. For short lifetimes, as in the present case, the measurement using the velocity at the reaction point is less sensitive to the uncertainties related to the degrader thickness or the energy loss table employed for the analysis. Therefore, the final value is the one obtained using the tracked spectrum, Neyman's χ^2 and velocity at the reaction point, corresponding to $\tau_{2_2^+} = 63^{+28}_{-16}$ fs.

An analogous discourse can be made for the 3_1^+ state measurement. The values obtained using the different methods are consistent and compatible within the experimental error bars, as presented in Figure 4.17. The final value is $\tau_{3_1^+} = 55^{+16}_{-18}$ fs.

4.5. Estimation of the systematic error

The errors computed in the previous sections were only related to the statistic uncertainties, while systematic errors need to be computed independently.

As explained in detail in Chapter 3, the Monte Carlo simulation has been optimized in order to reduce the possibility of systematic errors. However, certain uncertainties could not be removed from the analysis. The influence of these possible sources of systematic errors is investigated in this section. In the present analysis, the following sources have been considered:

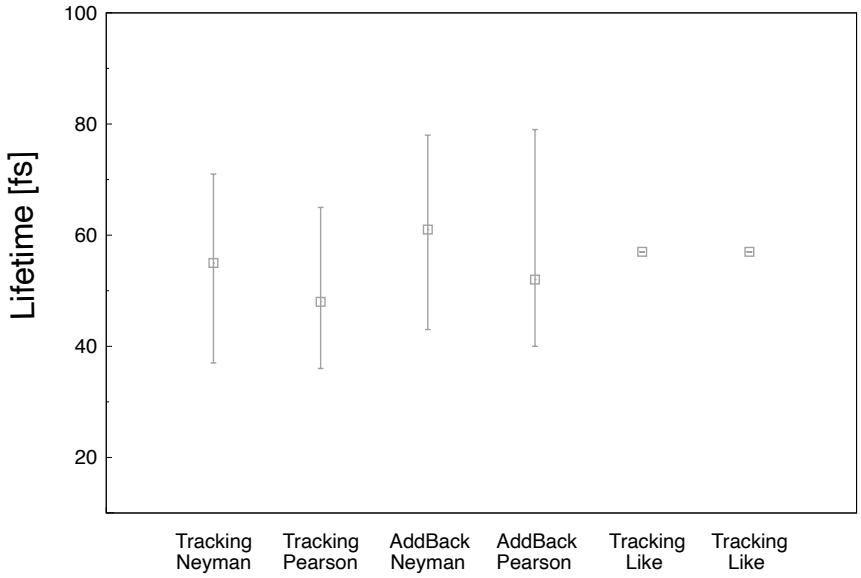

Figure 4.17.: Summary of the experimental results for the lifetime of the 3_1^+ state using different approaches. All the values result to be compatible within the error bars.

- thickness and density of the target;
- thickness of the degrader;
- background;
- number of events of the simulation.

4.5.1. Uncertainties on the target

As illustrated in Section 2.6, the thickness of the target was investigated using an electronic microscope. In the analysis, the presence of inhomogeneity in the surface has been observed, especially on the border of the target. Moreover, the density of a plastic material such as the deuterated polyethylene can variate depending on the procedure followed for the production of the target. The density of the material is important for the calculation of the energy loss of the ion in the target. Uncertainties on the thickness of the target and on the density of the material influence the uncertainties on the velocity used for the Doppler correction.

A variation of ± 0.05 mg/cm^2 on the target thickness has been considered, in order to include both thickness and density uncertainties. A series of simulations with a target of 0.25 mg/cm^2 and 0.35 mg/cm^2 were performed for the 2_2^+ state and compared to those with a 0.30 mg/cm^2-thick target. The energy of the transition used as input was 2396.6 keV, corresponding to the energy where the minimum χ^2 was found.

In the range of possible uncertainties on the real thickness of the target, no variation has been observed in the expected lifetime value, as shown in Figure 4.18. This is realistic considering that a variation in target thickness of 0.05 mg/cm^2 at the reaction energy for ^{20}O

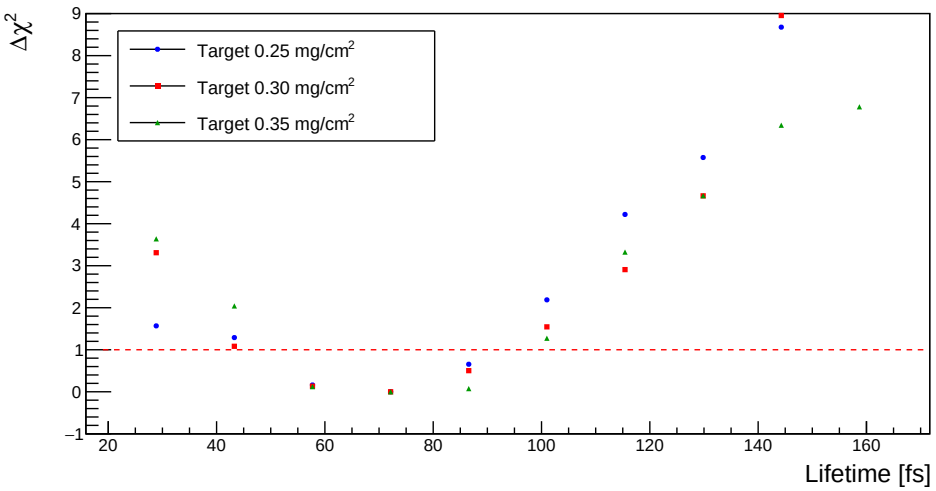

Figure 4.18.: $\Delta\chi^2$ for the different simulated target thickness.

corresponds to a $\Delta\beta = 0.4\%$, which do not affect significantly the measurement. This test proves the validity of using a thin target that, while leading to lower statistics, guaranteed a small spread in energy. However, the thickness of the target seems to slightly influence the error bars. A thinner target would lead to an increased error bar towards shorter values of lifetimes. On the other side, a thicker target would point in the opposite direction, with the error bar increased for longer lifetime values. These effects can be taken into account by adding a 5% of systematic error.

4.5.2. Uncertainties on the degrader

Similarly to the case of the target, the uncertainty on the real thickness of the degrader reflects on the uncertainty on the reconstructed velocity and therefore on the Doppler correction. It was not possible to measure the thickness of the degrader, that although was tested in Section 3.1.10 and 3.2.7.

A variation of ± 2 mg/cm^2 on the thickness has been considered. A series of simulations with a degrader of 22.4 mg/cm^2 and 26.4 mg/cm^2 were performed for the 2_2^+ state. The energy of the transition used as input was 2396.6 keV, corresponding to the energy where the minimum χ^2 was found.

No significant change in the expected value of the lifetime was observed for the different values of degrader thickness. This can be explained considering that the lifetime of the state is short enough to mainly decay in the degrader itself and changing the thickness of $\pm$ 2 mg/cm^2 is not sufficient to see any visible effect. However, bigger variations of the thickness would lead to visible effects in the shape of the 2_1^+ peak and are therefore excluded.

4.5.3. Uncertainties on the background

The optimization of the background has been discussed in Section 3.2.5. However, due to the low statistics and to the sensitivity of this measurement to events located where the tail of

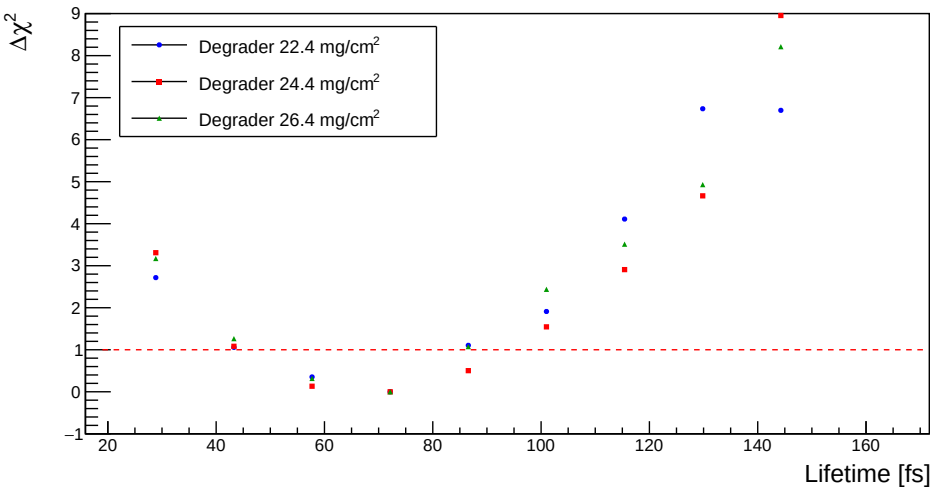

Figure 4.19.: $\Delta\chi^2$ for the different simulated target thickness.

the peak is expected, the effects of a change in the background are investigated.

The background is defined by three parameters:

- Number of background γ-ray events per good event;
- Slope of the background;
- Maximum energy of the background event.

The background is expected to follow a decay curve, where the slope is defined by the second parameter. This parameter can be adapted in order to investigate the sensitivity of the lifetime measurement to background events. Three possible values of the background slope have been tested: 2.0, 3.0 and 4.0. The first value corresponds to a flatter background but with a slightly higher number of counts, while the last one has a more pronounced slope and fewer events of background, especially in the tail.

As presented in Figure 4.20, the three different values do not affect significantly the background. However, a small change in the minimum can be observed, in particular to shorter lifetimes. For this reason, an additional 5% systematic error connected to the uncertainties on the background is considered.

4.5.4. Influence of the number of events

The simulations have been performed with a higher number of events with respect to the experimental peak and then have been normalized. This procedure reduces the statistical fluctuation and leads to a smoother lineshape. For the analysis, 10^6 events have been simulated, corresponding to a scaling factor of ~ 0.01. The lifetimes for 10^5 simulated events, corresponding to a scaling factor of $\sim 0.1\%$, and 10^4, scaling factor ~ 1, have been extracted.

No significant influence has been observed depending on the number of events, as shown in Figure 4.21. However, as expected, the simulations with 10^4 events show more fluctuations while the simulations with a larger number of events present a smoother profile in the χ^2. A scaling factor of at least 0.10 is necessary to guarantee a better accuracy of the estimation.

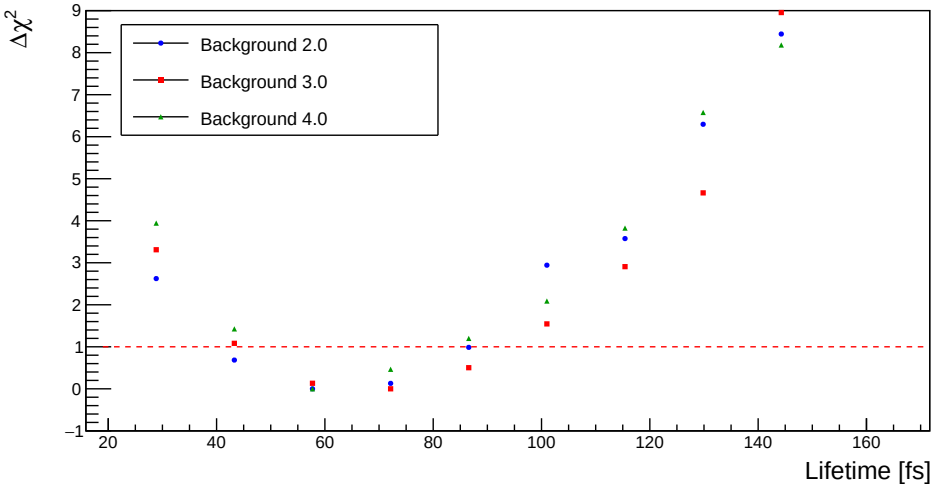

Figure 4.20.: $\Delta\chi^2$ for the different simulated background.

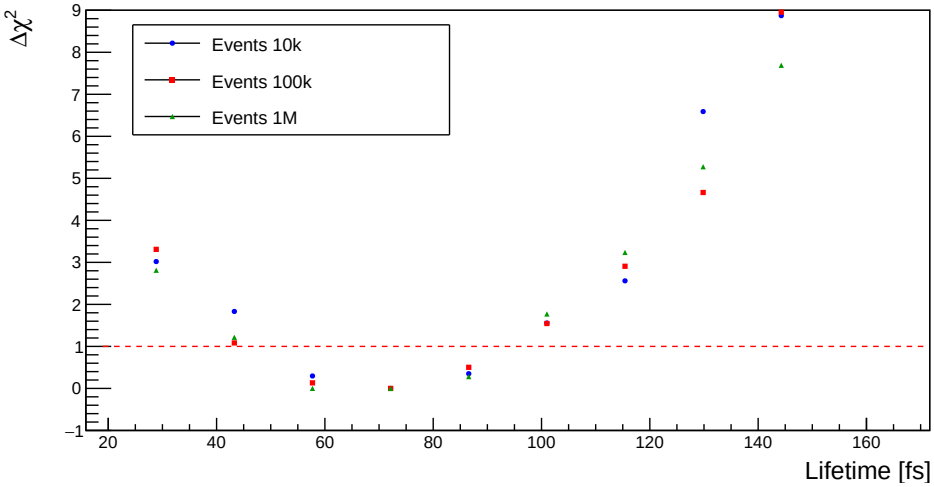

Figure 4.21.: $\Delta\chi^2$ for the different simulated number of events.

5 Theoretical results and interpretation

The structure of the ^{20}O nucleus has been investigated using different and complementary methods. First, *ab initio* calculations are introduced, with particular focus on methods that have been employed for studying electromagnetic properties in medium-mass nuclei. The results obtained from the previous calculations, employing Many-Body Perturbation theory and In-Medium Similarity Renormalization group method, are illustrated and compared to previous experimental results and to this work. An alternative *ab initio* method, already employed in the past for studying oxygen isotopes, is introduced. Then, the nucleus has been investigated using shell model calculations performed using the ANTOINE code. In this study, the predicted values of $B(E2)$ and $B(M1)$ are compared to the experimental results. Moreover, the influence of the orbital position on the excitation energies of the states and lifetime prediction has been studied.

5.1. Ab initio calculations

In the last decade, the capabilities of *ab initio* calculations have grown exponentially, allowing for the exploration of new regions of the nuclear chart. In fact, if *ab initio* calculations started from nuclei with few nucleons, they first extended the study of closed-shell nuclei, then to semi-magic nuclei and finally to open-shell nuclei, as presented in Figure 5.1. Since the 2000s, new techniques such as the Similarity Renormalization Group (SRG) [96] and the Effective Field Theory (EFT) [11] have been successfully employed to extend the calculations to new nuclei. Among the different methods, Many Body Perturbation Theory (MBPT) [97] calculations opened the study to the lower *sd*-shell nuclei. Other techniques that allowed a control on the level of truncation of the calculations, such as Self-Consistent Green's Function (SCGF) [98], In-Medium SRG (IMSRG) [99] and Couple Cluster (CC) [100] were also developed and successfully employed.

One of the most outstanding results of *ab initio* calculations was the possibility of benchmarking the same nuclear interactions using different methods such as RG, EFT and many-body methods. In addition, these different methods allow for a systematic framework that can be used to understand the reasons behind different results [101]. A perfect playground for testing these different calculations was provided by the oxygen isotopic chain. As already introduced in Chapter 1.1, different *ab initio* approaches employing NN+3N interactions cor-

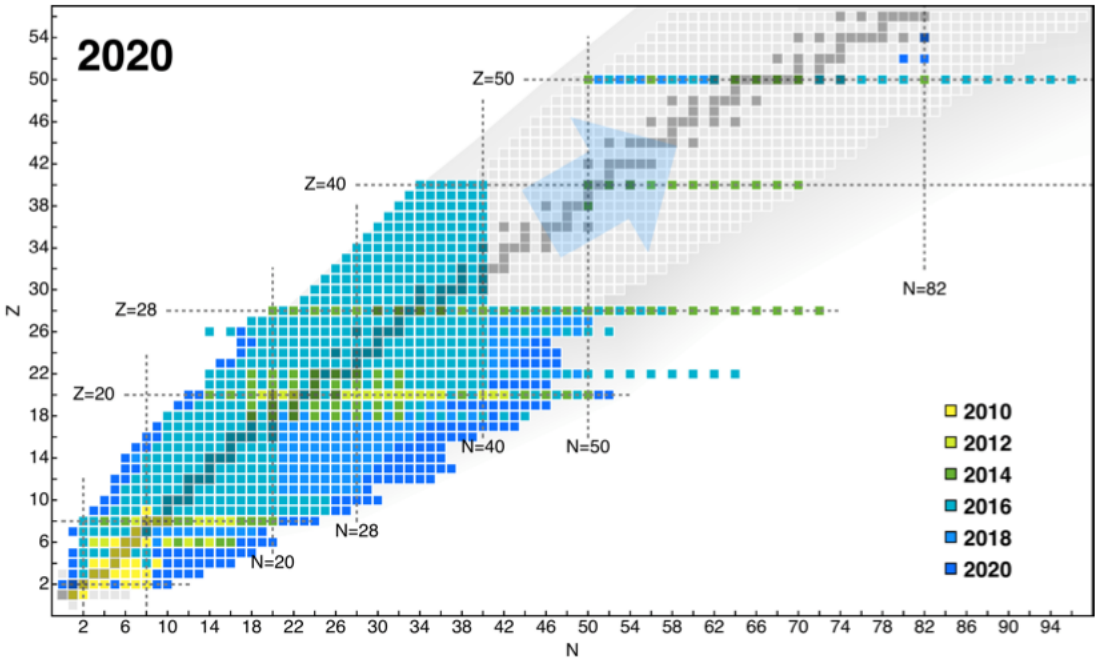

Figure 5.1.: Nuclei explored via different *ab initio* methods in the last decade. Figure taken from [101].

rectly reproduced the ground state energy of the neutron-rich oxygen nuclei. A similar study was extended to calcium isotopes, where the two-neutron separation energies, good indicators of shell- and subshell-closures, were calculated from $A = 36$ to $A = 62$ and compared to experimental values, witnessing a good agreement.

These results suggest the possibility of extending the use of *ab initio* calculations not only for heavier-mass nuclei or increasing number of valence nucleons, but also for more observables, such as nuclear radii and electromagnetic transitions. Predictions of nuclear radii were provided for calcium isotopes using Multi-Reference IMSRG [102] and compared to experimental results, observing an underestimation with respect to measurements. In the second half of the decade, the interest in calculating electromagnetic transitions using IMSRG, CC and SCGF methods has increased. In particular, the calculations for states dominated by few-nucleons configurations report a general agreement with experimental values, while the study for collective transitions is affected by the needed truncations.

In a recent work [103], some electromagnetic properties of ^{14}C, ^{22}O and ^{32}S such as the excitation energies of the first 2^+ state and the quadrupole transition matrix elements for the $2^+ \rightarrow 0^+$ transition were calculated. The 2^+ energies were well reproduced for the three nuclei. The E2 transition was well reproduced for ^{14}C, while it was underestimated of about 25-30% for ^{32}S. For ^{22}O, the predicted E2 transitions were only one third of what observed experimentally. This discrepancy could be solved by extending the VS-IMSRG to a *psd* valence space.

These results prove that it is possible to employ *ab initio* methods for making predictions of electromagnetic properties in medium-mass nuclei. Different *ab initio* methods have been employed for studying the ^{20}O nucleus and, in particular, its electromagnetic properties. MBPT and VS-IMSRG calculations were employed in Ref. [30] and compared to experimental

values such as the reduced transition probabilities of the $2_2^+ \rightarrow 2_1^+$ transition. The comparison between these calculations and the experimental results obtained from this work and from a previous experiment [30] are reported in the following section. New calculations are also introduced in the last section.

5.1.1. Comparison with previous works

The ^{20}O nucleus was previously studied in an experiment that took place in GANIL, aimed at measuring the lifetime of the 2_2^+ state. In this experiment, the nucleus was populated using a beam of ^{18}O at 126 MeV impinging on a 6.6 mg/cm^2-thick ^{181}Ta target. The projectile-like recoils, among which the ^{20}O, were detected by the VAMOS++ spectrometer at forward angles and the velocity of the recoils was measured around $\beta \sim 10\%$. The γ rays emitted by the de-exciting nuclei were detected using the AGATA array, that at the time counted 31 crystals positioned between 115°-117°, while the ring at 90° was covered by two large-volume $LaBr_3$ detectors and two clusters of the PARIS array [104]. In the reaction, both deep-inelastic and transfer channels were open, leading to high statistics.

The lifetime of the 2_2^+ was measured using the DSAM technique. In this experiment, the degrader corresponded to the target itself. The transition chosen for the measurement was the $2_2^+ \rightarrow 2_1^+$ transition measured at 2396 keV, with a measured branching ratio of 79(5)%. For the lineshape analysis, a series of Monte Carlo simulations were produced. The angular distributions were simulated based on those measured by VAMOS++ and the reaction kinematic, and a random probability of interaction in the whole target thickness was considered. Then, different lifetimes of the state and different transition energies were simulated. Finally, the simulations were analysed using the least-χ^2 method for three different angular ranges.

This analysis resulted in a lifetime of the 2_2^+ state of $\tau = 150^{+80}_{-30}$ fs for a transition energy of $E_\gamma = 2395(1)$ keV. The experimental result was then compared to two different theoretical calculations: the Many-Body Perturbation Theory (MBPT) [97] and the Virtual-Space In-Medium Similarity Renormalization Group (VS-IMSRG) [105].

MBPT calculations started from the ^{16}O core and add the $sdf_{7/2}p_{3/2}$ shells as valence space [11]. NN and normal order 3N interactions were used while residual 3N interactions were neglected. A good agreement with the experimental value from literature was found for the 2_1^+ state, where MBPT calculations predicted a lifetime of $\tau_{2_1^+} = 11.7$ ps, compared to the measured lifetime of 10.5(4) ps. The reduced transition probabilities of the $2_2^+ \rightarrow 2_1^+$ transition resulted to be $B(M1) = 0.015\mu_N^2$ and $B(E2) = 0.051e^2\text{fm}^4$. The 2_2^+ lifetime was calculated through the $2_2^+ \rightarrow 2_1^+$ transition considering the branching ratio 79(5)% and the transition energy 2395(1) keV measured in the experiment. The lifetime calculated resulted to be 217 fs.

A second series of MBPT calculations were performed neglecting the 3N forces to see the effect of this assumption on the lifetime of the states. While the 2_1^+ state was unaffected by the absence of 3N forces, the lifetime of the 2_2^+ state was found to be 60% longer with respect to the previous value. This result confirms that the 2_1^+ state, being based on a pure $(d_{5/2})^4$ configuration, is not sensitive to the relative position of the $s_{1/2}$ and $d_{3/2}$ orbitals, contrary to the 2_2^+.

The lifetime was also calculated using a second *ab initio* method: the VS-IMSRG. Similarly to the MBPT, for these calculations the NN+3N interactions (EM1.8/2.0 [106]) were

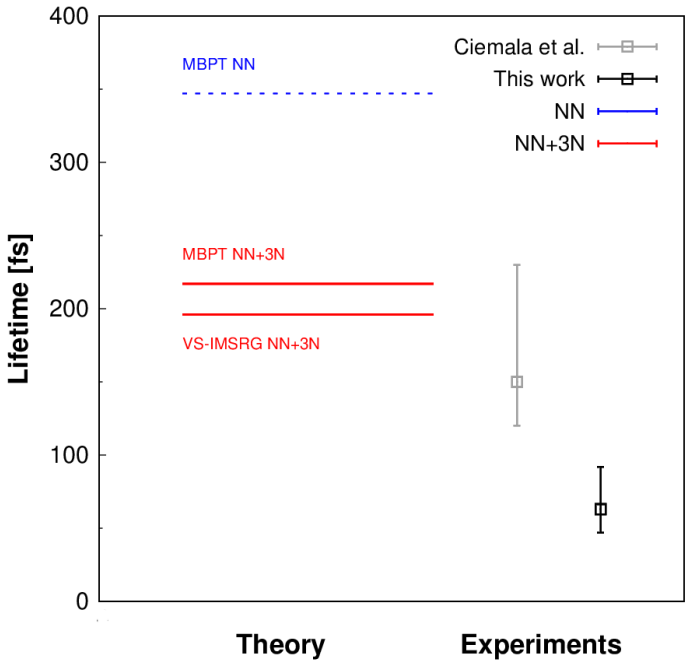

Figure 5.2.: MBPT and IMSRG calculations are compared to the result of Ciemała *et al.* and to the present work. Lifetime values for theoretical calculations and previous result are taken from Ref. [30].

employed. With respect to the previous method, in VS-IMSRG it is not possible to exclude the contribution of 3N forces, that are naturally included in this formalism. This method guarantees a good agreement of the theoretical energy levels to the experimental ones, where the 2_1^+ state is found at 1629 keV (1674 keV experimentally) and the 2_2^+ is found at 4051 keV (4071 keV), leading to a discrepancy of about 50 keV and 20 keV respectively, contrary to the MBPT that presented a discrepancy of about 400 keV (NN+3N) and 1 MeV (NN) with respect to the experimental results. The reduced transition probabilities of the $2_2^+ \rightarrow 2_1^+$ transition were $B(M1) = 0.0166\mu_N^2$ and $B(E2) = 0.0684e^2\text{fm}^4$. The lifetime of the 2_2^+ state obtained with this method resulted to be 197 fs.

Both the MBPT including 3N forces and the IMSRG agree with the previous experimental value within the experimental error bars.

5.1.2. This work

In the present experiment, the lifetime of the 2_2^+ state was measured at $\tau_{2_2^+} = 63^{+28}_{-16}$ fs, while the lifetime of the 3_1^+ state was measured at $\tau_{3_1^+} = 55^{+16}_{-19}$ fs. As presented in Figure 5.2, the present value is placed at a shorter lifetime with respect to the previous one and to theoretical calculations. The shorter lifetime points in the direction of the 3N forces, and seems to exclude completely the NN hypothesis.

The discrepancies with the lifetime measurement of the 2_2^+ of the previous experiment can be attributed to two main factors: the difference in the target thickness and the uncontrolled feeder. In the previous experiment, a thick target was employed both for the production of

the nucleus and the DSAM experiment. This thick target increased the number of events, guaranteeing large statistics. However, it led to a larger spread in the energy of the recoil, corresponding to a spread in velocity. Moreover, there was no control over where the reaction took place. In thin targets, one can assume the reaction to happen at the centre of the target or a uniform distribution of the cross section. However, this is not true for targets thicker than 1 mg/cm^2. This larger spread influences the lineshape of the peak that was employed for the lifetime measurement.

Moreover, in the previous experiment it was not possible to have control on the direct population of the states. A Q-value gate was required, which helped reduce the contamination coming from higher-lying states. However, with thick targets the entry point of the ^{20}O and the cross section of the different states might change depending on the energy of the beam at the reaction point, namely depending on where the reaction happened in the target. Despite the fact that the $3_1^+ \rightarrow 2_2^+$ transition was not observed, the possibility of feeding transitions that influence the measurement cannot be excluded. As shown in Section 4.3.1, an unobserved feeder would increases the lifetime measurement.

The discrepancies with previous calculations will be investigated by computing new *ab initio* calculations using a different technique, which is introduced in the following.

5.1.3. Self-Consistent Green's Function

The Self-Consistent Green's Functions (SCGF) theory is one of the *ab initio* many-body approaches developed in the last decade. Formalisms and computational algorithms have been developed to study both infinite and finite nuclear matter. Initially, this method was limited to double-magic nuclei. However, recently, calculations have been extended to semi-magic nuclei and open-shell nuclei using the Gorkov Green's Functions by breaking particle conservation symmetry and reformulating theories in terms of Hartree-Fock Bogolioubov reference states [98, 107, 108].

Let us define a N-body ground-state $\left|\Psi_0^N\right\rangle$ as the solution of equation [98]

$$H\left|\Psi_k^N\right\rangle = E_k^N\left|\Psi_k^N\right\rangle \tag{5.1}$$

for the lowest eigenvalue. In Green's Function theory, the one-body operator is defined as

$$i\mathcal{G}_{ab}^{N,N}(t,t') \equiv \left\langle\Psi_0^N\right|T\{a_a(t)a_b^\dagger(t')\}\left|\Psi_0^N\right\rangle, \tag{5.2}$$

where a_a is a set of basis of a one-body Hilbert space $\mathcal{H}$ and T is an operator that orders a and $a^\dagger$ depending on the time from larger and descending. By knowing $\mathcal{G}$, it is possible to calculate the expectation values of all one-body operators. It is also possible to define two-, three-, many-body propagators in an analogous way, in order to evaluate N-nucleon observables. The so-obtained equations form a system of N-coupled equations that can be solved.

The formalism has been extended to include $3N$ interactions and it has been tested by applying it to the oxygen isotopic chain [109]. In this work, the ground-state binding energy of the oxygen isotopes was calculated, resulting to be compatible to the experimental values with an accuracy of at least 5%. The single-particle energies of the $1d_{5/2}$, $2s_{1/2}$ and $1d_{3/2}$

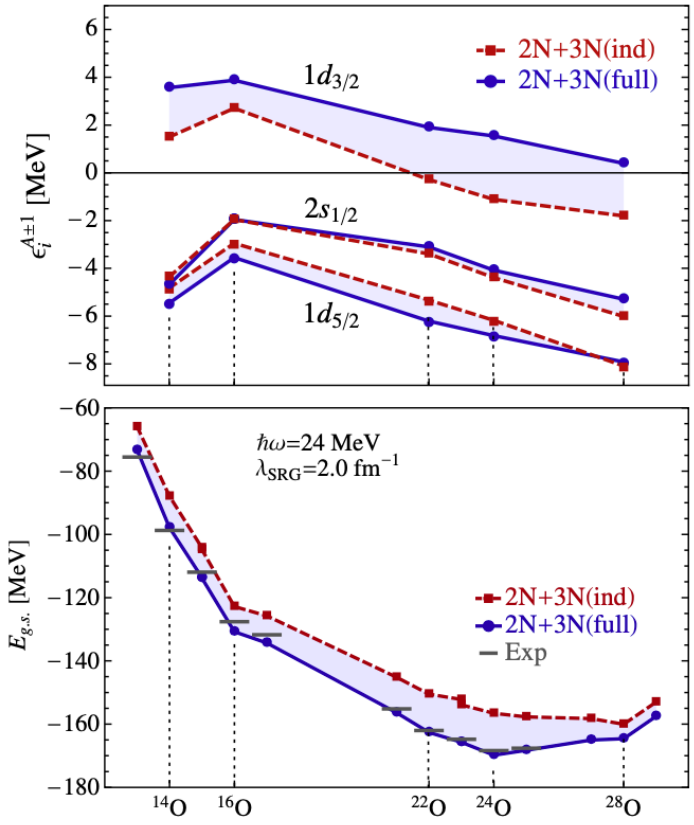

Figure 5.3.: (top) Single particle energies of the $1d_{5/2}$, $2s_{1/2}$ and $1d_{3/2}$ orbitals calculated using "induce" (red) or "fully" included (blue) 3N forces. (bottom) Ground state energy of the oxygen isotopes. The comparison to the experimental values for the calculations with "fully" included 3N forces (blue) has an accuracy of at least 5%. Figure taken from [109].

orbitals were also calculated: while calculations where $3N$ forces were obtained by evolving only original NN N^{3}LO Hamiltonian ("induced" 3N) fail in reproducing the dripline of the oxygen chain, those where the Hamiltonian was generated by evolving both initial NN and $3N$ forces together ("full") correctly predict the ^{24}O to be the last bound isotope, as shown in Figure 5.3.

This work [109] proved that the oxygen isotopic chain is suitable to be studied using the SCGF method in the Gorkov formalism. Calculations will be performed in order to extend the study to spectroscopic quantities such as branching ratio and transition probabilities.

5.2. Shell model calculations

The ^{20}O nucleus has been studied via shell model calculations, performed using the ANTOINE code [7, 110], employing the USDB interaction [29]. Three orbitals have been considered outside of the *sp*-core: the $1d_{5/2}$, the $2s_{1/2}$ and the $1d_{3/2}$.

Five states were explored in this study: the ground state, the 2_1^+ at 1.674 MeV, the 4_1^+ at

3.572 MeV, the 2_2^+ at 4.071 MeV and the 3_1^+ at 5.225 MeV. The USDB interaction foresees the SPE of the $d_{5/2}$ to be at -3.9257 MeV, the $s_{1/2}$ at -3.2079 MeV while the $d_{3/2}$ is at 2.1117 MeV. These values correspond to the SPEs of the ^{16}O core.

With these SPEs, the predicted energy of the excited states is 1.775 MeV for the 2_1^+ state, 3.683 MeV for the 4_1^+ state, 4.218 MeV for the 2_2^+ state and 5.428 MeV for the 3_1^+ state. The discrepancy between the measured and predicted excitation energy increases from 100 keV for the 2_1^+ to 200 keV for the 3_1^+ state.

The states can be divided into two categories based on their predicted expectancy: those mainly based on a pure $(d_{5/2})^4$ and those based on mixed $(d_{5/2})^3(s_{1/2})^1$. According to the present calculations, the 0_1^+ state is mainly based on a $(d_{5/2})^4$ configuration (75%) and only partially on a $(d_{5/2})^2(s_{1/2})^2$ (15%). The 2_1^+ state is predicted to be mainly based on the $(d_{5/2})^4$ configuration (63%) and on the $(d_{5/2})^3(s_{1/2})^1$ (23%). The 4_1^+ is the one that present the highest percentage of pure configuration $(d_{5/2})$ (87%) and only on a minor percentage based on a $(d_{5/2})^2(s_{1/2})^2$ (7%). The non-yrast states, instead, are predicted to have a different configuration. The 2_2^+ state is expected to be mainly based on a $(d_{5/2})^3(s_{1/2})^1$ configuration (76%) and in smaller percentages on $(d_{5/2})^2(s_{1/2})^2$ (10%) and $(d_{5/2})^4$ (8%). Finally the 3_1^+ state is mainly based on the $(d_{5/2})^3(s_{1/2})^1$ configuration (87%) and in small percentage on a $(d_{5/2})^2(s_{1/2})^1(d_{3/2})^1$ configuration.

The calculated $B(E2; 2_2^+ \rightarrow 0_1^+) \uparrow$ was 1.20 e^2fm^4. The $2_2^+ \rightarrow 0_1^+$ transition was first chosen because of its pure $E2$ nature, while the $2_2^+ \rightarrow 2_1^+$ transition is composed of a mix between $E2$ and $M1$. Considering a branching ratio of 12(1)% measured in the experiment for the 4071-keV transition and an internal conversion coefficient of $\alpha = 0.001196(17)$ calculated using BrICC [111], the reduced transition probability of the $2_2^+ \rightarrow 0_1^+$ transition is $1.4^{+0.5}_{-0.4} e^2\text{fm}^4$. This value of the $B(E2)$ is compatible with the value predicted by shell model calculations within one sigma.

For the $2_2^+ \rightarrow 2_1^+$, the allowed multipolarities are M1, E2, M3 and E4. The transition is expected to be based on a mixing between M1 and E2. Theoretical calculations predict a $B(E2) = 0.00044\, e^2\text{fm}^4$ and a $B(M1) = 0.022\, \mu_N^2$. In order to calculate the experimental reduced transition probabilities for a mixed transition, the mixing ratio is needed. However, due to low statistics, it was not possible to calculate the experimental mixing ratio. It is however possible to calculate it from shell model calculations, using Equation 1.18, and it results to be $\delta = -0.0029$. Under the assumption of using the theoretical mixing ratio, knowing the measured lifetime of the state, the measured branching ratio (see Section 4.1.1), the internal conversion coefficient ($\alpha = 0.000509(8)$, obtained from [111]) and the energy of the transition, one can evaluate the experimental $B(E2)$ and $B(M1)$ reduced transition probabilities. The expected $B(E2; 2_2^+ \rightarrow 2_1^+)$ has been calculated as

$$B(E2; 2_2^+ \rightarrow 2_1^+) = \frac{BR_\gamma}{1.223 \times 10^9 E_\gamma^5 (1+\alpha)\tau} \frac{\delta^2}{1+\delta^2} \tag{5.3}$$

where E_γ in MeV in the experimental energy and the $B(E2) = 1.22^{+0.41}_{-0.38} \times 10^{-3} e^2\text{fm}^4$. Considering $\alpha = 0.000407(6)$, the $B(M1; 2_2^+ \rightarrow 2_1^+)$ has been calculated as

$$B(M1; 2_2^+ \rightarrow 2_1^+) = \frac{BR_\gamma}{1.779 \times 10^{13} E_\gamma^3 (1+\alpha)\tau} \frac{1}{1+\delta^2} \tag{5.4}$$

$J_i \to J_f$	δ	σL	$B(\sigma L)_{\text{exp}}$	$B(\sigma L)_{\text{theo}}$
$2_2^+ \to 0_1^+$		$E2$	$1.4^{+0.5}_{-0.4}$	1.2
$2_2^+ \to 2_1^+$	-0.0029	$E2$	$1.22^{+0.41}_{-0.38} \times 10^{-3}$	0.44×10^{-3}
$2_2^+ \to 2_1^+$	-0.0029	$M1$	$0.056^{+0.019}_{-0.017}$	0.022
$3_1^+ \to 2_1^+$	-0.154	$E2$	$0.424^{+0.206}_{-0.096}$	0.89
$3_1^+ \to 2_1^+$	-0.154	$M1$	$0.0155^{+0.0075}_{-0.0035}$	0.033
$3_1^+ \to 2_2^+$	-0.0222	$E2$	$1.06^{+0.52}_{-0.24}$	1.96
$3_1^+ \to 2_2^+$	-0.0222	$M1$	$0.198^{+0.097}_{-0.044}$	0.37

Table 5.1.: Comparison between experimental and theoretical $B(\sigma L)$. The values of δ are extracted from theoretical calculations. All the $B(E2)$ are reported in $e^2\text{fm}^4$, while all the $B(M1)$ are reported in μ_N^2.

and resulted to be $B(M1) = 0.056^{+0.019}_{-0.017}\mu_N^2$.

Similar calculations have been performed for the 3_1^+ state. The two γ-ray transitions from this state decay to the 2_2^+ with a branching of 30(1)% and to the 2_1^+ with a branching of 70(1)%. In both cases, the transitions are expected to be a mixing of E2 and M1 multipolarities. Shell model calculations predicted a $B(E2) = 0.89e^2\text{fm}^4$ and $B(M1) = 0.033\mu_N^2$ for the $3_1^+ \to 2_1^+$ transition at 3556 keV, corresponding to a $\delta = -0.154$, calculated with equation (1.18). The experimental $B(E2)$ has been calculated using Equation (5.3), with $\alpha = 0.001013(15)$, and resulted to be $B(E2) = 0.424^{+0.206}_{-0.096}e^2\text{fm}^4$. The experimental $B(M1)$ has been calculated using Equation (5.4), with $\alpha = 0.000895(13)$, and resulted to be $B(M1) = 0.0155^{+0.0075}_{-0.0035}\mu^2$.

The same calculations have been performed for the $3_1^+ \to 2_2^+$ transition at 1156 keV. Shell model calculations predict $B(E2) = 1.96e^2\text{fm}^2$ and $B(M1) = 0.37\mu_N^2$, which give a mixing ratio $\delta = -0.0222$. Considering $\alpha = 0.0001127(17)$, the experimental $B(E2) = 1.06^{+0.52}_{-0.24}e^2\text{fm}^4$, while with $\alpha = 8.1(1) \times 10^{-5}$, $B(M1) = 0.198^{+0.097}_{-0.044}\mu_N^2$. All the results are summarized in Table 5.1.

The $B(E2; 2_2^+ \to 0_1^+)$ obtained from shell model calculations is in agreement with the one calculated from the experimental lifetime. This $B(E2)$ corresponds to $0.43^{+0.16}_{-0.12}W.u.$: such a low transition probability reinforce the hypothesis of a single-particle state nature of the 2_2^+, as already suggested by previous studies (see Chapter 1).

The theoretical $B(E2; 2_2^+ \to 2_1^+)$ is about one third of the experimental result. Similarly, the theoretical $B(M1; 2_2^+ \to 2_1^+)$ results to be half of the expected value. Both theoretical and experimental calculations predict a strongly suppressed $B(E2)$, especially if compared to the results obtained with *ab initio* calculations (see Section 5.1.1). However, it was not possible to compare the theoretical mixing ratio to the experimental one and the $B(E2)$ are strongly affected by the value of δ^2.

An opposite trend is observed for the $B(\sigma L)$ of the transitions from the 3_1^+ state. The theoretical calculations predict transition probabilities systematically higher than what expected experimentally, suggesting a shorter lifetime of the state. In particular, all the $B(\sigma L)$ result to be twice the experimental value. Similarly to the previous case, the mixing ratio strongly influences the result.

In general, the results obtained from theoretical calculations agree on the order of mag-

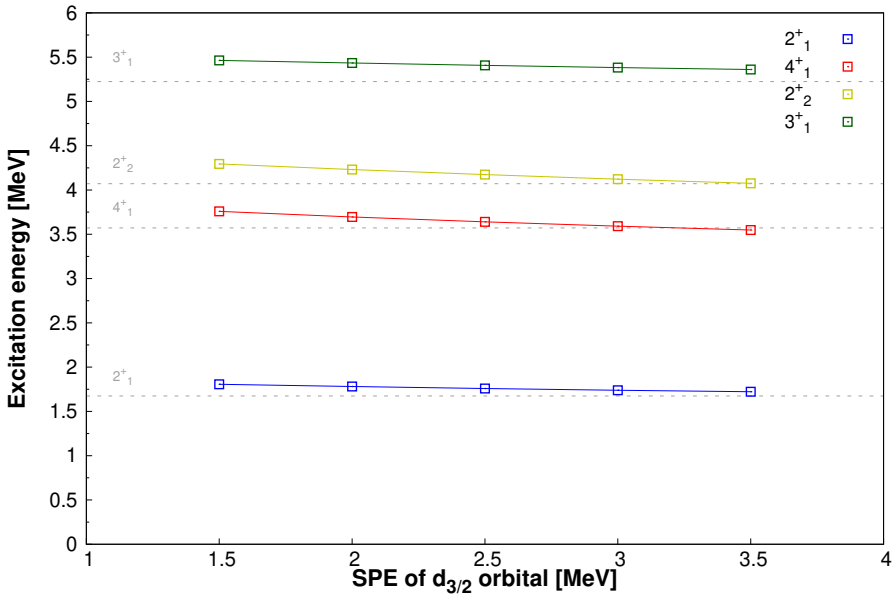

Figure 5.4.: Excitation energy of the ^{20}O state as a function of the SPE of the $d_{3/2}$ orbital. The experimental values are also reported in the graphic (grey dashed lines).

nitude of the reduced transition probabilities and minor discrepancies are observed. An experimental measurement of the mixing ratio for the $2_2^+ \rightarrow 2_1^+$, $3_1^+ \rightarrow 2_1^+$ and $3_1^+ \rightarrow 2_2^+$ transitions would help clarifying the situation.

5.2.1. Influence of the orbital position

Shell model calculations have been performed to investigate the influence of the SPE of $s_{1/2}$ and $d_{3/2}$ orbitals on the excitation energy and on the reduced transition probabilities. As explained in the work of Otsuka *et al.* [16], the inclusion of 3N forces influences the SPE of the orbitals. The shell model calculations performed with ANTOINE are effective, therefore all the effect of NN/3N forces are hidden in the SPEs. By changing the SPEs, it is possible to have an idea of what kind of dependence one can expect from the inclusion of 3N forces in calculations where they can be included explicitly.

A first series of calculations was performed by changing the $d_{3/2}$ SPE in a range from 1.5 to 3.5 MeV with a step of 0.5 MeV. In this range, the $d_{3/2}$ orbital remains at positive SPE values. The raising of the orbital has the effect of lowering the excitation energy of the considered states, reducing the discrepancy with the experimental results. The results for this test are presented in Figure 5.4. The experimental values for the excitation energy of the level are also reported.

The $B(E2; 2_2^+ \rightarrow 0_1^+)$ value increases, going from 1.18 $e^2\text{fm}^4$ when the SPE of the $d_{3/2}$ orbital is 1.5 MeV to 1.23 $e^2\text{fm}^4$ at 3.5 MeV, as presented in Figure 5.5. All the theoretical values result to be compatible to the experimental one.

A second series of calculations was performed by changing the $s_{1/2}$ SPE in a range from -3.5 to -1.5 MeV with a step of 0.5 MeV. Within this range, the $s_{1/2}$ remains between the $d_{5/2}$ and the $d_{3/2}$ orbitals, without crossing them. The lowering of the $s_{1/2}$ orbital to values

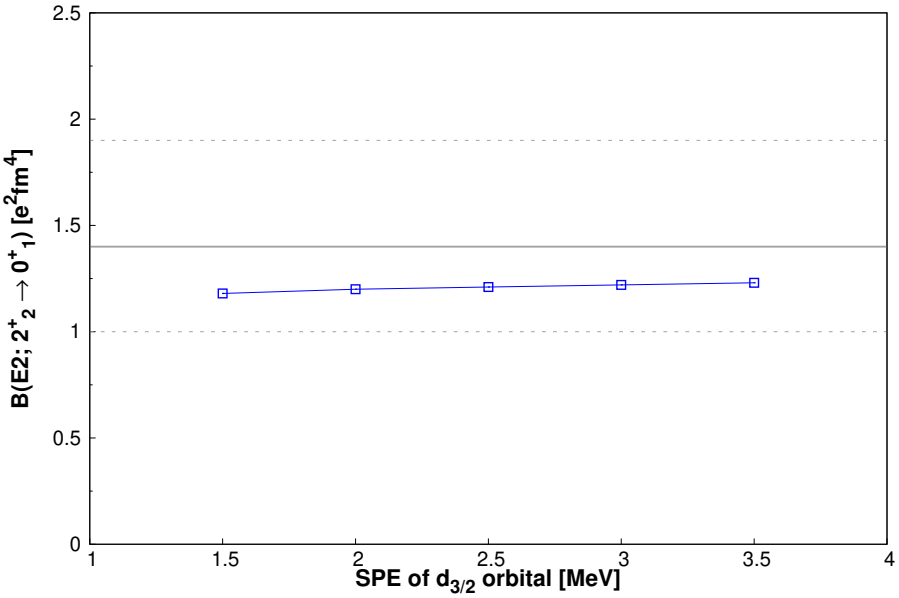

Figure 5.5.: Reduced transition probabilities of the $2_2^+ \rightarrow 0_1^+$ transition as a function of the SPE of the $d_{3/2}$ orbital. The experimental value is also reported in the graphic (grey continuous line) with the corresponding uncertainties (grey dashed lines).

further from the $d_{3/2}$ orbital and closer to the $d_{5/2}$ orbital has the effect of lowering the excitation energy of the 2_2^+ and 3_1^+ states, reducing the discrepancy with the experimental values. The 4_1^+ state, on the other side, present an opposite trend, where the excitation energy is lowered by the raising of the $s_{1/2}$ orbital but with a weaker dependence. Finally, the 2_1^+ state is not affected by the changing in the $s_{1/2}$ orbital SPE. The results for this test are presented in Figure 5.6 and the experimental values are reported as a reference.

Similarly to the previous case, the $B(E2; 2_2^+ \rightarrow 0_1^+)$ value increases with the raising of the $s_{1/2}$ orbital, going from $1.12e^2\text{fm}^4$ when the SPE is -3.5 MeV to $1.49e^2\text{fm}^4$ at -1.5 MeV. The trend presents a stronger dependence from the SPE, as shown in Figure 5.7; however, due to the large uncertainties of the measurement, the values remain compatible with the measured $B(E2)$.

The large variation of SPE in ANTOINE calculations do not change significantly the expected transition probabilities. The $B(E2; 2_2^+ \rightarrow 0_1^+)$ seems to be more sensitive to the position of the $s_{1/2}$ orbital, where a variation of 2 MeV to higher energy leads to a larger $B(E2)$ of about 25%. The more the gap between the $s_{1/2}$ and the $d_{5/2}$ increases, the shorter the expected lifetime is. A similar pattern is observed for the variation of the gap between $d_{5/2}$ and $d_{3/2}$. However, the position of the $d_{3/2}$ orbital seems to be less influential, where a change of few percentage is observed for the same ΔE.

The excitation energies of the states do not strongly depend on the SPE of the $d_{3/2}$ orbital: a slight decrease is observed for all the states with the increasing energy of the SPE of the orbital. Instead, a significant variation in the excitation energy of the 2_2^+ and 3_1^+ states is observed when changing the SPE of the $s_{1/2}$ orbital, absent in the 2_1^+ and 4_1^+ states. This is coherent with the interpretation that predict the lower states to be dominated by a $(d_{5/2})^4$ configuration.

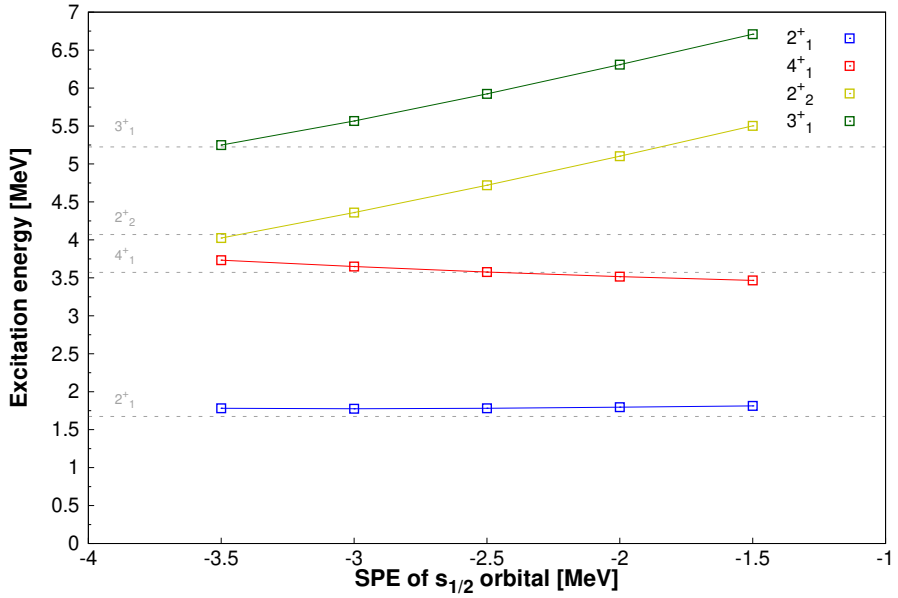

Figure 5.6.: Excitation energy of the ^{20}O state as a function of the SPE of the $s_{1/2}$ orbital. The experimental values are also reported in the graphic (grey dashed lines).

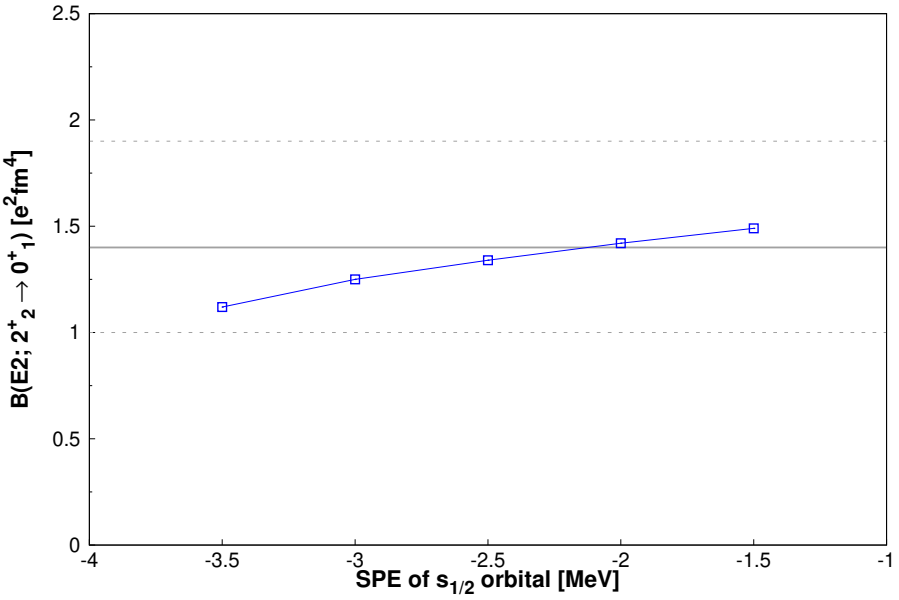

Figure 5.7.: Reduced transition probabilities of the $2^+_2 \rightarrow 0^+_1$ transition as a function of the SPE of the $s_{1/2}$ orbital. The experimental value is also reported in the graphic (grey continuous line) with the corresponding uncertainties (grey dashed lines).

These results stress again the necessity of new calculations using a framework that is sensitive to the inclusion of 3N forces, such as those presented in Section 5.1.

6 Conclusions and future perspective

The quantification of three-body forces contribution in the neutron-rich side of light nuclei is still a challenging study. The difficulty of both shell-model and *ab initio* calculations increases when three-body forces are included and they become unfeasible for higher-mass nuclei. Precise experimental information can put useful constraints in order to benchmark the calculations. In this sense, spectroscopic quantities have proven to be particularly sensitive to the contribution of three-body forces and hence constitute good observables to be studied.

In the context of the oxygen isotopic chain, the experimental difficulties in reaching the more exotic isotopes have limited the study to the lifetime measurement of the first excited states, such as the ^{20}O and the ^{22}O [112] or only bulk properties, as in the case of ^{24}O [14, 15]. By being closer to the stability valley, ^{20}O has been accessible for more in-depth analysis of the lifetime of higher states and in particular non-yrast states, such as in the work of Ciemała *et al.* [30] and in the present work.

The AGATA and MUGAST arrays constitute the state-of-the-art of γ-rays and light charged-particle detectors respectively. Thanks to the great angular and energy resolution, they allow for a good reconstruction of the energy and of the impinging angle. In the present work, the MUGAST array has been used for the measurement of the protons emitted in the reaction. From the energy and angular information of the target-like partner, it was possible to reconstruct the velocity vector of the beam-like recoil, namely the ^{20}O nucleus. The event-by-event Doppler correction can increase significantly the energy resolution with respect to the one obtained using the average velocity of the recoils, and the Full-Width Half Maximum of the peak emitted in-flight resulted to be comparable to the intrinsic resolution of the germanium detectors.

Thanks to this precision, using the dataset with the CD_2-only target, it was possible to study the spectroscopy of the nucleus, improve the precision on the energy of the transitions, identify new transitions and measure the branching ratios of the transitions decaying from the 2_1^+ and 3_1^+ states.

The experimental apparatus and the Monte Carlo simulation have been optimized in order to reduce the source of systematic errors. This procedure allowed for a thorough study of the input parameters and their influences on the simulation. Aspect such as the velocity distribution, the resolution of the detectors, the smearing of the recoils and the γ rays were investigated.

The lifetimes of the 2_2^+ and 3_1^+ states were measured using the Doppler Shift Attenuation

Method. The experimental lineshapes of the γ-ray peaks were compared to the simulated one using the least-χ^2 and the maximum likelihood method. The influence of different analysis methods, such as the binning of the histograms or the different Doppler correction methods employed, were tested. The lifetimes of the 2_2^+ and 3_1^+ states were measured and the statistical and systematic errors evaluated.

Finally, the experimental results were compared to Many Body Perturbation Theory and In-Medium Similarity Renormalization Group calculations and to the previous measurement. Moreover, new *ab initio* calculations are introduced. Knowing the lifetime of the states, the reduced transition probabilities were calculated and compared to shell model calculations performed using the USDB interaction and the ANTOINE code. The influence of the orbital position is also investigated.

This experiment has proven that (d, p) reactions, by guaranteeing a strong control on the population of the excited states, are useful tools for studying precise quantities such as lifetimes using the Doppler Shift Attenuation Method. For this reason, the collaboration of the experiment analysed in the present work proposed two similar experiments devoted to measuring the lifetimes of excited states in ^{16}C and ^{24}Ne.

6.1. Study of ^{16}C

Similarly to the oxygen isotopic chain, the carbon chain presents interesting aspects. The ^{16}C nucleus in particular gained much interest when an anomalous reduction of the $B(E2; 2_1^+ \rightarrow 0_{\text{g.s.}}^+) = 0.63e^2\text{fm}^4$ (corresponding to $\tau = 77$ ps) was observed by Imai *et al.* [113], if compared to the one obtained for ^{14}C, indicating a suppressed proton collectivity. The $B(E2)$ was calculated from a lifetime measurement obtained using the Recoil Shadow Method (RSM). However, due to the discrepancy with theory, the lifetime of the 2_1^+ state was re-measured and it resulted to be $\tau = 18.3 \pm 1.4 \pm 4.8$ ps, about four times shorter [114]. The same lifetime was re-measured again in two Recoil Distance Doppler Shift experiments by Wiedeking *et al.* [115] and Petri *et al.* [116] and resulted to be $\tau = 11.7(20)$ ps and $\tau = 11.4(9)$ ps, respectively, in agreement with $p-sd$ shell model and *ab-initio* No-Core Shell-Model (NCSM) calculations [21].

In the second paper, three additional transitions were observed coming from 2_2^+, $3_1^{(+)}$ and 4_1^+ states, decaying to the 2_1^+ state. In the plunger dataset, the $2_2^+ \rightarrow 2_1^+$ transition at 2217 keV presented only an in-flight component, suggesting a lifetime of the 2_2^+ more suitable for DSAM measurements and only an upper limit of 4 ps to the lifetime of the 2_2^+ was assigned. The $3_1^{(+)} \rightarrow 2_1^+$ and $4_1^+ \rightarrow 2_1^+$ transitions at 2317 and 2374 keV respectively did not have enough statistics to draw a conclusion, but previous measurements [115] suggest a lifetime shorter than 4 ps. Moreover, no $2_2^+ \rightarrow 0_1^+$ transition was observed in this experiment, setting a limit to the branching ratio to $BR(2_2^+ \rightarrow 2_1^+) > 91.2\%$ and $BR(2_2^+ \rightarrow 0_1^+) < 8.8\%$ at 3σ confidence level.

These results were compared to different calculations [21]: No-Core Shell Model (NCSM) employing the two-body effective CDB2k interaction and SRG-transformed NN and chiral NN+$3N$ interactions. It was observed that the strong suppression of the $2_2^+ \rightarrow 0_1^+$ transitions was well represented by the calculations that included the $3N$ contribution. Moreover, the $3_1^+ \rightarrow 2_1^+$ transition appeared to be particularly sensitive to the inclusion of $3N$ forces. The comparison between the experimental results and the theoretical calculations underlined the

sensitivity of electromagnetic observables in ^{16}C to the details of the nuclear Hamiltonian.

Recently, another experiment aimed at measuring the lifetime of the 2_2^+ state in ^{16}C via DSAM was performed in GANIL [30]. However, due to low statistics on the transition, only an upper limit of 180 fs was assigned. A strong dependence of the lifetime on the exact energy of the $2_2^+ \rightarrow 2_1^+$ transition was observed.

Acknowledging the great interest around the electromagnetic properties of this nucleus, we proposed an experiment to measure the lifetime of higher-lying states in ^{16}C at the Argonne National Laboratories (ANL) using GRETINA [55] coupled to ORRUBA [117] (GODDESS configuration [118]). The reaction was chosen based on a previous experiment performed at ANL [119] where the ^{16}C was populated using a (d, p) reaction with a beam of ^{15}C at 8.2 MeV/A, impinging on a CD_2 target. The protons emitted in the reaction were detected using the Helical Orbit Spectrometer (HELIOS) [120], designed to study reactions in inverse kinematics. In the proposed experiment the same beam at the same energy was employed, impinging on a 0.3 μg/cm^2-CD_2 target deposited on a 20 mg/cm^2-Au degrader.

The experiment was submitted to the ANL Program Advisory Committee (PAC) in March 2021 and was performed in July 2021. The analysis of this experiment is still in the preliminary phase and will be carried out within the next year. However, the preliminary results obtained from the online analysis of the experiment seem promising and the lineshape of the $2_2^+ \rightarrow 2_1^+$ transitions suggests that the lifetime of the 2_2^+ state is in the range of sensitivity. More details on the preparation and optimization of the experiment are reported in the Appendix C.

6.2. Study of ^{24}Ne

The same collaboration aimed at continuing this study by measuring the lifetimes of excited states in ^{24}Ne. This nucleus presents a level scheme similar to the one observed for ^{16}C and ^{20}O, as presented in Figure 6.1.

The ^{24}Ne was previously studied in an experiment [121] where the ^{24}Ne was populated using a ^{22}Ne(t, p) reaction using a triton beam at 2.9 MeV provided by the Lockheed 3.0-MV Van de Graaff accelerator, impinging on a solid ^{22}Ne film frozen on a gold backing. The γ rays emitted by the nucleus were detected using Ge(Li) detectors, after requiring the coincidence with the protons in order to select the channel of interest. In this experiment, the lifetimes of the 2_1^+ and 2_2^+ states were measured using the DSAM. The lifetime of the 2_1^+ resulted to be 0.89(30) ps, in agreement with the theoretical calculations [122] that predicted a lifetime of 0.71 ps. The lifetime of the 2_2^+ was outside of the range of sensitivity, with a $F(\tau) = 0.902$, and only an upper limit of $\tau < 180$ fs was assigned.

HPGe detectors present a better energy resolution with respect to Ge(Li) detectors and can achieve better precision in lifetime measurements using the DSAM. Moreover, by adapting the thickness of the degrader, it is possible to push the sensitivity of the measurement to shorter lifetimes. For these reasons, an experiment aimed at measuring the lifetime of the 2_2^+ state and possibly re-measuring the lifetime of the 2_1^+ state was proposed in GANIL.

The nucleus will be populated in a (d, p) reaction using a ^{23}Ne radioactive beam at 8 MeV/A provided by the SPIRAL1 complex, impinging on a CD_2 target evaporated on a 10 mg/cm^2-thick Au degrader. This reaction has been already measured in an experiment with SHARC-TIGRESS [123], where the absolute cross sections and spectroscopic factors were

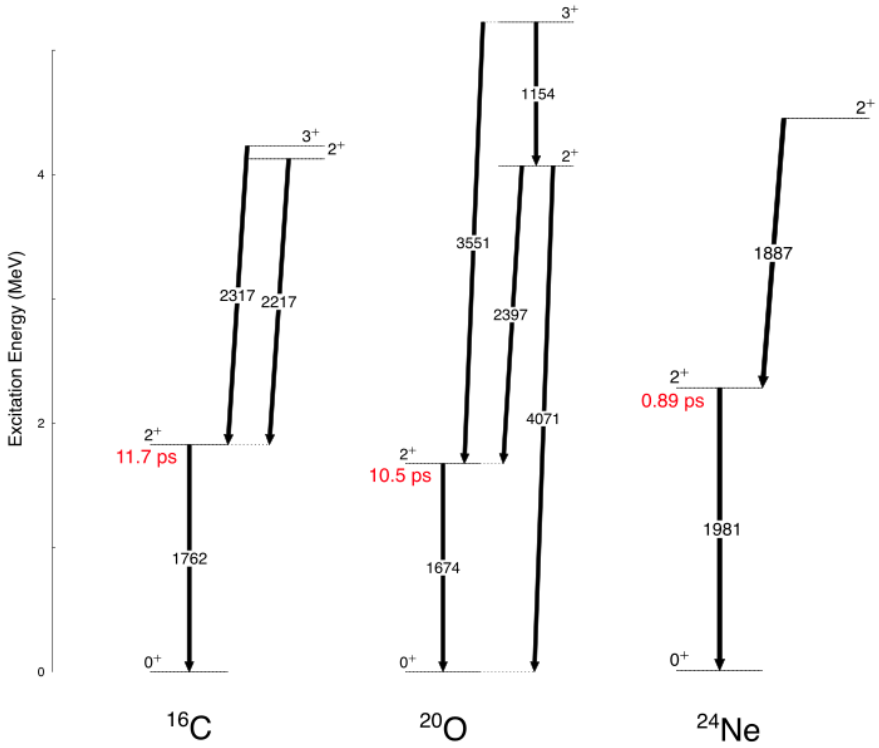

Figure 6.1.: Experimental level scheme of the ^{16}C, ^{20}O and ^{24}Ne. In red, the lifetimes of the 2_1^+ states are reported, taken from [115], [12] and [121], respectively.

measured. The protons will be detected using the DSSD array in order to select the entry point in ^{24}Ne, while the tri-foils setup will be employed to select the channel of interest. The γ-ray emitted by the nucleus will be detected using EXOGAM [51] in a 12 clovers capsule configuration. A simulation of the response function of the EXOGAM detectors has been performed in order to determine the sensitivity of the detectors. For this experiment, the lifetime will be extracted from the centroid shift of the peak, as the angular resolution of EXOGAM does not allow a lineshape analysis.

This experiment has been first submitted to GANIL PAC as a Letter of Intent in April 2021 and later as a proposal in October 2021. The proposal is still under evaluation and, if accepted, the experiment is expected to be performed in 2023.

A Direct reactions

A direct reaction is a reaction where the final state is directly formed from the initial state without passing through the formation of an intermediate compound nucleus. Contrary to compound-nucleus reactions, in direct reactions the particles involved interact mainly at a surface level and, for this reason, are also called *peripheral* reactions. These reactions typically involve the exchange of one or few valence nucleons between the target and the beam ion, while the other nucleons act as simple spectators in the reaction.

When considering a nuclear reaction, both direct and compound nuclear reactions can contribute. Because of the different nature of these two processes, it is important to distinguish between them and quantify the contribution of each of them to determine which one is predominant. One of the main experimental differences between the two is that direct processes are generally faster than the processes involving a compound nucleus. Direct processes occur in a time comparable to the orbital period of the nucleons in the nucleus, hence of the order of 10^{-22} s. On the contrary, processes that require the formation of a compound nucleus are typically slower, of the order of 10^{-16}-10^{-18} s [124]. Another difference that is observable experimentally is the difference in angular distribution, where direct reactions are expected to present a sharper distribution.

When studying nuclear reactions, one is usually interested in the cross section, which is defined as the ratio between the number of produced nuclei and the incoming flux. An important aim of nuclear reaction theory is to provide an exact description of the different processes in order to be able to make predictions on the magnitude of different cross sections.

A systematic approach to direct reactions is the scattering theory, presented in the following section.

A.1. Scattering theory and the optical model

The scattering theory aims at providing a mathematical treatment of the scattering problem in order to be able to make reliable predictions on the differential cross section of the reaction. In this approach, we consider the interaction between an incident beam and a nuclear potential as a series of incident waves that are scattered by a potential. Let us consider a mass partition $\alpha = a + A$, where a is the projectile and A is the target. The problem is then reduced to the

solution of the Schrödinger equation:

$$H\Psi_\alpha = E\Psi_\alpha. \tag{A.1}$$

The Hamiltonian H of the system will consist of an internal part H_α, a kinetic part K_α and an interaction potential V_α.

In order to solve the Schrödinger equation, it is necessary to set some boundaries. In particular, for the present case, the incident wave is represented by a plane wave while after the interaction with the target, a series of spherical waves are formed. Asymptotically, the solution for outgoing waves will have the form of:

$$\Psi^{(+)}_{\vec{K_\alpha}}(\vec{R},\xi) \longrightarrow \Phi_\alpha(\xi)\exp^{i\vec{K_\alpha}\cdot\vec{R_\alpha}} + (\text{other channels}), \tag{A.2}$$

where Φ contains the information on the internal states of the target and projectile. The form of Ψ^+ changes depending on the nature of the reaction and the outgoing channels that are being considered.

For example, in the case of a transfer reaction, the $\Psi^{(+)}$ will have the form of

$$\Psi^{(+)}_{\vec{K_\alpha}} \longrightarrow \sum_{\beta\neq\alpha} \Phi_\beta(\xi_\beta) f_{\beta,\alpha}(\theta)\frac{\exp^{i\vec{K_\beta}\cdot\vec{R_\beta}}}{R_\beta}, \tag{A.3}$$

where the sum over $\beta \neq \alpha$ refers to all the possible channels. Since in a transfer reaction the partition α is not present, the plane wave part disappears from the solution. Another important term that appears in the formula is the scattering amplitude $f_{\beta,\alpha}$. This quantity is related to the differential cross section as:

$$\left(\frac{d\sigma}{d\Omega}\right)_{\alpha\to\beta} = \frac{\mu_\alpha}{\mu_\beta}\frac{K_\beta}{K_\alpha}|f_{\beta,\alpha}(\theta)|^2, \tag{A.4}$$

where θ is the scattering angle in the center of mass.

The problem of calculating the differential cross section of the reaction is reduced to projecting the asymptotic solution onto the final state to extract the scattering amplitude. However, the wave function Ψ is too complicated and the total number of final states of a reaction is prohibiting. For these reasons, it is useful to use approximations to restrict the problem to the channels of interest for the case of study. The wave function Ψ is defined as the sum of the channels of interest Ψ_P and the negligible channels Ψ_Q. The Hamiltonian H_{eff} will be formed by a part that represents the space of the channels of interest P and a part that represents the coupling between P and Q spaces.

The simplest case that one can consider is elastic scattering, where the target and the projectile are in the ground state. The effective Hamiltonian of the system will be formed by an internal part H_α and an effective potential $U_\alpha(\vec{R})$. The potential $U_\alpha(\vec{R})$, called *optical potential*, contains an imaginary part that accounts for the channels that have not been included in the wave function. A typical parametrization of U_α for a phenomenological potential is to consider it as the sum of a Coulombian real term and a nuclear term. The

nuclear part is typically written as a Wood-Saxon potential with a real and an imaginary part.

Since $U_\alpha(\vec{R})$ only depends on the distance between the nucleus, the wave function can be expanded in spherical harmonics:

$$\chi_0^{(+)}(\vec{K},\vec{R}) = \frac{1}{KR}\sum_\ell i^\ell(2\ell+1)\chi_\ell(K,R)P_\ell(\cos\theta), \tag{A.5}$$

where the angular functions $P_\ell(\cos\theta)$ are Legendre polynomials. The following step is to find the solutions for the equation:

$$\left[\frac{\hbar^2}{2\mu}\nabla^2 + \frac{\hbar}{2\mu}\frac{\ell(\ell+1)}{R^2} + U(R) - E_0\right]\chi_\ell(K,R) = 0. \tag{A.6}$$

In the case where the potential is zero, the solution is a plane wave. If the potential is different from zero, the solution must still verify the condition as before for large value of R, meaning for when the potential is negligible, and at great distances it will follow the asymptotic behaviour

$$\chi_0^{(+)}(\vec{K},\vec{R}) \longrightarrow \exp^{i\vec{K}\cdot\vec{R}} + f(\theta)\frac{e^{iKR}}{R}. \tag{A.7}$$

Knowing that the solution is expected in the form of (A.5) and to have the asymptotic behaviour described in (A.7), $\chi_0^{(+)}$ will be

$$\chi_0^{(+)}(\vec{K},\vec{R}) \longrightarrow \exp^{i\vec{K}\cdot\vec{R}} + \frac{1}{K}\sum_\ell(2\ell+1)^\ell e^{i\delta_\ell}\sin\delta_\ell P_\ell(\cos\theta). \tag{A.8}$$

It is useful to define the so-called *phase-shifts* T_ℓ as

$$T_\ell = e^{i\delta_\ell}\sin\delta_\ell \tag{A.9}$$

and the *reflection coefficient* S_ℓ, also called S-matrix

$$S_\ell = 1 + 2iT_\ell = e^{2i\delta_\ell}. \tag{A.10}$$

The S-matrix is useful to describe the effect of the potential on the outgoing wave, depending on the nature of the potential.

Comparing Equation (A.7) to the solution (A.8), it is possible to extract the scattering amplitude of an elastic process as

$$f(\theta) = \frac{1}{2iK}\sum_\ell(2\ell+1)(S_\ell - 1)P_\ell(\cos\theta) \tag{A.11}$$

and the cross section will be

$$\frac{d\sigma}{d\Omega} = |f(\theta)|^2. \tag{A.12}$$

This is only the most simplified case, and in general the problem of finding the differential cross section of an elastic reaction is more complex.

A.2. Inelastic scattering and the Distort-Wave Born Approximation

Atomic nuclei are complex objects with an internal structure that can influence the reaction. A typical example is the excitation of the nucleus in the interaction with a nuclear potential of another nucleus in a collision. When this happens without the exchange of nucleons between the target and the projectile, the reaction is called inelastic scattering. Experimentally, it is possible to determine the excitation of the nucleus by measuring the energy of the recoil. In fact, the energy required to excite the nucleus is taken from the kinetic energy of the reaction, hence the recoil will have a lower energy than the one expected in elastic scattering.

The mathematical treatment of inelastic scattering is more complex than the elastic scattering. The P space of the channels of interest now has to include both the elastic and inelastic channels.

Let us consider a simpler case where only the projectile a is excited in the reaction, while the target A is treated as an inert object. The Hamiltonian of the system will be

$$H = -\frac{\hbar^2}{2\mu}\nabla^2_{\vec{R}} + H_a(\xi) + V_\alpha(\xi, \vec{R}), \tag{A.13}$$

where H_a is the internal Hamiltonian of the projectile. It is important to notice that now the potential has an explicit dependence on the internal variable ξ. The total wave function now has the form of

$$\Psi^{(+)}(\vec{R}, \xi) = \phi_0(\xi)\chi_0(\vec{R}) + \sum_{n>0}^{N} \phi_n(\xi)\chi_n(\vec{R}), \tag{A.14}$$

where $\phi_n(\xi)$ are the internal states of the projectile and $\chi_n(\vec{R})$ are the coefficients that quantify the probability of a state to be populated. The procedure of expanding the total wave function into a set of internal states is called coupling channel (CC) method. If we insert the wave function as written in A.14 into the Schrödinger equation and multiply $\phi^*_n(\xi)$ on the left we obtain

$$[E - \varepsilon_n - \widehat{T_{\vec{R}}} - V_{n,n}(\vec{R})]\chi_n(\vec{R}) = \sum_{n' \neq n} V_{n,n'}(\vec{R})\chi_{n'}(\vec{R}), \tag{A.15}$$

then, integrating on the internal coordinates we obtain the expression for the coupling po-

tentials

$$V_{n,n'}(\vec{R}) = \int d\xi \phi_n^*(\xi) V(\xi, \vec{R}) \phi_{n'}(\xi). \tag{A.16}$$

We are considering a physical case where both the projectile and the target are initially in the ground state and only the projectile is excited in the reaction. The asymptotic behaviour of the wave function at long distance will have the form of

$$\Psi_{\vec{K_0}}^{(+)}(\vec{R}, \xi) \longrightarrow \left\{ e^{i\vec{K_0}\cdot\vec{R}} + f_{0,0}(\theta)\frac{e^{iK_0R}}{R} \right\} \phi_0(\xi) + \sum_{n>0}^{N} f_{n,0}(\theta)\frac{e^{iK_nR}}{R}\phi_n(\xi)), \tag{A.17}$$

where the first two terms refer to the elastic component of the reaction and the projectile is not excited while the third term contains all the possible excitation of the projectile from the ground state. In this case, the cross section of the process of exciting the state n from the ground state can be obtained from

$$\left(\frac{d\sigma(\theta)}{d\Omega}\right)_{0\to n} = \frac{K_n}{K_0}|f_{n,0}(\theta)|^2. \tag{A.18}$$

The problem of solving the coupled equation is not trivial. In fact, even when considering only the excitation of one nucleus from the ground state, the number of possible states is still high. However, some states are less likely to be populated from the ground state and can be treated perturbatively. The coupled equations can be solved by iteration, starting from the elastic channel. Then the solution $\chi_0(\vec{K_0}, \vec{R})$ is inserted into the equation for the excited state n to find an approximation of $\chi_n(\vec{K_0}, \vec{R})$. This procedure is known as Distorted-Wave Born Approximation (DWBA). The potential is written as $V(\vec{R}, \xi) = V_0(R) + \Delta V(\vec{R}, \xi)$, where ΔV is small compared to V_0. The central potential is used to solve the Schrödinger equation and find the initial and final wave function $\chi_i^{(+)}$ and $\chi_f^{(+)}$ respectively. The scattering potential calculated at the first order, hence using the DWBA, is

$$f_{f,i}^{DWBA}(\theta) = -\frac{\mu}{2\pi\hbar^2}\int \chi_f^{(-)*}(\vec{K}_f, \vec{R})\Delta V_{if}(\vec{R})\chi_i^{(+)}(\vec{K}_i, \vec{R})d\vec{R}, \tag{A.19}$$

where the coupling potential is defined as

$$\Delta V_{if}(\vec{R}) \equiv \int \phi_f^*(\xi)\Delta V(\vec{R}, \xi)\phi_i(\xi)d\xi. \tag{A.20}$$

A.3. Transfer reactions

There are many different type of direct reactions, such as the elastic and inelastic scattering and the transfer reactions. This last category is particularly interesting because they are a useful tool for the extraction of information on nuclear structure. The great advantage of this type of direct reactions, compared to compound-nucleus reactions, is their high selectivity that permits to have control on the states that one wants to populate. For example, reaction

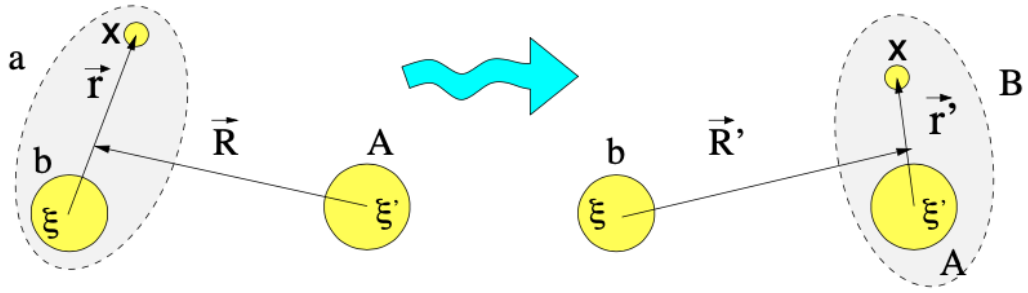

Figure A.1.: Scheme of a transfer reaction where an ensemble of nucleons x is transferred from the nucleus a to the nucleus A. Figure taken from [125].

where one neutron is transferred, also called (d, p) reactions, typically populate single particle states, while reactions where one proton is transferred prefer single hole states. Both these reactions are often employed in the study of low-lying shell-model states.

In a (d, p) reaction, for example, it is possible to select one state in particular by gating on the excited energy of the particle in the analysis. Once an excited state is selected, it is possible to study the angular distribution of the emitted particles correspondent to that specific state in order to infer information on the structure. In particular, in direct transfer reactions the angular distributions have characteristic shapes that depend on the transferred angular momentum and can be used to determine the spin and parity of the populated state.

Let us consider a simple reaction defined as $a + A \rightarrow b + B$, where an incoming particle a becomes an outgoing particle b after interacting with the nucleus A. Given that particle a has an initial momentum of $\vec{p_a}$ that becomes $\vec{p_b}$ after the reaction, the recoil B will have momentum $\vec{p} = \vec{p_a} - \vec{p_b}$ and will be placed in a orbit with angular momentum $\ell = Rp$. Hence, knowing the kinematic of the reaction it is possible to calculate the transferred angular momentum and, if the initial state of the particles involved is known, it is possible to obtain information on the spin and parity of the populated state.

Transfer reactions can be treated with the same formalism used for the elastic and inelastic channels, as discussed before. Similarly to the inelastic case, also in the transfer reaction a wide number of different transfer channels are possible, and in addition the excitation of the projectile-like and target-like should also be considered. However, some channels will be weakly coupled and have a small probability of being populated in the reaction, hence requiring some approximations.

Let us consider a reaction where $\alpha = a + A$ is the initial mass partition and $\beta = b + B$ is the final mass partition. If in the reaction one or more nucleons are transferred from a to A, the reaction can be written as $(x + b) + A \rightarrow b + (x + A)$, where $a = x + b$ and $B = x + A$, as illustrated in Figure A.1.

The potential describing the projectile-target interaction will have a part relative to the interaction between b and x, V_{xb}, and a second part relative to the interaction between b and A, U_{bA}. By adding and subtracting the same auxiliary potential relative to the motion between the particles, the potential will be written as

$$V_\beta(\vec{R'}, \vec{r'}) = U_\beta(\vec{R'}) + [V_{xb} + U_{bA} - U_\beta(\vec{R'})] \equiv U_\beta(\vec{R'}) + \Delta V_\beta. \tag{A.21}$$

The potential $U_\beta(\vec{R}')$ describes the general motion of the two nuclei, is the dominant term and depends only on the variable $\vec{R}'$, while ΔV_β represents the residual interaction and is small compared to the other term. Hence, it is possible to treat the problem using the DWBA. The scattering amplitude results to be

$$f_{\beta,\alpha}(\theta) = -\frac{\mu_\beta}{2\pi\hbar^2}\int \chi_\beta^{(-)*}(\vec{K_\beta},\vec{R}')\Phi_\beta^*(\xi_\beta)\Delta V_\beta \chi_\alpha^{(+)}(\vec{K_\alpha},\vec{R})\Phi_\alpha(\xi_\alpha)d\xi_\beta d\vec{R}'. \tag{A.22}$$

The functions on the left of the residual potential correspond to the final state while those on the right correspond to the initial state. The functions χ contain the information on the relative motion between the nuclei of the partition and are obtained from the optical potentials, while the function Φ contains the information on the internal states and are defined as

$$\begin{aligned}\Phi_\alpha(\xi_\alpha) &= \varphi_a(\xi,\vec{r})\phi_A(\xi')\\ \Phi_\beta(\xi_\beta) &= \varphi_b(\xi)\phi_A(\xi',\vec{r'}).\end{aligned} \tag{A.23}$$

Let us consider a situation where a deuteron (a in out partition) interact with another nucleus A and transfer its neutron in the process, leading to a final partition composed of one proton and a nucleus $B = A + n$. For medium-mass and heavy nuclei, the mass change of B in the process will be small compared to its own mass and the wave function of B can be expanded in states of A as follow

$$\Phi_B(\xi',\vec{r'}) = C_{BA}^{\ell j}\phi_A(\xi')\varphi_{nA}(\vec{r'}) + \sum_{A\neq A'}\phi_{A'}(\xi')\varphi_{nA}^{\ell' j'}(\vec{r'}), \tag{A.24}$$

where $C_{BA}^{\ell j}$ is the spectroscopic amplitude.

After applying the needed substitution, we can obtain the expression for the differential cross section of the (d,p) reaction for medium-mass and heavy nucleus

$$\left(\frac{d\sigma}{d\Omega}\right)_{\beta,\alpha} = \frac{\mu_\alpha\mu_\beta}{(2\pi\hbar^2)^2}|C_{BA}^{\ell jI}|^2|\int\int \chi_p^{(-)*}(\vec{K_p},\vec{R}')\varphi_{nA}^{\ell jI,*}(\vec{r'})V_{pn}(\vec{r})\chi_d^{(+)}(\vec{K_d},\vec{R})\varphi_d(\vec{r})d\vec{r'}d\vec{R}'|^2. \tag{A.25}$$

The square module of the spectroscopic amplitude is called *spectroscopic factor*. The spectroscopic factor is a useful quantity that can help finding a correlation between data and calculations. While the states in the calculations are pure shell-model states, this is not true in reality. While the calculations will reproduce the angular dependence of the cross section, they will not be able to reproduce accurately the amplitude of the cross section. The cross section for each state will be multiplied by its spectroscopic factor $S_{BA}^{\ell jI} = |C_{BA}^{\ell jI}|^2$ to correlate the calculated cross section to the experimentally measured one as [3]

$$\left(\frac{d\sigma}{d\Omega}\right)_{\text{meas}} = S\left(\frac{d\sigma}{d\Omega}\right)_{\text{calc}}. \tag{A.26}$$

This factor gives an estimation on the purity of the shell-model state and it may vary from

0 to 1, where a pure shell-model state would have $S = 1$. From the comparison between the calculations and the measurements, it is possible to extract the different S-factors of the states.

B The least-χ^2 test and the maximum likelihood

In this appendix, two statistical methods are presented: the least-χ^2 and the maximum likelihood. These two statistical approaches are often used in Physics to test hypotheses and the goodness of a fit. The relation between these two methods is also presented in the limit of large numbers.

B.1. The least-χ^2 test

The χ^2 distribution is a special case of the wider class of functions called Γ distributions and it is widely used in Statistic. It is so defined: given N independent Gaussian random variables x_i, the sum

$$z = \sum_{i=1}^{N} \left(\frac{x_i - \mu}{\sigma_i} \right)^2 \tag{B.1}$$

follows the χ^2 distribution with N degrees of freedom. For large values of N, the χ^2 distribution approaches the Gaussian distribution [126].

A typical application of this distribution is the χ^2 test, a method often used in fitting procedures to test the goodness of a fit, hypotheses testing and optimization of parameters. Given a series of N experimental data point (x_i,y_i) with their error bars σ_i and a fitting function $f(x_i)$ defined by M free parameters θ_k, it is possible to define the quantity [95]

$$\chi^2 = \sum_{i=1}^{N} \left(\frac{y_i - f(x_i)}{\sigma_i} \right)^2 . \tag{B.2}$$

This method can be used for three main purposes:

- determine the goodness of the fit;
- optimize the free parameters of the fitting function;
- provide an error estimation of the parameters.

For the first purpose, it is useful to define the reduced χ^2, which is obtained from Equation B.2 by dividing the so-defined χ^2 by the number of degrees of freedom (dof), corresponding to the number of data point N minus the number of free parameters M. For a good fit, this quantity is expected to tend to one for large values of N. Hence, it is possible to compare different theories and test their goodness by verifying that the reduced χ^2 value is close to one. This kind of test is reliable only in the limit of large numbers.

The optimization of the parameters can be performed by minimizing the χ^2 (least-χ^2 method). The quantity defined in Equation B.2 is calculated for different values of the parameters to find the set of α_k that minimizes the χ^2. In order to optimize the procedure, a sensitive range and step for the test must be chosen [95].

The least-χ^2 method can be used to compare different histograms, as in the case of this work. We will consider a histogram having k bins, where n_i is the number of events in the i-th bin and N is the total number of events $N = \sum_i n_i$. We are interested in comparing the data histogram with a theoretical curve with M parameters, where y_i is the number of events predicted by the model to be in the i-th bin and $N_0 = \sum_i y_i$.

For the present analysis, the theoretical curve corresponds to the histogram produced by the Monte Carlo simulation, which depends on two parameters: the lifetime of the state and the energy of the γ-ray transition. The simulated histogram is renormalized so that $N_0 = N$.

It is important to underline that if the total number of events N is fixed, as in the present case, then the distribution of the events among the bins is expected to follow the multinomial distribution, while the Poisson distribution is used when the experiment is designed to measure N.

We define two possible weighted least-squares statistics [127]: the Pearson's χ^2:

$$\chi^2_P = \sum_i \frac{(n_i - y_i)^2}{y_i}, \tag{B.3}$$

and the Neyman's χ^2:

$$\chi^2_N = \sum_i \frac{(n_i - y_i)^2}{n_i}. \tag{B.4}$$

In the case of multinomial problems, it is important that $N = N_0$, which is guaranteed by the normalization.

B.2. The maximum likelihood

The likelihood function is a tool to estimate the goodness of fit of a model to a data set, depending on unknown parameters. Similarly to the procedure of minimization of the χ^2, the maximum likelihood estimation allows one to determine the parameters for which the model better fits the experimental data. For a set of measured quantities x_i, the likelihood of a set of parameters $\theta = (\theta_1, ..., \theta_n)$ is $\mathcal{L}(\theta) = P(x|\theta)$; however, for computational reasons, the natural logarithm of the likelihood is commonly used [126].

In case data consists of a set of independent values $x = (x_1, ..., x_n)$, where each component follows the same probability density function (p.d.f.) $f(x;\theta)$, the likelihood is

$$\mathcal{L}(\theta) = \prod_{i=1}^{n} f(x_i;\theta) \tag{B.5}$$

where the number of total events n is fixed. In case the number of events depends on the parameters θ, this dependence must be included in the estimation of the likelihood.

In the case of large samples of data, it is convenient to bin the values into a histogram with N bins. In this way, data are stored in a vector on N elements $n = (n_1, ..., n_N)$ where each element is the number of events contained in that bin. If the total number of events is fixed, then the $f(x_i;\theta)$ can be written as:

$$f_M(n;\theta) = \frac{n_{TOT}!}{n_1! \cdots n_N!} p_1^{n_1} \cdots p_N^{n_N}, \tag{B.6}$$

where p_i depends on the parameters θ_i and are calculated as the number of events in the bin *i-th* normalized by the total number of events of the simulation, so that $\sum_{i=1}^{N} p_i = 1$.

The likelihood results to be:

$$\ln \mathcal{L}(\theta) = \ln(n_{tot}!) + \sum_{i=1}^{N} \ln\left(\frac{p_i^{n_i}}{n_i!}\right) \tag{B.7}$$

The likelihood can be used to test the goodness of the fit by using this theorem that allows one to convert the likelihood function into χ^2 statistic [127]. Let us consider

$$\lambda = \frac{\mathcal{L}(y;n)}{\mathcal{L}(m;n)} \tag{B.8}$$

where m corresponds to the true value of the parameters. According to the theorem, the likelihood χ^2 is defined as

$$\chi^2_\lambda = -2\ln\lambda = -2\ln\mathcal{L}(y;n) + 2\ln\mathcal{L}(m;n). \tag{B.9}$$

which is expected to follow a χ^2 distribution for high statistics. In the case of histograms, the unknown m can be replaced with the corresponding maximum likelihood. This leads to the multinomial likelihood χ^2 being defined as

$$\chi^2_{\lambda,m} = 2\sum n_i \ln(n_i/y_i). \tag{B.10}$$

For the estimation of the error bars on the parameters θ, the formula is:

$$\ln\mathcal{L}(\theta) = \ln\mathcal{L}_{max} - \sigma^2/2 \tag{B.11}$$

where σ is the number of standard deviation. Hence, the error at $\pm\sigma$ is $\Delta\ln\mathcal{L}(\theta) = 0.5$.

However, this formula is valid only in the limit of large number where, following Equation (B.9), it corresponds to the condition $\Delta\chi^2 = 1$.

C

The ^{15}C(d,p) experiment at ANL

The experimental details regarding the preparation and execution of the ^{15}C(d,p) experiment at ANL are reported in this chapter. The experiment was performed in July 2021, in the context of the GODDESS campaign, which involved the γ-ray array GRETINA [55] coupled with the silicon array ORRUBA [117, 118]. At forward angle, a Fast Ionization chamber was also present.

As introduced in Chapter 6, the aim of the experiment was populating the 2_2^+ state of ^{16}C with a one-neutron reaction using a ^{15}C beam at 123 MeV from the In-Flight facility at ATLAS. The purity of the beam was expected to be at least at 50%, but during the experiment resulted to be above 99%. Using the previous experience of the ^{20}O experiment in GANIL, two targets were employed to acquire two distinct datasets. The first target was a thin CD_2 foil, 380 μg/cm^2-thick: this target was chosen to perform a spectroscopic study of the nucleus and measure with better precision the energy of the γ-ray transitions. The second target was a 350 μg/cm^2-thick CD_2 layer deposited on a 22(1) mg/cm^2 layer of gold. The measurement of the degrader was performed by weighting the foil. This second target was employed for the lifetime measurement.

The protons emitted in the reaction were detected by the ORRUBA array while the γ rays emitted by the de-excitation of ^{16}C was detected by the GRETINA array. A photo of the apparatus with ORRUBA and GRETINA in complete configuration is shown in Figure C.1. During the experiment, 12 quadruplets were mounted, 2 at forward angles, 4 at 90° and 6 at backward angles. Seeing the kinematics of the reaction, the most forward annular detector of ORRUBA was removed, since the protons could not be stopped in the detector due to the high energy. The angular coverage was between 50 degrees and 165 degrees. Similarly to the ^{20}O experiment, from the information carried by the protons, namely the energy and the (θ,ϕ) angles, it is possible to reconstruct the kinematics of the reaction and in particular the velocity, the angles and the excitation energy of ^{16}C. From the information on the emitting nucleus, an event-by-event Doppler correction can be performed. Moreover, the reconstructed excitation energy can be used to select the direct population of the state of interest, keeping under control the feeding of the states from higher-lying ones, which could limit the precision of the measurement. In the present experiment, due to the closeness in excitation energy, it was not possible to distinguish the 2_2^+ and the 3_1^+ states. However, no feeders are expected from the 3_1^+ to the 2_2^+ state.

Finally, in order to select events coming from the (d,p) transfer reaction, the new Fast

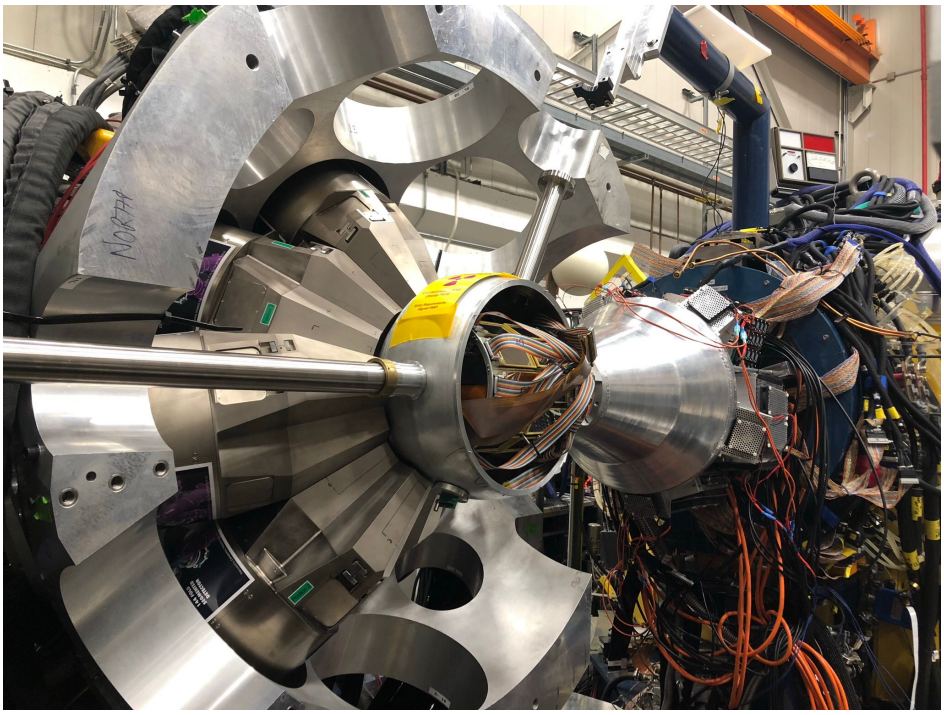

Figure C.1.: The GRETINA array coupled to the ORRUBA array in the GODDESS configuration at ANL. Courtesy of M. Siciliano.

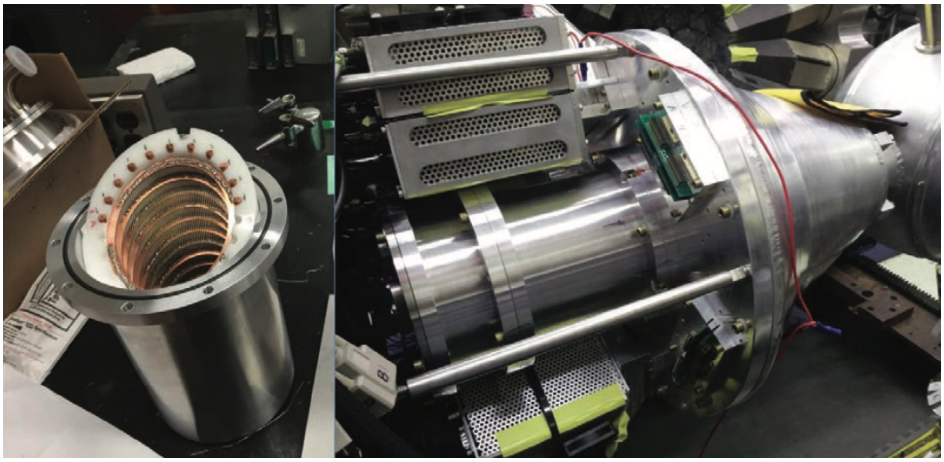

Figure C.2.: The tilted-grid fast ionization chamber installed in the GODDESS setup. Figure taken from [118].

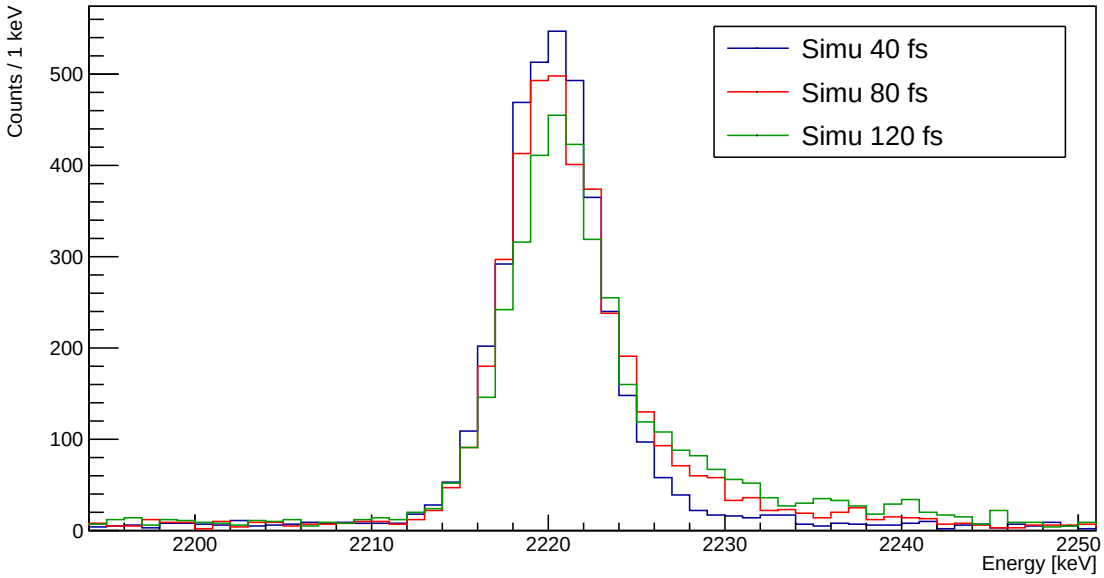

Figure C.3.: Lineshape of the $2_2^+ \rightarrow 2_1^+$ transition of ^{16}C for $\tau = 40, 80, 120$ fs. Only backward detectors have been employed in the simulation.

Ionization Chamber (FIC) [118] was used to disentangle the carbon ions from the fusion-evaporation (FE) and fusion-fission products coming from the reaction on the carbon in the target and the thick gold degrader respectively. This new FIC also permitted the determination of the direction of the carbon ions, crucial information for the Doppler correction of the emitted γ rays. The FIC has been successfully employed in two experiments during the GODDESS experimental campaign in 2019 to study ^{30}P(d,pγ) [128] and ^{134}Te(d,pγ) [129], and is presented in Figure C.2. To fully stop the FE residues a minimum CF_4 pressure of 100 Torr was calculated, while to stop the beam and the transfer product 295 Torr of CF_4 were required. For the experiment, a pressure of 403.8 Torr and 300 Torr was set for the runs using the CD_2-only and the CD_2+Au target respectively.

The ^{16}C nucleus is produced at $\beta = 0.126$ and exits the gold layer at $\beta = 0.117$ after about 280 fs. With this velocity, we expect to be sensitive in the range of interest, down to 30 fs. Considering that the present upper limit is 180 fs, this measurement can significantly improve the constraints for the theoretical calculations. The effect on the lineshape of the peak due to the lifetime expected for the present experiment have been simulated and presented in Figure C.3 for $\tau = 40, 80, 120$ fs.

Additional simulations have been performed with the VIKAR code [130]. The angular distributions have been calculated using ADWA calculations for 0_1^+, 2_1^+, 0_2^+ and the $2_2^+/3_1^+$ doublet. Figure C.4 shows the expected excitation energy spectrum for ^{16}C with the single-particle condition (black) and with the coincidence with the FIC (red), suppressing the FE events. A realistic resolution of the detector and beam spot has been adopted. Figure C.5 shows the particle energy as a function of the scattering angle. The FE background events are reported in black, while proton events are reported in blue and deuterons in red.

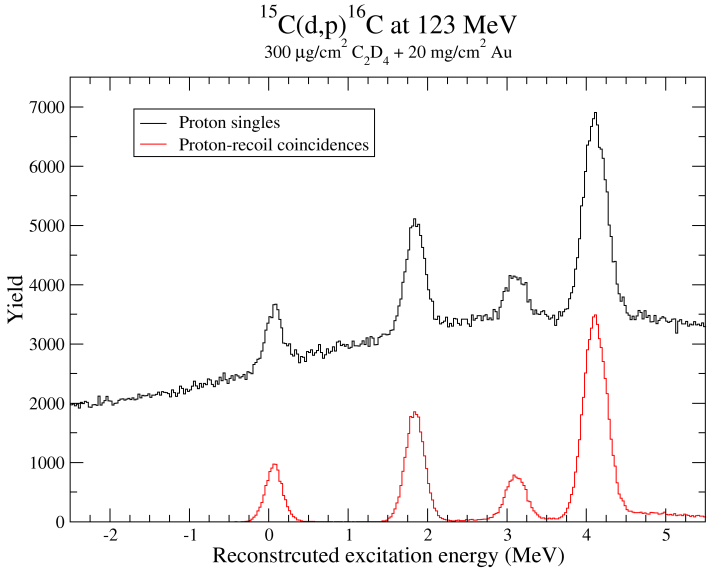

Figure C.4.: Simulated excitation energy spectrum without any condition (black) and with the required coincidence with the FIC (red). Courtesy of S. Pain.

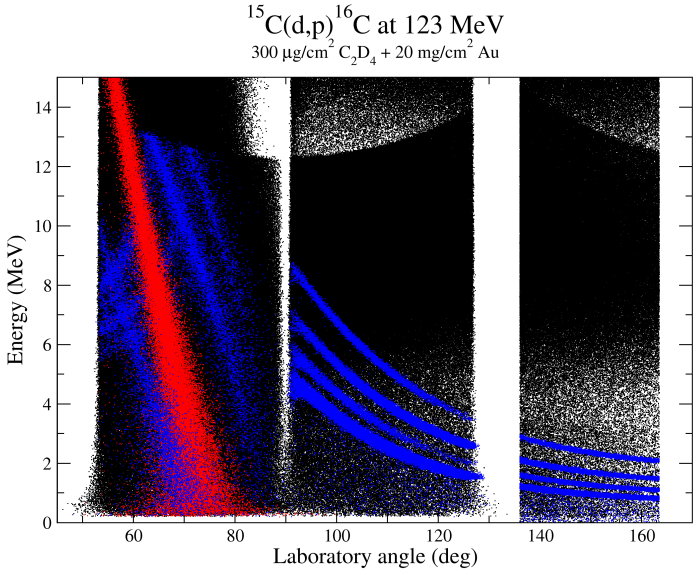

Figure C.5.: Simulated energy of the particle as a function of the angle. Background events are reported in black, while protons are in blue and deuterons in red. Courtesy of S. Pain.

Bibliography

[1] K. Heyde. *The Nuclear Shell Model* (Springer-Verlag, 1994).

[2] K. Heyde. *Basic ideas and concepts in Nuclear Physics* (Institute of Physics Publishing, 1994).

[3] K. Krane and D. Halliday. *Introductory nuclear physics* (Wiley New York, 1988).

[4] M. Mayer-Goepper. *Nuclear Configurations in the Spin-Orbit Coupling Model. I. Empirical Evidence.* Physics Review Journal 78 (1950).

[5] O. Haxel, J. Jensen and H. Seuss. *On the "Magic Numbers" in Nuclear Structure.* Physics Review Journal 75 (1949).

[6] E. Caurier, G. Martinez-Pined, F. Nowacki, A. Poves and K. Sieja. *Isolde Shell Model Course for Non-Practitioners* (2013).

[7] E. Caurier, G. Martínez-Pinedo, F. Nowacki, A. Poves and A. P. Zuker. *The shell model as a unified view of nuclear structure.* Review of Modern Physics 77, 427 (2005).

[8] M. Dufour and A. P. Zuker. *Realistic collective nuclear Hamiltonian.* Physical Review C 54, 1641 (1996).

[9] G. Hagen, T. Papenbrock, D. J. Dean, A. Schwenk, A. Nogga, M. Włoch and P. Piecuch. *Coupled-cluster theory for three-body Hamiltonians.* Physical Review C 76, 034302 (2007).

[10] E. Epelbaum, H.-W. Hammer and U.-G. Meißner. *Modern theory of nuclear forces.* Review of Modern Physics 81, 1773 (2009).

[11] K. Hebeler, J. Holt, J. Menéndez and A. Schwenk. *Nuclear Forces and Their Impact on Neutron-Rich Nuclei and Neutron-Rich Matter.* Annual Review of Nuclear and Particle Science 65, 457 (2015).

[12] A. Sonzogni et al. *Nudat 2.*

[13] R. Janssens. *Unexpected doubly magic nucleus.* Nature 459, 1069 (2009).

[14] R. Kanungo, C. Nociforo, A. Prochazka, T. Aumann, D. Boutin, D. Cortina-Gil, B. Davids, M. Diakaki, F. Farinon, H. Geissel, R. Gernhäuser, J. Gerl, R. Janik, B. Jonson, B. Kindler, R. Knöbel, R. Krücken, M. Lantz, H. Lenske, Y. Litvinov, B. Lommel, K. Mahata, P. Maierbeck, A. Musumarra, T. Nilsson, T. Otsuka, C. Perro, C. Scheidenberger, B. Sitar, P. Strmen, B. Sun, I. Szarka, I. Tanihata, Y. Utsuno, H. Weick and

M. Winkler. *One-Neutron Removal Measurement Reveals* ^{24}O *as a New Doubly Magic Nucleus.* Physical Review Letter 102, 152501 (2009).

[15] C. Hoffman, T. Baumann, D. Bazin, J. Brown, G. Christian, D. Denby, P. DeYoung, J. Finck, N. Frank, J. Hinnefeld, S. Mosby, W. Peters, W. Rogers, A. Schiller, A. Spyrou, M. Scott, S. Tabor, M. Thoennessen and P. Voss. *Evidence for a doubly magic* ^{24}O. Physics Letters B 672, 17 (2009).

[16] T. Otsuka, T. Suzuki, J. D. Holt, A. Schwenk and Y. Akaishi. *Three-Body Forces and the Limit of Oxygen Isotopes.* Physical Review Letter 105, 032501 (2010).

[17] A. P. Zuker. *Three-Body Monopole Corrections to Realistic Interactions.* Physical Review Letter 90, 042502 (2003).

[18] R. F. Garcia Ruiz, M. L. Bissell, K. Blaum, A. Ekström, N. Frömmgen, G. Hagen, M. Hammen, K. Hebeler, J. D. Holt, G. R. Jansen, M. Kowalska, K. Kreim, W. Nazarewicz, R. Neugart, G. Neyens, W. Nörtershäuser, T. Papenbrock, J. Papuga, A. Schwenk, J. Simonis, K. A. Wendt and D. T. Yordanov. *Unexpectedly large charge radii of neutron-rich calcium isotopes.* Nature Physics 12, 594 (2016).

[19] P. Gysbers, G. Hagen, J. D. Holt, G. R. Jansen, T. D. Morris, P. Navrátil, T. Papenbrock, S. Quaglioni, A. Schwenk, S. R. Stroberg and K. A. Wendt. *Discrepancy between experimental and theoretical β-decay rates resolved from first principles.* Nature Physics 15, 428 (2019).

[20] A. Kumar, R. Kanungo, A. Calci, P. Navrátil, A. Sanetullaev, M. Alcorta, V. Bildstein, G. Christian, B. Davids, J. Dohet-Eraly, J. Fallis, A. T. Gallant, G. Hackman, B. Hadinia, G. Hupin, S. Ishimoto, R. Krücken, A. T. Laffoley, J. Lighthall, D. Miller, S. Quaglioni, J. S. Randhawa, E. T. Rand, A. Rojas, R. Roth, A. Shotter, J. Tanaka, I. Tanihata and C. Unsworth. *Nuclear Force Imprints Revealed on the Elastic Scattering of Protons with* ^{10}C. Physical Review Letter 118, 262502 (2017).

[21] C. Forssén, R. Roth and P. Navrátil. *Systematics of* 2^+ *states in* C *isotopes from the no-core shell model.* Journal of Physics G: Nuclear and Particle Physics 40, 055105 (2013).

[22] V. F. Weisskopf. *Radiative Transition Probabilities in Nuclei.* Physical Review 83, 1073 (1951).

[23] P. Brussaard and P. Glaudemans. *Shell-model applications in nuclear spectroscopy* (North-Holland, 1977).

[24] D. Cline. *Nuclear shapes studied by Coulomb excitation.* Annual Review of Nuclear and Particle Science 36, 683 (1986).

[25] U. Kneissl, H. Pitz and A. Zilges. *Investigation of nuclear structure by resonance fluorescence scattering.* Progress in Particle and Nuclear Physics 37, 349 (1996).

[26] A. Dewald, S. Harissopulos and P. Von Brentano. *The differential plunger and the differential decay curve method for the analysis of recoil distance Doppler-shift data.* Zeitschrift für Physik A 334, 163 (1989).

[27] A. Dewald, O. Möller and P. Petkov. *Developing the Recoil Distance Doppler-Shift technique towards a versatile tool for lifetime measurements of excited nuclear states.* Progress in Particle and Nuclear Physics 67, 786 (2012).

[28] A. Schwarzschild and E. Warburton. *The measurement of short nuclear lifetimes.* Annual Review Nuclear Science 18, 265 (1968).

[29] B. A. Brown and W. A. Richter. *New "USD" Hamiltonians for the sd shell.* Physical Review C 74, 034315 (2006).

[30] M. Ciemała et al. *Testing ab initio nuclear structure in neutron-rich nuclei: Lifetime measurements of second* 2^+ *state in* ^{16}C *and* ^{20}O. Physical Review C 101, 021303 (2020).

[31] R. W. Nightingale, J. A. Becker, R. E. McDonald and D. Kohler. $^{18}\mathrm{O}(t,p_1\gamma)\mathrm{O}^{20}$ *Angular Correlation.* Physical Review C 1, 893 (1970).

[32] S. LaFrance, H. T. Fortune, S. Mordechai, M. E. Cobern, G. E. Moore, R. Middleton, W. Chung and B. H. Wildenthal. ^{20}O *from* ^{18}O*(t,p).* Physical Review C 20, 1673 (1979).

[33] A. A. Pilt, M. A. M. Shahabuddin and J. A. Kuehner. *States in* ^{20}O *below 6 MeV excitation via the* ^{18}O*(t,p)* ^{20}O *reaction.* Physical Review C 19, 20 (1979).

[34] K. C. Young, D. P. Balamuth, J. M. Lind and R. W. Zurmühle. *States in* ^{20}O *by use of* $^{18}\mathrm{O}(t,p\gamma)$ *measurements.* Physical Review C 23, 980 (1981).

[35] A. Rutten, A. Holthuizen, J. De Raedt, W. Sterrenburg and G. Van Middelkoop. *Measurement of the g-factor and lifetime of the first-excited state of 20O.* Nuclear Physics A 344, 294 (1980).

[36] E. Khan, Y. Blumenfeld, N. Van Giai, T. Suomijärvi, N. Alamanos, F. Auger, G. Colò, N. Frascaria, A. Gillibert, T. Glasmacher, M. Godwin, K. Kemper, V. Lapoux, I. Lhenry, F. Maréchal, D. Morrissey, A. Musumarra, N. Orr, S. Ottini-Hustache, P. Piattelli, E. Pollacco, P. Roussel-Chomaz, J. Roynette, D. Santonocito, J. Sauvestre, J. Scarpaci and C. Volpe. *Low-lying collective states in neutron-rich oxygen isotopes via proton scattering.* Physics Letters B 490, 45 (2000).

[37] E. Tryggestad, T. Aumann, T. Baumann, D. Bazin, J. Beene, Y. Blumenfeld, B. Brown, M. Chartier, M. Halbert, P. Heckman, J. Liang, D. Radford, D. Shapira, M. Thoennessen and R. Varner. *Low-lying dipole strength in* ^{20}O. Physics Letters B 541, 52 (2002).

[38] E. Tryggestad, T. Baumann, P. Heckman, M. Thoennessen, T. Aumann, D. Bazin, Y. Blumenfeld, J. R. Beene, T. A. Lewis, D. C. Radford, D. Shapira, R. L. Varner, M. Chartier, M. L. Halbert and J. F. Liang. *Low-lying* $E1$ *strength in* ^{20}O. Physical Review C 67, 064309 (2003).

[39] M. Wiedeking, S. L. Tabor, J. Pavan, A. Volya, A. L. Aguilar, I. J. Calderin, D. B. Campbell, W. T. Cluff, E. Diffenderfer, J. Fridmann, C. R. Hoffman, K. W. Kemper, S. Lee, M. A. Riley, B. T. Roeder, C. Teal, V. Tripathi and I. Wiedenhöver. $p-sd$ *Shell*

Gap Reduction in Neutron-Rich Systems and Cross-Shell Excitations in ^{20}O. Physical Review Letter 94, 132501 (2005).

[40] C. R. Hoffman, B. B. Back, B. P. Kay, J. P. Schiffer, M. Alcorta, S. I. Baker, S. Bedoor, P. F. Bertone, J. A. Clark, C. M. Deibel, B. DiGiovine, S. J. Freeman, J. P. Greene, J. C. Lighthall, S. T. Marley, R. C. Pardo, K. E. Rehm, A. Rojas, D. Santiago-Gonzalez, D. K. Sharp, D. V. Shetty, J. S. Thomas, I. Wiedenhöver and A. H. Wuosmaa. *Experimental study of the* $^{19}\mathrm{O}(d,p)^{20}\mathrm{O}$ *reaction in inverse kinematics.* Physical Review C 85, 054318 (2012).

[41] O. Kamalou, P. Delahaye, M. Dubois and A. Savalle. *Status report on GANIL and upgrade of SPIRAL1.* In *22nd Int. Conf. and their Applications* (JACoW, 2019), p. 9.

[42] P. Delahaye, M. Dubois, L. Maunoury, A. Annaluru, J. Angot, O. Bajeat, B. Blank, J. Cam, P. Chauveau, R. Frigot, S. Hormigos, B. Jacquot, P. Jardin, O. Kamalou, V. Kuchi, P. Lecomte, B. Osmond, B. Retailleau, A. Savalle, T. Stora, J. Thomas, V. Toivanen, E. Traykov, P. Ujic and R. Vondrasek. *New exotic beams from SPIRAL 1 upgrade.* Nuclear Instruments and Methods in Physics Research Section B: Beam Interactions with Materials and Atoms 463, 339 (2020).

[43] *GANIL webpage.*

[44] G. F. Knoll. *Radiation detection and measurement* (John Wiley & Sons, 1979).

[45] D. Bazzacco. *The Advanced Gamma Tracking Array AGATA.* Nuclear Physics A 746, 248c (2004).

[46] P. Twin, P. Nolan, R. Aryaeinejad, D. Love, A. Nelson and A. Kirwan. *TESSA: A multi-detector* γ*-ray array designed to study high spin states.* Nuclear Physics A 409, 343 (1983).

[47] C. Alvarez. *The GASP array.* Nuclear Physics News 3, 10 (1993).

[48] C. Beausang, S. Forbes, P. Fallon, P. Nolan, P. Twin, J. Mo, J. Lisle, M. Bentley, J. Simpson, F. Beck, D. Curien, G. deFrance, G. Duchêne and D. Popescu. *Measurements on prototype Ge and BGO detectors for the Eurogam array.* Nuclear Instruments and Methods in Physics Research Section A: Accelerators, Spectrometers, Detectors and Associated Equipment 313, 37 (1992).

[49] I.-Y. Lee. *The GAMMASPHERE.* Nuclear Physics A 520, c641 (1990). Nuclear Structure in the Nineties.

[50] F. Beck. *EUROBALL: Large gamma ray spectrometers through european collaborations.* Progress in Particle and Nuclear Physics 28, 443 (1992).

[51] G. de France. *Gamma-ray spectroscopy studies at GANIL: Status and perspectives.* The European Physical Journal A - Hadrons and Nuclei 20, 59 (2003).

[52] A. Goasduff et al. *The GALILEO* γ*-ray array at the Legnaro National Laboratories.* Nuclear Instruments and Methods in Physics Research Section A: Accelerators, Spectrometers, Detectors and Associated Equipment 1015, 165753 (2021).

[53] W. Mueller, J. Church, T. Glasmacher, D. Gutknecht, G. Hackman, P. Hansen, Z. Hu, K. Miller and P. Quirin. *Thirty-two-fold segmented germanium detectors to identify γ-rays from intermediate-energy exotic beams.* Nuclear Instruments and Methods in Physics Research Section A: Accelerators, Spectrometers, Detectors and Associated Equipment 466, 492 (2001).

[54] N. Warr et al. *The Miniball spectrometer.* The European Physical Journal A 49, 40 (2013).

[55] I.-Y. Lee. *Gamma-ray energy tracking array: GRETINA.* Journal of Physics: Conference Series 420, 012156 (2013).

[56] S. Akkoyun et al. *AGATA—Advanced GAmma Tracking Array.* Nuclear Instruments and Methods in Physics Research Section A: Accelerators, Spectrometers, Detectors and Associated Equipment 668, 26 (2012).

[57] I. Lee, R. Clark, M. Cromaz, M. Deleplanque, M. Descovich, R. Diamond, P. Fallon, A. Macchiavelli, F. Stephens and D. Ward. *GRETINA: A gamma ray energy tracking array.* Nuclear Physics A 746, 255 (2004). Proceedings of the Sixth International Conference on Radioactive Nuclear Beams (RNB6).

[58] A. Gadea et al. *Conceptual design and infrastructure for the installation of the first AGATA sub-array at LNL.* Nuclear Instruments and Methods in Physics Research Section A: Accelerators, Spectrometers, Detectors and Associated Equipment 654, 88 (2011).

[59] C. Domingo-Pardo, D. Bazzacco, P. Doornenbal, E. Farnea, A. Gadea, J. Gerl and H. Wollersheim. *Conceptual design and performance study for the first implementation of AGATA at the in-flight RIB facility of GSI.* Nuclear Instruments and Methods in Physics Research Section A: Accelerators, Spectrometers, Detectors and Associated Equipment 694, 297 (2012).

[60] E. Clément et al. *Conceptual design of the AGATA 1π array at GANIL.* Nuclear Instruments and Methods in Physics Research Section A: Accelerators, Spectrometers, Detectors and Associated Equipment 855, 1 (2017).

[61] A. Wiens, H. Hess, B. Birkenbach, B. Bruyneel, J. Eberth, D. Lersch, G. Pascovici, P. Reiter and H.-G. Thomas. *The AGATA triple cluster detector.* Nuclear Instruments and Methods in Physics Research Section A: Accelerators, Spectrometers, Detectors and Associated Equipment 618, 223 (2010).

[62] F. Zocca, A. Pullia, D. Bazzacco and G. Pascovici. *A Time-Over-Threshold Technique for Wide Dynamic Range Gamma-Ray Spectroscopy With the AGATA Detector.* IEEE Transactions on Nuclear Science 56, 2384 (2009).

[63] *RecalEnergy - subversion repository.*

[64] B. Bruyneela, P. Reiter, A. Wiens, J. Eberth, H. Hess, G. Pascovici, W. J, S. Aydin, D. Bazzacco and F. Recchia. *Crosstalk corrections for improved energy resolution with highly segmented HPGe-detectors.* Nuclear Instruments and Methods in Physics Research Section A: Accelerators, Spectrometers, Detectors and Associated Equipment 608, 99 (2009).

[65] *xTalkSort - subversion repository.*

[66] N. Goel, C. Domingo-Pardo, T. Habermann, F. Ameil, T. Engert, J. Gerl, I. Kojouharov, J. Maruhn, N. Pietralla and H. Schaffner. *Characterisation of a symmetric AGATA detector using the γ-ray imaging scanning technique.* Nuclear Instruments and Methods in Physics Research Section A: Accelerators, Spectrometers, Detectors and Associated Equipment 700, 10 (2013).

[67] M. Descovich, P. Nolan, A. Boston, J. Dobson, S. Gros, J. Cresswell, J. Simpson, I. Lazarus, P. Regan, J. Valiente-Dobon, P. Sellin and C. Pearson. *The position response of a large-volume segmented germanium detector.* Nuclear Instruments and Methods in Physics Research Section A: Accelerators, Spectrometers, Detectors and Associated Equipment 553, 512 (2005).

[68] B. Bruyneel, B. Birkenbach and P. Reiter. *Pulse shape analysis and position determination in segmented HPGe detectors: The AGATA detector library.* European Physical Journal A 52 (2016).

[69] R. Venturelli and D. Bazzacco. *Adaptive Grid Search as Pulse Shape Analysis Algorithm for γ-Tracking and Results.* Laboratori Nazionali di Legnaro (2004).

[70] B. Bruyneel, B. abd Birkenbach, J. Eberth, H. Hess, G. Pascovici, P. Reiter, A. Wiens, D. Bazzacco, E. Farnea, C. Michelagnoli and F. Recchia. *Correction for the hole trapping in AGATA detectors using pulse shape analysis.* European Physical Journal A 49, 61 (2013).

[71] L. Darken. *Role of disordered regions in fast-neutron damage of HPGe detectors.* Nuclear Instruments and Methods in Physics Research Section B: Beam Interactions with Materials and Atoms 74 (1993).

[72] A. Latina, A. Stefanini, S. Beghini, B. Behera, L. Corradi, G. De Angelis, A. De Rosa, E. Fioretto, A. Gadea, M. Gulmini, G. Inglima, M. La Commara, G. Maron, R. Menegazzo, N. Marginean, G. Montagnoli, D. Napoli, D. Pierroutsakou, G. Pollarolo, M. Romoli, M. Sandoli, F. Scarlassara, S. Szilner, N. Toniolo, M. Trotta and Y. Wu. *PRISMA - a magnetic spectrometer for heavy ions at LNL.* Nuclear Physics A 734, E1 (2004). Proceedings of the Eighth International Conference on Nucleus-Nucleus Collisions (NN2003).

[73] F. Cappuzzello, C. Agodi, D. Carbone and M. Cavallaro. *The MAGNEX spectrometer: Results and perspectives.* The European Physical Journal A 52, 167 (2016).

[74] M. Rejmund, B. Lecornu, A. Navin, C. Schmitt, S. Damoy, O. Delaune, J. Enguerrand, G. Fremont, P. Gangnant, L. Gaudefroy, B. Jacquot, J. Pancin, S. Pullanhiotan and C. Spitaels. *Performance of the improved larger acceptance spectrometer: VAMOS++.* Nuclear Instruments and Methods in Physics Research Section A: Accelerators, Spectrometers, Detectors and Associated Equipment 646, 184 (2011).

[75] C. Schmitt, M. Rejmund, A. Navin, B. Lecornu, B. Jacquot, G. de France, A. Lemasson, A. Shrivastava, P. Greenlees, J. Uusitalo, K. Subotic, L. Gaudefroy, C. Theisen, B. Sulignano, O. Dorvaux and L. Stuttgé. *New gas-filled mode of the large-acceptance*

spectrometer VAMOS. Nuclear Instruments and Methods in Physics Research Section A: Accelerators, Spectrometers, Detectors and Associated Equipment 621, 558 (2010).

[76] D. Beaumel. *The GASPARD project*. Nuclear Instruments and Methods in Physics Research Section B: Beam Interactions with Materials and Atoms 317, 661 (2013).

[77] Y. Blumenfeld, F. Auger, J. Sauvestre, F. Maréchal, S. Ottini, N. Alamanos, A. Barbier, D. Beaumel, B. Bonnereau, D. Charlet, J. Clavelin, P. Courtat, P. Delbourgo-Salvador, R. Douet, M. Engrand, T. Ethvignot, A. Gillibert, E. Khan, V. Lapoux, A. Lagoyannis, L. Lavergne, S. Lebon, P. Lelong, A. Lesage, V. Ven, I. Lhenry, J. Martin, A. Musumarra, S. Pita, L. Petizon, E. Pollacco, J. Pouthas, A. Richard, D. Rougier, D. Santonocito, J. Scarpaci, J. Sida, C. Soulet, J. Stutzmann, T. Suomijärvi, M. Szmigiel, P. Volkov and G. Voltolini. *MUST: A silicon strip detector array for radioactive beam experiments*. Nuclear Instruments and Methods in Physics Research Section A: Accelerators, Spectrometers, Detectors and Associated Equipment 421, 471 (1999).

[78] E. Pollacco, D. Beaumel, P. Roussel-Chomaz, E. Atkin, P. Baron, J. Baronick, E. Becheva, Y. Blumenfeld, A. Boujrad, A. Drouart, F. Druillole, P. Edelbruck, M. Gelin, A. Gillibert, C. Hounarner, V. Lapoux, L. Lavergne, G. Leberthe, L. Leterrier, V. Le Ven, F. Lugiez, L. Nalpas, L. Olivier, B. Paul, B. Raine, A. Richard, M. Rouger, F. Saillant, F. Skaza, M. Tripon, M. Vilmay, E. Wanlin and M. Wittwer. *MUST2: A new generation array for direct reation studies*. In *The 4th International Conference on Exotic Nuclei and Atomic Masses* (Springer, Berlin, Heidelberg, 2005).

[79] M. Assié, E. Clément, A. Lemasson, D. Ramos, A. Raggio, I. Zanon, F. Galtarossa, C. Lenain, J. Casal, F. Flavigny, A. Matta, D. Mengoni, D. Beaumel, Y. Blumenfeld, R. Borcea, D. Brugnara, W. Catford, F. de Oliveira, F. Delaunay, N. De Séréville, F. Didierjean, C. Diget, J. Dudouet, B. Fernández-Domínguez, C. Fougères, G. Frémont, V. Girard-Alcindor, A. Giret, A. Goasduff, A. Gottardo, J. Goupil, F. Hammache, P. John, A. Korichi, L. Lalanne, S. Leblond, A. Lefevre, F. Legruel, L. Ménager, B. Million, C. Nicolle, F. Noury, E. Rauly, K. Rezynkina, E. Rindel, J. Rojo, M. Siciliano, M. Stanoiu, I. Stefan and L. Vatrinet. *The MUGAST-AGATA-VAMOS campaign: Set-up and performances*. Nuclear Instruments and Methods in Physics Research Section A: Accelerators, Spectrometers, Detectors and Associated Equipment 1014, 165743 (2021).

[80] A. Matta, P. Morfouace, N. de Séréville, F. Flavigny, M. Labiche and R. Shearman. *NPTool: a simulation and analysis framework for low-energy nuclear physics experiments*. Journal of Physics G: Nuclear and Particle Physics 43, 045113 (2016).

[81] S. Ottini-Hustache, C. Mazur, F. Auger, A. Musumarra, N. Alamanos, B. Cahan, A. Gillibert, A. Lagoyannis, O. Maillard, E. Pollacco, J. Sida and M. Riallot. *CATS, a low pressure multiwire proportionnal chamber for secondary beam tracking at GANIL*. Nuclear Instruments and Methods in Physics Research Section A: Accelerators, Spectrometers, Detectors and Associated Equipment 431, 476 (1999).

[82] M. Febbraro, D. Walter, S. Shadrick, S. Pain, K. Chipps, C. Thornsberry and E. Lesser. *Improved technique for preparation of deuterated-polyethylene targets*. Nuclear Instruments and Methods in Physics Research Section B: Beam Interactions with Materials and Atoms 410, 53 (2017).

[83] S. Devons, G. Manning and D. S. P. Bunbury. *Measurement of γ-Transition Lifetimes by Recoil Methods.* Proceedings of the Physical Society 68, 18 (1955).

[84] T. Alexander and J. Forster. *Lifetime measurements of excited nuclear levels by Doppler-shift methods.* In *Advances in Nuclear Physics* (Springer, 1978), pp. 197–331.

[85] J. Lindhard, M. Scharff and H. E. Schiøtt. *Range concepts and heavy ion ranges* (Munksgaard Copenhagen, 1963).

[86] A. Lopez-Martens, K. Hauschild, A. Korichi, J. Roccaz and J.-P. Thibaud. *γ-ray tracking algorithms: a comparison.* Nuclear Instruments and Methods in Physics Research Section A: Accelerators, Spectrometers, Detectors and Associated Equipment 533, 454 (2004).

[87] D. Bazzacco. *The Advanced Gamma Ray Tracking Array AGATA.* Nuclear Physics A 746, 248 (2004). Proceedings of the Sixth International Conference on Radioactive Nuclear Beams (RNB6).

[88] *Radware webpage.*

[89] E. Clement, R. Pérez-Vidal, J. Dudouet, J. Ljugvall, A. Lopez-Martens, A. Korichi and J. Piot. *On the AGATA performances at low γ-ray energies.* In preparation (2021).

[90] S. Agostinelli et al. *Geant4—a simulation toolkit.* Nuclear Instruments and Methods in Physics Research Section A: Accelerators, Spectrometers, Detectors and Associated Equipment 506, 250 (2003).

[91] J. F. Ziegler, M. Ziegler and J. Biersack. *SRIM – The stopping and range of ions in matter (2010).* Nuclear Instruments and Methods in Physics Research Section B: Beam Interactions with Materials and Atoms 268, 1818 (2010). 19th International Conference on Ion Beam Analysis.

[92] O. Tarasov and D. Bazin. *LISE++: Exotic beam production with fragment separators and their design.* Nuclear Instruments and Methods in Physics Research Section B: Beam Interactions with Materials and Atoms 376, 185 (2016). Proceedings of the XVIIth International Conference on Electromagnetic Isotope Separators and Related Topics (EMIS2015), Grand Rapids, MI, U.S.A., 11-15 May 2015.

[93] *Nuclear Data Service webpage.*

[94] E. Farnea, F. Recchia, D. Bazzacco, T. Kröll, Z. Podolyák, B. Quintana and A. Gadea. *Conceptual design and Monte Carlo simulations of the AGATA array.* Nuclear Instruments and Methods in Physics Research Section A: Accelerators, Spectrometers, Detectors and Associated Equipment 621, 331 (2010).

[95] P. Young. *Everything You Wanted to Know About Data Analysis and Fitting but Were Afraid to Ask* (Springer International Publishing, 2015).

[96] S. Bogner, R. Furnstahl and A. Schwenk. *From low-momentum interactions to nuclear structure.* Progress in Particle and Nuclear Physics 65, 94 (2010).

[97] A. Tichai, J. Langhammer, S. Binder and R. Roth. *Hartree–Fock many-body perturbation theory for nuclear ground-states.* Physics Letters B 756, 283 (2016).

[98] V. Somà, T. Duguet and C. Barbieri. *Ab initio self-consistent Gorkov-Green's function calculations of semimagic nuclei: Formalism at second order with a two-nucleon interaction.* Physical Review C 84, 064317 (2011).

[99] H. Hergert, S. Bogner, T. Morris, A. Schwenk and K. Tsukiyama. *The In-Medium Similarity Renormalization Group: A novel ab initio method for nuclei.* Physics Reports 621, 165 (2016). Memorial Volume in Honor of Gerald E. Brown.

[100] G. Hagen, T. Papenbrock, M. Hjorth-Jensen and D. J. Dean. *Coupled-cluster computations of atomic nuclei.* Reports on Progress in Physics 77, 096302 (2014).

[101] H. Hergert. *A Guided Tour of ab initio Nuclear Many-Body Theory.* Frontiers in Physics 8, 379 (2020).

[102] A. Ekström, G. R. Jansen, K. A. Wendt, G. Hagen, T. Papenbrock, B. D. Carlsson, C. Forssén, M. Hjorth-Jensen, P. Navrátil and W. Nazarewicz. *Accurate nuclear radii and binding energies from a chiral interaction.* Physical Review C 91, 051301 (2015).

[103] N. M. Parzuchowski, S. R. Stroberg, P. Navrátil, H. Hergert and S. K. Bogner. *Ab initio electromagnetic observables with the in-medium similarity renormalization group.* Physical Review C 96, 034324 (2017).

[104] A. Maj, F. Azaiez, D. Jenkins, C. Schmitt, O. Stezowski, J. Wieleczko, D. Balabanski, P. Bednarczyk, S. Brambilla, F. Camera, D. Chakrabarty, M. Chełstowska, M. Ciemała, S. Courtin, M. Csatlos, Z. Dombradi, O. Dorvaux, J. Dudek, M. Erduran, S. Ertuürk, B. Fornal, S. Franchoo, G. Georgiev, J. Gulyás, S. Harissopoulos, P. Joshi, M. Kicińska-Habior, M. Kmiecik, A. Krasznahorkay, G. Anil Kumar, S. Kumar, M. Labiche, I. Mazumdar, K. Mazurek, W. Meczyński, S. Myalski, V. Nanal, P. Napiorkowski, J. Peyre, J. Pouthas, O. Roberts, M. Rousseau, J. Scarpaci, A. Smith, I. Stefan, J. Strachan, D. Watts and M. Ziebliński. *The PARIS project.* In *Acta Physica Polonica B* (2009), volume 40, p. 565.

[105] K. Tsukiyama, S. K. Bogner and A. Schwenk. *In-medium similarity renormalization group for open-shell nuclei.* Physical Review C 85, 061304 (2012).

[106] J. Simonis, S. R. Stroberg, K. Hebeler, J. D. Holt and A. Schwenk. *Saturation with chiral interactions and consequences for finite nuclei.* Physical Review C 96, 014303 (2017).

[107] V. Somà, C. Barbieri and T. Duguet. *Ab initio self-consistent Gorkov-Green's function calculations of semi-magic nuclei: Numerical implementation at second order with a two-nucleon interaction.* Physical Review C 89, 024323 (2014).

[108] V. Somà, C. Barbieri and T. Duguet. *Ab initio Gorkov-Green's function calculations of open-shell nuclei.* Physical Review C 87, 011303 (2013).

[109] A. Cipollone, C. Barbieri and P. Navrátil. *Isotopic Chains Around Oxygen from Evolved Chiral Two- and Three-Nucleon Interactions.* Physical Review Letter 111, 062501 (2013).

[110] *Shell model code ANTOINE webpage.*

[111] *BrIcc calculator webpage.*

[112] P. Thirolf, B. Pritychenko, B. Brown, P. Cottle, M. Chromik, T. Glasmacher, G. Hackman, R. Ibbotson, K. Kemper, T. Otsuka, L. Riley and H. Scheit. *Spectroscopy of the* 2_1^+ *state in* ^{22}O *and shell structure near the neutron drip line.* Physics Letters B 485, 16 (2000).

[113] N. Imai, H. J. Ong, N. Aoi, H. Sakurai, K. Demichi, H. Kawasaki, H. Baba, Z. Dombrádi, Z. Elekes, N. Fukuda, Z. Fülöp, A. Gelberg, T. Gomi, H. Hasegawa, K. Ishikawa, H. Iwasaki, E. Kaneko, S. Kanno, T. Kishida, Y. Kondo, T. Kubo, K. Kurita, S. Michimasa, T. Minemura, M. Miura, T. Motobayashi, T. Nakamura, M. Notani, T. K. Onishi, A. Saito, S. Shimoura, T. Sugimoto, M. K. Suzuki, E. Takeshita, S. Takeuchi, M. Tamaki, K. Yamada, K. Yoneda, H. Watanabe and M. Ishihara. *Anomalously Hindered E*2 *Strength* $B(E2; 2_1^+ \rightarrow 0^+)$ *in* ^{16}C. Physical Review Letter 92, 062501 (2004).

[114] H. J. Ong, N. Imai, D. Suzuki, H. Iwasaki, H. Sakurai, T. K. Onishi, M. K. Suzuki, S. Ota, S. Takeuchi, T. Nakao, Y. Togano, Y. Kondo, N. Aoi, H. Baba, S. Bishop, Y. Ichikawa, M. Ishihara, T. Kubo, K. Kurita, T. Motobayashi, T. Nakamura, T. Okumura and Y. Yanagisawa. *Lifetime measurements of first excited states in* ^{16,18}C. Phys. Rev. C 78, 014308 (2008).

[115] M. Wiedeking, P. Fallon, A. O. Macchiavelli, J. Gibelin, M. S. Basunia, R. M. Clark, M. Cromaz, M.-A. Deleplanque, S. Gros, H. B. Jeppesen, P. T. Lake, I.-Y. Lee, L. G. Moretto, J. Pavan, L. Phair, E. Rodriguez-Vietiez, L. A. Bernstein, D. L. Bleuel, J. T. Burke, S. R. Lesher, B. F. Lyles and N. D. Scielzo. *Lifetime Measurement of the First Excited* 2^+ *State in* ^{16}C. Physical Review Letter 100, 152501 (2008).

[116] M. Petri, S. Paschalis, R. M. Clark, P. Fallon, A. O. Macchiavelli, K. Starosta, T. Baugher, D. Bazin, L. Cartegni, H. L. Crawford, M. Cromaz, U. Datta Pramanik, G. de Angelis, A. Dewald, A. Gade, G. F. Grinyer, S. Gros, M. Hackstein, H. B. Jeppesen, I. Y. Lee, S. McDaniel, D. Miller, M. M. Rajabali, A. Ratkiewicz, W. Rother, P. Voss, K. A. Walsh, D. Weisshaar, M. Wiedeking, B. A. Brown, C. Forssén, P. Navrátil and R. Roth. *Structure of* ^{16}C*: Testing shell model and ab initio approaches.* Physical Review C 86, 044329 (2012).

[117] S. D. Pain, D. W. Bardayan, J. C. Blackmon, K. Y. Chae, K. A. Chipps, J. A. Cizewski, R. Hatarik, M. S. Johnson, K. L. Jones, R. Kapler, R. L. Kozub, C. Matei, B. H. Moazen, C. D. Nesaraja, P. O'Malley, M. S. Smith and J. S. Thomas. *Development of the ORRUBA Silicon Detector Array.* AIP Conference Proceedings 1090, 570 (2009).

[118] S. Pain, A. Ratkiewicz, T. Baugher, M. Febbraro, A. Lepailleur, A. Ayangeakaa, J. Allen, J. Anderson, D. Bardayan, J. Blackmon, R. Blanchard, S. Burcher, M. Carpenter, S. Cha, K. Chae, K. Chipps, J. Cizewski, A. Engelhardt, H. Garland, K. Jones, R. Kozub, E. Lee, M. Hall, O. Hall, J. Hu, P. O'Malley, I. Marsh, B. Rasco, D. Santiago-Gonzales, D. Seweryniak, S. Shadrick, H. Sims, K. Smith, M. Smith, P.-L. Tai, P. Thompson, C. Thornsberry, R. Varner, D. Walter, G. Wilson and S. Zhu. *Direct Reaction Measurements Using GODDESS.* Physics Procedia 90, 455 (2017). Conference

on the Application of Accelerators in Research and Industry, CAARI 2016, 30 October – 4 November 2016, Ft. Worth, TX, USA.

[119] A. H. Wuosmaa, B. B. Back, S. Baker, B. A. Brown, C. M. Deibel, P. Fallon, C. R. Hoffman, B. P. Kay, H. Y. Lee, J. C. Lighthall, A. O. Macchiavelli, S. T. Marley, R. C. Pardo, K. E. Rehm, J. P. Schiffer, D. V. Shetty and M. Wiedeking. ^{15}C$(d,p)^{16}$C *Reaction and Exotic Behavior in* ^{16}C. Physical Review Letter 105, 132501 (2010).

[120] J. Lighthall, B. Back, S. Baker, S. Freeman, H. Lee, B. Kay, S. Marley, K. Rehm, J. Rohrer, J. Schiffer, D. Shetty, A. Vann, J. Winkelbauer and A. Wuosmaa. *Commissioning of the HELIOS spectrometer.* Nuclear Instruments and Methods in Physics Research Section A: Accelerators, Spectrometers, Detectors and Associated Equipment 622, 97 (2010).

[121] B. A. Watson, J. A. Becker and T. R. Fisher. *Lifetimes of levels in* ^{24}Ne. Physical Review C 9, 1200 (1974).

[122] R. G. H. Robertson and B. H. Wildenthal. *Shell-Model Study of* ^{24}Ne. Physical Review C 8, 241 (1973).

[123] G. Lotay. *Private communication.*

[124] G. Satchler. *Direct Nuclear Reactions* (Oxfort University Press, 1983).

[125] A. M. Moro. *Models for nuclear reactions with weakly bound systems* (2019).

[126] M. Tanabashi et al. *Review of Particle Physics.* Phys. Rev. D 98, 030001 (2018).

[127] S. Baker and R. Cousins. *Clarification of the use of chi-square and likelihood functions in fits to histograms.* Nuclear Instruments and Method in Physics Research 221, 437 (1984).

[128] S. Pain. *ATLAS experiment 1707.*

[129] S. Pain. *ATLAS experiment 1484.*

[130] *VIKAR code webpage.*

List of Figures

List of Tables